UNIVERSITA' DEGLI STUDI DI MESSINA

DOTTORATO DI RICERCA IN FISICA - XXIX CICLO

LASER DRIVEN NUCLEAR ASTROPHYSICS STUDY AT ELI-NP

ANNAMARIA MUOIO

PhD THESIS

COORDINATORE:

PROF. L. TORRISI

TUTOR:

PROF. A. TRIFIRÒ

SSD: FIS/04

CO-TUTOR:

PROF. S. TUDISCO

I spent many days working hard on my doctoral thesis. I have had difficult moments, others joyful, others sad, and without the help and the proximity of my little Mariaemilia, Caterina and Carolina would never managed to find the strength to complete this work. A big thanks goes to my mother Emilia and my father Peppino who has always supported me but now it flew away. Finally a big thank to Gaetano that is my classmate and life partner.

Dedicated to my dear family

"God was always invented to explain mystery. God is always invented to explain those things that you do not understand. Now, when you finally discover how something works, you get some laws which you're taking away from God; you don't need him anymore. But you need him for the other mysteries. So therefore you leave him to create the universe because we haven't figured that out yet; you need him for understanding those things which you don't believe the laws will explain, such as consciousness, or why you only live to a certain length of time — life and death — stuff like that. God is always associated with those things that you do not understand. Therefore I don't think that the laws can be considered to be like God because they have been figured out."

Richard Feynman

ABSTRACT

Given its nature, the plasma state is characterized by a complexity that vastly exceeds the one exhibited by the solid, liquid, and gaseous states.

Correspondingly, the physical properties of nuclear matter (structure, lifetimes, reaction mechanisms etc.) may change inside the plasma.

Thus, the study of these properties represents one of the most far ranging, difficult and challenging research areas today. Implications can cover also others fields, from quantum physics to cosmology, astrophysics etc.

One of the crucial topics related to nuclear reactions in the ultra-low energy regime is the electron screening, which prevents a direct measurement of the bare nucleus cross section at the energies of astrophysical interest.

Since in the laboratory interacting particles are in the form of neutral atoms, molecules or ions, in direct experiments at very low beam energy, electron clouds partially screen the nuclear charges thus reducing the Coulomb suppression. This results in an enhancement of the measured cross section compared with the bare nucleus one.

The electron screening effect is significantly influenced by the target conditions and composition. In this context, it is of particular importance the measurement of cross-sections at extremely low energetic domains including plasmas effect, i.e. in an environment that under some circumstances and assumptions can be considered as "stellar-like" (for example, the study of the role played by free/bounded electrons on the Coulombian screening can be done in dense and warm plasmas).

A further key point is connected with the fact that in such environment nuclear reactions can be triggered also by the excited states of the interacting nuclei.

Thus, determining the appropriate experimental conditions that set the role of the excited states in the stellar environment can strongly contribute to the development of nuclear astrophysics. The study of direct measurements of reaction rates in plasma offers this chance.

The future availability of high-intensity laser facilities capable of delivering tens of peta-watts of power into small volumes of matter at high repetition rates will give

the unique opportunity to investigate nuclear reactions and fundamental interactions under extreme plasma conditions, including also the influence of huge magnetic and electric fields, shock waves, intense fluxes of X and γ-rays originating during plasma formation and expansion stages.

A laser is a unique tool to produce plasma and very high fluxes of photon and particle beams in very short duration pulses. Both aspects are of great interest for fundamental nuclear physics studies. In a plasma, the electron–ion interactions may modify atomic and nuclear level properties. This is of prime importance for the population of isomeric states and for the issue of energy storage in nuclei. Nuclear properties in the presence of very high electromagnetic fields, nuclear reaction rates or properties in hot and dense plasmas are new domains of investigation. Furthermore, with a laser it is possible to produce electric and magnetic fields strong enough to change the binding energies of electronic states. If nuclear states happen to decay via internal conversion (IC) through these perturbed states, a modification of their lifetimes will be seen. The excitation of nuclear levels by means of energy transfer from the atomic part to the nuclear part of an atom is the subject of a large number of investigations. Their goal is to find an efficient mechanism to populate nuclear isomers in view of further applications to energy storage and development of lasers based on nuclear transitions. In addition, other new topics can be conveniently explored such as three-body fusion reactions as those predicted by Hoyle.

Several Laser facilities are under construction around the world to push the physics beyond the actual level of knowledge. Among of these, the Extreme Light Infrastructure for Nuclear Physics at Magurele (Bucharest) in Romania, will be the only one devoted to nuclear physics studies.

ELI-NP will be made up of a very high intensity laser system, consisting of two 10 PW laser arms able to reach intensities of 10^{23} W/cm2 and electrical fields of 10^{15} V/m, and very short wavelength γ beams with very high brilliance (10^{13} γ/s) and energy up to 19.5 MeV. This combination allows for three types of experiments: stand-alone high power laser experiments, stand-alone γ beam experiments and combined experiments of both facilities. Here the low repetition rate (1/min) of the high power laser requires the same low repetition rate for the γ beam in combined experiments. While the standalone γ beam will be used with typically

120 kHz, the low repetition mode requires few very intense γ pulses. With the high power laser we do not plan to interact with nuclear dynamics directly, but we use the laser for ion acceleration or to produce relativistic electron mirrors followed by a coherent reflection of a second laser beam in order to generate very brilliant X-ray or γ beams. We plan to use these beams later to produce exotic nuclei or to perform new γ spectroscopy experiments in the energy or time domain. The production of heavy elements in the Universe, a central question of astrophysics, will be studied within ELI-NP in several experiments.

In this Ph.D. thesis some of the activities, related to the project of study of nuclear astrophysics at ELI-NP will be reported and discussed.

The Thesis is organized as follows;

Chapter I: a general introduction is given to present the main open problems on nuclear astrophysics and the opportunity offered by the laser matter interaction scheme.

Chapter II: the physics of laser matter interaction is discussed.

Chapter II: a short presentation of the Laser facility around the world is given with special attention to the ELI-NP.

Chapter III: the research project et ELI-NP is presented.

Chapter IV: the studies performed to prepare the future activities at ELI-NP are discussed: simulations, laser matter interaction test, R&D activities on plasma and nuclear detectors.

Chapter V: the results of the tests performed on the detector prototypes are presented and discussed.

More in detail, in Chapter III the idea of using a colliding plasma suitable for nuclear physics studies and the proposed schema of interaction is presented. A first laser pulse imping on a primary solid target producing plasma through the TNSA (Target Normal Sheath Acceleration) acceleration scheme. The rapidly streaming plasma impacts on a secondary plasma, prepared through the interaction of a second synchronized laser pulse on a gas jet target.

The produced ions expand along a cone, whose axis is normal to the target surface, with a relatively low emittance, while the properties of the secondary plasma

(working as a "plasma target") can be modified or tuned, depending on the energetic domains one wants to explore. By using femtosecond pulses, secondary plasma temperatures lie in the tens of eV range. For reactions with fully thermalized plasmas at medium-high ion temperatures, the duration of the secondary laser beam can be extended in the nanosecond domain. Simulations about the two plasmas interaction have been performed with different models. Such work has been focalized to evaluate the total reaction rate and further the possible information, which could be extracted on the reaction cross-sections.

Chapter IV is dedicated to the TNSA studies. Target Normal Sheath Acceleration is the key mechanism for the production of the primary plasma using a high power - femtosecond laser beam imping on a solid thin target (1-20 μm). TNSA was intensively studied in the last years; experiments and models show that this acceleration scheme works very well in the intensity domain between 10^{18}-10^{20} W/cm2. The observed ion energy distributions have an exponential shape with a high-energy cut-off, linearly depending on the laser intensity and scaling with the atomic number. These experimental observations are well described and predicted by theoretical models. A further fine-tuning can be done acting on other parameters such as the laser incident angle or polarization, the structure of the target surface, or the target thickness. In this respect, we performed several experimental campaigns in order to refine the information on TNSA. The activity was conduced at the Intense Laser Irradiation Laboratory (ILIL), in Pisa in the area of CNR-INO. By using the available 10 TW/10Hz system, we carried out a systematic experimental investigation to identify the role of target properties on TNSA, with special attention to target thickness and dielectric properties. It has focused on the results obtained using a Thomson Parabola Spectrometer (TPS). During the experiment several targets have been used. These targets have been selected to study the acceleration mechanism and its dependence on the surface/bulk contribution or on the possible dependence of a metal layer deposited on the irradiated surface, etc.

Chapter V is focussed on the R&D activity performed on the prototypes of a highly segmented detection system for neutrons and charged particles which will be realized and installed at ELI-NP for the conduction of the experiments. The segmentation is required for the reconstruction of the reaction's kinematics.

The "ideal" neutron detection module for these studies must have high efficiency, good discrimination of gammas from neutrons, good timing performance for Time of Flight neutron energy reconstruction. In addition, it must be able to work in hard environmental conditions, like the ones established in the laser-matter interaction area.

All these requirements can be fulfilled by a configuration based on PPO-Plastic scintillators plus a SiPM readout and a totally digital acquisition of the multi-hit signals.

The charged particle detectors must be able to work in plasma environment and then must be insensible to visible light and experience high resistance to radiation damage. SiC detectors have been recently proven to have excellent performance in this respect joint to the high energy and time resolution.

CONTENTS

LIST OF TABLES

LIST OF FIGURES

(S1) AND EXCITED TRIPLET (T1) STATES NONRADIATIVELY RELAXES TO THE
CONFIGURATION, AS SHOWN .THE BASIC PHYSICAL PROCESSES LEADING TO THE DELAYED
FLUORESCENCE CHARACTERISTIC OF NEUTRON EXCITATION OF ORGANICS WITH PHENYL
GROUPS IS SHOWN. SINCE THE TRIPLET IS KNOWN TO BE MOBILE IN SOME COMPOUNDS,
THE ENERGY MIGRATES UNTIL THE COLLISION OF TWO TRIPLETS COLLIDE AND
EXPERIENCE AN AUGER UPCONVERSION PROCESS, SHOWN AS EQUATION 1:T1+T1→S0+S1
.IN EQUATION 1, T1 IS A TRIPLET, S0 IS THE GROUND STATE, AND S1 IS A FIRST EXCITED
STATE. FINALLY, THE DELAYED SINGLET EMISSION OCCURS WITH A DECAY RATE
CHARACTERISTIC OF THE MIGRATION RATE AND CONCENTRATION OF THE TRIPLET
POPULATION, WHICH IS REPRESENTED AS EQUATION 2: S1→S0+HV . IN EQUATION 2, HV IS
FLUORESCENCE, WHILE S0 IS THE GROUND STATE AND S1 IS A FIRST EXCITED STATE. THE
ENHANCED LEVEL OF DELAYED EMISSION FOR NEUTRONS ARISES FROM THE SHORT
RANGE OF THE ENERGETIC PROTONS PRODUCED FROM NEUTRON COLLISIONS (THEREBY
YIELDING A HIGH CONCENTRATION OF TRIPLETS), COMPARED TO THE LONGER RANGE OF
THE ELECTRONS FROM THE GAMMA INTERACTIONS. THE RESULTING HIGHER
CONCENTRATION OF TRIPLETS FROM NEUTRONS, COMPARED TO GAMMA INTERACTIONS,
LEADS TO THE FUNCTIONALITY OF PSD. THE OBSERVATION OF PSD IS BELIEVED TO BE IN
PART RELATED TO THE BENZENE RING STRUCTURE, ALLOWING FOR THE MIGRATION OF

LIST OF APPENDICES

.

CHAPTER I

FUNDAMENTAL ASPECT OF NUCLEAR PHYSICS IN PLASMA

I.1 Introduction

Accurate measurements of nuclear reaction rates of proton and alpha burning processes are essential for the correct understanding of many astrophysical processes, such as stellar evolutions, supernova explosions and Big Bang nucleosynthesis, etc.

To this aim direct and indirect measurements of the relevant cross sections have been performed over the years. Since in the laboratory interacting particles are in the form of neutral atoms, molecules or ions, in direct experiments at very low beam energy, electron clouds partially screen the nuclear charges thus reducing the Coulomb suppression [Sal54]. This results in an enhancement of the measured cross section compared with the bare nucleus one [NACRE]. The electron screening effect is significantly affected by the target conditions and composition [Lip10]; it is of particular importance the measurement of cross-sections at extremely low energetic domains including plasmas effect, i.e. in an environment that under some circumstances and assumptions can be considered as "stellar-

like" (for example, for the study of the role played by free/bounded electrons on the Coulombian Screening can be done in dense and warm plasmas).

Electron screening prevents a direct measurement of the bare nucleus cross section at the energies of astrophysical interest. In the last decade, the bare cross section has been successfully measured in certain cases by using several indirect methods [Spi11].

Usually, astrophysical relevant reactions are performed in laboratories with both target and projectile in their ground state. However, at temperatures higher than about 10^8K, an important role can be also played by the excited states, as already deeply discussed in the pioneering theoretical work of Bahcall and Fowler [Bah69]. In that case, the authors studied the influence of low lying excited ^{19}F states on the final ^{19}F(p,alpha) reaction, predicting an increase of a factor of about 3 in reaction rate at temperatures of about 1-5 GK.

Thus determining the appropriate experimental conditions that allow the role of the excited states in the stellar environment could strongly contribute to the development of nuclear astrophysics. The study of direct measurements of reaction rates in plasma offers this chance. In addition others new topics can be conveniently explored such as three body fusion reactions as those predicted by Hoyle [Hoy46], lifetime changes of unstable elements [Lim06] or nuclear and atomic levels [Han07] in different plasma environments; other fundamental physics aspects like non-extensive statistical thermodynamics [Tsa09] can be investigated in order to validate/confute the general assumption of local thermal equilibrium that is traditionally done for plasmas.

The future availability of high-intensity laser facilities capable of delivering tens of peta-watts of power (e.g. ELI-NP) into small volumes of matter at high repetition rates will give the unique opportunity to investigate nuclear reactions and fundamental interactions under extreme conditions of density and temperature that can be reached in laser generated plasmas [Mas10], including the influence of huge magnetic and electric field, shock waves, intense fluxes of X and ©-ray

originated during plasma formation and expansion stages. In the next paragraphs, all these aspects will be described in detail.

I.2 Termonuclear reactions

The Sun and other "main sequence" stars (quiescent burning hydrogen in their core quiescently) evolve very slowly by adjusting their central temperature in such a way that the average thermal energy of a nucleus is small compared to the Coulomb repulsion encountered by an ion-ion pair encounters. This is how stars live for astronomically long times. The classical turning point radius for a projectile of charge Z_2 and kinetic energy E_p

(in a Coulomb potential $V_C = Z_1 Z_2 e^2/r$, and an effective height of the Coulomb barrier $E_C = Z_1 Z_2 e^2/R_n = 550$ keV for a p+p reaction), is $r_d = Z_1 Z_2 e^2/E_p$. Thus, classically a p+p reaction would proceed only when the kinetic energy exceeds 550 keV. Since the number of particles traveling at a given speed is given by the Maxwell – Boltzmann distribution $\phi(E)$, only the tail of the Maxwell – Boltzmann distribution above 550 keV is effective when the typical thermal energy is 0.86 keV ($T_9 = 0.01$). The ratio of the tails of the Maxwell – Boltzmann distributions, $\phi(550$ keV$)/\phi(0.86$ keV$)$, is quite minuscule, and thus classically at typical stellar temperatures this reaction will be virtually absent. Although classically a particle with projectile energy E_p cannot penetrate beyond the classical turning point, quantum mechanically, one has a finite value of the square wave function at the nuclear radius R_n : $|\psi(R_n)|^2$. The probability that incoming particle penetrates the barrier is

$$P = \frac{|\psi(R_n)|^2}{|\psi(R_C)|}$$

Where $\psi(r)$ are the wavefunctions at correponding points. Bethe [Bet37] solved the Schroedinger equation for the Coulomb potential and obtained the transmission probability

$$P = e^{\left(-2KR_C\left[\frac{tan^{-1}\left(\frac{R_C}{R_n}-1\right)^{1/2}}{\left(\frac{R_C}{R_n}-1\right)^{1/2}} - \frac{R_n}{R_C}\right]\right)}$$

with $K = \left[\frac{2\mu}{\hbar^2}(E_C - E)\right]^{\frac{1}{2}}$.

This probability reduces to a much simpler relation at the low energy limit E<<E$_c$, which is equivalent to the classical turning point R$_c$ being much larger than the nuclear radius R$_n$. The probability is

$$P = e^{\left[-\frac{2\pi Z_1 Z_2 e^2}{(hv)}\right]} = e^{\left[-31.3 Z_1 Z_2\left(\frac{\mu}{E}\right)^{1/2}\right]}$$

where in the second equality μ is the reduced mass in u and E is the center of mass energy in keV. The exponential quantity involving the square brackets in the second expression is called the Gamow factor. The reaction cross section between particles of charge Z$_1$ and Z$_2$ has this exponential dependence due to the Gamow factor. In addition, because the cross sections are essentially "area" proportional to $\lambda^2 \propto \frac{1}{E}$, it is customary to write the cross section with these two energy dependencies filtered out,

$$\sigma(E) = \frac{e^{-2\pi\eta}}{E} S(E)$$

where the factor S(E) is called the astrophysical (or nuclear) S-factor.
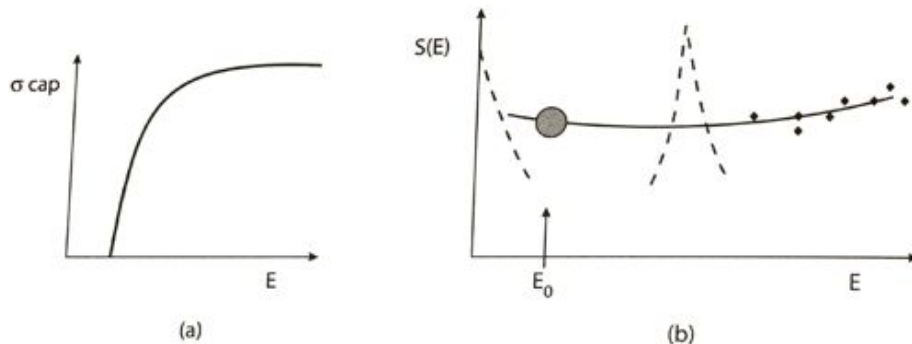
fig. I-1 Cross section and astrophysical S-factor for charged particle reactions as a function of beam energy. The effective range of energy in stellar interiors is usually far less than the Coulomb barrier energy E$_c$ or the lower limit E$_L$, where laboratory measurements can be carried out. The cross section drops sharply in the region of astrophysical interest, whereas the change much less severe

for the S-factor. Therefore, necessary extrapolation of laboratory data to lower energies relevant for astrophysical situations is more reliable in the case of the S-factor.

The S-factor may contain degeneracy factors due to spin, for example, $\left[\frac{(2J+1)}{(2J_1+1)(2J_2+1)}\right]$, as reaction cross sections are summed over final states and averaged over initial states. Because the rapidly varying parts of the cross section (with energy) are thus filtered out, the S-factor is a slowly varying function of the center of mass energy, at least for the non-resonant reactions. It is thus much safer to extrapolate S(E) to the energies relevant for astrophysical environments from the laboratory data, which are usually available generated at higher energies (due to difficulties of measuring small cross sections), than directly to extrapolate the σ(E), which contains the Gamow transmission factor (see fig. I-1)

Additionally, in order to relate σ(E) quantity measured in laboratory and S(E) (relevant quantity in solar interior, a correction factor f_0 due to the effects of electron screening needs to be taken into account [Sal54]. In the stellar core with a temperature T, reacting particles have many different velocities (energies) according to a Maxwell–Boltzmann distribution

$$\phi(v) = 4\pi v^2 \left(\frac{\mu}{2\pi kT}\right)^{3/2} e^{\left[-\frac{\mu v^2}{2kT}\right]} \propto E e^{\left(-\frac{E}{kT}\right)}$$

Nuclear cross-section or the reaction rates which also depend upon the relative velocity (or equivalently the center of mass energy) therefore need to be averaged over the thermal velocity (energy) distribution. Therefore, the thermally averaged reaction rate per particle pair is

$$\langle \sigma v \rangle = \int_0^\infty \phi(v)\sigma(v)v\,dv = \left(\frac{8}{\pi\mu}\right)^{1/2} \frac{1}{(kT)^{3/2}} \int_0^\infty \sigma(E)E e^{\left(-\frac{E}{kT}\right)}\,dE.$$

Utilizing the astrophysical S-factor and the energy dependence of the Gamow factor, the thermally averaged reaction rate per pair is:

$$\langle \sigma v \rangle = \left(\frac{8}{\pi\mu}\right)^{1/2} \frac{1}{(kT)^{3/2}} \int_0^\infty S(E) e^{\left(-\frac{E}{kT}-\frac{b}{\sqrt{E}}\right)}\,dE,$$
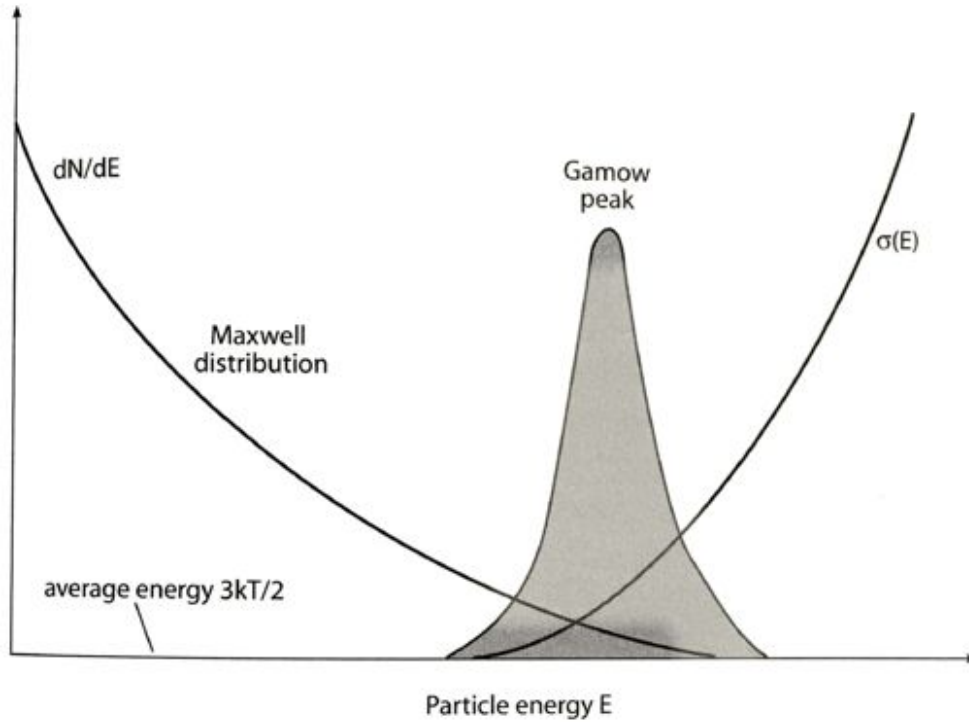
fig. I-2 The Gamov peak is a convolution of the energy distribution of the Maxwell-Boltzmann probability and the quantum mechanical Coulomb barrier transmission probability. The peak in the shaded region near energy E_0 is the Gamow peak that gives the highest probability for charged particle reactions to take place. Usually the Gamow peak is at a much higher energy than kT, and in the figure the ordinate scale(for Gamow peak) is magnified with respect to those of the Maxwell-Boltzmann and barrier penetration factors.

with $b^2 = E_G = 2\mu(2\pi^2 e^2 Z_1 Z_2/h)^2 = 0.978 \ \mu \ (Z_1 Z_2)^2$ MeV, E_G being called the Gamow energy. Note that in the expression for the reaction rate above, at low energies, the exponential term $\exp(-b/E^{1/2}) = \exp[-(E_G/E)^{1/2}]$ becomes very small, whereas at high energies the Maxwell – Boltzmann factor $\exp(-E/kT)$ vanishes. Hence there would be a peak (at energy, say, E_0) of the integrand for the thermally averaged reaction rate per pair (see fig. I-2). The exponential part of the energy integrand can be approximated as

$$e^{\left[-\frac{E}{kT} - bE^{-1/2}\right]} \sim C e^{\left[-\left(\frac{E-E_0}{\Delta/2}\right)^2\right]},$$

where

$$C = e^{\left[-\frac{E_0}{kT} - bE_0^{-1/2}\right]} = e^{\left(-\frac{3E_0}{kT}\right)} = e^{(-\tau)},$$

with

$$E_0 = \left(\frac{bkT}{2}\right)^{\frac{3}{2}} = 1.22 keV (Z_1^2 Z_2^2 \mu T_6^2)^{\frac{1}{3}},$$

Since most stellar reactions happen at a fairly narrow band of energies, S(E) will have a nearly constant value over this band averaging to S_0. With this, the reaction rate per pair of particles turns out to be

$$\langle \sigma v \rangle = \left[\frac{8}{\pi \mu (kT)^3}\right]^{1/2} S_0 \int_0^\infty e^{\left(-\tau - 4\left(\frac{E-E_0}{\Delta}\right)^2\right)} dE = 4.5 \times 10^{14} \frac{S_0}{A Z_1^2 Z_2^2} \tau^2 e^{-\tau} cm^3 s^{-1}.$$

Here,

$$\tau = 3\frac{E_0}{kT} = 42.5 \left(\frac{Z_1^2 Z_2^2 \mu}{T_6}\right)^{\frac{1}{3}}.$$

The maximum value of the integrand in the above equation is

$$I_{max} = e^{(-\tau)}.$$

The values of E_0, I_{max}, Δ, and of the Coulomb barrier for several reactions are shown in table I-1 for $T_6=15$.

Table I- 1 Parameters of the thermally averaged reaction rates at $T_6=15$

Reaction	Coulomb barrier (MeV)	Gamow peak (E_0) (keV)	I_{max} ($e^{-3E_0/kT}$)	Δ (keV)	$(\Delta)I_{max}$
p + p	0.55	5.9	1.1×10^{-6}	6.4	7×10^{-6}
p + N	2.27	26.5	1.8×10^{-27}	13.6	2.5×10^{-26}
$\alpha + C^{12}$	3.43	56	3×10^{-57}	19.4	5.9×10^{-56}
$O^{16} + O^{16}$	14.07	237	6.2×10^{-239}	40.4	2.5×10^{-237}

As the nuclear charge increases, the Coulomb barrier increases, and the Gamow peak E_0 also shifts toward higher energies. Note how rapidly the maximum of the integrand I_{max} decreases with the nuclear charge and the Coulomb barriers. The

effective width Δ is a geometric mean of E_0 and kT, and $\Delta/2$ is much less rapidly varying between reactions (for kT $<<E_0$). The rapid variation of I_{max} indicates that, of several nuclei present in the stellar core, the nuclear pairs with the smallest Coulomb barrier will have the largest reaction rates. The relevant nuclei will be consumed quite rapidly at that stage. When nuclei with the smallest Coulomb barrier are consumed, there is a temporary dip in the nuclear generation rate, and the star contracts gravitationally until the temperature rises to a point where nuclei with the next lowest Coulomb barrier will start burning. The above discussion assumes that a bare nuclear Coulomb potential is seen by the charged projectile. For nuclear reactions measured in the laboratory, the target nuclei are in the form of atoms with electron clouds surrounding the nucleus and giving rise to a screened potential, the total potential then goes to zero outsides the atomic radius. Thus the effect of the screening is to reduce the effective height of the Coulomb barrier. Atoms in the stellar interiors are in most cases in a highly stripped state, and nuclei are immersed in a sea of free electrons that tend to cluster near the nucleus.

I.3 Electron screening

The rates of many thermonuclear reactions, which can take place under various conditions in the interior of the Sun and stars, have been and are being calculated ([Bet39], [Gam49], [Sal53]). These reactions can be pictured as follows. At the high temperatures of the stellar interiors all (or practically all) the atoms are ionized. Two bare nuclei (of charge Z_1 and Z_2 respectively) collide with each other with relative kinetic energy E, arising from the thermal motion of the gas. For the two nuclei to undergo a nuclear transformation they must approach to distances of the order of 10^{-13} cm (nuclear radius). As the particles approach each other they experience a Coulomb repulsion and the Coulomb barrier (electrostatic potential for a separation of the order of a nuclear radius) is very large compared to the mean thermal energy kT. An important factor in the reaction rate then is the barrier penetration factor, the probability that nuclei approach each other so

closely that nuclear forces come into play. The reaction rate is proportional to the following integral

$$\int_0^\infty dE[E^{\frac{1}{2}}e^{-E/kT}]P(E)\sigma_{nuc.}(E).$$

The first term in this integrand is the Maxwell-Boltzmann distribution factor (probability of kinetic energy being E). The second factor P is the barrier penetration factor, which depends very strongly on E and on Z_1Z_2 . The last factor σ_{nuc} is a purely nuclear factor which depends on details of the interaction after barrier penetration and usually (but not always) varies fairly slowly with E. In stellar interiors the gas density ρ is high and the average distance **a** between a nucleus and neighbouring electrons and nuclei is small. Each nucleus, even though completely ionized, attracts neighbouring electrons and repels neighbouring nuclei and thus polarizes the surrounding gas somewhat. The nucleus is then completely screened by **a** spherically symmetric negative charge cloud. The radius **R** of this charge cloud is of the same order of the inter-particle distance **a** or larger, depending on the ratio of Coulomb repulsion between neighbouring charges to the mean thermal energy. Hence, when two nuclei approach each other in a collision, each of them carries its screening charge cloud with it and this screening affects the interaction energy between the nuclei. We write the total interaction energy as

$$U_{tot.}(r_{12}) = Z_1Z_2e^2/r_{12} + U(r_{12}).$$

Whether in the laboratory or in the star, nuclear reaction rates are modified due to the presence of electrons. There are two limiting cases, referred to as weak screening and strong screening. Weak screening [Sal54] is applicable when there is a low–density plasma of ions and electrons characterized by a Debye radius and when the average Coulomb energy is much smaller than the thermal energy. In the Debye approximation, the potential between nuclei with nucleon numbers (A_1, Z_1) and (A_2, Z_2) becomes of Yukawa form:

$$V_{screen}(r) = \frac{Z_1Z_2e^2}{r}e^{(-r/r_D)},$$

with the Debye radius being $r_D = \sqrt{\frac{kT}{4\pi e^2 \rho_e N_A \zeta}}, \rho_e$ the electronic density, N_A the Avogadro's number and $\zeta = \sum_i \left[\frac{Z_i(Z_i+1)X_i}{A_i}\right]$ the charge of the plasma. If the fusion reaction happens at distances much smaller than the Debye radius, then the potential can be expanded to first order and the energy shift from the screened potential compared to the unscreened one becomes $U_0 = -\frac{Z_1 Z_2 e^2}{r_D}$. If $U_0 \ll E$, it can be shown that in the weak screening case, the reaction rates become

$$\langle \sigma v \rangle_{ws} = f_{ws} \langle \sigma v \rangle_{vacuum}$$

with a factor $f_{ws} = e^{\left[\frac{U_0}{kT}\right]}$. The other screening limit corresponds to a picture where the nucleus is surrounded by a cloud of uniformly distributed electrons of radius comparable to the inter-ionic distance. This strong screening is typical of the laboratory scenario. In this case, the medium is no longer locally neutral and reactions take place under the influence of strong screening [Sal69]. Many astrophysical reactions are somewhere in between and a number of models have been developed to account for these processes more accurately [Dzi95]

I.4 State of art Electron Screening

Electron Screening has raised a strong interest among nuclear astrophysicist due to its consequences on the calculation of reaction rates at energies in the Gamow peak. Pioneering experiments of Rolfs and collaborators [Str01] [Ali01] put in evidence the enhancement of the cross-section due to the effect of electron clouds surrounding the interacting nuclei. This enhancement is found to be important at low relative energy (few keV) and magnified in implanted metals [Rol01]. In all cases, the electron screening potential energy (U_e) has been deduced by comparing direct data with theoretical extrapolations or with unscreened data obtained via indirect methods [Lan96] [Spi03].

Against the simplified assumption that both projectile and target nuclei were entities without electrons, when trying to reproduce in the laboratory a nuclear reaction between charged particles, projectile and target are in the form of ions and atoms or even ions and molecules respectively.
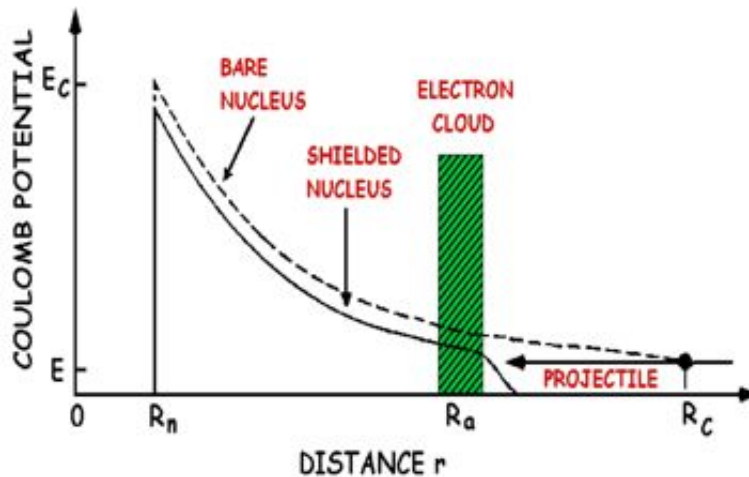
fig. I- 3 Representation of the Coulomb potential modified by the presence of the electrons cloud. The dashed line represents the situation of the bare nucleus. R_a, R_n, E_c and R_c indicates the atomic radius, the nuclear interaction radius, the height of the Coulomb barrier for the bare core and the classical turning point for a particle with energy E.

Considering the case of the target nucleus shown in fig. I-3, for distances greater than the atomic radius **Ra**, the electrostatic potential is annulled, taking the target nucleus not to feel the Coulomb repulsion until it does not overtake the electronic cloud. In the case of high-energy reactions such contribution is not important for the purposes of the dynamics

In the approximation of Born-Oppenheimer, in which atomic and nuclear degrees of freedom are treated separately and dynamic effects such as polarization and deformation of the cloud are neglected, it is possible to derive the shape of the Ue screening potential, which assumes the form:

$$U_{eff}(r) = \frac{Z_a Z_A}{r} - U_e$$

where a and A are the projectile and target nuclei.

Because of importance of calculating precise nuclear fusion rates at low energy in connection with increasingly precise solar-neutrino experiments, attentions has recently been drawn to the question of electron screening in solar fusion reaction. [Sal54] [Dzi95] [Mit77] [Gru01] [Bah98] [Car88] [Lan95] [Sha96] [Dar96] [Bro97] [Gru01] [Joh92].

In this framework, the problem of electron screening has been studied by Salpter for the solar proton-proton fusion reaction by solving numerically the relevant Schrodinger equation, assuming the so called weak screening limit, which corresponds to the Debye Huckel mean field theory. Salpter's derivation was based on a thermodynamic argument, but an alternative approach recovers the same results. The energy dependence of the fusion cross section is given by

$$\sigma(E) \equiv \frac{S(E)}{E} e^{(-2\pi\eta)}.$$

The controlling factor, $e^{(-2\pi\eta)}$ takes into account the probability for the nuclei to tunnel through the Coulomb barrier. In the stellar interior each nucleus, even completely ionized, attracts neighbouring electrons and repels neighbouring nuclei. Thus, the potential between two colliding nuclei is no longer a pure Coulomb one, but a screened potential $V_{sc}(r)$:

$$V_{sc}(r) = \frac{Z_1 Z_2 e^2}{r} e^{(-r/r_D)},$$

where

$$r_D = \zeta^{-1/2} \left(\frac{k_B T_a}{e^2} \right)^{1/2} a$$

is the Debye radius of the cloud. For screened potential, the penetration factor is then given by

$$\Gamma(E) = e^{\left(\frac{-2r_c}{\hbar} \sqrt{2\mu E} \int_0^1 \left[\frac{1}{u} e^{(x(1-u))-1} \right]^{1/2} du \right)},$$

where $x = x(E) = r_c / r_D$. Here r_c is the classical turning point when $V_{sc}(r_c) = E$. If $x \ll r_c$, by expanding the exponential factor, one obtains a simplified expression of the penetration factor given by

$$\Gamma(E) = e^{\left[-2\pi\eta\left(1-\frac{x}{2}\right)\right]} = e^{-2\pi\eta}e^{x\pi\eta},$$

where $x\pi\eta$ depends on the energy. The effect of the correction on the thermally averaged cross section can be approximated by evaluating $x\pi\eta$. Comparing the calculated cross section of the p+p reaction for a standard Coulomb potential with the one using a screened Coulomb potential (calculation is done with Wentzel–Kramers–Brillouin (WKB) method that finds approximate solutions to linear differential equations with spatially varying coefficients), one can determine the screening correction. In Figure I-4 the WKB (dashed curve) and numerical (solid curve) results are shown for the screening correction for the p+p reaction as a function of relative momentum k. The two behaviours are very similar.
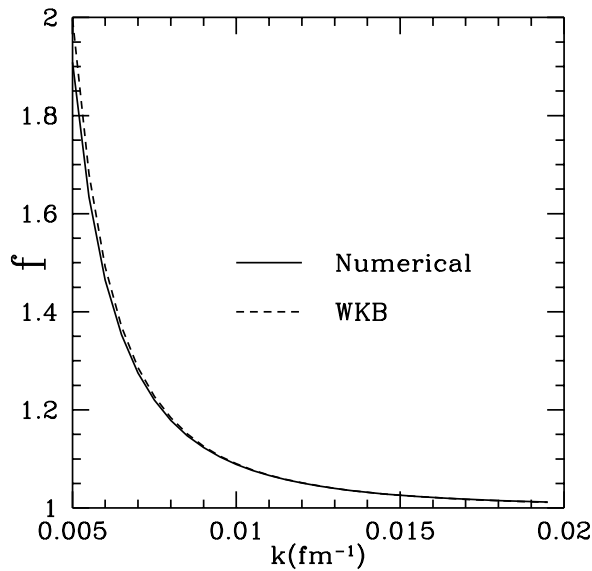
fig. I- 4 The screening enhancement factor as a function of k, where k=μv/h is the center-of-mass momentum. The dashed curve is that for the WKB result, and the solid curve is that for the numerical result.

Suppose that electrons are distributed on a surface of radius R_a, that the projectile is completely ionized, and the target is an atom globally neutral. In this case, U_e may be determined using a simplified model [Ass01]: it considers the potential generated by the cloud at distances of the order of R_a as constant and given by $V_a = Z_a e / R_a$ [Rol04]. Consequently the barrier that incident particle must cross in order that the reaction will take place is:

$$U_{eff}(R_n) = U_{coul}(R_n) - U_e(R_n) = \frac{Z_a Z_A e^2}{R_n} - \frac{Z_a Z_A e^2}{R_a}$$

with R_n the nuclear radius, equal to the sum of the radii of the incident nucleus and the target. For distances less than the atomic radius,

$U_e = Z_a Z_A e^2 / R_a$ will cause a reduction of the barrier that prevents fusion, which results in an increase of the reaction cross section with respect to the case of bare nuclei.

The effect of the electron screening has been studied also in metallic environments, in particular for d + d. The screening effect in metallic environments is much stronger than that for atomic or molecular gas targets and significantly stronger than the appropriate theoretical expectations. Due to the exponential behaviour of the relation

$$f(E) = \frac{\sigma_{scr}}{\sigma_{bare}} = \frac{\frac{1}{E+U_e} S(E+U_e) e^{-2\pi\eta(E+U_e)}}{\frac{1}{E} S(E) e^{-2\pi\eta(E)}} \, ,$$

the increase of the screening energy can cause a drastic enhancement of the nuclear cross-section, especially in the case of the strong coupled plasma, where the average Coulomb potential energy of ions exceeds their thermal energy [Cze01]. The enhanced electron screening decreases with increasing temperature, where the data agree with the plasma model of Debye applied to the quasi-free metallic electrons [Rai02]. All data on the enhanced electron screening in deuterated metals can be explained quantitatively with the Debye model. It was argued [Rai04] that most of the conduction electrons are frozen by quantum effects and only electrons close to the Fermi Energy (FE) actually should contribute to screening, with $n_{eff}(T) = 0.67 kT / E_F \propto T$ and thus there should be essentially no temperature dependence for $U_{e,D}$. However, this argument applies only to insulators and semiconductors with a finite energy gap, while for metals there is no energy gap and the Fermi energy lies within the conduction band. Another feature that was studied is the temperature dependence of electron screening in the d(d,p)t reaction in deuterated metals. Metals of groups 3 and 4

have a high hydrogen solubility, of the order of one, and thus behave like insulators; all other metals and the lanthanides show a solubility of a few per cent at T=200 °C (compared to T=20°C) and a large screening also becomes observable [Rai02]. As compared to measurements performed with gaseous D_2 target (U_e=25 eV), a large screening was observed in the metals (of order U_e=300 eV), while a small (gaseous) screening was found for the insulators and semiconductors. The important results show the first observation of temperature dependence of a nuclear cross section [Ful01] [Rai03].

Another result is that the enhancement of the cross-section comes from the gain in electronic binding energy (screening energy U_e) which can be transferred to the relative motion of the colliding nuclei. In an adiabatic limit, i.e. with velocities $v_{nuclear} \ll v_{electron}$, this energy shift can be treated as constant [Ass01]. The experimental data, however, systematically indicate that a significantly larger energy shift is required in order to account for the low energy enhancement of the fusion cross section [Lan93]. Very interesting is to study the effect of coupling between the tunnelling motion and the electromagnetic field, taking a different approach from Flambaum and Zlevinsky [Hag02]. It has been employed the semi-classical approximation to the transition amplitude in the path integral representation and the effect is almost negligible for nuclear astrophysical reactions, since the large electron screening problem remains unsolved. The radiation correction used is even smaller than the vacuum polarization effect radiation correction to the nuclear fusion process without the electrons. In the adiabatic approximation, the electrons contribute only as a constant shift in the potential energy between the projectile and the target, and therefore the result cannot be altered qualitatively even after the electrons are taken into account. The origin of the discrepancy between the measured and the calculated electron screening energies still seems to be an open problem. In the last ten years many experiments have shown that an unexpectedly high electron screening effect on nuclear fusion rate occurs during accelerator-driven low energy (<10 kV) ion bombardment of solid targets [Str01]. These effects become particularly important

for E/ U_e<100 (where E is the ion energy) [Mil01]. In the experiments of the LUNA [Lun03] project two important points are highlighted:

- there is an enormous mass density enhancement in solid-state targets, orders of magnitude higher than that achievable in gaseous and plasma phases. Presumably this could be due to the screening from band-electrons in a solid target. However, the enhancement cannot be explained by the band-electrons alone.
- there is a periodic structure in the strength of the screening effect among various elements; the screening effect varies significantly in different groups of element.

Simultaneously other experiments have studied equilibration of strongly coupled ions in ultra-cold plasma produced by photo-ionizing laser-cooled and trapped atoms. By varying the electron temperature, it is possible to observe that the electron screening modifies the equilibrium ion temperature. Even with few electrons in a Debye sphere, the screening is well described by a model using a Yukawa ion-ion potential [Che04]. It has been studied ion equilibration during the first microsecond after the plasma is observed. For many years, this phenomenon has been the subject of intense study through analytic calculations [Gou75] and simulations [Han01, Bon77, Zwi99, Mora01, Mor03, Poh04] of one-component strongly coupled plasmas, but it has not previously been observed experimentally. The oscillations and their damping reflect universal dynamics of a Coulomb system with spatial correlations. It confirms once again the systematic discrepancy between experimental and theoretical values for the electron screening potential, thus leaving the electron screening understanding as an important open question for nuclear physics and astrophysics.

I.5 *Alpha Decay*

In the last twenty years the Electron Screening energy (U_e) has been deduced by comparing direct data and theoretical extrapolation or direct and indirect (non ES affected) data [Lan93] [Spi03]. This approach presents some limits, the most important being the absence of unambiguous theoretical extrapolations and, from the experimental point of view, the lack of knowledge of stopping powers at such low energies. As mentioned before in this scenario [Mus01] a puzzling result concerns the comparison between the deduced electron screening potential energy U_e and the commonly accepted maximum theoretical value, deduced by energy conservation: the so called adiabatic limit. In fact, in most of the cases the experimental value widely exceeds the theoretical one. In order to explain this discrepancy several arguments either theoretical and experimental have been spread around, but still this evidence remains problematic. In order to overcome the present limitation on the determination of ES energy, it was proposed to simplify the approach by considering the simplest system affected by Electron Screening, i.e. the alpha emitter nucleus. In this case the screening comes out from the full electron clouds surrounding the emitter and the two-body model to be considered consists of a bare light nucleus (alpha) and a neutral multi-electron atom (alpha-emitter). In fact, the effect of screening on alpha-decay has been introduced since 40's by adding a constant energy contribution to the Q_a value before calculating penetrability factors. A lot of valuable experimental and theoretical work in this field has been done [Per57]. It has been clearly demonstrated the dramatic consequences of introducing ES (or Ue) by using the Thomas-Fermi statistical model [Erm57]. It is easy to show that the Erma's approach corresponds to the limit of ES and variations of lifetimes of "bare nuclei" with respect to neutral atoms from 50% to 100% are expected in this scenario. Considering the actual new trends in ES one can wonder what is the "real" lifetime of a "bare" alpha-emitter and if the deduced electron screening energy of a neutral alpha-emitter can exceed the adiabatic value. The theoretical minimum and maximum electron screening; energy U_e are calculated within adiabatic limits

[Lio03]. This can be found by considering the value of electrostatic potential at the nucleus V due to the electrons, deduced long time ago by Hartree calculations. It is possible to have a simple formula that fits the values tabulated by Dickinson[Dic50] with non relativistic calculations in the full range of atoms; but this formula has the disadvantage of underestimating the screening energy for heavy nuclei (20% for Uranium) with respect to relativistic calculations, otherwise it works well for lighter nuclei. Finally it is possible to compute immediately the adiabatic limit U_e^{al} for a charged particle decay process just by considering the difference in the total electron binding energies between the initial parent atom E(Z1+Z2) and the final daughter E(Z2), meaning that all the available energy can be transferred from the electrons to the nuclear motion:

$$U_e^{al} = E_B(Z_2 + Z_1) - E_B(Z_2).$$

This limit can be estimated using the recent formula [Lun03], which provides a very good approximation to the total binding energies of electrons in neutral atoms as a function of Z. It demonstrates that the adiabatic limit, in case of charged particle decay, leads to the same electron screening energy. For a generic decay of a light charged particle with charge Z_1 from a parent nucleus of charge Z_2 and supposing V does not change during the decay.(It is possible consider the theoretical minimum and maximum electron screening potential energy Ue calculated within the adiabatic limits; it can be found by considering the value of the electrostatic potential at the nucleus V due to the electrons, this has been deduced by Hartree calculations. A simple formula is: $U^{sl} = Z_1 e V$.) It can simply write:

$$U^{al} = E_B(Z_2 + Z_1) - E_B(Z_2) = Z_1 e V = U^{sl}.$$

In case of alpha decay:

$$U_{max} = U^{al} = E_B(Z_2 + 2) - E_B(Z_2) = Z_2 e V = U^{sl} = U_{min}.$$

It is possible to deduce that all the available electron energy must go to the alpha daughter relative motion allowing electronic shells readjusting without any further energy relaxation. The ansatz is valid for any light charged particle decay from

heavy nuclei. The scenario of electron screening in a natural alpha-decay changes, because it is possible to have a fixed value; specifically screening can be evaluated by subtracting to the total screened decay energy Q_a, known by alpha-decay systematic, the screening energy U_e and considering the new corrected "bare" total energy $Q_a{}^* = Q_a - |U_e|$.

The question is if it is possible to have some experimental information on electron screening by using the excellent alpha decay systematic; but this is not an easy task because models of alpha-decay predicts a very large range spectroscopic factors. In a recent paper [Ket06], it was proposed that medium corrections to alpha decay may speed up its timescales in transuranic nuclear waste material by embedding it in metals at low temperature. However, it was later demonstrated that such an effect is likely to be very small, if present at all.

I.6 Indirect Method

In this section, indirect methods are discussed as an alternative way to determine cross sections of astrophysical interest at low energy, overcoming the main issues of direct measurement. In particular, we will focused on

- – Coulomb Dissociation (CD);
- – Asymptotic Normalization Coefficient (ANC);
- – Trojan Horse Method (THM).

Which are among those most used in the last two decades. The first two methods are applied mainly to radioactive capture reactions, while the third is used for reactions with charged particles or neutrons in the output channel.

I.6.1 Method of Coulomb dissociation

The method of the CD is an indirect method to study radioactive capture reactions at energies corresponding to the Gamow peak such as, the $^{12}C(\alpha, \gamma)^{16}O$ [Ber94], a key reaction in the process of synthesis of heavy elements in massive stars that will change evolution of the stages following the burning of ^4He ,or the $^7Be(p, \gamma)^8Be$ [Mot94], [Ber94], critical to the solar neutrino problem. This method uses a reaction three bodies, to study the radiative capture cross section of astrophysical interest through the break-up of a projectile core induced by virtual photons of the Coulomb field mediators generated by the heavy nucleus Z_T:

$$a + Z_T \rightarrow b + c + Z_T$$
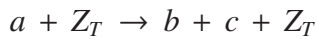
where the nucleus a is described as a cluster configuration a = b $\oplus$ c. Such break-up is the tool for the study of the photo-disintegration reaction

$$a + \gamma \rightarrow b + c$$
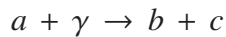
from which, with the detailed balance principle, it is possible to derive the cross section for the reaction of interest:

$$b + c \rightarrow a + \gamma$$
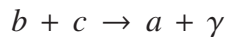
This method has two advantages:

• selecting appropriate kinematic conditions it is possible to perform more precise measurements of the reaction at astrophysical energies using particle beams with energies above the Coulomb barrier, thereby making it easier to reveal the fragments from the projectile nucleus, and also allows the use with a thick targets to increase the rate of reaction, rate, favoured by the low energy straggling [Bau94];

• there has been a rise in the rate of reaction compared to capture direct radiative processes and photo-disintegration because the particle a is hit by a large number of virtual photons due to the presence of Z_T, which has a high atomic number.

• for large impact parameters (i.e. small scattering angles) in the projectile-target scattering, the nuclear contribution to the interaction potential can be neglected.

I.6.2 Method of Asymptotic Normalization Coefficient

The method of Asymptotic Normalization Coefficient allows to derive the cross-section for radiative capture reactions (p, γ) and (α, γ) at energies of astrophysical interest, starting from the observation that direct proton/alpha capture reactions of astrophysical interest involve systems where the binding energy of the captured charged particle is low. Hence at stellar energies, the capture proceeds through the tail of the nuclear overlap function. The shape of the overlap function in this tail region is determined by the Coulomb interaction, so the amplitude of the overlap function alone dictates the rate of the capture reaction. The ANC, C, for A + p ↔ B or A + α ↔ B specifies the amplitude of the tail of the overlap function for the system [Muk99],[Tra98],[Azh01].

Now consider the peripheral transferred particle. The process can be described by using the diagram in fig. I-5.
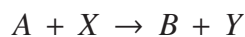
$$A \ + \ X \ \rightarrow \ B \ + \ Y$$

in which X = Y + a, B = A + a and a is the particle transferred (figure I-5)
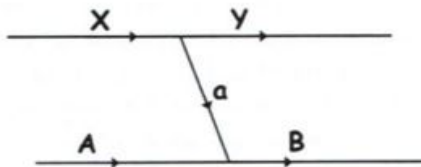
fig. I- 5 Sketch reaction A+X → B+Y, where X=Y+a and B=A+a. The particle a is transferred from nucleus X to A.

Both the nucleus **X** in the initial state and the nucleus **B** in the final state are bound states of the transferred nucleus a. In this approach, the cross section will depend on the C_{Ya} and C_{Aa}. If one ANC is known, e.g. C_{Ya} from elastic scattering experiments, the second one C_{Aa} can be extracted from the indirect experiment and it is just the

one needed to determine the capture reaction cross section. In order to reduce the dependence of the result on the potential (or nuclear phase shift) in the scattering state of the $Y + a$ system, only the S factor close to zero energy is considered. This procedure is justified for reactions where the nuclei Y and a are only weakly bound in the ground state of X.

I.6.3 Method of Trojan Horse

The method of the Trojan Horse (THM) is based on the theory of direct nuclear reactions, in particular of the quasi-free break-up mechanisms [Sat90]. The idea is to determine the cross section of the binary $A + x \rightarrow c + C$ process at astrophysical energies by measuring the two-body to three-body ($2 \rightarrow 3$) process, $A + a \rightarrow c + C+s$, in the quasifree (QF) kinematics regime, where the "Trojan Horse" particle, a has a strong $x \oplus s$ cluster structure. The a + A interaction takes place at energies above the Coulomb barrier, such that nucleus a undergoes breakup leaving particle x already in the nuclear field of A, while s remains spectator to the binary reaction. It is assumed that the inter-cluster motion occurs in s-wave, which requires that the momentum distribution for this motion has a maximum at 0 MeV/c [Sat90] .
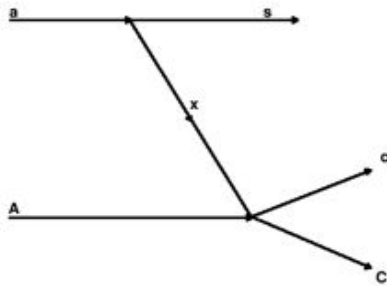
fig. I- 6 Pseudo-Feynman diagram for the process (A, C c) s. In the top the projectile splits into two clusters x and s; this does not interact with the target A and gives a virtual reaction A + x →C+ c. x is a spectator for the reaction, and keeps the impulse before the break-up.

In this framework it is possible to apply the Pole Approximation. This method remains valid independent of the particle break-up, either target nucleus or projectiles, or if the relative motion x-s does not occur in s-wave. The A + a relative

motion is compensated for by the x − s binding energy, [Tum03] determining the so called "quasi-free two-body energy" given by:

$$E_{qf} = E_{Ax} - B_{x-s}$$

where E_{Ax} is the beam energy in the center of mass reference system of the system A - x and B_{x-s} it is the x-s binding energy. In this context, the x-s intercluster motion inside the nucleus **a** has the task of setting the range of energies accessible in the vicinity of the quasi-free energy. Furthermore, being above the Coulomb barrier in the A+a→c+C+s makes negligible the phenomena of electron screening.

I.7 Nuclear decays in plasma

A laser is a unique tool to produce plasma and very high fluxes of photon and particle beams in very short duration pulses. Both aspects are of great interest for fundamental nuclear physics studies. In a plasma the electron–ions interactions may modify atomic and nuclear level properties. This is of prime importance for the population of isomeric states and for the issue of energy storage in nuclei. Nuclear properties in the presence of very high electromagnetic fields, nuclear reaction rates or properties in hot and dense plasmas are new domains of investigation. Furthermore, with a laser it is possible to produce electric and magnetic fields strong enough to change the binding energies of electronic states. If nuclear states happen to decay via internal conversion (IC) through these perturbed states, a modification of their lifetimes will be seen. The excitation of nuclear levels by the transfer of energy from the atomic part to the nuclear part of an atom is the subject of a large number of investigations. Their goal is to find an efficient mechanism to populate nuclear isomers in view of further applications to energy storage and development of lasers based on nuclear transitions. This process called NEET (Nuclear Excitation by Electronic Transition) has been first suggested by Morita for the excitation of a level at approximately 13 keV in ^{235}U [Mor73]. This process is the inverse of the resonant nuclear internal conversion between bound atomic states (BIC),

which has been demonstrated in 125Te [Att95], [Car00]. In this case, the well-known variation of the electron-binding energy with Q, the charge state of an ion, was used to reach the condition Q = 45$^+$ in which the energy matching between the atomic energy transition and the nuclear energy is realized. In the search for NEET in plasma induced by a laser, the laser beam is used to create a dense and hot plasma of uranium matter. In the plasma, U atoms are ionized and have a charge state distribution that depends on the plasma temperature. Furthermore, to each of the charge states correspond several different configurations due to the coupling between the electron spins. Each atomic configuration corresponds to a particular set of atomic energy transitions. Some configurations undergo transitions that match more or less closely the nuclear energy transition between the ground state and the first excited state in ^{235}U (see fig. I-7). The nucleus can absorb only the virtual photon emitted from the atomic transition if the energy mismatch between the two energy transitions is of the order of the width of the system. Because of electron–ion collisions in the hot plasma, the widths of the excited atomic levels are strongly increased. As an example, the natural width of a 5d hole in the U atom is of the order of 10^{-5} eV. In a plasma at a temperature of 100 eV, this width becomes dominated by the Stark broadening effect and reaches values as large as 20 MeV. This greatly enhances the possible matching between the atomic and the nuclear energy transitions.
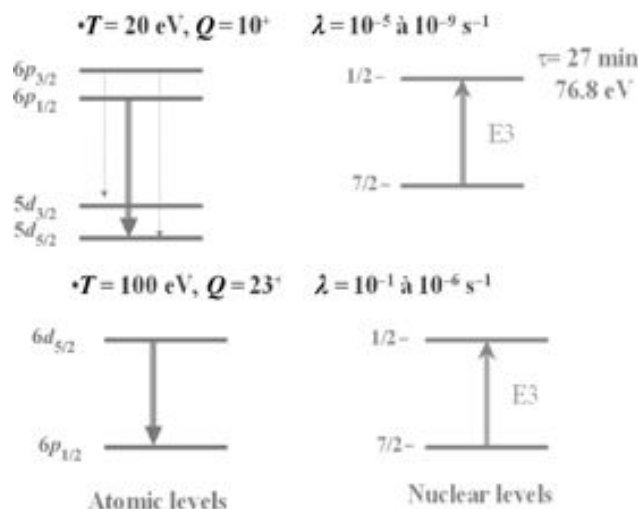
fig. I- 7 Energy levels in ^{235}U at two different plasma temperature T where electronic transition energies are nearly resonant with the nuclear ($\pm$4eV). The corresponding predicted nuclear excitation rate λ[Har01].

In ^{235}U the nuclear transition between ground state and the first excited state is an E3 transition whose characteristics are known with poor accuracy. The transition energy is $E_n = (76.8 \pm 0.8)$ eV. The half-life of the $1/2^-$ excited level is 26.8 min depending slightly on the chemical state of U. The internal conversion coefficient is very large, approximately 10^{20}, but has never been measured. In spite of these uncertainties it has been shown that the atomic transitions $6p - 5d$ in U ions with $Q = 10$ and $6d_{5/2} - 6p_{1/2}$ in U ions with $Q = 23$ have energies nearly equal to E_n. Owing to the combined uncertainties on En and on the calculated atomic energies leading to an energy mismatch of 4 eV, theoretical values of the nuclear excitation rate range between 10^{-9} and 10^{-5} s^{-1} for the first group of transitions and between 10^{-5} and 10^{-1} s^{-1} for the second one [Har99]. The calculations have been performed for an electronic density of 10^{19} cm^{-3} in the plasma. Several experiments have been done over the last 30 years to observe the excitation of the extremely low energy level at 76eV in ^{235}U using a pulsed high-intensity laser beam. In these experiments, the plasma generated in the interaction of the laser with the U target was collected on a catcher foil subsequently placed in front of an electron multiplier. The excitation of the isomeric level was detected by means of the internal conversion electrons from its decay. The results of these experiments are controversial. Using a 1 J CO_2 laser and a target of natural Uranium [Iza79] where it has been observed a strong signal of delayed low-energy electrons, has been observed, attributed to the decay of the 76 eV level after excitation by a NEET process. [Gol81] In these experimental conditions the excitation probability by NEET should be very small and they proposed a new interpretation of the excitation of the nucleus in terms of NEEC. NEEC is the excitation of the nucleus by the capture of a free electron into a bound orbital. The energy gained by the system can be resonantly transferred to the nucleus. [Aru91] A similar experiment has been done with a CO_2 laser (5 J, 200 ns) and a ceramic target 6% enriched in ^{235}U but failed to observe the excitation of the isomeric state. In a second experiment the same group observed an excitation of the isomeric state detected in plasma induced by a high-intensity beam of 500 keV electrons. The temperature of the plasma was of the order of 20 eV. That this positive result was most probably due to a direct excitation of the U nuclei by inelastic electron scattering from the

incident beam rather than to a NEET or a NEEC mechanism [Har99]. In fact, it is very difficult to compare these results because of the lack of details on the experimental conditions such as laser beam focusing, the plasma temperature, number of collected atoms on the catcher foil, electron detection efficiency, and parasitic electron emission phenomena. A more recent attempt to excite the isomeric level in ^{235}U [Bou92] was done with a CO_2 laser interacting with a 93% enriched U target generated a U vapour, which was illuminated by a ps laser to create plasma. The intensity of the ps laser beam was deduced from a measurement of the charge state distribution of the U ions in the plasma. They found an intensity ranging between 10^{13} and 10^{15} W/cm^2. The U ions were deposited on a plate and the delayed electron emission was analysed. An electric field permitted the separation between neutral and ionized U species. A time of flight measurement of the collected U ions provided with a crude estimation of the number of ions in charge states ranging between 1^+ and 5^+.

I.8 Hoyle State

Heavy-ion collisions are a powerful tool for exploring structure and nuclear equation of state (EoS) of nuclear matter under laboratory controlled conditions. In these complex dynamical systems, particle-particle correlations probe nuclear dynamics and spectroscopy of produced nuclear systems. The study of correlation functions can also be used as a powerful tool to explore certain spectroscopic properties of unbound states of exotic nuclei, such as the spin [Tan04]. During dynamical evolution of a system, several loosely bound nuclear species are produced in terms of clusters for a very short time and subsequently decay. The idea that, under certain conditions, nuclei may be made out of clusters dates back from the beginning of nuclear physics when, analysing one of the most basic observables, e.g., the binding energy per nucleon, it was realized that by far the most bound nuclei are those which have even and equal numbers of neutrons and protons.

A relevant case of clustering is given by carbon nuclei. In fact, an excited, spin-less, resonant state of ^{12}C produced via the triple-alpha process was predicted to exist by Fred Hoyle in 1954 [Hoy01]; it can decay through a simultaneous breakup, e.g. ^{12}C → α−α−α, or through a sequence of two binary processes passing through the formation of intermediate ^{8}Be unbound states, ^{12}C →^{8}Be-α followed by ^{8}Be→ 2α. Four particles p-p-α-α correlation functions has been also studied to probe the decay of unbound states of ^{10}C [Gre08]; the results reveal the existence of four-body direct decay mechanisms and sequential decay ones proceeding through the production of intermediate unbound states in ^{9}B, ^{8}Be and ^{6}Be nuclei. All these states are relevant to both nuclear physics and astrophysics.

Furthermore, in 1968 Ikeda suggested that for all nuclei with N = Z and A = 4n, clustering would occur with a prominence related to the proximity to the decay threshold for that channel [Bri08]. This is shown in the Fig. 1.10, in what is known as the "Ikeda diagram". This opened a new view of nuclei as composed by clusters.

The existence of the Hoyle state is essential for the nucleosynthesis of carbon in helium-burning red giant stars, and predicts an amount of carbon production in a stellar environment, which matches observations. The existence of the Hoyle state has been confirmed experimentally, but its precise properties are still being investigated [Che01]. The importance of this state lies not only in its role in the synthesis of carbon, but also in its characteristic structure. From nuclear structure point of view too, the Hoyle state presents many unique features, which are yet to be understood properly.

In 2011, an ab initio calculation of the low-lying states of ^{12}C found (in addition to the ground and excited spin-2 state) a resonance with all of the properties of the Hoyle state. This occurs if the considered nucleus possesses an excited state in the vicinity of the cluster decay threshold. Recent sophisticated molecular dynamics calculations confirm this scenario. Therefore the structure of this state is still controversial. For instance, according to the Fermionic Molecular Dynamics model, the ground-state of ^{12}C (the first excited 0+ state of ^{12}C) and the Hoyle state, that is the first excited 0+ state of ^{12}C, correspond to a mixture of different cluster configurations where one may even identify a pre-formed ^{8}Be [Che01]. Moreover,

cluster structures seem to be peculiar not only to Nα nuclei: neutron and proton-rich nuclei could show molecular-like structures, as well. Two examples in this sense are given by various excited states in ^{13}Be and ^{11}B that show advanced cluster configurations [Kan01]. Recently, Raduta et al. [Rad11] reported a rather high branching ratio of 17% for the direct 3α decay of the Hoyle state formed in the ^{40}Ca+^{12}C reaction, and an evidence of the α condensation. In this work, in order to obtain a complete kinematic characterization of individual decay events, charged reaction products have been detected by the CHIMERA high-granularity 4π multi-detector [Pag04]. However, Raduta's observation was in contradiction with the result obtained later by Freer et al. [Lah12]; he demonstrated that the Hoyle state decays predominantly through 8Begs (^{12}C→ ^{8}Begs + α → α + α + α), and a possible contribution from a mechanism that uniformly spans the three body phase space should be smaller than 4%. The result of Raduta et al. work has naturally triggered new experimental activity; a relevant example is another detailed study of the ^{12}C Hoyle state decay in 3 α in ^{12}C+^{24}Mg collisions at 35 A.MeV [Qth15], where an important probability (between 20 and 60 %) of direct decay was estimated. Also this results is in contrast with the ones obtained in experiments performed with direct [Lis93] and inelastic scattering reactions, that report a very low or even negligible direct contribution in decay of Hoyle state. These discrepancies could be due to medium effects on nuclear structure properties. With respect to direct reactions, a heavy ion collisions are characterized by a longer interaction time and by more dissipative processes, then in this case, one may expect that nuclear properties could be modified by the medium where the decay of these unbound state occurs. This topics may trigger new directions to study in-medium nuclear structure, an important perspective for research on nuclear interactions.

I.9 References

[Ali01]M. L. Aliotta et al., Nucl. Phys. A 690, 790 (2001).

[Aru91]R.V. Arutyunyan et al.: Sov. J. Nucl. Phys. 53, 23, (1991)

[Ass87] H.J. Assenbaum, K Langanke, and Rolfs, Z. Phys. A 327 461 (1987)

[Att95] F. Attallah et al. Phys. Rev. Lett. 75, 1715 (1995),

[Azh01]   Ashari et al. Asymptotic normalization coefficients and the 7Be(p,γ)8B astrophysical S factor. Physical Review C, 63(5):055803. (2001).

[Bah98] J. N. Bahcall , Physical Review C vol. 57 num.5 (1998)

[BAH69] N.A. Bahcall and W.A. Fowler Astrophysical Journal 157 (1969) 645

[Bau94] Baur, G. and Rebel, H. Coulomb dissociation studies as a tool of nuclear astrophysics. Journal of Physics G Nuclear Physics, 20:1–33. (1994)

[Ber94] Bertulani, C. A. The astrophysical reactions c12(α,γ)16o and be7(p,γ)8b and coulomb dissociation experiments. Physical Review C, 49:2688–2694. (1994).

[Bet39] H. A. Bethe ,PhY8. Rev. 55: 434. (1939)

[Bet37] H.A. Bethe , Rev. Mod. Phys. 9 (1937) 69

[Bey00] Beyer M, Sofianos S A, Kuhrts C, Rӧpke G and Schuck P Phys. Lett. B 448 247, 2000

[Bon77] M. Bonitz, D. Semkat, and D. Kremp, Phys. Rev. E 56, 1246 (1997)

[Bou92] J.A. Bounds, P. Dyer: Phys. Rev. C 46, 852 (1992)

[Bri08] D.M. Brink. J. Phys. Conf. Ser., 111:012001, 2008.

[Bro97] L.S.Brown and R.F. Sawyer, Rev. Mod. Phys. 69, 411 (1997)

[Car88] C. Carraro et al, ibi. 331, 565(1988)

[Car00] T. Carreyre et al. Phys. Rev. C 62, 24311 (2000)

[Che07] Chernykh, M.; Feldmeier, H.; Neff, T.; Von Neumann-Cosel, P.; Richter, A. "Structure of the Hoyle State in 12C" (PDF). Physical Review Letters. 98 (3) 032501, (2007).

[Che04] Y.C. Chen et al, Physical Review Letters (2004)

[Cze01] K. Czerski et al., Europhys. Lett, 54(4), pp. 449-455 (2001)

[Dar96] A. dar and G. Shaviv, ibid.468,993 (1996)

[Dzi95] H. Dzitko et al., Astrophys. J. 447,428 (1995).

[Dzi95] H. Dzitko,S. Turck-Chieze, P.Delbourgo-Salvador and C. Lagrange,, Astro. J. 447 (1995) 428

[Free94] M. Freer et al. Phys. Rev. C 49 R1751 (1994)

[Ful01] Zs. Fulop et al

[Fun08] Funaki Y, Yamada T, Horiuchi H, Rӧpke G Schuck P and Tohsaki A Phys. Rev. Lett. 101 082502, 2008

[Gam49] G. GAMOW, and C.L. CRITCHFIELD," Theory of Atomic Nucleus." p. 264. (Clarendon Press: Oxford.) (1949)

[Gol81]V.I. Goldansky, V.A. Namiot: Sov. J. Nucl. Phys. 33, 169 (1981)

[Gou75] H. Gould and G.F. Mazenko, Phys. Rev. Lett. 35, 1455 (1975)

[Gre08] F. Grenier et al. Nucl. Phys. A, 811:233, 2008.

[Gru01] Gruzinov, Andrei V. Astrophys.J. 496 (1998) 503 astro-ph/9702064 IASSNS-AST-97-9 Astrophys.J.,469,503

[Hag02] K. Hagino et al, Physical review C 66. 055801 (2002)

[Han74] J. P. Hansen, E. L. Pollock, and I. R. McDonald, Phys. Rev. Lett. 32, 277 (1974)

[Han07] F. Hannachi et al., 2007 Plasma Phys. Control. Fusion 49 B79

[Har99] M.R. Harston, J.F. Chemin: Phys. Rev. C 59, 2462 (1999)

[Hoy54] Hoyle, F. "On Nuclear Reactions Occurring in Very Hot Stars. I. the Synthesis of Elements from Carbon to Nickel.". The Astrophysical Journal Supplement Series. 1, (1954).

[Hoy46] F. Hoyle, Monthly Notices of the Royal Astronomical Society 106 (1946) 343

[Iza79] Y. Izawa, C. Yamanaka: Phys. Lett. 88B, 59 (1979)

[Joh92] C. W. Johnson et al., Astrophys. J. 392,320(1992)

[Kan12] Kanada-En'yo Y 2012 Phys. Rev. C 85 044320; Suhara T and Kanada-En'yo Y Phys. Rev. C 85, 054320 , 2012

[Lah12] T. A. Lähde D. Lee E. Epelbaum, H. Krebs and Ulf.G. Mei_ner. Phys. Rev. Lett., 109:252501, 2012.

[Lan93] K. Langanke, in Advances in Nuclear Physics, edited by J.W.Negele and E.Vogt (Plenum, New York, 1993), Vol. 21, Chap2

[Lan95] K. Langanke, in Solar Modelling, edited by A. B. Balantekin and J. N. Bahcall(World Scientific Singapore) (1995)

[Lan96] K. H. Langanke, T.D. Shoppa, C.A. Barnes and C. Rolfs, Phys. Lett. B 369, 211 (1996).

[Lim06] B.N. Limata, Eur. Phys. J. A 27, s01, (2006) 193

[Lip10] M. Lipoglavsek et al., Eur. Phys. Jou. A 44 (2010) 71, and ref. there in

[Lis93] M. A. Lisa et al. Phys. Rev. Lett, 70:2545, 1993 [MAS10] D. Mascali et al. Advances in Plasma Astrophysics, Proceedings. of IAU Symposium 274, (2010) 44

[Mil01] G.H. Miley et al, IEEE (2004)

[Mit77] H. E. Mitler, Astrophys. J. 212, 513 (1977)

[Mor03] I. V. Morozov and G. E. Norman, J. Phys. A 36, 6005 (2003)

[Mor73] M. Morita: Prog. Theor. Phys. 49, 1574 (1973)

[Mora01] K. Morawetz, M. Bonitz, V. G. Morozov, G. Ro¨ pke, and D. Kremp, Phys. Rev. E 63, 020102 (2001)

[Mot94] Motobayashi et al. Coulomb dissociation of 8B and the 7Be(p,γ)8B reaction at low energies. Physical Review Letters, 73:2680–2683. (1994)

[Mur01] M. S. Murillo, Phys. Rev. Lett. 87, 115003 (2001)

[Mus01] A. Musmarra private comunication

[NACRE] http://pntpm.ulb.ac.be/Nacre/nacre.htm

[Oer06] Von Oertzen W Eur. Phys. J. A 29 133, 2006

[Pag04] A. Pagano et al. Nucl. Phys. A, 734:504, 2004

[Poh04] T. Pohl, T. Pattard, and J.M. Rost, J. Phys. B 37, 183 (2004).

[Qth15] L. Quattrocchi, Thesis, Doctorate XXVIII cycle, Univ. Messina (2015) [Rai02] F. Raiola et al, Phys, Lett B547 (2002) 193

[Rad11] Ad.R. Raduta, et al., Phys. Lett. B, 705 (2011), p. 65

[Rai04] Raiola Fetal Eur.Phys.J.A 19283 (2004)

[Rai03] F. Raiola et al, Phys. Lett B

[Rol88] Rolfs, C.E.and Rodney, W. (1988). University of Chicago Press.

[Rol04]C. Rolfs et al., Prog. Theor. Phys. Supp. 154, 373 (2004).

[Rop98] Ropke G, Schnell A, Schuck P and Nozieres P Phys. Rev. Lett. 80 3177, 1998

[Sal53] E. E. Salpeter ,Annu. Rev. Nuclear Sci. 2: 41. (1953)

[Sal54] E. E. Salpeter,Aust. J. Phys. 7. 373 (1954).

 [Sal69] E. E. Salpeter and H. M. Van Horn, Astro. J. (1969) 183

 [Sat90]Satchler, G. Introduction to Nuclear Reaction. Oxford University Press. (1990).

[Sha96] N. Shaviv and G. Shaviv, Astrophys. J. 468, 433(1996)

[Sog09] Sogo T, Lazauskas R, Ro¨pke G. and Schuck P Phys. Rev. C 79 051301, 2009

[Spi03] C. Spitaleri et al., Nucl. Phys. A 719, 99 (2003).

[Spi11] C. Spitaleri et al., PAN 74 (2011) 1725 and ref. there in

[Str01]F. Strieder, C. Rolfs, C. Spitaleri and P. Corvisiero, Naturwissenschaften 88, 461 (2001).

[Tan04] W.P. Tan et al. Phys. Rev. C, 69:061304, 2004

[Toh01] Tohsaki A, Horiuchi H, Schuck P and R¨opke G Phys. Rev. Lett. 87 192501, 2001

[Tra98] Trache et al. Asymptotic normalization coefficients for 13C+p→14N. Physical Review C, 58:2715–2719. (1998).

[Tsa99] C. Tsallis, "Introduction to Nonextensive Statistical Mechanics…", Springer 2009

[Tum03] Tumino, et al. Validity test of the "Trojan horse" method applied to the 6Li(p,α)3He reaction. Physical Review C, 67(6):065803. (2003).

[Yam04] Yamada T and Schuck P Phys. Rev. C 69 024309, 2004

[Zwi99] G. Zwicknagel, Contrib. Plasma Phys. 39, 155 (1999)

CHAPTER II

.

PLASMA SCENARIO

II.1 Definition of Plasma

Any ionized gas cannot be called a plasma, of course; there is always some small degree of ionization in any gas. A useful definition is as follows: a plasma is a quasi-neutral gas of charged and neutral particles which exhibits collective behaviour.
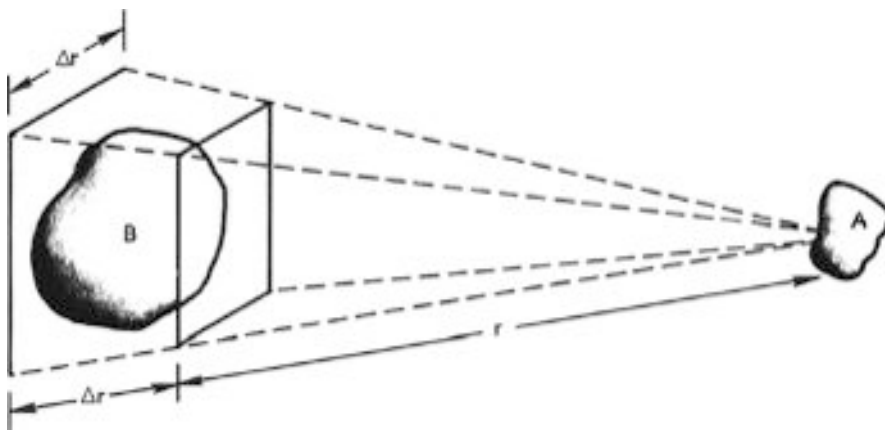
fig. II- 1 Illustrating the long range of electrostatic forces in a plasma

What is meant by "collective behaviour" is as follows. Consider the forces acting on a molecule of, say, ordinary air. Since the molecule is neutral, there is no net electromagnetic force on it, and the force of gravity is negligible. The molecule moves undisturbed until it makes a collision with another molecule, and these collisions control the particle's motion. A macroscopic force applied to a neutral

gas, such as from a loudspeaker generating sound waves, is transmitted to the individual atoms by collisions. The situation is totally different in a plasma, which has charged particles. As these charges move around, they can generate local concentrations of positive or negative charge, which give rise to electric fields. Motion of charges also generates currents, and hence magnetic fields. These fields affect the motion of other charged particles far away. Let us consider the effect on each other of two slightly charged regions of plasma separated by a distance r (fig. II-1). The Coulomb force between A and B diminishes as $1/r^2$. However, for a given solid angle (that is, $\Delta r/r$=constant), the volume of plasma in B that can affect A increases as r^3. Therefore, elements of plasma exert a force on one another even at large distances. It is this long-ranged Coulomb force that gives the plasma a large repertoire of possible motions and enriches the field of study known as plasma physics. In fact, the most interesting results concern so-called "collision-less" plasmas, in which the long-range electromagnetic forces are so much larger than the forces due to ordinary local collisions that the latter can be neglected altogether. By "collective behaviour" we mean motions that depend not only on local conditions but on the state of the plasma in remote regions as well.

The word "plasma" seems to be a misnomer. It comes from the Greek πλάσμα, -ατος, τό, which means something molded or fabricated. Because of collective behaviour, a plasma does not tend to conform to external influences; rather, it often behaves as if it had a mind of its own.

II.2 Concept of Temperature

Before proceeding further, it is well to review and extend our physical notions of "temperature." A gas in thermal equilibrium has particles of all velocities, and the most probable distribution of these velocities is known as the Maxwellian distribution. For simplicity, consider a gas in which the particles can move only in one dimension. One-dimensional Maxwellian distribution is given by

$$f(u) = A exp\left(\frac{-\frac{1}{2}mu^2}{KT}\right)$$

where f du is the number of particles per m^3 with velocity between u and u + du, 1/2 mu^2 is the kinetic energy, and K is Boltzmann's constant,

$$K = 1.38 \times 10^{-23} \frac{J}{°K}$$

Note that a capital K is used here, since lower-case k is reserved for the propagation constant of waves. The density n, or number of particles per m^3, is given

$$n = \int_{-\infty}^{+\infty} f(u)du$$

The constant A is related to the density n by

$$A = n \left(\frac{m}{2\pi KT}\right)^{1/2}$$
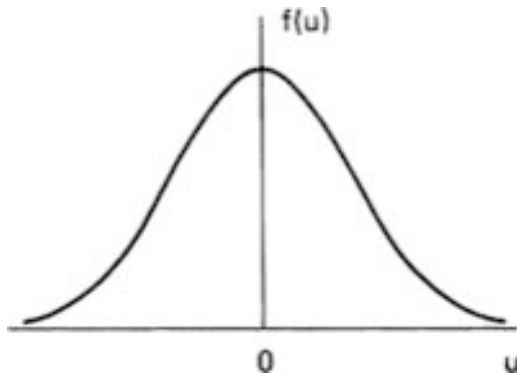
fig. II- 2 A Maxwellian velocity distribution

The width of the distribution is characterized by the constant T, which we call the temperature. To see the exact meaning of T, we can compute the average kinetic energy of particles in this distribution:

$$E_{av} = \frac{\int_{-\infty}^{+\infty} \frac{1}{2}mu^2 f(u)du}{\int_{-\infty}^{+\infty} f(u)du} \quad .$$

After many integrals we have:

$$E_{av} = \frac{\frac{1}{2}mAv_{th}^3 \frac{1}{2}}{Av_{th}} = \frac{1}{4}mv_{th}^2 = \frac{1}{2}\kappa T \, ,$$

where κ is Boltzmann constant κ = 1.380658(12) × 10−23 J/K and κT indicates the thermal energy. Thus the average kinetic energy is 1/2 KT. It is easy to extend this result to three dimensions. Therefore the unit of κT is Joule (J) in SI unit.

Since T and E_{av} are so closely related, it is customary in plasma physics to give temperatures in units of energy. It is interesting that a plasma can have several temperatures at the same time. It often happens that the ions and the electrons have separate Maxwellian distributions with different temperatures T_i and T_e. This can come about because the collision rate among ions or among electrons themselves is larger than the rate of collisions between an ion and an electron. Then each species can be in its own thermal equilibrium, but the plasma may not last long enough for the two temperatures to equalize.
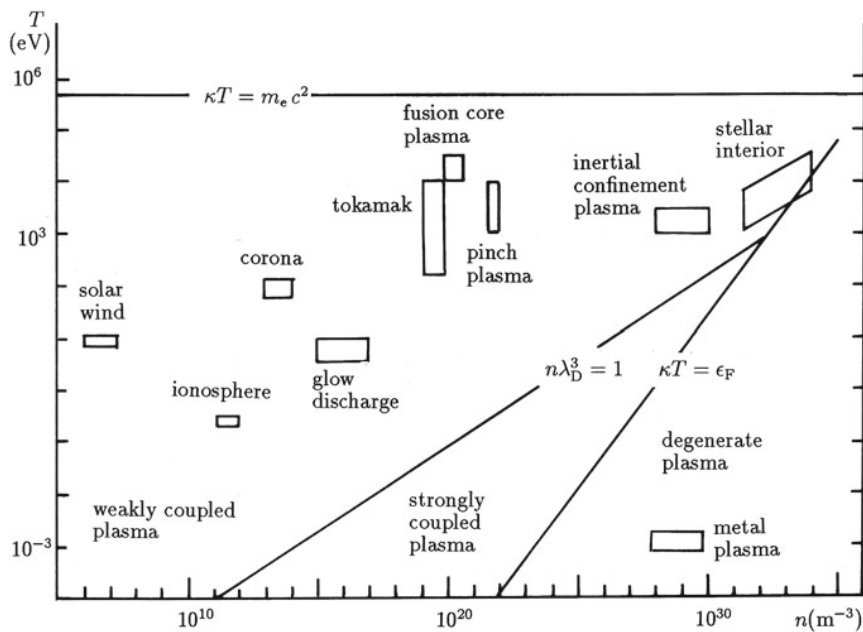
fig. II- 3 Various plasma domain in n−T diagram

Plasmas are found in nature in various forms (see fig. II-3). There exits the ionosphere in the heights of 70–500 km (density n ∼ 10^{12} m−3, T ∼ 0.2 eV). Solar wind is the plasma flow originated from the sun with n ∼ $10^{6\sim7}$ m−3, T ∼ 10 eV. Corona extends around the sun and the density is ∼10^{14} m−3 and the electron

temperature is ~ 100 eV although these values depend on the different positions. White dwarf, the final state of stellar evolution, has the electron density of $10^{35\sim 36}$ m^{-3}.

Various plasma domains in the diagram of electron density n(m^{-3}) and electron temperature T (eV) are shown in fig. II-3. Active researches in plasma physics have been motivated by the aim to create and confine hot plasmas in fusion researches. Plasmas play important roles in the studies of pulsars radiating microwave or solar system. Application of plasma physics is the study of the earth's environment in space. Practical applications of plasma physics are MHD (magneto-hydrodynamic) energy conversion for electric power generation, ion rocket engines for space crafts, and plasma processing which attracts much attention recently.

II.3 Occurrence the plasma in nature

It is now believed that the universe is made of 69% dark energy, 27% dark matter, and 1% normal matter. All that we can see in the sky is the part of normal matter that is in the plasma state, emitting radiation. Plasma in physics, not to be confused with blood plasma, is an "ionized" gas in which at least one of the electrons in an atom has been stripped free, leaving a positively charged nucleus, called an ion. Sometimes plasma is called the "fourth state of matter." When a solid is heated, it becomes a liquid. Heating a liquid turns it into a gas. Upon further heating, the gas is ionized into a plasma. Since a plasma is made of ions and electrons, which are charged, electric fields are rampant everywhere, and particles "collide" not just when they bump into one another, but even at a distance where they can feel their electric fields. Hydrodynamics, which describes the flow of water through pipes, say, or the flow around boats in yacht races, or the behaviour of airplane wings, is already a complicated subject. Adding the electric fields of a plasma greatly expands the range of possible motions, especially in the presence of magnetic fields. Plasma usually exists only in a vacuum. Otherwise, air will cool the plasma

so that the ions and electrons will recombine into normal neutral atoms. In the laboratory, we need to pump the air out of a vacuum chamber. In the vacuum of space, however, much of the gas is in the plasma state, and we can see it. Stellar interiors and atmospheres, gaseous nebulas, and entire galaxies can be seen because they are in the plasma state. On earth, however, our atmosphere limits our experience with plasmas to a few examples: the flash of a lightning bolt, the soft glow of the Aurora Borealis, the light of a fluorescent tube, or the pixels of a plasma TV. We live in a small part of the universe where plasmas do not occur naturally; otherwise, we would not be alive. The reason for this can be seen from the Saha equation, which tells us the amount of ionization to be expected in a gas in thermal equilibrium:

$$\frac{n_i}{n_n} \approx 2.4 \times 10^{21} \frac{T^{3/2}}{n_i} e^{-U_i/KT}.$$

Here n_i and n_n are, respectively, the density (number per m^3) of ionized atoms and of neutral atoms, T is the gas temperature in °K, K is Boltzmann's constant, and U_i is the ionization energy of the gas that is, the number of ergs required to remove the outermost electron from an atom. For ordinary air at room temperature, we may take $n_n \approx 3 \times 10^{25} m^{-3}$, $T \approx 300°$, and $U_i = 14.5 eV$ (for nitrogen), where $1\ eV = 1.6 \times 10^{-19} J$.

The fractional ionization $n_i/(n_n + n_i) \approx n_i/n_n$ is:

$$\frac{n_i}{n_n} \approx 10^{-22}$$

As the temperature of a material is raised, the degree of ionization remains low until U_i is only a few times KT. Then n_i/n_n rises abruptly, and the gas is in a plasma state. Further increase in temperature makes n_n less than n_i, and the plasma eventually becomes fully ionized. This is the reason plasmas exist in astronomical bodies with temperatures of millions of degrees, but not on the earth. Life could not easily coexist with a plasma at least, plasma of the type we are talking about. The natural occurrence of plasmas at high temperatures is the reason for the designation "the fourth state of matter." Although it does not intend to emphasize the Saha equation, it should point out its physical meaning. Atoms in a gas have a

spread of thermal energies, and an atom is ionized when, by chance, it suffers a collision of high enough energy to knock out an electron. In a cold gas, such energetic collisions occur infrequently, since an atom must be accelerated to much higher than the average energy by a series of "favorable" collisions. Once an atom is ionized, it remains charged until it meets an electron; it then very likely recombines with the electron to become neutral again. The recombination rate clearly depends on the density of electrons, which we can take as equal to n_i. The equilibrium ion fraction, therefore, should decrease with n_i.

II.4 Debye Shielding

A fundamental characteristic of the behaviour of plasma is its ability to shield out electric potentials that are applied to it. Suppose we tried to put an electric field inside a plasma by inserting two charged balls connected to a battery (fig. II-4). The balls would attract particles of the opposite charge, and almost immediately a cloud of ions would surround the negative ball and a cloud of electrons would surround
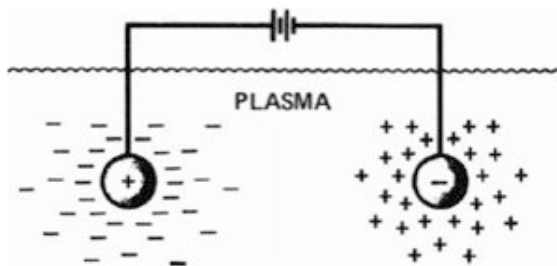
fig. II- 4 Potential distribution near a grid in a plasma
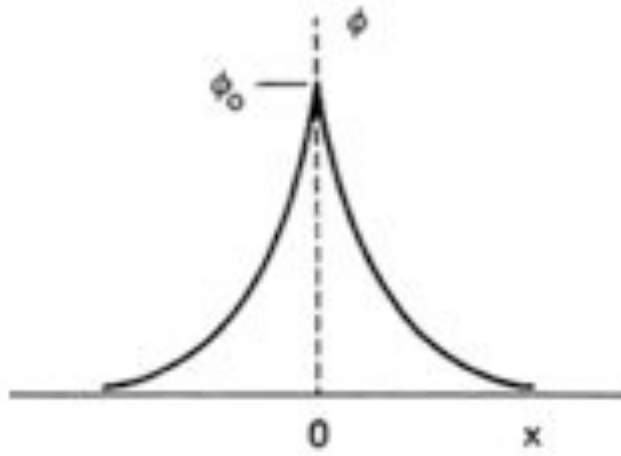
fig. II- 5 Potential distribution near a grid in a plasma

the positive ball. If the plasma were cold and there were no thermal motions, there would be just as many charges in the cloud as in the ball, the shielding would be perfect, and no electric field would be present in the body of the plasma outside of the clouds. On the other hand, if the temperature is finite, those particles that are at the edge of the cloud, where the electric field is weak, have enough thermal energy to escape from the electrostatic potential well. The "edge" of the cloud then occurs at the radius where the potential energy is approximately equal to the thermal energy KT of the particles, and the shielding is not complete. Potentials of the order of KT/e can leak into the plasma and cause finite electric fields to exist there. It is possible to compute the approximate thickness of such a charge cloud. Imagine that the potential ϕ on the plane x =0 is held at a value φ_0 by a perfectly transparent grid (fig. II-5). We wish to compute $\phi(x)$. For simplicity, we assume that the ion-electron mass ratio M/m is infinite, so that the ions do not move but form a uniform background of positive charge. To be more precise, we can say that M/m is large enough that the inertia of the ions prevents them from moving significantly on the time scale of the experiment. Poisson's equation in one dimension is

$$\varepsilon_0 \nabla^2 \phi = \varepsilon_0 \frac{d^2\phi}{dx^2} = -e(n_i - n_e) \quad (Z = 1).$$

If the density far away is n_∞, we have

$n_i = n_\infty.$

Defining

$$\lambda_D \equiv \left(\frac{\varepsilon_0 KT}{ne^2}\right)^{1/2}$$

where n stands for n_∞ and KT_e is in joules. KT_e is often given in eV, in which case, we will write it also as T_{eV}. We can write the solution

$$\phi = \phi_0 exp \left(-|x|/\lambda_D\right).$$

The quantity λ_D, called the Debye length, is a measure of the shielding distance or thickness of the sheath. Note that as the density is increased, λ_D decreases, as one would expect, since each layer of plasma contains more electrons. Furthermore, λ_D increases with increasing KT_e. Without thermal agitation, the charge cloud would collapse to an infinitely thin layer. Finally, it is the electron temperature which is used in the definition of λ_D because the electrons, being more mobile than the ions, generally do the shielding by moving so as to create a surplus or deficit of negative charge. The plasma is "quasi-neutral"; that is, neutral enough so that one can take $n_i \cong n_e \cong n_\infty$ where n is a common density called the plasma density, but not so neutral that all the interesting electromagnetic forces vanish.

II.5 The Plasma Parameter

The picture of Debye shielding that we have given above is valid only if there are enough particles in the charge cloud. Clearly, if there are only one or two particles in the sheath region, Debye shielding would not be a statistically valid concept. We can compute the number N_D of particles in a "Debye sphere":

$$N_D = n \frac{4}{3}\pi\lambda_D^3 = 1.38 \times 10^6\, T^{3/2}/n^{1/2} \quad (T\ in\ °K)$$

In addition to $\lambda_D \ll L$, "collective behaviour" requires

$$N_D \gg 1$$

A third condition has to do with collisions. The weakly ionized gas in an airplane's jet exhaust, for example, does not qualify as a plasma because the charged particles collide so frequently with neutral atoms that their motion is controlled by ordinary hydrodynamic forces rather than by electromagnetic forces. If ω is the frequency of typical plasma oscillations and τ is the mean time between collisions with neutral atoms, we require $\omega\tau>1$ for the gas to behave like a plasma rather than a neutral gas. The three conditions a plasma must satisfy are therefore:

$$1. \lambda_D \ll L$$

$$2. N_D \gg 1$$

$3. \omega\tau > 1$.

II.6 Toroidal Magnetic Confinement

The problem of magnetic confinement in mirror fields is unsatisfactory because Coulomb collisions continuously scatter particles into the loss-cone region of velocity space. These particles leave the mirror at both ends and represent an intolerably large loss, which prevents a long confinement time. It suggests itself to avoid these losses by bending the straight field lines into a torus, which removes the end losses. These ring-shaped confinement schemes are known as tokamaks and stellarators. The avoidance of end losses comes at a prize, namely the inhomogeneity and curvature of the magnetic field.

Tokamaks and stellarators have the common feature that the toroidal magnetic field is created by external field coils, as shown for a simple torus in fig. II-9. In this section we will discuss the basic ideas of plasma confinement in terms of the single particle model.

The toroidal field is generated by field coils, which have a winding density n/l per unit length that is greater at the inner edge of the torus than on the outer edge.
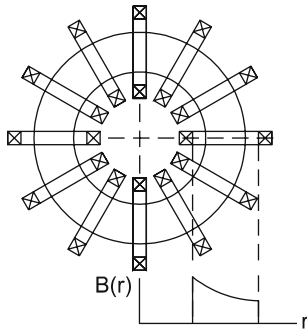
fig. II- 6 Simple torus with field coils that generate the toroidal magnetic field. The inset shows that the toroidal magnetic field strength decays as $B_t \propto 1/r$

Hence, the magnetic field will be radially inhomogeneous, as can be seen by applying Ampere's law

$$\oint H\, ds = 2\pi H_t(r) = nI.$$

Here, the integration follows a field line of radius *r* which encircles the total current *nI*, when *n* is the number of windings. This means that the toroidal magnetic flux density $B_t = \mu_0\, H_t$ decreases radially as

$$B_t = \mu_0\, \frac{nI}{2\pi r}.$$

In this inhomogeneous and curved magnetic field, charged particles experience the combined toroidal drift, which is dependent on the sign of the charge and effects charge separation in vertical direction. This charge separation leads to the establishment of a vertical electric field that is responsible for a secondary E×B drift driving both ions and electrons radially outwards (see fig.II-7).
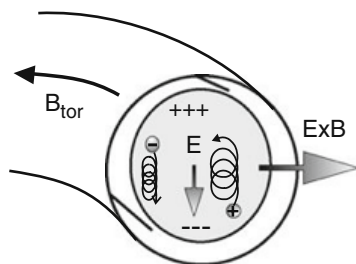
fig. II- 7 The toroidal drift leads to charge separation and a subsequent particle loss by ExB drift.

The net outward drift of the particles in a simple magnetized torus can be compensated by twisting of the toroidal field lines in such a way that a field line on the
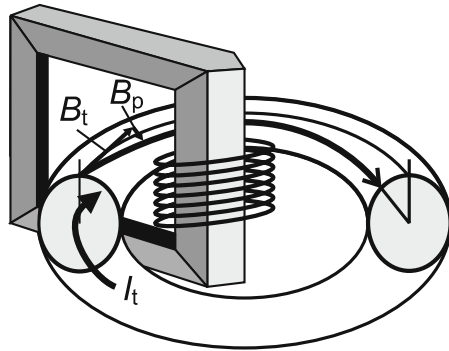
fig. II- 8 Generation of a rotational transform by an induced toroidal current. Only one yoke of the transformer is shown. The transformer of the JET experiment has eight yokes.

outside of the torus moves to the inside of the torus after a few revolutions about the major axis of the torus. Such a *rotational transform* of the magnetic field can be achieved by superimposing a *poloidal magnetic field* B_p. In a tokamak, such a poloidal field is generated by inducing a toroidal current I_t into the plasma ring, which forms a one-turn secondary of a huge transformer. fig. II-8 shows the principle of a tokamak and the twisting of the field lines. While tokamaks have been successfully used to demonstrate energy gain by fusion reactions their operation is limited to some ten seconds because of the necessity to ramp-up the magnetic field in the transformer to drive the toroidal current by induction, which is ultimately limited by the saturation of the transformer's iron core. A mode of quasi-steady state operation can be achieved, in principle, by driving the toroidal current by other means, for example by the radiation pressure of intense radio waves or microwaves [Erc01], [Pra01].
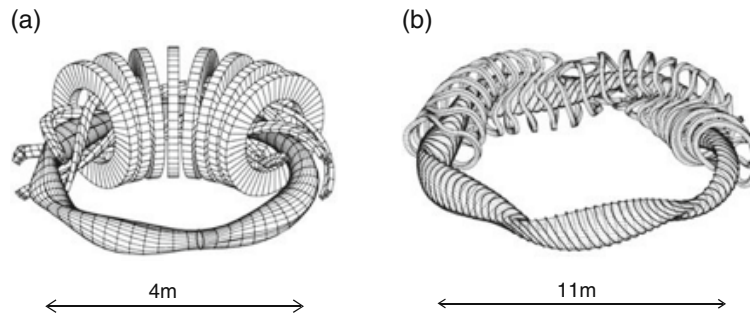
fig. II- 9 *(a)Field coil arrangements for the Wendelstein 7-A stellarator with planar toroidal field coils and two pairs of helical windings. (b) Wendelstein 7-X stellarator with superconducting modular fields coils that simultaneously produce toroidal and poloidal fields. (Reproduced with permission.(c)IPP/MPG)*

II.6.1 The Stellarator Principle

In a stellarator, the rotational transform is produced by external currents. This makes the stellarator attractive because it allows steady-state operation. In a classical stellarator, the poloidal field is generated by pairs of conductors that are wound in a helix around the torus. Fig. II-9a shows such an arrangement for the Wendelstein 7-A stellarator [Wob01]. The plasma has an elliptical cross-section with sudden bends and changes in the orientation of the major axis.

Modern stellarator concepts use non-planar field coils, which produce both a toroidal and a poloidal magnetic field. The most recent development is the stellarator Wendelstein 7-X, which is under construction in Greifswald, Germany. A sketch of the arrangement of the superconducting modular coils is shown in fig.II-9b The vacuum vessel and the cryostat are omitted.

Rotational Transform. The angle ι (iota), by which a magnetic field line is twisted after one revolution about the torus is easily understood for a tokamak and can be estimated as follows. Let us denote the major radius of the torus by R and the minor radius of the plasma by a. Further, r is a radial coordinate measuring from the center of the plasma. Assuming that the current density is approximately homogeneous in the plasma, we have a current density flowing in toroidal direction

$$j_t = \frac{I_t}{\pi a^2}$$

where I_t is the total toroidal current. The poloidal magnetic field H_p follows from Ampere's law

$$2\pi r H_p = I(r) = \pi r^2 j_t.$$

The poloidal magnetic flux density B_p then increases with r

$$B_p = \mu_0 \frac{I_t}{2\pi a^2}.$$

The poloidal angle, by which a field line is twisted around the torus can be estimated in the following way.
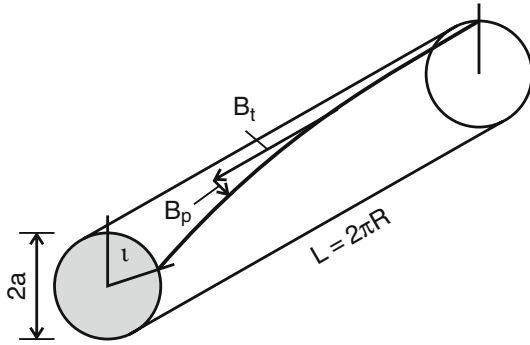
fig. II- 10 The rotational transform $\iota(\mathbf{r})$ is estimated by straightening a torus into a cylinder.

Consider the torus being cut and bent into a cylinder of length $L = 2\pi\,R$ and radius r as shown in fig. II-12. Then, the arc segment $r\,\iota(r)$ is given by

$$r\,\iota(r) = 2\pi R \frac{B_p(r)}{B_t} = 2\pi R \frac{\mu_0 I_t}{2\pi a^2 B_t} r$$

and

$$\iota(r) = \frac{\mu_0 I_t R}{a^2 B_t} r$$

which is independent of r. Hence, the transformation angle is the same for all radial positions and the magnetic field is unsheared. In a real tokamak, however, the current density peaks in the center of the plasma and the magnetic field is sheared. The *rotational transform* is defined as $\iota/2\pi$, and its reciprocal value $q = 2\pi/\iota$ is called the *safety factor*, which is the number of toroidal revolutions a field line has to make to complete one poloidal revolution. Many detailed investigations of plasma confinement were made in stellarators, which can be operated in a steady state mode.

II.7 Inertial Confinement Fusion

The ideas behind the Lawson criterion can be applied to two different scenarios. In magnetic confinement fusion, the plasma density is low ($\approx 10^{20}\,\mathrm{m}^{-3}$) and the energy confinement time is long ($\tau_E \approx 1$ s). Inertial confinement fusion (ICF) uses the opposite concept with a high plasma density and a short confinement time. The

idea is to burn a great part of the D-T content of a small pellet before the plasma has significantly expanded. Modern ICF concepts have been described in reviews [Lin01], [Nak01] and in a tutorial [Ros01].

II.7.1 Inertial Confinement Time

The confinement time for a homogeneous sphere of hot plasma can be estimated as follows: let us assume that the high-pressure plasma of radius R is surrounded by a vacuum. Then a rarefaction wave will propagate at the sound speed c_s from the vacuum boundary into the plasma, communicating that there is a vacuum out there to which it is free to expand. This rarefaction wave reaches a radial position r after a time $\tau(r) = (R - r)/c_s$, and upon arrival this part of the plasma is no longer

confined. The global confinement time for this system is then the mass-average of these local confinement times

$$\tau_c = \frac{1}{M} \int_0^R \frac{R-r}{c_s} 4\pi\rho r^2 dr = \frac{1}{4}\frac{R}{c_s}.$$

Here, $M = (4\pi/3)\rho\, R^3$ is the total mass. This result seems plausible because in a sphere of uniform density half of the mass is found in the outer 20% of radius. Therefore, τ_c is substantially smaller than a naïve estimate R/c_s.

II.7.2 Spherical Implosion

When intense laser radiation with a power density of 10^{14}–10^{15} W m^{-2} impinges on a spherical target, the energy is absorbed on the surface to generate a plasma of (2–3) keV temperature and a few hundred megabars pressure. Currently discussed fusion targets have a design as shown in fig. II-11. The outermost layer (ablator) is made of plastic foam or a low-Z material like beryllium. On the inside, a layer of D–T ice is deposited with about 80 μm thickness. The volume is filled with D–T gas with a mass density of 0.3 mg cm^{-3}, corresponding to 30 bar

pressure at room temperature. The intention is to heat and compress the central gas filling to fusion temperature of about 5 keV while the surrounding main fuel stays dense and relatively cold. This concept assumes self-ignition in the central hot spot. The pressure from the ablated surface material accelerates the outer shell of the target towards the center. The acceleration mechanism is the same as for rocket propulsion.
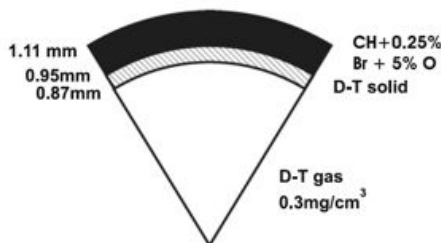
fig. II- 11 NIF pellet design. A plastic microsphere with the main fuel as a follow shell of D-T ice. The volume is filled with D-T gas at 30 bar normal pressure to form a hot spot.(Reprinted with permission ©2004, American Institute of Physics)

When the accelerated fuel collides in the center, compression and heating occurs. In inertial-confinement fusion experiments, the radius of the compressed fuel is about 1/30 of the original pellet radius. The achievable final velocity of the imploding shell of solid D–T can be estimated from the rocket equation

$$v_{shell} = v_{exhaust} ln \left(\frac{m_{ablator}}{m_{DT}} \right).$$

Typical implosion velocities vary from $(2-4)\times 10^5$ m s^{-1} [Lin01].

II.7.3 Ignition

In ICF, ignition occurs when the α-particles from the D–T fusion can deposit their energy inside the hot spot more rapidly than the heat content is lost by plasma expansion. Assuming that the density of the hot spot is high enough to stop all α-particles by collisions, we can use the Lawson condition for ignition, $n_e\tau_E > 1.5\times 10^{20}$ m^{-3} s and insert the confinement time τ_c to obtain

$$n_e R_{hs} = (1.5\times 10^{20} m^{-3})\times 4 c_s.$$

This is a condition for the product of plasma density and radius to achieve ignition. Introducing the mass density $\rho_m = \left(\frac{5}{2} \right) n_e m_p$, m_p being the proton mass, this defines a critical value for the product $(\rho_m R)_{crit} \approx 0.4$ g cm^{-2}, which is sufficient to stop the α-particles [Nak01]. Unfortunately, the ignition condition is not yet sufficient for an optimum use of the D–T fuel.

II.7.4 Burn Fraction

For an efficient fusion process, a considerable fraction (usually 1/3) of the main fuel must be burned during the confinement time. The rate, at which tritium (and deuterium) react in a 50% D/50% T fuel is

$$\frac{dn_T}{dt} = \frac{dn_D}{dt} = -n_D n_T \langle \sigma v \rangle_{DT}.$$

Inserting the total fuel density $n = 2n_T = 2n_D$, the burn process obeys

$$\frac{dn}{dt} = -\frac{1}{2}n^2\langle\sigma v\rangle_{DT},$$

which can be easily integrated from t = 0 to τ_c with the result

$$\frac{1}{2} - \frac{1}{n_0} = \frac{\tau_c}{2}\langle\sigma v\rangle_{DT},$$

where n_0 is the initial density of the compressed fuel. We define the burn fraction $f_b = 1 - \left(\frac{n}{n_0}\right)$ and introduce the initial mass density $\rho_{m0} = \left(\frac{5}{2}\right)n_0 m_p$, m_p being the proton mass. After simple algebraic manipulations we obtain

$$f_b = \frac{\rho_{m0}R}{\rho_{m0}R + g(T)},$$

with $g(T) = \frac{20m_p c_s}{\langle\sigma v\rangle_{DT}}$. g(T) takes a minimum of 6 g cm⁻² at 30 keV. To achieve a burn fraction of 1/3, we need $\rho_{m0}R \approx 3\,\text{g cm}^{-2}$, which is an order of magnitude higher than the mass per area for ignition.

In retrospect, we can ask why we need a highly compressed target for ICF. The functional dependence on the mass per area, $\rho_m R$, might suggest to work with solid D–T at a density of $\rho_m = 0.21\,\text{g cm}^{-3}$ and a corresponding larger radius of R $\approx$ 14.3 cm. The need for compression becomes clear, when we consider the total mass in a sphere of radius R that fulfils the constraint $\rho R \approx 3\,\text{g cm}^{-2}$

$$M_s = \frac{4}{3}\pi\rho_m R^3 = \frac{4}{3}\pi\frac{(\rho_m R)^3}{\rho_m^2}.$$

This shows that the mass of D–T fuel shrinks as ρ_m^{-2}. The energy yield of the DT–fuel is $\varepsilon_{DT} = 17.6\,MeV/(5m_p) = 3.4 \times 10^{11}$ J/g. The mentioned R=14 cm ball of D–T ice represents about 2.5 kg fusionable material with an explosive yield of about 70 kilotons TNT [Ros01]. Compressing the radius by a factor of 10 would increase the density by a factor of 1000 and reduce the fuel content by 10⁻⁶ to 2.5 mg equivalent to 70 kg TNT, or $\approx$ 300 MJ which can be handled in a fusion reactor. For a power plant design, about 5 shots per second can be envisaged with a total thermal power of $\approx$ 1.5 GW. The NIF capsule contains only about 1 mg D–T in view of the power handling capacity of the NIF target chamber.

II.7.5 Lawson Criterion for ICF

The balance equations of ICF are based on characteristic $\rho_m R$ values rather than on the $n_e \tau_E$ criterion of magnetic fusion devices. In the spirit of

$$n_e R_{hs} = (1.5 \times 10^{20} m^{-3} s) \times 4 c_s.$$

it is possible to rewrite the characteristic $\rho_m R = 3\,\mathrm{g\,cm^{-2}}$ for a burn fraction of 1/3 in terms of number density and confinement time $n\tau_c = 2 \times 10^{21}\,\mathrm{m^{-3}\,s}$ [Ros01].

Thus the Lawson criterion for ICF is typically a factor of 20 higher than that of magnetic fusion due to the inefficiencies in assembling the fuel that ICF has to overcome.

II.8 Interaction Between Pulsed Laser and Materials

The research on laser-matter interaction can bridge the gap between practical problems and applications of lasers, which offers an important way to study material properties and to understand intrinsic microstructure of materials. The laser irradiation-induced effects on materials refer to numerous aspects, including optical, electromagnetic, thermodynamic, biological changes in material properties. The laser-matter interaction is an interdisciplinary and complicated subject [All01]. When the material is irradiated with lasers, the laser energy will be firstly transformed into electronic excitation energy and then transferred to lattices of materials through collisions between electrons and lattices. The deposition of laser energy will produce a series of effects, such as temperature rise, gasification and ionization. The physical processes of interactions between lasers and matters can be grouped into linear and nonlinear responses of materials to laser pulses, namely thermal effects, nonlinear interactions, laser plasma effects and so forth [Woo01,Blo01].

The basis of all laser-triggered nuclear reactions is the acceleration of particles such as electrons, protons, and ions as well as the generation of high-energy bremsstrahlung photons by the interaction of very intense laser pulses incident on

matter. The mechanisms of particle acceleration change sensitively with the target material and chemical phase. The choice of target material in conjunction with the laser parameters is important for the control of plasma conditions and therewith for the control of optimum particle acceleration. Gaseous targets and underdense plasmas are suited best for the acceleration of electrons to energies of several tens of MeV [Mal01, Fau01, Ged01, Man01].
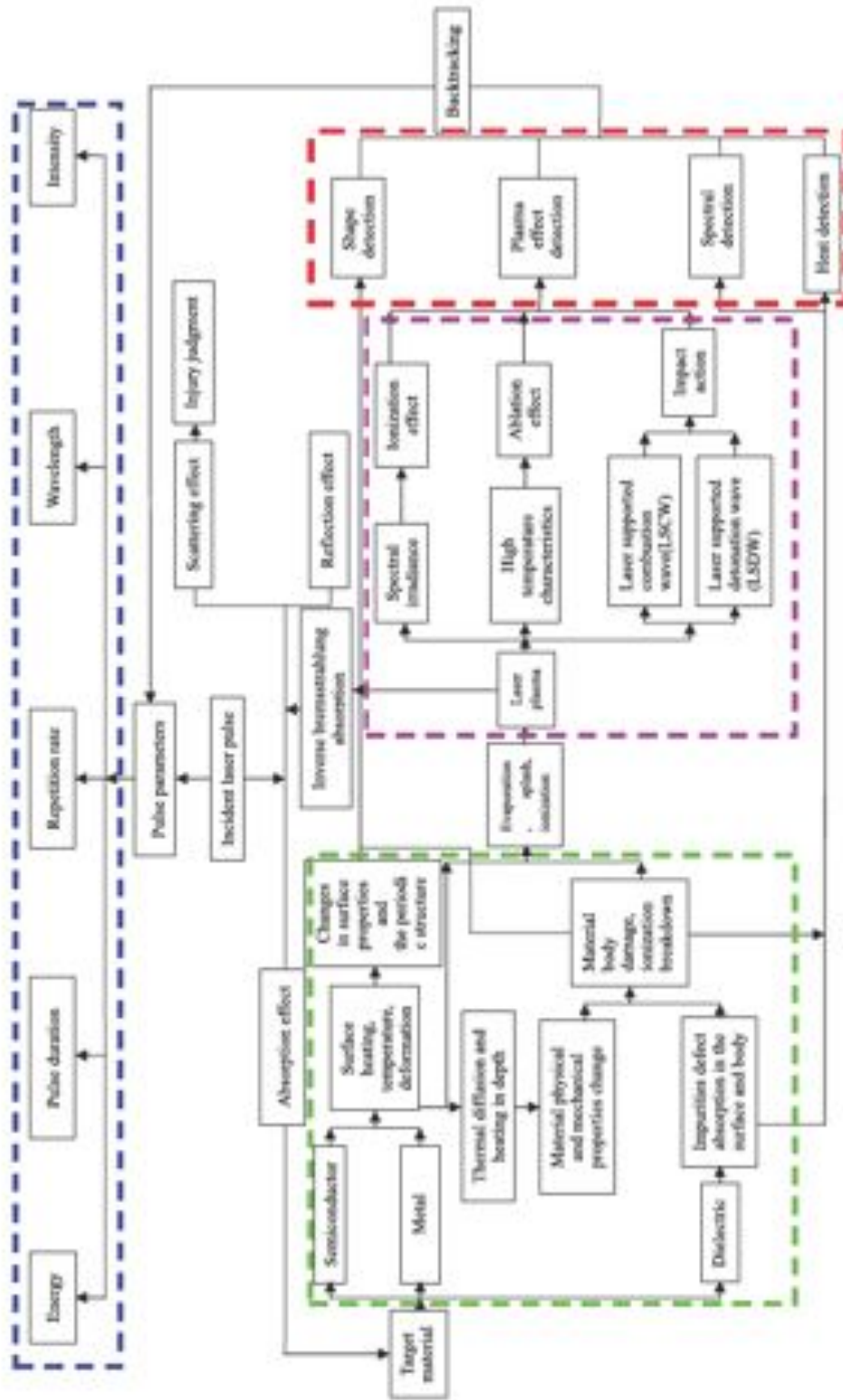
fig. II- 12 Laser matter interactions involve numerous complicated processes, inclusive of physical, mechanical, thermal, optical effects, etc. A full understanding of laser-matter interactions continues to be elusive.

Thin solid targets, in contrary, are used to accelerate protons and ions [Yan01, Kal01, Cow01, Mak01]. Deuterium fusion reactions have been realized with both heavy water droplets and deuterium-doped plastic [Pre01, Nem01, Kar01].

II.9 Plasma Physics at High Energy Density

II.9.1 Introduction

High-energy-density (HED) plasma physics is the study of ionized matter at extremely high density and temperature. Quantitatively, HED physics is defined to begin when matter is heated or compressed (or both) to a point that the stored energy in the matter exceeds about 10^{10} J/m^3, the energy density of solid material at 10,000 K ($\sim$1 eV), which corresponds to a pressure of about 10^5 atmospheres or a light intensity 16 orders of magnitude greater than the Sun's intensity at Earth.

By this definition, matter under HED conditions does not retain its structural integrity and cannot be sustained or contained by ordinary matter or vessels. Thus HED matter must be produced transiently in terrestrial laboratories, although it is common in high-energy astrophysics under both steady-state and rapidly changing conditions. For example, the center of the Sun, where fusion reactions have been converting hundreds of millions of metric tons of hydrogen into helium each second for billions of years, is estimated to have an energy density of 2×10^{16} J/m^3 (15 million K and 150 g/cm^3). Supernova explosions are obvious examples of transient HED astrophysical plasmas. Small-laboratory HED plasmas include the nanometer-sized clusters irradiated by very high intensity lasers, and the $\sim$1 μm, 10^7 K, near-solid-density plasmas produced when dense plasma columns carrying a high current implode unstably to form short-lived micropinches. By contrast, the magnetic confinement fusion plasmas of the current report are limited to perhaps 10^6 J/m^3, which allows them to be confined by magnetic fields produced by steady-state electromagnets that are supported by common structural materials.

II.9.2 What Constitutes HED Plasma Physics?

The lowest temperature end of HED parameter space is condensed matter pushed beyond its limits, such as occurs when matter at room temperature is subjected to 1 million atm. At temperatures above a few thousand kelvin, any material becomes at least partially ionized, so HED physics is necessarily HED plasma physics. Such "warm dense matter" lies at the intersection of plasma science and condensed matter/materials science. At the opposite end of the parameter space are plasmas in which particles are at such high temperatures that relativistic effects must be considered, an exotic state of matter thought to exist in sources of extra- galactic gamma-ray bursts as well as in the plasmas produced by lasers focused to very high intensity (more than 10^{20} W/cm^2) on solid surfaces. Some of these states are illustrated in fig. II-13.
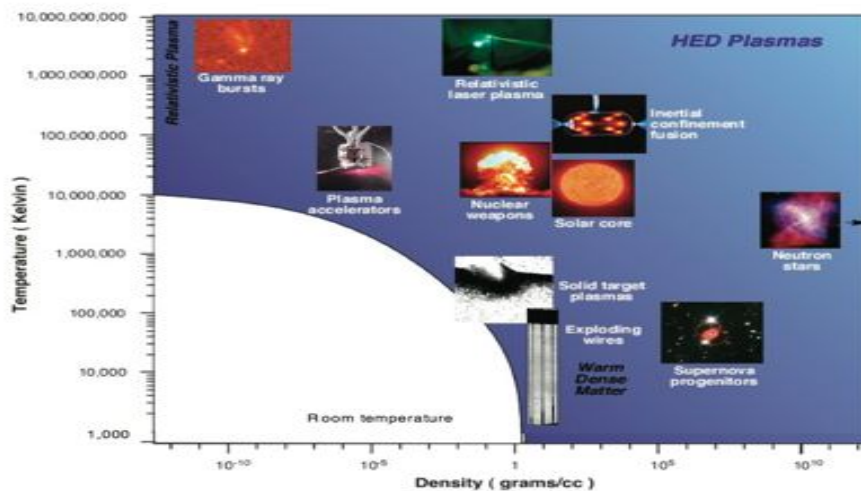
fig. II- 13 HED plasma space showing sample HED plasmas.

The portion of plasma parameter space accessible in the laboratory has been expanding to higher and higher energy density because of new technologies developed and facilities built to study matter under conditions that are reached in nuclear explosions. The widespread laboratory study of HED plasmas enabled by various facilities exemplifies that new plasma regimes have become the subject of plasma physics research in the past decade. These facilities, including powerful

lasers and pulsed power machines, are enabling plasma physicists, materials scientists, and atomic physicists to investigate states of matter that were not previously accessible for in-depth study in the laboratory. This trend will continue as facilities now under construction. The development of high-power lasers and pulsed power technology was originally driven by the quest for inertial confinement fusion (ICF) in the first case and laboratory-scale nuclear weapon effects testing in the second. HED plasma research in recent years has been largely driven by four applications that can be represented as follow:

- Inertial confinement fusion (ICF).
- Stockpile stewardship.
- Plasma accelerators.
- Laboratory plasma astrophysics.

II.9.3 Frontiers of Plasma Science

Atomic physics. HED drivers generate highly stripped, near-solid-density plasmas made of mid- and high-atomic-number atoms at temperatures of millions of degrees, with and without magnetic fields. Studying such plasmas contributes to our understanding of atomic processes and structure in complex ions subject to the strong electric and magnetic fields. Under- standing dense radiating plasmas in the laboratory and in the interior of astrophysical objects often relies on our understanding of highly stripped atoms in extremely dense plasmas. HED plasmas enable theoretical pre- dictions of atomic energy levels, rate coefficients, and so on, to be tested experimentally.

Condensed matter physics and materials science. Studies of "warm dense matter" straddle the boundary between condensed matter and plasma physics. The kinds of equations of state and dynamic properties of materials questions being addressed by experiments on warm, dense, partially ionized matter at high pressure connect to the questions being addressed by materials science studies. Thus physicists and materials scientists interested in low-temperature matter at a

pressure of 1 million atm do the same experiment on the same pulsed power machine to obtain relevant data as does the plasma physicist who is studying partially ionized matter at solid density and a few thousand degrees.

Nuclear physics. A potentially important connection between HED plasma science and nuclear physics will materialize if and when ignition is achieved in ICF experiments on the National Ignition Facility (NIF). Between 10^{17} and 10^{18} energetic neutrons will be emitted from a micrometer source in less than 1 ns, offering the possibility of neutron-induced reactions in nearby target nuclei that have already been excited by a previous neutron interaction.

Accelerator physics and high-energy physics. The high cost and size associated with conventional radio-frequency accelerator technologies has for nearly three decades been the main driver of a new approach to accelerating charged particles. It has now been demonstrated that the interaction of powerful lasers and particle beams with plasmas can generate plasma waves with extremely large electric fields. Although the physics of plasmas and the physics of charged particle beams are distinct areas of research, there are important connections between the two disciplines in the areas of physical concepts, mathematical formulation, computational tools, applications, and terminology.

Pulsed x-ray sources for various applications. Laser-driven plasmas and accelerators produce electron bunches of very short duration that can be converted to ultrashort pulses of x-ray radiation. These radiation bursts are so short that they can be used as a strobe light to freeze-frame the motion of complex systems, such as materials being compressed by shock waves or molecules undergoing chemical reactions. By enabling this diagnostic capability, HED technology impacts material science, chemistry, biology, and medical sciences.

Fluid dynamics. There is close intellectual coupling between plasma physics and fluid dynamics through various hydrodynamic and magnetohydrodynamic instabilities and turbulence. This certainly applies to the instabilities present in imploding inertial fusion fuel capsules.

Astrophysics. Plasma and atomic physicists have collaborated for decades to make plasma spectroscopy a valuable tool for astrophysicists. HED plasmas are now being used to develop a database on equations of state, x-ray spectra, and radiation transport, all of which are also thought to be relevant to astrophysical observations. Whether HED plasmas can help to illuminate the dynamics in spatially distant cosmological events that take place on vastly different time and spatial scales is an open question.

II.10 Laboratory Simulation of Astrophysical Phenomena

The universe has become the subject of much more probing studies in recent years because of new telescopes that cover the entire electromagnetic spectrum. They have permitted phenomenally high-energy events to be observed but not understood. Can we possibly do HED experiments in the laboratory that can illuminate these dramatic but spatially and temporally distant events? How can we test hypotheses concerning the physics of an observation that took place millions or even billions of light years away? the goal of laboratory plasma astrophysics is to discern the physical principles that govern extreme astrophysical environments through the laboratory study of HED physics. The challenge here is to develop physically credible scaling relationships that enable, through the intermediary of a computer code, laboratory experiments on the scale of centimetres or metres to illuminate physical processes taking in a distant part of the universe over enormous length scales. There is general agreement that laboratory experiments can and do provide atomic physics, equations of state, and other data on HED states of matter similar to those hypothesized to exist in distant objects. Laboratory plasma physicists, atomic physicists, and astrophysicists have, in fact, collaborated for many decades to make plasma spectroscopy a valuable tool for astrophysicists. The fresh twist is that laboratory experiments now allow experimentalists to investigate macroscopic volumes of HED plasma in states that are thought to be relevant to astrophysics and to determine equations of state, x-ray spectra, and radiation transport coefficients.

The use of HED laboratory experiments to investigate physical processes thought to be operative in astrophysical phenomena is a relatively new and controversial endeavour. It is generally believed that laboratory experiments cannot directly simulate an astrophysical situation even if some of the relevant dimensionless parameters are on the same side of some critical value, whatever that might be, in both the laboratory and the cosmos. However, the new generation of laboratory HED facilities can investigate matter under conditions that enable some of the physical processes that are thought to underlie observed phenomena to be studied. Examples of processes and issues that can be experimentally addressed in the laboratory under conditions that may be relevant to a range of astrophysical phenomena are compressible hydrodynamic mixing, strong-shock phenomena, magnetically collimated jets, radioactive shocks, radiation flow, complex opacities, photo-ionized plasmas, equations of state of highly compressed matter, and relativistic plasmas. The laboratory experiments can, therefore, be used to validate the computer codes that are being used by astrophysicists to try to understand the observations, assuming that the scaling laws imply that the experimental regime scales in some reasonable way to the astrophysical phenomenon. Thus, although the growing capacity of experimental studies has potentially opened new windows on cosmic plasmas and their behaviour, it is not yet clear that these experiments will one day become standard tools for addressing issues of astrophysical plasmas.

Many complex large-scale structures observable in the universe result from the nonlinear evolution of flows emanating from compact objects. Astrophysical plasma jets are a prime example of this class of phenomena and are also a good example of how laboratory experiments might contribute to an understanding of astrophysical observations. These collimated flows range over size scales from the 0.1 parsec associated with planetary nebulae and young stellar objects to the kilo-parsec jets driven by active galactic nuclei. The most pressing questions concerning these flows center on the processes responsible for their formation and collimation as well as their interaction with ambient media. In particular, the effects of radioactive cooling, magnetic fields, and intrinsic pulsing on jet structures have received much attention in the literature. In addition to the

examples cited, a massive star's evolution, jets arising during gravitational collapse may play an important role in the explosion of some types of supernovas.

Experiments designed to be relevant to these astrophysical phenomena are performed using high intensity lasers and conical wire arrays on pulsed-power facilities. The laboratory jets are formed hydrodynamically in these experiments, in some cases through converging conical flows that were either shock-driven or ablatively driven. In some of these experiments, radioactive cooling has been achieved in the jets, allowing issues such as collimation to be studied. In other cases, the propagation of a jet through an ambient medium has been studied. Jet bending via the ram pressure of a crosswind has also been explored. Issues such as stability, collimation, and shock physics associated with jets might be addressed, but their relevance to astrophysical observations requires similarity of the physical situation, as determined by dimensionless parameters, and evidence that the scaling laws adequately connect the two hugely disparate situations. [PSP10]

II.10.1 Long pulses

It tackles the processes characteristic of short pulse interactions, however, it is helpful to recall the established theories of resonant absorption, since these will serve as a long pulse benchmark. From the theoretical viewpoint, long laser pulses (that is of several picoseconds duration and longer) have the advantage that things tend to be in equilibrium. Thus, one can safely assume that the laser and plasma are in pressure balance, which mathematically stated, means that:

$$P_{\mathrm{e}} = n_e k_B T_e = \frac{I_0}{c} = \frac{E_0^2}{8\pi}.$$

Physically, this implies that the density profile near the critical point adjusts according to the local laser pressure and temperature, that is:

$$n_e = \frac{I_0}{c k_B T_e} \cong 200 \frac{I_{18} \lambda_\mu^2}{\mathrm{T}_{keV}} n_c.$$

Contrast this with the short pulse case, where the electron density is essentially pinned to the solid density via the quasi-neutrality condition $n_e = Zn_i$. The last relationship is appropriate if the ions have sufficient time to move in response to the laser pressure. Below the reflection point, an underdense, outwardly streaming plasma 'shelf' will also form [Kru01]. An equation for the equilibrium energy balance can be obtained by simply assuming that the absorbed laser flux is entirely carried away by a population of free–streaming hot electrons with a temperature T_h.

$$\eta_\alpha I_0 = \beta n_h v_h \frac{m v_h^2}{2},$$

where h_a is the usual absorption fraction, $v_h = (k_B T_h/m)^{1/2}$ and n_h are the mean hot electron velocity and number density respectively. The constant $\beta = \sqrt{2/\pi}$ arises from the assumption that the hot electrons form a 1-dimensional Maxwellian distribution. Thus, in this standard picture, the hot electrons determine the energy balance, whereas the cold bulk electrons are responsible for momentum (or pressure) balance a situation which will prevail as long as $n_h < n_c \ll n_e$.

In particle-in-cell simulations carefully set up to ensure pressure balance from the outset, Forslund, Kindel and Lee (denoted FKL) argued that the hot electron temperature should scale like:

$$T_h^{FKL} \cong 14 \left(I_{16} \lambda_\mu^2 \right)^{1/3} T_e^{1/3},$$

where I_{16} denotes the laser intensity in units of 10^{16} Wcm^{-2} , l_m is the laser wavelength in mm and T_e the temperature of the cold, bulk electrons in keV. This scaling law is based on the physically appealing ansatz that an electron which is resonant with a plasma wave will gain an energy:

$$T_h \sim e\Delta\phi = e E_p L,$$

where E_p is the local longitudinal electric field and L the half-width of the density perturbation (which in turn, is proportional to the density scale- length). [For01] found that in their simulations, L turned out to be the geometric mean of the

plasma skin depth in the upper shelf region, the Debye length at the critical density, and the laser wavelength divided by 2p. In other words,

$$L \cong \left(\frac{c^2 v_{te}}{\omega^2 \omega_p}\right)^{1/3},$$

A similar analysis of hot electron spectra resulting from resonance absorption was made independently by Estabrook [EST78]. They found a much stronger inverse dependence of the steepened density scale-length on the intensity: $L \propto I^{-0.48}$ and deduced two empirical formulae for T_h by varying I and T_e in their 2D PlC simulations:

$$T_h^{EK1} = 20T_e^{1/4}\left(I_{16}\lambda_\mu^2\right)^{0.39},$$

$$T_h^{EK2} = T_e + 21T_e^{0.04}\left(I_{16}\lambda_\mu^2\right)^{0.42}.$$

With increasing intensity, higher plasma electric fields are generated but their resonance width is reduced, so that the net energy gain by an electron, $\Delta U \sim e E_p L$, will scale more weakly than $E_p \sim I^{1/2}$. These two model curves, depicted in fig. II-15, predict 50% lower temperatures, but very similar scaling, to data from nanosecond laser-plasma experiments over a wide range of parameters.
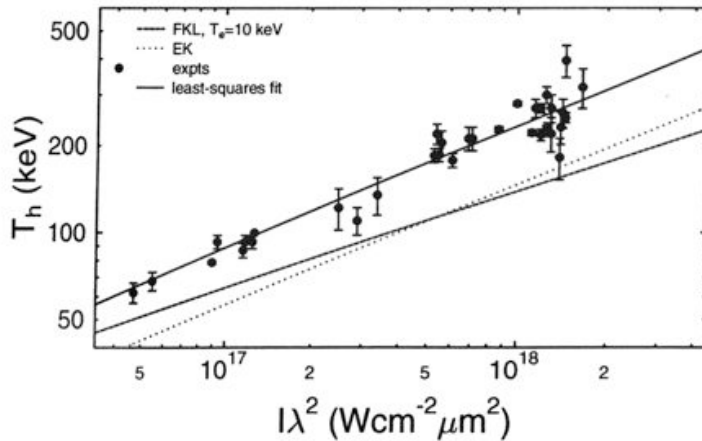
fig. II- 14 Scaling of hot electron temperature with intensity according to steady-state theories and experimental x-rays measurements made with the Los Alammos nanosecond CO2 laser [Pri81]. The least-squares fit is given by $T_h=89(I_{17}\lambda^2)^{0.42\pm0.12}$ keV.

II.10.2 Short pulses

Turning now to femtosecond laser-plasma interactions, the first point to note is that the steady-state picture above is unlikely to apply for two reasons:

i)   the much sharper density and field profiles

ii) the non-equilibrium nature of the interaction on this short time-scale. So what should we use instead?

The variety of absorption mechanisms makes it difficult to formulate a comprehensive theory of hot electron generation along the lines just described. Nevertheless, one can at least construct approximate scaling-laws for T_h from the absorption models as they stand. Let us start with the Brunel model, in which electrons are directly accelerated by the laser field incident on a step-like density profile. According to the simple electro-static version of this model, the electrons acquire velocities $v_d = 2v_{os}\sin\vartheta$. The hot electron temperature is therefore just

$$T_h^B = \frac{mv_d^2}{2} \cong 3.7 I_{16}\lambda_\mu^2,$$

where, as before, I_{16} is the intensity in 10^{16} Wcm^{-2} and l_m, the wavelength in microns. The above estimate does not allow for pump depletion or relativistic effects, which would reduce this scaling at higher intensities.

Since $\eta_B \sim I_0^{1/2}$, this can only be consistent if n_h is independent of I_0. In the experimentally more relevant case of a single, obliquely incident pump onto a steep but finite density gradient $(L/\lambda < 0.1)$ electromagnetic simulations with fixed ions give a much weaker scaling [Gib01]:

$$T_h^{GB} \cong 7(I_{16}\lambda^2)^{1/3},$$

which is similar to T_h^{FKL} for long-pulse resonance absorption in steepened density profiles, but numerically a factor of two or so lower depending on the density scale-length.

The weak scaling for small L/λ and fixed ions partly comes about because the absorption fraction decreases with intensity. Thus one would have:

$$T_h \sim 7(I\lambda^2)^{2/9} \left(\frac{n_h}{n_c}\right)^{-2/3}.$$

Comparing this expression to T_h^{GB} above would suggest that the hot electron fraction must also decrease weakly with laser intensity ($\sim I^{1/6}$) under these conditions. Analogous simulations with somewhat longer pulse lengths and mobile ions [Gib02] yield temperatures more in line with T_h^{FKL}. Although there is still no pressure balance in this case, a quasi-stationary state is rapidly reached in which the bulk ions form a shock in the over-dense region, but a small fraction is also pulled out, forming an under-dense shelf. Under these conditions, the absorption is dramatically enhanced (reaching values of 80%) and more electrons are able to sample the full laser field, leading to higher temperatures.

Another school of thought on hot electron generation [Wil01]

argues that at 'relativistic' intensities, $T_h \propto e\phi_p$, where f_p is the ponderomotive potential due to the standing wave field formed when the laser is reflected by the target surface. This appealingly simple expression arises naturally from the j x B mechanism, which when generalized to relativistic intensities, predicts that

$$T_h^W \cong mc^2(\gamma - 1) = mc^2 \left[\left(1 + \frac{p_{os}^2}{m^2 c^2}\right)^{1/2} - 1\right]$$

$$\cong 511 \left[\left(1 + 0.73 I_{18}\lambda_\mu^2\right)^{1/2} - 1\right] keV.$$

It is expected to apply at normal incidence for intensities above 10^{18} Wcm^{-2} , where the j x B mechanism becomes significant and other mechanisms are suppressed because the laser electric field vector is perpendicular to the density gradient. However, the simulations were all performed with mobile ions, meaning that the absorption and hot electron generation was accompanied by hole boring adding further nuances to the interaction physics. Hole boring, or any kind of surface deformation for that matter, modifies the interaction geometry in such a way that the laser field may couple directly to plasma oscillations parallel to the density gradient.

II.11 Hot electron generation

There are at least three tell-take signatures of high-intensity collective effects in laser-plasma interactions: high, angular-dependent absorption into hot electrons, hard x-ray emission and fast ion generation. Over the last decade, many experiments have been performed which consistently verified this picture of sub-ps interactions. As seen in the previous section, absorption in excess of 50% for p-polarized light has been measured for intensities of 10^{16} Wcm^{-2} [Kie01],[Kle01],[Mey01],[Teu01],[Sau01], x-rays in the keV-MeV range have been detected [Kme01],[Kle01],[Che01],[Rou01],[Sch01],[Teu02] and fast ion blow-off was also seen quite early on [Met01] and [Few01]. All of the collision-less absorption mechanism will result in the superheating of some fraction of electrons to energies much higher than the initial bulk plasma temperature T_e. More often than not, this suprathermal electron component has a Maxwellian-form with a characteristic temperature $T_h >> T_e$ see fig.II-15. This is perhaps quite surprising, given that the hot electrons are accelerated by a coherent electric field , whether belonging to the laser itself or within the plasma: one might expect to see a more monochromatic beam-like tail with some thermal spread. However [Bez01] the random, stochastic nature of the particle acceleration in standing-wave fields leads to strong cycle-to-cycle fluctuations in the trajectories and energies acquired by electrons. Averaging these single-particle distributions over time inevitably leads to a Maxwellian velocity distribution.
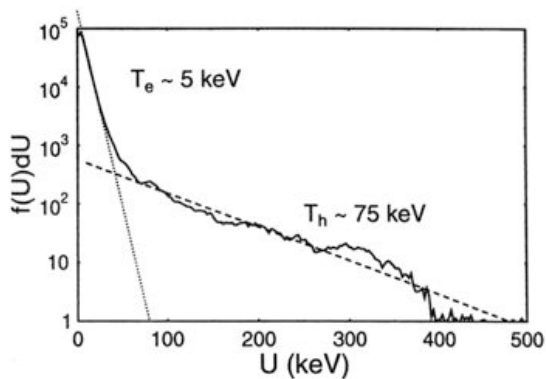
fig. II- 15 *Typical bi-Maxwellian electron distribution resulting from collisionless heating by a laser. This example is aPIC simulation using the BOPS code with a laser irradiance* $5 \times 10^{16} W\, cm^{-2} \mu m^2$ *incident at 45°P onto a plasma with* $\frac{n_e}{n_c} = 3$ *and* $\frac{L}{\lambda} = 0.2$

This radical departure of the electron distribution function from a pure (single-temperature) Maxwellians is a hallmark of collective heating mechanisms. Contrast this with collisional heating, which leads to a broadening of f(v) and corresponding increase T_e. The determination of the hot electron temperature, T_h, and its associated hot electron fraction (that is, number of suprathermal electrons, n_h, often expressed relative to the critical density n_c) poses one of the most important physics issues in short-pulse laser–solid interactions. Many applications-from femtosecond diffractometry to fast ignitor schemes depend crucially on achieving the highest possible conversion efficiency of laser energy into hot electrons of a specific energy. To date, this issue remains controversial because the interaction physics consists of many competing effects, which vary in importance according to the conditions: laser intensity, target material, contrast ratio.

II.12 References Chapter II

[All01]M. von Allmen and A. Blatter, *Laser-Beam Interactions with Materials: Physical Principles and Applications, 2nd Edition, Springer-Verlag, Berlin & Heidelberg, Germany, 1995.*

[Bez01]B.Bezzerides et al. Randomness, *Phys.Rev.Lett.,44,651-654(1980)*

[Blo01] N. Bloembergen, *Laser-induced electric breakdown in solids, IEEE J.Quantum. Electron. 10, 375-386, 1974.*

[Che01]H. Chen et al. , *Phys.Rev.Lett. 70,3431-3434(1993)*

[Cow01]T. Cowan et al.: *Phys. Rev. Lett. 92, 204801 (2004)*

[Erc01]V. Erckmann, U. Gasparino, *Plasma Phys. Control. Fusion 36, 1869 (1994)*

[EST78] K.G.Estabrook and al., *PRL40,42-45 (1978)*

[Fau01]J. Faure et al. : *Nature 431, 541 (2004)*

[Few01]A.P.Fews et al., *Phys.Rev.Lett.,73,1801-1804(1994)*

[For01]D.W Forslund et al.,*Phys.Rev.Lett,39,284-288(1977)*

[Ged01] C. Geddes et al.: Nature 431, 538 (2004)

[Gib01]P.Gibbon et al., Phys.Rev.Lett.,68,1535-1538,(1992)

[Gib02]P.Gibbon, PhysRevLett.,73,664-667(1994)

[Kal01]M. Kaluza et al.: Phys. Rev. Lett. 93, 045003 (2004)

[Kar01] S. Karsch et al.: Phys. Rev. Lett. 91(1), 015001 (2003)

[Kie01] J.C. Kieffer et al. , Phys. Rev. Lett.,62,760-763(1989b)

[Kle01]D.E.Klem et al. , 98-102 Short-pulse high-intensity lasers and applications II, vol 1860. SPIE, (1993)

[Kme01]J.D.Kmetec et al., Phys.Rev.Lett., 68, 1527-1530(1992)

[Kru01]W.L.Kruer , The Physics of Laser Plasma Interactions. Addison-Wesley N.Y.(1988)

[Mak01]A. Maksimchuk et al.: Plasma Phys. Rep. 30, 473 (2004)

[Mal01]V. Malka et al.: Science 298, 1598 (2002)

[Man01]S. Mangles et al.:Nature 431, 535(2004)

[Mey01]D.D. Meyerhofer , IEEE J.QuantumElec,33 1935-1941(1997)

[Nem01] K. Nemoto et al.: Appl. Phys. Lett. 78(5), 595 (2001)

[Pra01]R. Prater, Phys. Plasmas 11, 2349 (2004)

[Pre01]G. Pretzler et al.:Phys. Rev. E 58, 1165 (1998)

[Pri81] W. Priedhorsky , D. Lier , R. Day & D. Gerke 1981 Phys. Rev. Lett. 47 , 1661 .

[PSP10] Plasma Science, Plasma 2010 Committee, ISBN:0-309-10944-2

[Rou01]A.Rousse et al., Phy.Rev.E., 50,2200(1994)

[Sau01]R. Sauerbrey et al. , Phys. Plasmas, 1 1635-1642(1994)

[Sch01]M.Schnurer et al., Phys.Plasmas,2,3106(1995)

[Teu01] U.Teubner et al. , Phys Rev. Lett. 70, 794-797(1993)

[Teu01]U.Teubner et al. , Phys.Rev.E,54,4167-4177(1996a)

[Wil01]S.C Wilks et al. , Phys.Rev.Lett,69,1383-1386,(1992)

[Wob01]H. Wobig, talk on the occasion of the retirement of G. Grieger (2000)

[Woo01]R. M. Wood, Laser-induced damage of optical materials, IOP Publishing Ltd., London, UK, 2003.

[Yan01]J.M. Yang et al.: Appl. Phys. Lett. 84, 675 (2004)

CHAPTER III

NUCLEAR PHYSICS @ ELI-NP

III.1 ELI-NP Project

Today's top specifications of high power pulsed laser systems are characterized by a peak power between one and two petawatts at very low (sub Hz) repetition rates, this being unchanged over more than one decade now. The majority of high intensity systems, however, still rests at the 100 TW level. ELI aims at another order of magnitude in peak power, into the 100 PW regime, by coherent combination of several such modules. With these parameters ELI will certainly lead the international high power laser scenario. ELI will be the first laser research infrastructure, which is the result of a coordinated effort of a multi-national scientific laser community.

In this context it is illustrative to view the global distribution of high-power laser systems beyond 100 TW peak power, and its temporal evolution, particularly in Europe. Figure III-1 shows the world map of high intensity systems in 2006 and the current situation in Europe, Russia and India by the end of 2010. The left part of the figure shows that high power lasers are pre-dominantly located in three global regions at moderate northern latitudes: North America (US and Canada), Europe (including Russia), and the Asian-Pacific region (including India). This general feature has not changed since 2006 except that now (in 2010) the overall

number of such systems has considerably increased. The Extreme Light Infrastructure is a major breakthrough compared with any other large- scale facility worldwide. Indeed, there is no such an integrated, multi-site laser facility dedicated to multi-disciplinary studies and secondary sources production and applications. ELI will extend the field of laser-matter interaction, now limited to the relativistic regime ($a_0 \sim$1-10, which corresponds to intensities 10^{18}W/cm^2 - 10^{20}W/cm^2), into the ultra-relativistic regime $a_0 \sim 10^2$-10^4.
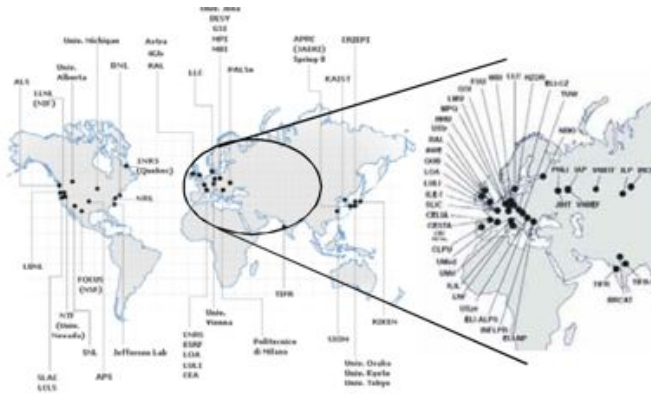
fig.III- 1 World map of high intensity systems in 2006(left) and the current situation in Europe, Russia and India by the end of 2010(right). Taken from the "International Committee on Ultra-High Intensity Lasers (ICUIL,wwwicuil.org).

By means of relativistic effects, these extreme intensities will provide access to extremely short pulse durations in the atto-second or zepto-second regime. ELI will comprise 4 branches: Ultra-High-Field Science centred on direct physics of the unprecedented laser field strength, Atto-second Laser Science, which will capitalize on new regimes of time resolution, High-Energy Beam Facility, responsible for development and use of ultra-short pulses of high-energy particles and radiation stemming from the ultra- relativistic interaction, and Nuclear Physics Facility with ultra-intense laser and brilliant gamma beams (up to 19 MeV) enabling also brilliant neutron beam generation with a largely controlled variety of energies. ELI will afford new investigations in particle physics, nuclear physics, gravitational physics, nonlinear field theory, ultrahigh- pressure physics, astrophysics and cosmology. Besides its fundamental physics mission, a paramount objective of ELI will be to provide ultra-short energetic particle (10-

100 GeV) and radiation (up to few MeV) beams produced from compact laser plasma accelerators.

In particular our interest is in Nuclear Physic; for ELI-NP the extreme light is realized in a twofold way: by very high optical laser intensities of high power laser and by the very short wavelength beams with very high brilliance. This combination allows for three types of experiments: stand-alone high power laser experiments, stand-alone γ beam experiments and combined experiments of both facilities. Here the low repetition rate (1/min) of the high power laser requires the same low repetition rate for the γ beam in combined experiments. While the stand-alone γ beam will be used with typically 120 kHz the low repetition mode requires few very intense γ pulses. With the high power laser we do not plan to interact with nuclear dynamics directly, but we use the laser for ion acceleration or to produce relativistic electron mirrors by laser acceleration followed by a coherent reflection of a second laser beam in order to generate very brilliant X-ray or γ beams. We plan to use these beams later to produce exotic nuclei or to perform new γ spectroscopy experiments in the energy or time domain. The production of heavy elements in the Universe, a central question of astrophysics, will be studied within ELI-NP in several experiments.

fig.III- 2 The image illustrates the ELI-NP (Extreme Light Infrastructure – Nuclear Physics) research infrastructure of the center that will be built in Magurele (Romania).

III.2 Nuclear Reactions in Laser Plasma

Given its nature, the plasma state is characterized by a complexity that vastly exceeds that exhibited in the solid, liquid, and gaseous states. Correspondingly, the physical properties of nuclear matter (structure, life times, reaction mechanisms etc.) could be drastically changed inside the plasma. These studies represent one of the most far ranging, difficult and challenging research areas today, implications could cover others fields, from quantum physics to cosmology, astrophysics etc. In this context, one of the most crucial aspects concerns the role of electron screening. Direct and indirect measurements of the relevant cross sections have been performed over the years. Direct measurements using accelerated beams show that, at very low energies, the electrons in the target's atoms partially screen the Coulomb barrier between the projectile and the target [Sal54], resulting in an enhancement of the measured cross section compared with the bare nucleus cross section [Nacre]. The electron screening effect is significantly affected by the target conditions and composition [Lip10], it is of particular importance for the measurement of cross-sections at extremely low energetic domains including plasma effects, i.e. in an environment that under some circumstances and assumptions can be considered as "stellar-like" (for example, for the study of the role played by free/bounded electrons on the Coulombian screening can be done in dense and warm plasmas). Electron screening prevents a direct measurement of the bare nucleus cross section at the energies of astrophysical interest. In the last decade, the bare cross section has been successfully measured in certain cases by using several indirect methods [Spi11].

Usually, astrophysically relevant reactions are performed in the laboratories with both target and projectile in their ground state. However, in high temperatures plasmas (10^8K), an important role can be also played by the excited states, as already deeply discussed in the pioneering theoretical work of Bahcall and Fowler [Bah69]. In that case, the authors studied the influence of low lying excited ^{19}F states on the final ^{19}F(p,alpha) reaction, predicting an increase of a factor of about 3 in reaction rate at temperatures of about 1-5 GK. Thus determining the appropriate experimental conditions that allow evaluating the role of the excited

states in the stellar environment could strongly contribute to the development of nuclear astrophysics. The study of direct measurements of reaction rates in plasma offers this chance. In addition, other new topics can be conveniently explored, such as three body fusion reactions as those predicted by Hoyle [Hoy46], lifetime changes of unstable elements [Lim06] or nuclear and atomic levels [Han07] in different plasma environments; other fundamental physics aspects like non-extensive statistical thermodynamics [Tas09] can be investigated in order to validate/confute the general assumption of local thermal equilibrium that is traditionally done for plasmas.
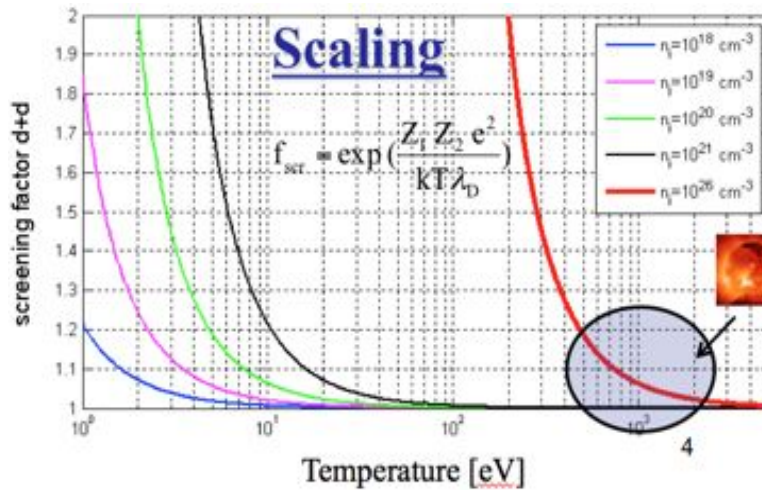
fig.III- 3 Calculated screening factor for the D+D reaction as a function of electron temperature and density (different colours from 10^{18} to 10^{23}). Highlighted are typical solar values.

Although it seems practically impossible to reproduce in the laboratory the extreme properties of stellar matter, according to a method commonly used in other fields of plasma physics, it is possible to rescale the plasma parameters (temperature and density) in order to make the laboratory conditions similar to the ones of an astrophysical plasma. As an example, fig.III-3 shows the calculation of the screening factor for the *D+D* reaction as a function of electron temperature and density. It can be noticed that the typical values of solar screening can be reproduced in alternative plasma conditions of temperature and density. The future availability of high-intensity laser facilities capable of delivering tens of petawatts of power (e.g. ELI-NP) into small volumes of matter at high repetition

rates will give the unique opportunity to investigate nuclear reactions and fundamental interactions under extreme plasma conditions [Mas10], including also the influence of huge magnetic and electric fields, shock waves, intense fluxes of X and γ-rays originating during plasma formation and expansion stages.

III.3 First cases of study

To investigate these research topics, we are proposing the construction of a general purpose experimental set-up, where it will be possible to study the electronic screening problem in a wide variety of cases and configurations with different purposes. In particular, we propose to study the screening effects on low energy fusion reactions and on weakly bound nuclear states (Hoyle, Efimov [Efi09] etc.). Concerning the first question, among the various nuclear reactions which have attracted relevant attention also for astrophysical or cosmological reasons, we would select the $^{13}C(^4He,n)^{16}O$ and $^7Li(d,n)^4He-^4He$ reactions: the former for its relevance in the frame of stellar nucleosynthesis, the latter for the role played in Big Bang primordial nucleosynthesis. Through the laser-target interaction, we aim at producing plasmas containing mixtures of $^{13}C + ^4He$ and $^7Li + d$ in order to investigate inner-plasma thermo-nuclear reactions.

The $^{13}C+^4He$ reaction is of key interest for the investigation of the helium burning process in advanced stellar phases [Mey94]. In particular, it can be activated at the base of AGB stars, thus constituting one of the most interesting neutron sources in stellar conditions. These are in turn important for the so-called "slow-process", i.e. the neutron induced reactions responsible of the heavy elements production. Thus, by gaining further knowledge about the $^{13}C+$alpha reaction, it will be possible to evaluate more carefully the available neutron flux for the following s-process nucleosynthesis. The astrophysical factor S(E) is shown in Figure 13(b) : we notice

that no experimental data are available in the region below 270 keV, but only model predictions.

The ^{7}Li(d,n)^{4}He-^{4}He reaction was recently addressed by Coc et al. [Coc10] as one of the most important reactions affecting the CNO abundances produced during the primordial nucleosynthesis (BBN). From such an analysis, it was found that the ^{7}Li nucleosynthesis is strongly influenced by the ^{7}Li(d,n) ^{4}He-^{4}He reaction rate. Data collected by these authors give a variation of two orders of magnitude on the ^{7}Li abundance during the BBN epoch, around 1 GK of temperature, with respect to the reaction rate measured by Boyd et al. [Boy93]; the latter is usually adopted for the BBN evaluation. These discrepancies can be explained if one considers that very few experimental data exist, and authors consequently assume a constant S-factor ranging between two extreme hypotheses from 5 to 150 MeV×b. Providing new experimental data focused on the determination of the outgoing neutron flux is essential in order to up-grade our knowledge of this process and consequently of the BBN at a temperature of about 1 GK. This critical temperature domain will be affordable by the peta-watts laser facility of ELI-NP [Gib05], including the configuration based on two laser beams producing colliding plasmas [Mas10] [Lab13].

In relation to the weakly bound nuclear states, as a first case of study we propose to investigate the ^{11}B(^{3}He, d)^{12}C* reaction in a plasma. Nucleonic matter displays a quantum-liquid structure, but in some cases finite nuclei behave like molecules composed of clusters of protons and neutrons. Clustering is a recurrent feature in light nuclei, from beryllium to nickel. Cluster structures are typically observed as excited states close to the corresponding decay threshold; the origin of this phenomenon lies in the effective nuclear interaction, but the detailed mechanism of clustering in nuclei has not yet been fully understood. The second J = 0+ state at 7.654 MeV in ^{12}C, first predicted by Hoyle [Hoy46] in 1953 and thus called the Hoyle state, plays a central role in nuclear physics. It is a well-known fundamental testing ground of models of the clustering phenomena in light nuclei, which is highlighted by recent developments of ab initio theoretical calculations that are able to calculate light nuclei such as ^{12}C. The Hoyle state plays a central role in

stellar helium burning by enhancing the production of ^{12}C in the Universe, allowing for life as we know it. It is the first and quite possibly still the best example of an application of the anthropic principle in physics. Early on after the discovery of the Hoyle state, it was suggested by Morinaga [Mor56] that we can learn more about the structure of the Hoyle state by studying the rotational band built on top of it, which led to a 50-yr long search for the second 2+ state in ^{12}C. Recently, the existence of the second 2+ state in ^{12}C has been the subject of much debate.

The current evaluation of the triple-a reaction rate assumes that the a decay of the 7.65 MeV, 0+ state in ^{12}C, proceeds sequentially via the ground state of ^{8}Be. This assumption has been sustained also by a new upper limit of 5×10^{-3} on the direct a decay of the Hoyle state at 95% of C.L. [Kir12] extracted from the study of the ^{11}B(^{3}He, d) reaction. This assumption is challenged by the recent identification of two direct a-decay branches with a combined branching ratio of 17.5% [Rad11]. If correct, this would imply a corresponding reduction in the triple-a reaction rate with important astrophysical consequences. This data has been extracted by the fragmentation of quasi-projectiles from the nuclear reaction ^{40}Ca + ^{12}C at 25 MeV/nucleon, used to produce excited states candidates to a-particle condensation. This approach differs from the previous one for the presence of nuclear medium. In the ^{11}B(^{3}He, d), carbon Hoyle state is populated and decay in vacuum while the fragmentation approach is populated and decay in presence of nuclear matter. For the important astrophysical consequence is mandatory to study these topics in a plasma environment.

To perform the proposed experiments, providing relevant data concerning the aforementioned reactions and others, we aim to take advantage from the excellent and unique performance of the ELI-NP facility and realize an experimental setup where two laser beams generate two colliding plasmas. The reaction products (neutrons and charged particles) will be detected through a new generation of plastic scintillators wall and through a new silicon carbides wall.

III.4 Experimental configuration

The use of colliding plasma plumes suitable for nuclear physics studies was proposed few years ago at LNS [Mas10] and recently adopted also by other research teams [Lab13]. One of the possible schemes may be the following: a first laser pulse imping on a ^{13}C, ^{7}Li or ^{11}B solid thin target (few micro-meters) producing, through the well-known TNSA (Target Normal Sheath Acceleration) acceleration scheme, boron, carbon or lithium plasma. The rapidly streaming plasma impacts on a secondary plasma, prepared through the interaction of a second laser pulse on a gas jet target (made by ^{4}He, D_2 or ^{3}He). TNSA was intensively studied in the last years; experiments [Mac13] and models [Pas08] show that this acceleration scheme works very well in the intensity domain between 10^{18}-10^{20} W/cm^2. The produced ions expand along a cone, whose axis is normal to the target surface, with a relatively low emittance [Bor04]. The observed ion energy distributions have an exponential shape [Dze10] with a high- energy cut-off, linearly depending on the laser intensity [Mac13] and scaling with the atomic number $E^i \propto Z$. Figure III-4(a) shows some carbon ions energy distributions [Car10] measured in a TNSA regime at 6-7$\times 10^{20}$ W/cm^2. These experimental observations are well described and predicted by theoretical models (see [Pas08] and reference there in). A further fine-tuning can be done acting on other parameters: i.e. the laser incident angle or polarization [Car10], the structure of the target surface [Buf10], or the target thickness [Dze10], [Fuc06]. The total number of accelerated ions obviously depends on the target composition [Mac13]; in particular, for a single component target we can estimate that it roughly corresponds to the removed mass. In this last condition also a fraction of protons was experimentally observed due to the presence of hydrogenated contaminants on the target surface. This component can be in any case reduced through a preliminary heating of the target surface. Due to the wide possibility of ions properties tuning (energy and number, especially), the idea underlying this proposal is to take advantage of the unique opportunities provided by ELI-NP (high rep. rate and petawatts laser) to operate in the TNSA domain (few

10^{18}W/cm^2) in order to ensure, by using large focal spots, the production of a *very large flux* of ions (some estimates are shown in fig. III-4b) with energy distributions optimized for our purpose (lower high energy cut- off) in order to make possible the study of nuclear reactions at very low cross- section in a plasma environment. As already mentioned before, after the production, B, C or Li ions forward- streaming towards the gas-jet made by ^{4}He, D^2 or ^{3}He. There, a second laser pulse synchronized with the first one, can be used to obtain a helium or deuterium (depending on the reaction under analysis) plasma with a low center of mass velocity, but with densities ranging in the 10^{18} - 10^{20} ions/cm^3 domain [Sch12]. The properties of the secondary plasma (working as a "plasma target") can be modified or tuned, depending on the energetic domains one wants to explore. By using femtosecond pulses, secondary plasma temperatures lie in the tens of eV range. For reactions with fully-thermalized plasmas at medium-high ion temperatures, the duration of the secondary laser beam can be extended in the nanosecond domain: temperatures or few keV for deuterons or alpha particles can be obtained in this case. Specific simulations have been done in order to describe and tune the experimental conditions under these assumptions. To optimize the experimental setup (e.g. number of ions, energy etc.) The goal is the manufacturing of targets with high light absorbance, tuned for ELI-NP laser wavelengths, by using nanostructured surfaces or materials [Zon04]. Such structured materials have been very well manufactured [Mal09], [Mal07], as an ordered array of metallic nanowires, by using nano-porous alumina as a template. Our goal is to replace the alumina substrate with bulk carbon (or lithium) and the metallic nanowires with carbon nanotubes [Ang10] (or lithium nanowires).

Moreover, the development of these materials could lead to the implementation of a third, alternative setup like the one shown in fig.III-4a, where two identical laser pulses impinge on a thick target with micro cells, filled with gaseous elements (He, D) and enclosed from both sides by thin nanostructured carbon or lithium foils. In such a configuration the "in-cell" gas is self-ionized by the impact with plasmas generated on the two surfaces and can be further compressed by the shock waves developed during the laser–matter interaction. High plasma densities are expected

in this case, however, contaminants due to nanotechnological and nanofabrication processes can play an important role, which has to be investigated.
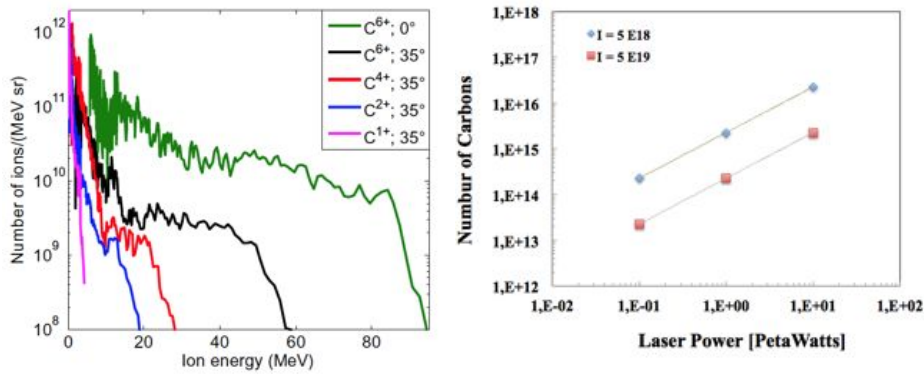
fig.III- 4 a)Carbon ions energy distributions measured along the target normal axis at the rear side for laser incident angles of 0° and 35° with respect to the target normal axis and intensities of ~5x10²⁰ W/cm². b) Maximum number of carbon ions expected at ELI-NP as a function of the laser power. The estimation has been obtained by using laser pulses focalized on a 1 µm fully drilled target, in order to achieve intensity (working with two focal spot radii of 160 and 50 µm respectively) of 5x10¹⁸ W/cm² and 5x10¹⁹ W/cm².

III.5 Ion Acceleration: TNSA

Introduction

In this paragraph it will discuss basic reference mechanisms for ion acceleration in laser-plasma interactions. The other mechanisms, namely shock acceleration, coulomb explosions and radiation pressure acceleration dominate over TNSA in particular conditions and may allow to develop advanced schemes of ion acceleration. The interest of ion acceleration in the superintense regime has been greatly boosted since the year 2000 when three experiments reported on the observation of collimated proton beams with multi-MeV energies from the rear

(non-irradiated) side of solid targets [Cla00], [Mak00],[Sna00]. The fast electrons produced in a high-intensity interaction with the front surface of a solid target propagate through the bulk and eventually reach the rear side, where they produce a negatively charged sheath. The electrostatic field generated in the sheath is almost normal to the surface and accelerates ions.

III.5.1 Initial Conditions

In the TNSA model originally proposed in [Wil01], fast electrons accelerated at the front side and crossing the bulk of the target enter the vacuum region at the rear side, where a charged sheath is formed. The electric field in the sheath back-hold electrons and accelerates ions outwards. The primary interaction of a high intensity, short laser pulse with a solid target strongly depends on the contrast of the laser pulse, that is the ratio of unwanted, preceding laser light to the main pulse. At peak intensities exceeding 10^{20} W/cm^2 even a contrast of 10^6 is insufficient not to excite a plasma that is expanding towards the incoming main pulse. As a common source of this unwanted laser light Amplified Spontaneous Emission (ASE) or pre-pulses, caused by a limited polarisation separation in regenerative amplifiers have been identified. The ablative plasma sets the stage for a wealth of uncontrolled phenomena at the interaction of the main pulse with the target. The laser beam can undergo self focusing due to ponderomotive force or relativistic effects, thereby strongly increasing the resulting intensity, the beam can break up into multiple filaments, and finally the beam can excite instabilities that ultimately lead to the production of energetic electrons. Moreover the ablative pressure of blow-off plasma caused by the incident laser energy prior to the main pulse launches a shock wave into the target, which can ultimately destroy the target before the arrival of the main pulse. It is possible to interpret the process generating a proton beam by TNSA as a new variation on a familiar theme – acceleration by a sheath electrostatic field generated by the hot electron component. The interaction of the intense laser pulse with the preformed plasma and the underlying solid target constitutes a source of hot electrons with an energy

spectrum related to the laser intensity. This cloud of hot electrons penetrates the foil and escapes into the vacuum behind the target. The targets capacitance however allows only a small fraction of the electrons to escape before the target is sufficiently charged that escape is impossible for even MeV electrons. Those electrons then are electrolytically confined to the target and circulate back and forth through the target, laterally expanding and forming a charge-separation field on both sides over a Debye length.[fig.III-5]
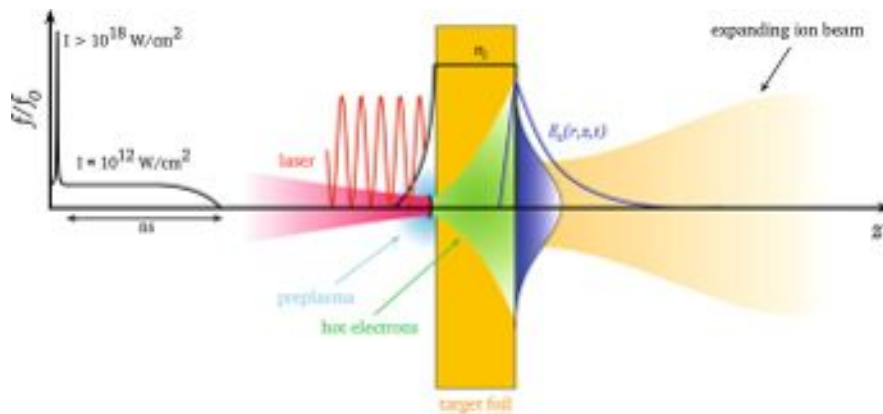
fig.III- 5 Target Normal Sheath Acceleration(TNSA). A thin target foil with thickness d=5-50 mm is irradiated by an intense laser pulse. The laser pre-pulse creates a pre-plasma on the target from side.

In this figure the Target Normal Sheath Acceleration(TNSA) is shown. A thin target foil with thickness d=5-50 mm is irradiated by an intense laser pulse. The laser pre-pulse creates a pre-plasma on the target from side. The main pulse interacts with the plasma and accelerates MeV-energy electrons mainly in forward direction. The electrons propagate through the target, where collisions with the background material can increase the divergence of the electron current. The electrons leave the rear side, resulting in a dense sheath. An electric field due to charge-separation is created. The field is on the order of the laser electric field (TV/m), which ionises atoms at the surface. The ions are the accelerated in this field, pointing in the target normal direction.

III.5.2 Electron Driver

Current laser systems are not capable of directly accelerating ions yet. Therefore all existing laser ion mechanisms rely on the driving electron component and the resulting strong electric fields cause by charge separation. Given intensities of modern short pulse lasers therefore copious amounts of energetic electrons are generated and, in contrast to thermal electrons in long pulse laser plasmas, are pushed into the target. A fair estimate is a fraction of $N = \eta E_L / k_B T_{hot}$ electrons in the MeV range are created, where EL is the laser energy. Those electrons have typical energies that their mean free path is much longer than the thickness of the targets typically used in experiments. While the electrons propagate through the target they constitute a current, which exceed the Alfvén-limit by orders of magnitude. Alfvén found that the main limiting factor on the propagation of an electron beam in a conductor is the self-generated magnetic field, which bends the electrons back towards the source [Alf39]. For parameters interesting for inertial confinement fusion a good review is given in [Dav04]. In order not to exceed the limit of $j_A = \frac{m_e c^3}{e} \beta\gamma = 17\beta\gamma \, [kA]$ the net current must be largely compensated by return currents in order to minimise the resulting magnetic field. The return currents will be driven by the charge separation in the laser plasma interaction region and strongly depends on the electrical conductivity of the target as the those currents are lower in energy and thereby affected by the material properties. The large, counter-streaming currents also give rise to instabilities which affects the forward motion of the electrons. The influence of a limited electrical conductivity on the inhibition of fast electron propagation has been addressed in [Bat02] also with respect to space charge separation. Without the return currents the electric field would stop the electrons in a distance of less than 1 nm [Bel06]. The electric field driving the return current in turn, can be strong enough to stop the fast electrons. This effect, known as transport inhibition, is prominent in insulators, but almost negligible in conductors [Pis00]. The propagation of electrons through the target is still an active field of research. As depicted in fig.III-5 the laser pushes the critical surface nc, leading to a steepening of the electron density profile. The motion of the ablated plasma causes a shock wave to be

launched into the target, leading to ionisation and therefore a modification of the initial electrical conductivity. As soon as the electrons penetrate
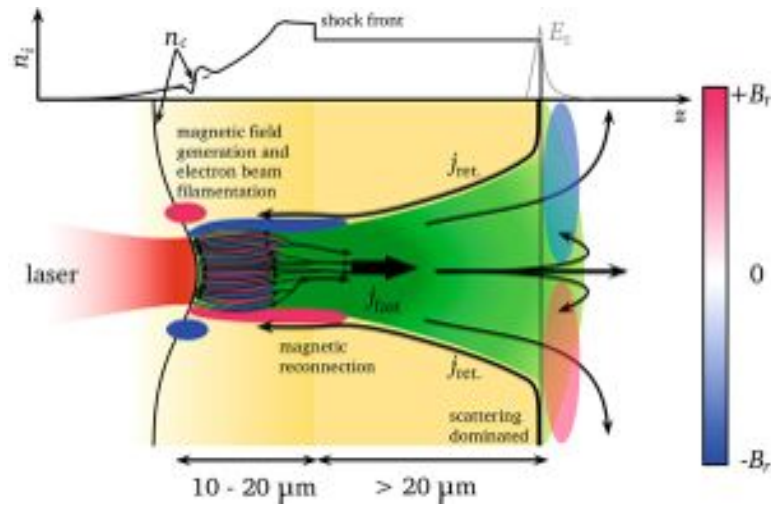
fig.III- 6 Schematic of laser-generated fast-electron transport. The laser impinges on a pre-plasma with exponential density profile from the left side.

In figure III-6 a sketch of laser-generated fast-electron transport. The laser impinges on a pre-plasma with exponential density profile from the left side. The light pressure leads to profile steepening, depicted in the one-dimensional scheme on top. An ablation plasma creates an inward travelling shockwave that heats, ionises, and compresses the target. fast electrons are created by the laser, propagating into the dense plasma towards the target rear side. The high electron current j_{fast} can lead to filamentation and magnetic field generation, as well as it drives a return current j_{ret}. The global magnetic field tends to pinch the fast-electron current. Electrons propagating in the dense, solid matter interact by binary collisions with the background material. This leads to a spatial broadening of the electron distribution, that becomes the major effect for longer distances. At the rear side, the electrons form a sheath and build up an electrostatic field E_z(curve in 1D-plot). This can lead to refluxing (recirculation) of the electrons, heating the target even more.

The transport full-cone angle of the electron distribution was determined to be dependent on laser energy, intensity as well as target thickness. Just recently it was shown that different diagnostics lead to different electron transport cone angles

[Lan07], so the question about the 'true' cone angle dependence with laser and target parameters still remains unclear. When the electrons reach the rear side, they form a dense charge-separation sheath. The fast electron sheath may be described in the assumption of Boltzmann equilibrium, and assumed to remain static during the acceleration of the fastest ions at least. We obtain the Boltzmann equilibrium condition with

$$n_e = n_0 \exp\left(\frac{e\phi}{T_e}\right)$$

The charge separation leads to an electric potential F in the vacuum region, according to the Poisson equation. In a one-dimensional consideration it is given as

$$\nabla^2 \phi = -4\pi\varrho = -4\pi e(n_i - n_e),$$

We start from

$$d_x^2 \phi = 4\pi e(n_e - Zn_i) = 4\pi e n_0 \left[e^{e\phi/T_e} - \Theta(-x)\right].$$

For a solution it is assumed that the solid matter in one half-space ($x \leq 0$) perfectly compensates the electric potential, whereas for $x \rightarrow 0$ the potential goes to infinity. Its derivative $d\phi/dz$ vanishes for $z \rightarrow \pm 0$. In the vacuum region ($x > 0$), the field can be obtained analytically [Cro75], the solutions in the vacuum region $x \geq 0$. Switching to dimensionless quantities

$\xi = x/\lambda_D, \phi = e\phi/T_e, E = eE_x\lambda_D/T_e$ becomes $d^2\phi = e^\phi - \Theta(-\xi)$. Multiplying both sides by $E = -d\phi/d\xi$ we obtain

$$\left(d_\xi \phi\right)\left(\delta_\xi^2 \phi\right) = d_\xi (d_\xi \phi)^2/2 = d_\xi(E^2/2) = \left(e^\phi - \Theta(-\xi)\right) d_\xi \phi.$$

Integrating over ξ from 0 to $+\infty$ and then from $-\infty$ to 0 yields the two relations

$$E^2(0)/2 = -e^{\phi(0)}, \;\; E^2(0)/2 = -e^{\phi(0)} + \phi(0) + 1.$$

For consistency we thus obtain $\phi(0) = -1 \; and \; E(0) = \sqrt{2/e}$ i.e. the field at the surface is given by

$$E_x(0) = \sqrt{2/e}\, E_0, \qquad E_0 = \sqrt{4\pi n_0 T_e}.$$

The values of φ (0) and E (0) can be used as boundary conditions to obtain the solution for x < 0 numerically, while an analytical solution can be found for x > 0. With some algebra we eventually obtain [Cro75]

$$\phi = -2\ln(\xi/\sqrt{2} + e), \ \ E = 2/(\xi + \sqrt{2}e).$$

The electric field profile is shown in fig. III-7.
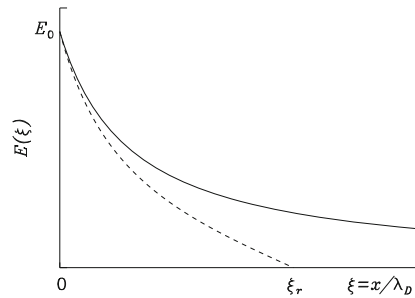
fig.III- 7 The sheath field in the vacuum region, assuming a standard Boltzmann distribution with temperature T_e ,(thick line) and a "truncated" distribution with maximum electron energy uT_e,(dashed line) for which E=0 for $x>x_r$.

The resulting potential is $\quad \Phi(z) = -\dfrac{2k_B T_{hot}}{e}\ln(1 + \dfrac{z}{\sqrt{2}\lambda_D})$

and the corresponding electric field reads

$$\mathrm{E}(z) = \frac{2k_B T_{hot}}{e}\frac{1}{z + \sqrt{2}\lambda_D}.$$

In this solution the electron Debye length

$$\lambda_D = \left(\frac{\varepsilon_0 k_B T_{hot}}{e^2 n_{e,0}}\right)^{1/2}$$

A possible way out of this difficulty is to assume that the range of electron energies is not infinite but has some upper cut-off, that seems physically reasonable in general. In such a case the binding potential will be limited with $\Phi(+\infty) = -E$ that also gives an upper limit to the maximum energy gain of test ions. Notice that an

energy distribution "truncated" to some upper value will always come out for isolated, warm plasma of finite size in 3D, which acquires a net charge Q because the escape energy for electrons has a finite value. Now, if we assume that the electron energy distribution has a cut-off at an energy, it is still possible to write down an analytical solution in which φ does not diverge but becomes constant at some distance from the surface [Pas04].The description of a static sheath may be improved by, e.g., more accurate considerations on the distributions of fast electrons [Pas10]. Actually the latter is the main source of uncertainty when comparing to experimental observations. Despite such difficulty, static models may reproduce the observed scalings for the cut-off energy of protons with good accuracy and a limited set of parameters, suggesting that the approximation of a static sheath is a fair one at least for the fastest protons. The out-flowing electrons lead to a toroidal magnetic field B_θ, that can spread the electrons over large transverse distances by a purely kinematic $E \times B_\theta$-force [Sen07], sometimes called fountain effect [Puk01]. The electric field created by the electron sheath is sufficiently strong to deflect lower-energy electrons back into the target, which then re-circulate. Experimental evidence for recirculating electrons was found in Refs. [Pin08], [San02], [Nis05]. According to Davies [Dav02] the generation of electromagnetic fields as well as recirculation of the electrons have to be taken into account, both making an estimate and even calculation very difficult. Recent experiments [Akl07] have shown that this is true at least for thin targets below 20um, but for thicker foils the assumption of strong recirculation overestimates the number of electrons. Simultaneously its relevance to proton acceleration [Mac02], who measured a strong enhancement of the maximum proton energy for thin foils below 10um, compared to thicker ones. With the help of computer simulations this energy-enhancement was attributed to an enhanced sheath density due to refluxing electrons. Further evidence of refluxing electrons was also found in an experiment discussed in [Sch08]. As just mentioned, the electric field strength instantly leads to ionisation of the atoms at the target rear surface, since it is orders of magnitude above the ionisation threshold of the atoms. A simple model to estimate the electric field strength necessary for ionisation is the Field

Ionisation by Barrier Suppression (FIBS) model [Aug89]. The external electric field of the laser overlaps with the Coulomb potential of the atom and deforms it. As soon as deformation is below the binding energy of the electron, it is instantly freed, hence the atom is ionised. The threshold electric field strength E_{ion} can be obtained with the binding energy U_{bind} as

$$E_{ion} = \frac{\pi \varepsilon_0 U_{bind}^2}{e^3 Z}$$

As the electron sheath at the rear side is relatively dense, the atoms could also be ionised by collisional ionisation. However, [Heg02] the cross section for field ionisation is much higher than the cross section for collisional ionisation for the electron densities and electric fields appearing at the target surface. Hence nearly all atoms (protons, carbons, heavier particles) at the rear side are instantly ionised and, since they are no longer neutral particles, they are then subject to the electric field and are accelerated. Some electrons can escape this field, whereas others with lower energy will be stopped and will be re-accelerated back into the target. Since the electron velocity is close to the speed of light and the distances are on the order of a micrometer (um), this happens on a few-fs time scale, leading to a situation where electrons are always present outside the rear side. The electric field being created does not oscillate but is quasi-static on the order of the ion-acceleration time. Therefore ultra-short laser pulses, although providing highest intensities, are not the optimum laser pulses for ion acceleration. The electric field is directed normal to the target rear surface, hence the direction of the ion acceleration follows the target normal, giving the process its name Target Normal Sheath Acceleration – TNSA.

III.5.3 Expansion Models

The laser-acceleration of ions from solid targets is a complicated, multi-dimensional mechanism including relativistic effects, non-linearities, collective as well as kinetic effects. Theoretical methods for the various physical mechanisms involved in TNSA range from analytical approaches for simplified scenarios over

fluid models up to fully relativistic, collisional three-dimensional computer simulations. Most of the approaches that describe TNSA neglect the complex laser-matter interaction at the front-side as well as the electron transport through the foil. These plasma expansion models start with a hot electron distribution that drives the expansion of an initially given ion distribution [Fuc06], [Crow75], [Sch06], [Fuc07], [Mor05], [Mor05bis], [Alb06], [Pas04]. Crucial features like the maximum ion energy as well as the particle spectrum can be obtained analytically, whereas the dynamics have to be obtained numerically. The plasma expansion description dates back to 1954 [Lan54]. Since then various refinements of the models were obtained, with an increasing activity after the first discovery of TNSA. These calculations resemble the general features of TNSA. Nevertheless, they rely on somewhat idealised initial conditions from simple estimates. In addition to that, the plasma expansion models are one-dimensional, whereas the experiments have clearly shown that TNSA is at least two-dimensional. Sophisticated three-dimensional computer simulation techniques have been developed for a better understanding of the whole process of short-pulse high-intensity laser-matter interaction, electron transport and subsequent ion acceleration. The simulation methods can be classified as (i) Particle-In-Cell (PIC), (ii) Vlasov, (iii) Vlasov-Fokker-Planck, (iv) hybrid fluid/particle and (v) gridless particle codes [Bel06].

III.5.4 Plasma Expansion Model

The plasma expansion often is described as an isothermal rarefaction wave into free space. There is quite a large similarity to the expansion models used to describe TNSA. The isothermal expansion model assumes quasi-neutrality $n_e = Z n_i$ and a constant temperature T_e. Using the two-fluid hydrodynamic model for electrons and ions, the continuity, momentum and energy conservation equations are used, usually with the assumption of an isothermal expansion (no temperature change in time), no further source term (no laser), no heat conduction, collisions or external forces and a pure electrostatic acceleration (no magnetic fields). One can find a self-similar solution [Eli02]. By posing

$$v(z,t) = c_s + \frac{z}{t}$$

$$n_e(z,t) = Zn_i(z,t) = n_{e,0}\exp\left(-\frac{z}{c_s t} - 1\right)$$

where v denotes the bulk velocity and n_i(n_e) the evolution of the ion (electron) density. The rarefaction wave expands with the sound velocity $c_S^2 = Zk_BT_e/m_i$. By combining these two equations, replacing the velocity with the kinetic energy $v_2 = 2E_{kin}/m$ and taking the derivative with respect to E_{kin}, the ion energy spectrum dN/dE_{kin} from the quasi-neutral solution per unit surface and per unit energy in dependence of the expansion time t is obtained as [Mor03]

$$\frac{dN}{dE_{kin}} = \frac{n_{e,0}c_s t}{\sqrt{2Zk_BT_{hot}E_{kin}}}exp\left(-\sqrt{\frac{2E_{kin}}{Zk_BT_{hot}}}\right).$$

The ion number N is obtained from the ion density as N = $n_{e,0}c_s$t. Additionally, the electric field in the plasma is obtained from the electron momentum equation $n_e eE = -k_BT_e\nabla n_e$ as

$$E = \frac{k_BT_e}{ec_S t} = \frac{E_0}{\omega_{pi}t},$$

with $E_0 = \left(n_{e,0}k_BT_e/\varepsilon_0\right)^{1/2}$ and $\omega_{pi} = \left(n_{e,0}Ze^2/m_i\varepsilon_0\right)^{1/2}$ denoting the ion plasma frequency.

Thus, we expect the exact field at the front (where charge separation effects can not be neglected) to have a peak, jumping from the self-similar value to approximately twice of that, and then decreasing down to zero in the sheath region beyond the front
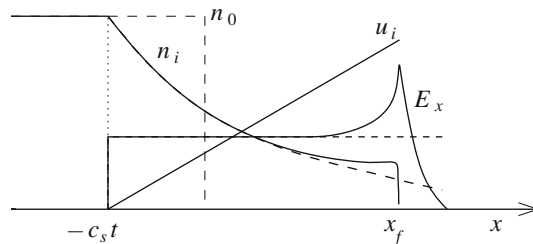
fig.III- 8 Sketch of the ion density(n_i, velocity(v) and electric field(E) profiles in 1D isothermal expansion of a step-boundary plasma.

The electric field is uniform in space (i.e. constant) and decays with time as t^{-1}. The temporal scaling of the velocity is obtained by solving the equation of motion $\dot{v} = Zq/mE$ with the electric field from above. This yields

$$v(t) = c_S \ln(\omega_{pi}t) + c_S$$

$$z(t) = c_S t(\ln(\omega_{pi}t) - 1) + c_S t.$$

However, at t = 0, the self-similar solution is not defined and has a singularity. Hence the model of a self-similar expansion is not valid for a description of TNSA at early times and has to be modified. Additionally, in TNSA there are more differences: firstly, the expansion is not driven by an electron distribution being in equilibrium with the ion distribution, but by the relativistic hot electrons that are able to extend in the vacuum region in front of the ions. There quasi-neutrality is strongly violated and a strong electric field will built up, modifying the self-similar expansion solution. Secondly, the initial condition of equal ion and electron densities must be questioned, since the hot electron density with ne $\approx 10^{20}$ cm^{-3} is about three orders of magnitude below the solid density of the rear side contamination layers. This argument can only be overcome by the assumption of a global quasi-neutrality condition $Zn_i = n_e$. Thirdly, it might not be reasonable to assume a model of an isothermal plasma expansion. It can be assumed, however, that the expansion is isothermal for the laser pulse provides 'fresh' electrons from the front side, i.e., the assumption is valid as long as the laser pulse duration. As will be shown below, the main acceleration time period is on the order of the laser pulse duration. This justifies the assumption of an isothermal expansion. The plasma expansion including charge separation was quantitatively described [Mor03],[Mor05],[Mor05bis] with high accuracy. The main point of this model is a plasma expansion with charge-separation at the ion front, in contrast to a conventional, self-similar plasma expansion. The plasma consists of electrons and protons, with a step-like initial ion distribution and an electron ensemble being in thermal equilibrium with its potential. The MeV electron temperature results in a charge separation being present for long times. It leads to enhanced ion-

acceleration at the front, compared to the case of a normal plasma expansion. This difference is sometimes named the TNSA-effect. After the laser- acceleration at the foil's front side the electrons arrive at the rear side and escape into vacuum. The atoms are assumed to be instantly field-ionised, leading to $n_i = n_e/Z$. Charge separation occurs and leads to an electric potential ϕ, according to Poisson's equation:

$$\varepsilon_0 \frac{\delta^2 \phi}{\delta z^2} = e\big(n_e(z) - n_i(z)\big).$$

The electron density distribution is always assumed to be in local thermal equilibrium with its potential:

$$n_e = n_{e,0} \exp\left(\frac{e\phi}{k_B T_{hot}}\right),$$

where the electron kinetic energy is replaced by the potential energy $e\phi$. The initial electron density is equal to $n_{e,0}$. The ions are assumed be of initial constant density $n_i = n_{e,0}$, with a sudden drop to zero at the vacuum interface. The boundary conditions are chosen, so that the solid matter in one half-space ($z \leq 0$) perfectly compensates the electric potential for $z \to -\infty$, whereas for $z \to \infty$ the potential goes to infinity. Its derivative $E = -d\phi/dz$ vanishes for $z \to \pm\infty$. In the vacuum region (initially $z > 0$), the field can be obtained analytically [Cro75]. The resulting potential is

$$\phi(z) = -\frac{2 k_B T_{hot}}{e} ln\left(1 + \frac{z}{\sqrt{2 \exp(1)}\, \lambda_{D,0}}\right) - \frac{k_B T_{hot}}{e}$$

and the corresponding electric field reads

$$E(z) = \frac{2 k_B T_{hot}}{e} \frac{1}{z + \sqrt{2 \exp(1)}\, \lambda_{D,0}}.$$

Temporal Evolution and Scaling

A crucial point in the ion expansion is the evolution of the electric field strength E_{front}, the ion velocity v_{front} and the position z_{front} of the ion front. Expressions given by Mora are

$$E_{front} \cong \left(\frac{2n_{e,0}k_B T_{hot}}{e\varepsilon_0} \frac{1}{1+\tau^2} \right)^{1/2},$$

$$v_{front} \cong 2c_S \ln\left(\tau + \sqrt{1+\tau^2} \right),$$

$$z_{front} \cong 2\sqrt{2e}\lambda_{D,0} \left[\tau \ln\left(\tau + \sqrt{1+\tau^2} \right) - \sqrt{1+\tau^2} + 1 \right],$$

where $e = \exp(1)$ and $\tau = \omega_{pi}t/\sqrt{2e}$. The other variables in these equations are the initial ion density $n_{i,0}$, the ion-acoustic (or sound) velocity $c_s = (Zk_B T_{hot}/m_i)^{1/2}$, T_{hot} is the hot electron temperature and $\omega_{pi} = \left(n_{e,0}Ze^2/m_i\varepsilon_0 \right)^{1/2}$ denotes the ion plasma frequency. Due to the charge separation, the ion front expands more than twice as fast as the quasi-neutral solution. The phrase fully quasi-neutral should point out, that in this solution there is no charge-separation at the ion front, hence there is no peak electric field. A drawback of the model is the infinitely increasing energy and velocity of the ions with time, which is due to the assumption of an isothermal expansion. Hence a stopping condition has to be defined. An obvious time duration for the stopping condition is the laser pulse duration t_L. However, as found by Fuchs et al. [Fuc06], [Fuc07], the model can be successfully applied to measured maximum energies and spectra, if the calculation is stopped at $\tau_{acc} = \alpha(\tau_L + t_{min})$.

III.6 TNSA: Ion Beam Characteristics

Part of the motivation of the extensive research on laser accelerated ion beams is based on their exceptional properties (high brightness and high spectral cut-off, high directionality and laminarity, short pulse duration), which distinguishes them from those of the lower energy ions accelerated in earlier experiments at moderate laser intensities. In view of this properties, laser-driven ion beams can be employed

Beam Parameter

Particle Numbers: One of the striking features of TNSA accelerated ion beams was the fact that the particle number in a forward-directed beam was very high.

Energy spectrum: Based on the acceleration mechanism and the expansion model described earlier the usual ion energy distribution is an exponential one with a cut- off energy that is dependent on the driving electron temperature. Without special target treatment and independently from the target material protons are always accelerated first as they have the highest charge-to-mass ratio. These protons stem from water vapour and hydrocarbon contamination, which are always present on the target surface due to the limited achievable vacuum conditions. Protons from the top-most contamination layer on the target surface are exposed to the highest field gradients and screen the electric field for protons and ions coming from the successive layers. The acceleration of particles from different target depths results in a broad energy distribution, which becomes broader with the contamination layer thickness. The inhomogeneous electron distribution in the sheath additionally leads to an inhomogeneous accelerating field in transverse direction. The resulting exponential ion energy spectrum constitutes the main disadvantage in laser- ion acceleration.

Opening angle. It demonstrates that the energy resolved opening angles; example protons with the highest energy are emitted with the smallest opening angle from the source. Protons with less energy subsequently are emitted in larger opening angles. It should be noted, that the term 'opening angle' is not equivalent to the beam 'divergence'. The divergence of the protons slightly increases with increasing energy, whereas the emitting area (source size) decreases with proton energy [Bor06], [Cow04]. These results in a total decrease of the opening angle measured experimentally.

Source size. The source size decreases with increasing energy. Protons with the highest energies are emitted from sources of about 10um diameter and less. For lower energies, the source sizes progressively increase, up to about 200um diameter. The energy-dependence of the source size is directly related to the

electric field strength distribution of the accelerating hot electron sheath at the source. Protons with high energies have been accelerated by a high electric field. It has concluded that the quasi-neutral plasma expansion, even though being the driving acceleration mechanism for late times, is not the physical mechanism explaining the observed source sizes.

Emittance. An important parameter in accelerator physics is the transverse emittance of an ion beam. In view of the nature of the ion sources used in conventional accelerators, there is always a spread in kinetic energy and velocity in a particle beam. Each point on the surface of the source emits protons with different initial magnitude and direction of the velocity vector. The emittance Σ provides a figure of merit for describing the quality of the beam, i.e., its laminarity [Hum08, Nur09]. Assuming the beam propagates in the z-direction. Each proton represents a point in the position- momentum space (x, p_x and y, p_y), the phase space. In general, the quality of charged-particle beams is characterised by their emittance, which is proportional to the volume of the bounding ellipsoid of the distribution of particles in phase space. By Liouville's theorem, the phase space volume of a particle ensemble is conserved during non-dissipative acceleration and focusing.

Ion species. The protons which are contained in impurity layers, ordinarily present on the surface of metal targets, are in a favourable condition for ion acceleration because they are initially located at the maximum of the sheath field and, thanks to their higher charge-to-mass ratio, they move faster than heavier ions and may screen the electric field. The ions are accelerated in the double layer potential and can reach significant particle energies expanding isotropically in all direction from the target front surface. Intense beams of multi-MeV protons and heavier ions have indeed a great potential for many applications where localized energy deposition in matter is required, since the deposited energy has a sharp maximum (the Bragg peak) at the end of their path, differently from electrons and photons.

Target Dependence. A high conducting ultra-thin target is the most favourable to be used for efficient ion acceleration. Moreover, as the electrons can distribute a

part of the energy provided by the laser into Bremsstrahlung, a low Z material is preferable. The ultimate thickness of the target is determined by the limited laser contrast as TNSA requires a sharp density gradient at the rear surface. For the effective acceleration of the ions, an undisturbed back surface of the target is crucial to provide a sharp ion density gradient as the accelerating field strength is proportional to T_{hot}/el_0, where T_{hot} is the temperature of the hot electrons and l_0 is the larger of either the hot-electron Debye length or the ion scale length of the plasma on the rear surface. The limited contrast of the laser causes a shock wave launched by the prepulse that penetrates into the target and causes a rarefaction wave that diminishes the density gradient on the back and therefore drastically reduces the accelerating field. The inward moving shock wave also alters the initial conditions of the target material due to shock wave heating and therefore changes, e.g., the target density and conductivity. As a trade- off one has, however, to note that on the other hand a certain pre-plasma at the front side is beneficial to the production of hot electrons, somehow contradicting the need for high contrast lasers. Also, as the lateral expansion of the electron sheath affects the evolution of the ion acceleration it has been found that to confine the electron by reducing the transverse dimensions of the targets also enhances the ion particle energy. So the ideal target would resemble an ultra-thin, low-Z, highly conducting target with small lateral dimensions and a large pre-plasma at the front side.

Beam Control. Ballistic focusing of laser accelerated proton beams is known since [Pat03] and has been investigated in detail because of the large importance for proton driven fast ignition [Rot01] and the generation of warm dense matter [Pel10]. The experiments in [Pat03] have indicated that a larger laser focal spot should minimise the second effect and thus result in a better focus quality. The bulk of the hot electrons follows the laser focal spot topology and creates a sheath with the same topology at the rear side[Fuc03]. The proton beam spatial profile as detected by a film detector was simulated with a simple electrostatic model. The authors took the laser beam profile as input parameter and assumed the electron transport to be homogeneous, with a characteristic opening angle

Radiation Pressure Acceleration

ElectroMagnetic waves carry momentum, which may be delivered to either an absorbing or a reflecting medium. Radiation pressure (RP) is the flow of delivered momentum per unit surface and can be computed (at least in principle) when the ElectroMagnetic fields at the surface are known, using the energy-momentum conservation theorem from Maxwell's equations. For a plane, monochromatic ElectroMagnetic wave of intensity I and frequency ω normally incident on the plane surface of a medium ("target") at rest, the RadiationPressure Prad is given by

$$P_{rad} = (1 + R - T)\,I/c = (2R + A)I/c\,,$$

where R and T are the reflection and transmission coefficients of the target as defined in the derivation of Fresnel formulas. Energy conservation implies R + T = 1 − A where A is the absorption coefficient, i.e. the fraction of the ElectroMagnetic wave intensity that is converted into internal energy. Limiting cases include a perfect mirror (R = 1, T = A = 0, P=2I/c), a perfectly absorbing medium (A = 1, R = T = 0, P = I/c) and a "thin" transmitting, non-absorbing target such that A = 0, T = 1−R, P = 2RI/c. In the present case it is instructive to show explicitly that the Radiation Pressure on a step-boundary overdense plasma ($n_e = n_0\Theta(x)$) is due to the ponderomotive force (PF). In fact, considering normal incidence and the non-relativistic case for simplicity, the PF is the cycle average and thus the total pressure is the integral of the volume force over the depth of the plasma:

$$P_{tot} = \int_0^\infty n_0 F_0 e^{-2x/l_S} dx = F_0 n_0 l_S/2 = (m_e c^2 n_{0)}(\omega/\omega_p)^2 a_0^2 = 2I/c\,,$$

where we used I = $m_e c^3 n_c a_0^2$ and $(\omega/\omega_p)^2 = n_c/n_0$. The Ponderomotive Force pushes and piles up electrons in the skin layer creating a static field $E_{0x} = f_p/e$ that acts on the ions, so that effectively the Radiation Pressure is exerted on the whole target. In a thick target, ions are thus accelerated at the front surface causing steepening of the density profile and, for a finite pulse in multi-dimensional geometry, Hole boring (HB) through the plasma. If the target is thin enough and

has a low mass, it may be accelerated as a whole up to high velocity: this is suggestively named the Light sail (LS) regime.

III.7 Particle-In-Cell Method (PIC)

The PIC method is the most widely used simulation technique.[Mac13] In PIC the Maxwell equations are solved as combined to local particles charges and current densities, obtained by a description of the particle distribution functions. The method resembles more or less a 'numerical experiment' with only little approximations, hence a detailed insight into the dynamics can be obtained. The disadvantage is that no specific theory serves as an input parameter and the results have to be analysed like experimental results, i.e., they need to be interpreted and compared to analytical estimates. The PIC method to solve the kinetic equation

$$\partial_t f_a + \nabla_{\mathbf{r}} \cdot (\dot{\mathbf{r}}_a f_a) + \nabla_{\mathbf{p}} \cdot (\dot{\mathbf{p}}_a f_a) = 0,$$

(PIC-1)

The most complete description of a classical, collisionless plasma is based on the knowledge, for each particle species a, of the distribution function $f_a = f_a(\mathbf{r}, \mathbf{p}, t)$ which gives the density of particles at the point $(\mathbf{r}, \mathbf{p})$ in the six-dimensional phase space at the time t. Where $\dot{r}_a = v = p/(m_a\gamma_a) = pc/(m^2_a c^2 + p^2)^{1/2}$, $\dot{p}_a = F_a$ with $F_a = F_a(r, p, t)$ the force on the particle, and the gradient operators ∇_r and ∇_p act on the space (r) and momentum (p) variables, respectively. This equation can be understood as a continuity equation in the phase space. But numerically the PIC method is based on the following representation for the distribution function

$$f(\mathbf{r}, \mathbf{p}, t) = A \sum_{l=0}^{N_p-1} g[\mathbf{r} - \mathbf{r}_l(t)]\delta^3[\mathbf{p} - \mathbf{p}_l(t)],$$

(PIC-2)

where $\mathbf{r}_l(t)$ and $\mathbf{p}_l(t)$ are functions of time and A is a proper normalization constant. In this equation $\delta^3(\mathbf{p}) = \delta(p_x)\delta(p_y)\delta(p_z)$ where $\delta(p)$ is the Dirac function,

and $g(\mathbf{r})$ is an even, localized function (with properties similar to δ^3) that will be specified later. By substituting (PIC-2) into (PIC-1) and integrating first over d^3p and then over d^3r, the following equations for $\mathbf{r}_l(t)$ and $\mathbf{p}_l(t)$ are obtained:

$$\frac{d\mathbf{r}_l}{dt} = \frac{\mathbf{p}_l}{m_a \gamma_l}, \qquad \frac{d\mathbf{p}_l}{dt} = \bar{\mathbf{F}}_l, \qquad \text{(PIC-3)}$$

where

$$\bar{\mathbf{F}}_l = \bar{\mathbf{F}}_l(\mathbf{r}_l, \mathbf{p}_l, t) = \int g[\mathbf{r} - \mathbf{r}_l(t)]\mathbf{F}(\mathbf{r}, \mathbf{p}, t)d^3r. \qquad \text{(PIC-4)}$$

The problem is thus reduced to $2N_p$ equations of motion and (PIC-3) describing the motion of N_p computational particles. First, the number of computational particles which may be allocated on a computer will be almost always lower by several order of magnitudes than the actual number of electrons and ions in the system under investigation, so that we actually have a very limited sample of the phase space. Second, the particles are accelerated by the mean ElectroMagnetic fields, consistently with Vlasov–Maxwell theory, and interparticle interactions are not computed. From Eq. (PIC-4) we infer that $g(\mathbf{r})$ describes the "shape" by computing the charge and current densities

$$\varrho(\mathbf{r}, t) = A \sum_{a,l} q_a g[\mathbf{r} - \mathbf{r}_{a,l}(t)], \qquad \mathbf{J}(\mathbf{r}, t) = A \sum_{a,l} q_a \mathbf{v}_l g[\mathbf{r} - \mathbf{r}_{a,l}(t)].$$

In the PIC approach, ρ and $\mathbf{J}$ as well as the ElectroMagnetic fields are discretized on a spatial grid. The position of the particle with respect to the grid and its charge distribution described by $g(\mathbf{r})$ determine both the contribution to the total current in the grid cells overlapping with the particle and the average force on the particle. The weights in the sum are proportional to the volume of the overlapping regions which, for a given $g(\mathbf{r})$, are well defined analytical functions of the particle and cell positions. Figure 2.5 shows the typical case of a triangular shape for which the particle overlaps to 3^D cells where D is the dimensionality of the problem. Although in principle also $g(\mathbf{r})$ may be a delta function describing a point particle,

this choice is rarely used since using "cloud-like" particles smooths out the resulting distribution and reduces noise fluctuations
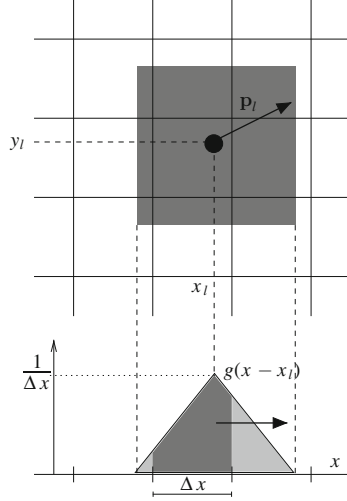
fig.III- 9 Example showing a particle moving across the grid in the PIC approach.

In the figure III-9 is described by a triangular density profile *g(x)* (normalized to unity) whose width is twice the grid spacing Δx. The particle thus overlaps to three cells in 1D and to nine cells in 2D(see upper frame). Where its shape function is *g(r-r_l)= g(x-x_l) g(y-y_l).* For codes developed for laser-plasma physics it is convenient to use the following normalizations: time in units of ω^{-1} with ω the laser frequency, space in units of c/ω, momenta in units of $m_e c$, fields in units of $m_e \omega c / e$, and densities in units of $n_c = m_e \omega^2 / 4\pi e^2$. In 1D geometry with x as the only spatial coordinate, the normalized Maxwell's equations for the transverse fields are

$$\partial_t E_y = -J_y - \partial_x B_z, \qquad \partial_t B_z = -\partial_x E_y,$$
$$\partial_t E_z = -J_z + \partial_x B_y, \qquad \partial_t B_y = \partial_x E_z,$$

which show that the two possible states of linear polarization are uncoupled. To integrate these equations, we introduce the auxiliary fields F± ≡ Ey ± Bz and G ± ≡ Ez ± By which satisfy the equations

$$(\partial_t \pm \partial_x)F_\pm = -J_y, \qquad (\partial_t \pm \partial_x)G_\mp = -J_z.$$

It is apparent that F$\pm$ and G$\mp$ describe waves propagating from left to right and right

to left, respectively.

$$F_\pm(x \pm \Delta x, t + \Delta t) = F_\pm(x, t) - J_y(x \pm \Delta x/2, t + \Delta t/2)\Delta t,$$
$$G_\pm(x \mp \Delta x, t + \Delta t) = G_\pm(x, t) - J_z(x \mp \Delta x/2, t + \Delta t/2)\Delta t,$$

where $\Delta x = \Delta t$, i.e. the spatial resolution (cell width) is taken equal to the timestep (in dimensional units, $x = c\,t$). The scheme is second-order accurate ($\sim O(\Delta t^2)$), as may be verified by a Taylor expansion. With such scheme, the injection of a laser pulse from the grid boundaries is straightforward. Notice that the transverse currents will be interlaced in time and space with the transverse fields: if F$\pm$ and G$\pm$ are defined at the cell boundaries(x_i =i x,i =0,1,2,...,N−1)and at integer time steps t_n = n Δt,n = 0,1,2,..., then J_y and J_z are defined at the cell centers x_i = (i + 1/2) x and at time steps t_n = (n + 1/2) t.

For the longitudinal field E_x, a quick explicit scheme is obtained directly by integrating the 1D Poisson's equation $\partial_x E_x = \rho$:

$$E_x(x, t) = E(x - \Delta x, t) + \int_{x-\Delta x}^{x} \varrho(x', t)dx'$$
$$= E(x - \Delta x, t) + \varrho(x - \Delta x/2, t)\Delta x + \mathcal{O}(\Delta x^2).$$

The charge density must therefore be defined at cell centers. Alternatively, one can use an implicit method to obtain E_x via the electrostatic potential Φ, from the equation $\partial_x^2 \Phi = -\rho$ which in discretized form yields

$$\frac{\Phi(x - \Delta x) - 2\Phi(x) + \Phi(x + \Delta x)}{\Delta x^2} + \mathcal{O}(\Delta x^2) = -\varrho(x).$$

where $x = \Delta t$, i.e. the spatial resolution (cell width) is taken equal to the time step (in dimensional units, $\Delta x = c\,\Delta t$). The scheme is second-order accurate ($\sim O(\Delta t^2)$),

as may be verified by a Taylor expansion. With such scheme, the injection of a laser pulse from the grid boundaries is straightforward. Notice that the transverse currents will be interlaced in time and space with the transverse fields: if $F\pm$ and $G\pm$ are defined at the cell boundaries ($x_i = i\,\Delta x$, $i = 0,1,2,...,N-1$)and at integer time steps $t_n = n\,\Delta t$, $n = 0,1,2,...,$ then J_y and J_z are defined at the cell centers $x_i = (i + 1/2)\,\Delta x$ and at time steps $t_n = (n + 1/2)\,\Delta t$.

For the longitudinal field E_x, a quick explicit scheme is obtained directly by integrating the 1D Poisson's equation $\partial_x E_x = \rho$:

$$
\begin{aligned}
E_x(x,t) &= E(x - \Delta x, t) + \int_{x-\Delta x}^{x} \varrho(x',t)dx' \\
&= E(x - \Delta x, t) + \varrho(x - \Delta x/2, t)\Delta x + \mathcal{O}(\Delta x^2).
\end{aligned}
$$

The charge density must therefore be defined at cell centers. Alternatively, one can use an implicit method to obtain E_x via the electrostatic potential Φ, from the equation $\partial^2_x \Phi = -\rho$ which in discretized form yields

$$
\frac{\Phi(x - \Delta x) - 2\Phi(x) + \Phi(x + \Delta x)}{\Delta x^2} + \mathcal{O}(\Delta x^2) = -\varrho(x).
$$

In grid coordinates $x_i = i\,\Delta x$ with $i = 0,1,...,N-1$ this equation becomes a linear system of N equations whose matrix of coefficients is tridiagonal, and may be solved by standard numerical methods of matrix inversion. To compute the charge and current densities in each cell as stated above the contribution of each particle to a cell is proportional to the volume of the overlapping region. For the 1D case and the triangular shape of fig. III-9, each particle contributes to three cells, with weights given by the area of the shaded regions in the bottom frame of fig. III-9, divided by the cell length x . The weighting factors are a function of the relative position $x_l - x_i$, where x_l and x_i are the positions of the particle and of the center of the parent cell (such that $|x_l - x_i| < \Delta x /2$), respectively. Explicitly, for the triangular shape

$$
S_{-1} = \frac{1}{2}\left(u - \frac{1}{2}\right)^2, \quad S_0 = \left(\frac{3}{4} - u^2\right), \quad S_{+1} = \frac{1}{2}\left(u + \frac{1}{2}\right)^2,
$$

To advance the particle momenta in time, we describe the widely used algorithm known as the Boris pusher (notice that the scheme operates in a 3D momentum space and may thus be used also in 2D and 3D codes). We start from the knowledge of the particle momentum p at the time step n − 1/2 and of the ElectroMagnetic fields (averaged on the particle) at the time step n. In conclusion, the Lagrangian code and the model developed by Mora shows, that TNSA-accelerated ions are emitted mainly in form of a quasi-neutral plasma, with a charge-separation at the ion front that leads to an enhanced acceleration compared to the expansion of a completely quasi-neutral plasma.

III.8 Fluid Model for TNSA

The model studied in [Mor03] is a isothermal, fluid model, in which the charge separation effects in the collisionless plasma expansion can be studied. In this model, at time $t = 0$, a plasma is assumed to occupy the half-space $x < 0$. The ions are cold and initially at rest with density $n_i = n_{i0}$ for $x < 0$ and $n_i = 0$ for $x > 0$ with a sharp boundary. The electron density n_e is continuous and corresponds to a Boltzmann distribution. One has $\Phi(-\infty) = 0$ and $n_{e0} = Z_i n_{i0}$, where Z_i is the ion charge state.

For $x + c_s t > 0$, a self-similar expansion is found if one assumes quasi-neutrality in the expanding plasma, with

$$n_e = Z_i n_i = n_{e0} \exp\left(-\frac{x}{c_s t} - 1\right),$$
$$v_i = c_s + \frac{x}{t},$$

where c_s is the ion sound speed, $c_s = \sqrt{Z_i k_B T_e / m_i}$, v_i is the ion velocity, and m_i is the ion mass. Based on the self-similar expansion and numerical solutions of the fluid model, Mora obtained the ion energy spectrum and the maximum ion energy, the electron temperature in [Mor03]. Following the way described in [Fuc06], we can

apply this fluid model of plasma expansion to study the TNSA scheme in the laser-target interaction. As in most of the experiments, a preformed plasma (preplasma) was present in front of the target owing to long-duration, low-level laser energy reaching the target before the main pulse. The electrons are accelerated into the target following the irradiation by the main pulse. As the electrons are accelerated over the laser pulse duration and spread over the surface of the sheath S_{sheath}, we have $n_{e0} = N_e/(c\tau_{\text{laser}}S_{\text{sheath}})$ where N_e is the total number of electrons and τ_{laser} is the laser pulse duration. The surface of the sheath S_{sheath} is given as

$$S_{\text{sheath}} = \pi(r_0 + d \times \tan\theta)^2.$$

S_{sheath} depends on the half-angle divergence ($\theta \sim 25^{\circ}$) of the hot electron inside the target [Fuc06], the target thickness d and the initial radius r_0 of the zone over which the electron are accelerated at the target front surface, that is, the laser spot. According to the model in [Mor03], the maximum (cutoff) energy that can be gained by the accelerated ions is then given as [Fuc06]

$$\mathbb{E}_{\max} = 2\mathscr{E}_0 \left[\ln\left(t_p + \sqrt{t_p^2 + 1} \right) \right]^2,$$

where $t_p = \omega_{\text{pi}}t_{\text{acc}}/\sqrt{2\exp}$ is the normalized acceleration time, and $E_0 = Z_i k_B T_e$. ω_{pi} is the ion plasma frequency, $\omega_{\text{pi}} = \sqrt{n_{e0}Z_i e^2/(m_i \varepsilon_0)}$. t_{acc} is the effective acceleration time (or limit time). As shown in [Fuc06], $t_{\text{acc}} \sim 1.3\tau_{\text{laser}}$ matches well with experimental results. The number of accelerated ions per unit energy is given as [Fuc06]

$$\frac{dN}{d\mathbb{E}} = \frac{n_{i0}c_s t_{\text{acc}}S_{\text{steath}}}{\sqrt{2\mathbb{E}\mathscr{E}_0}} \exp\left(-\sqrt{2\mathbb{E}/\mathscr{E}_0} \right),$$

In order to obtain the cutoff energy and the energy spectrum of the ions, the densities and temperature must be known. The electron temperature T_e is found numerically [Wil92] and experimentally [Mal96] to be given by the laser ponderomotive potential,

$$T_e = m_e c^2 \left[\sqrt{1 + I\lambda_{\mu m}^2 / 1.37 \times 10^{18}} - 1 \right],$$

where m_e is the electron mass, I is the laser intensity in W/cm^2, and $\lambda_{\mu m}$ is the laser wavelength in micrometers. As shown in [Fuc06], the total number of electrons accelerated into the target is

$$N_e = f E_{laser} / T_e,$$

where E_{laser} is the laser energy and f is the is the fraction of laser light that is absorbed into the preplasma.According to a recent fit of experiment results, the following dependence of the fraction f on the laser intensity can be adopted [Tow05, Dav09, Lev14],

$$f = \left(\frac{I\lambda_{\mu m}^2}{4.3 \times 10^{21} \mathrm{Wcm}^{-2} \mu m^2} \right)^{0.2661}.$$

This fit was shown to be an adequate fit from 2×10^{18} to 2×10^{20} Wcm^{-2}μm^2; beyond 2×10^{20} Wcm^{-2}μm^2 the absorption is leveling off or even falling [Dav09]. ˆ

III.8.1 Electromagnetic Particle-in-Cell (PIC) Computational Applications

The EPOCH family of PIC codes is based on the older PSC code written by Hartmut Ruhl and retains almost the same core algorithm for the field updates and particle push routines. EPOCH was written to add more modern features and to structure the code in such a way that future expansion of the code is made as easy as possible. EPOCH is a plasma physics simulation code which uses the Particle in Cell (PIC) method. In this method, collections of physical particles are represented using a smaller number of pseudoparticles, and the fields generated by the motion

of these pseudoparticles are calculated using a finite difference time domain technique on an underlying grid of fixed spatial resolution. The forces on the pseudoparticles due to the calculated fields are then used to update the pseudoparticle velocities, and these velocities are then used to update the pseudoparticle positions. This leads to a scheme which can reproduce the full range of classical micro-scale behaviour of a collection of charged particles. [Bra15]

III.9 Simulations for Nuclear Reactions in a Laser Plasma

The simulated ion energy distributions [Pas08] for carbon and lithium ions, generated by the interaction of a fs laser pulse impinging onto a thin target at two different laser intensities, are shown in fig.III-10. The predictions were validated also by comparison with experimental data reported in literature [Dze10], [Car10]. It is evident that, through the laser focal spot tuning on target, we are able to change both the beam intensity and the ion energy distribution, which can be properly tailored according to the energy intervals one would explore. When working in the range of few 10^{18} W/cm^2, it turns out that the energies of the produced ions are suitable to generate reactions of astrophysical interest. Due to hydrogenated contaminants on the target surface, we expect a fraction of protons, as shown in fig.III-10, during the production of carbon, lithium or boron. Such protons could be a source of secondary neutrons when colliding with the aluminum chamber walls, generating an unwanted background in the neutrons' detectors. This possibility is of course strongly dependent on the initial proton energies. Working at an intensity of the order of 10^{18} W/cm^2, we expect maximum proton energies of about 3 MeV, which is below the neutron production energy threshold on nuclei (including the weakly bound deuterons of the D gas-jet target), thus producing a negligible neutron background contribution as originating from target protons.
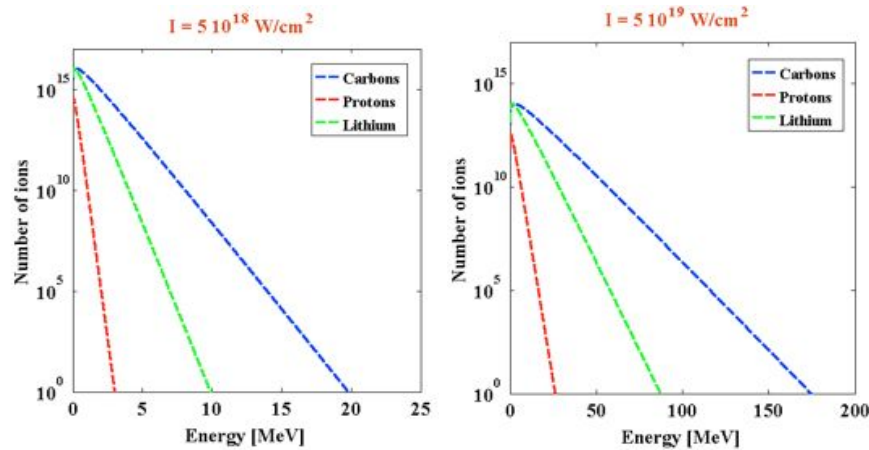
fig.III- 10 Energy distribution of carbon and lithium ions as well as of protons, simulated assuming the interaction of one petawatt laser on a 5 mm thick carbon or lithium foil. The total yield of protons was evaluated assuming a 10 nm layer of hydrogen contaminant on the surface [Mac13]. The distributions were obtained for two intensity values, 5 x 10¹⁸ and 5x10¹⁹W/cm², obtainable by working with two focal spot radii, 160 and 50 um, respectively.

In order to maximize the ion yields, and to better and better tailor the ion energy distributions, several techniques in the optimization of the laser-matter interaction can be attempted. It will particularly focus in activities about nano-structured target surfaces as described before, which can remarkably modify the efficiency of laser radiation absorption, as well as the properties of the nascent plasma.

III.9.1 Gas-Jet Target: Thin Mode

In this configuration, we intend to minimize the "plasma-plasma friction", i.e. the energy dissipation of the fast flowing plasma colliding with the gas-jet plasma, in order to work in a more "classical" nuclear physics experimental scheme (i.e. projectiles on a fixed target). Specific simulations have been done in order to describe the experimental conditions under these assumptions. In particular, complete neglecting the plasma effects and setting the helium or deuterium gas density at about 10^{18} atoms/cm^3 and using a gas jet thickness of few mm (e.g. $d =$ 5 mm) we estimate an energy threshold of few keV above which the stopping power of the incoming carbon ions can be neglected (i.e. no thermalization takes place in the gas-jet target); for boron and lithium ions these energies are even

lower. Practically, in this way all carbon or lithium ions pass through ionized gas (a plasma target), except the ones producing the nuclear reactions we want to study. In such conditions, the reaction rates can be easily estimated, once the corresponding astrophysical factor can be assumed to be known. Of course, the simulations do not take into account the effects of the plasma environment on the reactions (i.e. how does the plasma affect the reaction rate), but this is actually the main aim of the proposal.
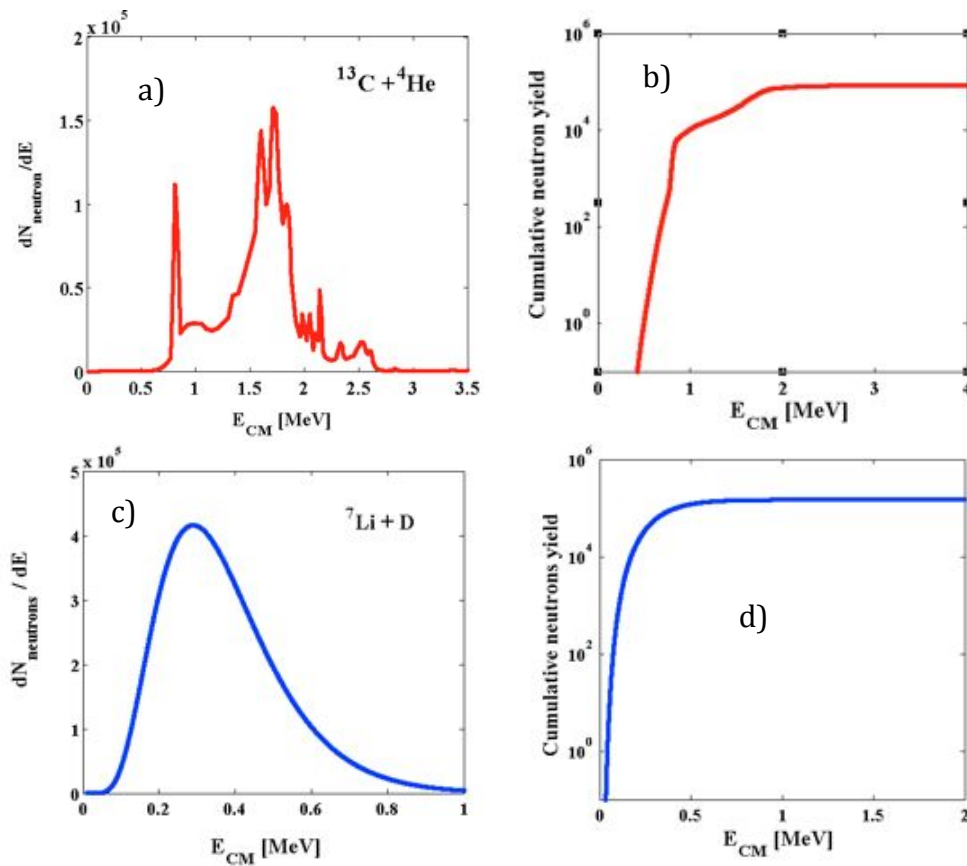
fig.III- 11 Expected number of neutrons as a function of the center of mass energy for the:$^{13}C+ {}^{4}He$ a) and b), $^{7}Li + d$ reactions c) and d). The yields are corresponding to one single laser shot of 0.1 petawatts on, 1 mm thick, carbon or lithium target, assuming an intensity of 3 x $10^{18}W/cm^2$ for the $^{13}C+ {}^{4}He$ and 2x $10^{18}W/cm^2$ for $^{7}Li + d$.

In fig. III.11 the expected number of neutrons as a function of the center of mass energy for the $^{13}C+^{4}He$ and $^{7}Li+d$ reactions are plotted, along with the corresponding cumulative yields. These calculations are related to "single shot" laser pulses of 0.1 petawatts on carbon or lithium target, 1 m thick, assuming an

intensity of 3 10^{18} W/cm^2 for the ^{13}C+^{4}He and 2 10^{18}W/cm^2 for the ^{7}Li+d reaction. Such parameters were chosen to ensure the detection of about one neutron for each detection module (see fig.III-10) per shot; this also takes in to account that the overall efficiency for a single neutron detector placed at two meters from the target is about 10^{-5} [Dro80]. Under these conditions, we can reach a good sensitivity in the determination of center of mass energies in the range between 0.8 and 2.6 MeV for the ^{13}C+^{4}He reaction, and between 0.1 and 0.8 MeV for the ^{7}Li+D, while the statistical significance of the collected data is guaranteed by the performance (repetition rates up of 10 Hz) which will be achievable at the ELI-NP facility. In such operative conditions we are also able to estimate the astrophysical factors by reconstructing the neutron energies using time of flight (TOF) measurements. In fig. III-12 we plot the center of mass energy uncertainty as a function of the neutron-detected energy for both reactions. The calculation was done assuming a standard 1 ns overall time resolution, but we are confident to improve this value up to 0.5 ns or better, which is particularly useful in the case of the ^{7}Li+d reaction.
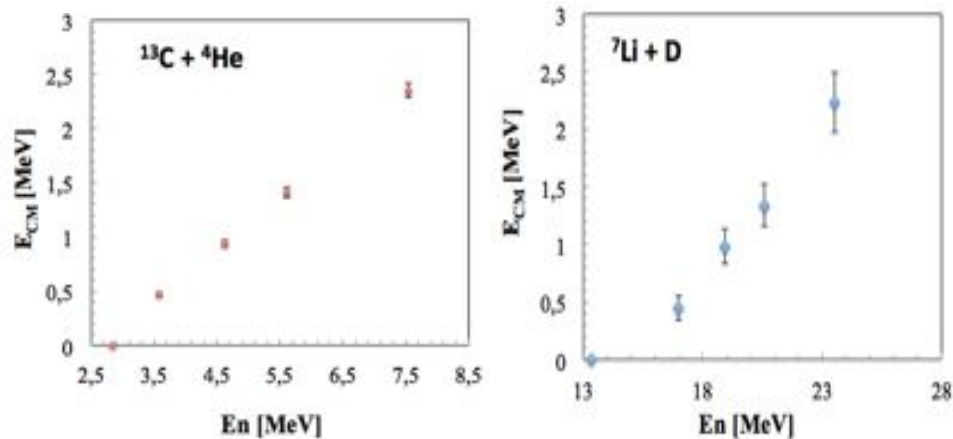
fig.III- 12 Center of mass energy as a function of the detected neutron energy for ^{13}C+ ^{4}He and ^{7}Li+d reactions. The error bars are obtained assuming an overall time resolution of 1 ns.

In order to change the working energy range for both reactions at higher values, it is possible to increase the laser intensity (up to 5×10^{18}W/cm^2) and use a thin degrader (few m of Mylar), introduced between the carbon or lithium target foil and the gas-jet. Such operative conditions allow the tuning of the carbon or lithium

energy distributions in order to significantly reduce the contribution of the low energy part of the spectra. Increasing the laser intensity, the laser spot size considerably reduces thus producing a smaller amount of C/Li ions available for the reactions; this problem can be partially compensated thanks to the unique ELI-NP laser, which allows to operate at the full laser power (10 PW), but still in high repetition rate mode.
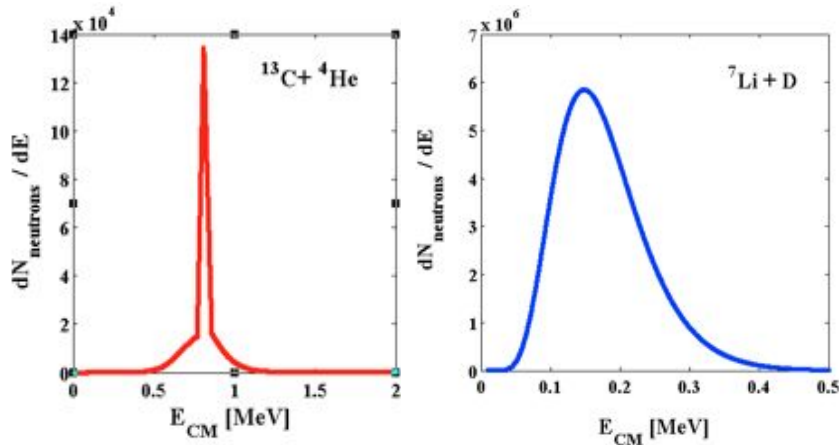
fig.III- 13 Neutron energy distribution for the $^{13}C+^4He$ and ^7Li+d reactions at 10 petawatts laser power at 0.7×10^{18} W/cm^2 of intensity, obtained by using 10 mm of carbon foil and 1 mm lithium foil. The gas jet density is 10^{18} Atoms/cm^3

For the low center-of-mass energy domain (i.e. <0.8 MeV), the cross-section is drastically reduced, but also in this condition the formidable ELI-NP laser performances should allow to obtain – with sufficient accumulated statistics – meaningful physical results. By decreasing the laser intensity (to $0.7 \ 10^{18}$W/cm^2 for example), the number of ions produced at each laser shot considerably increases, obtaining a significant increase of the rates in the following energy ranges: 0.5 – 1 MeV for $^{13}C+^4He$ and 50 - 400 keV for ^7Li+d. When working at the full power pf 10 PW and maximum repetition rate, without changes in the experimental setup, we are also able to extract information on ^7Li+d. In fig.III-13 the neutron energy distributions for both reactions are plotted, again we still expect to detect – for the ^7Li+d – a single neutron per each detection module per shot. For the $^{13}C+^4He$ reaction (as can be noticed by the expected yields) it will be necessary to change the TOF path, reducing it at 1 m, in order to increase the overall efficiency of a single neutron detection module up to $4 \ 10^{-4}$, thus also

increasing the detection efficiency to about 0.5 neutrons per shot. As an alternative to the aforementioned technique, and for further investigation at lower energies, we also plan to work in a thick gas-jet target configuration.

III.9.2 Gas-Jet Target: Thick Mode

Operations in the "thick" gas-jet target mode (that means most of the streaming primary plasma is stopped/thermalized into the secondary one) are possible, when the gas density (up to 10^{20} atoms/cm^3) is increased in addition to its physical thickness; the changes should contribute to enhance the total reactions rates at lower energy (or lower temperature). In particular, the fast streaming carbon or lithium plasma will be stopped at the plasma jet target, forming a new plasma made by a mixture of carbon and helium, or lithium and deuterium. After the thermalization phase (tens of pico-second), such plasma has a final temperature that is determined by both the initial temperatures of the two starting plasmas. This temperature, as well as the final plasma volume, can be properly measured. Also in this case, the plasma temperature tuning is enabled by changing the laser parameters, the solid target thickness, the gas-jet target density and the secondary plasma temperature, etc. The expected neutron yields for both reactions are shown in fig.III-14. As can be noticed, there is a direct access to the reaction rates as a function of the temperature, which is the main goal of the astrophysicist, moreover, also in this case it is possible to extract in an indirect way the astrophysical S factor by de-convolving the thermal distributions. In conclusion, through the proposed set-up and thanks to the unique characteristics of the ELI-NP laser facility it will be possible to explore nuclear reaction rates in energy regions otherwise inaccessible and, more importantly, inside a plasma. These studies can be, obviously, extended to many others astrophysical relevant reactions.
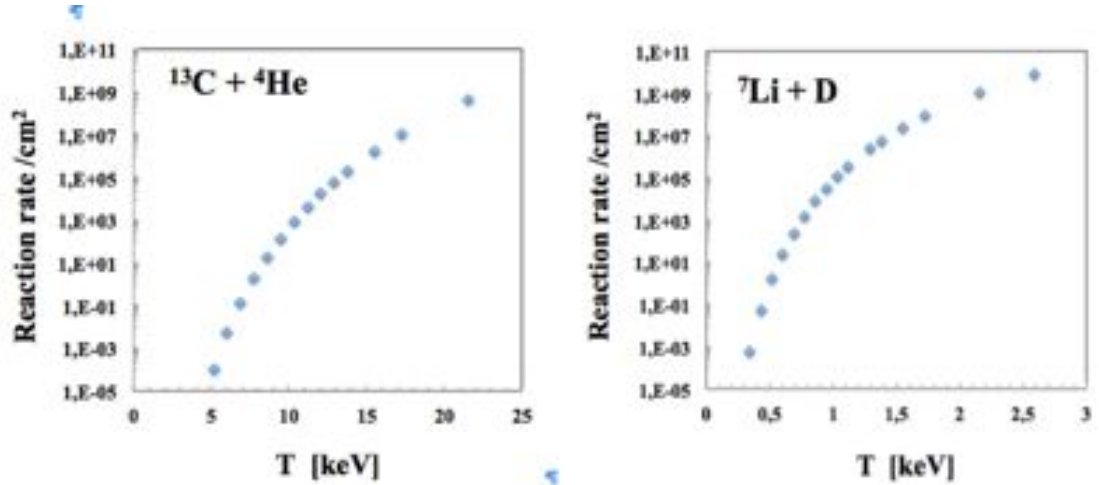
fig.III- 14 Neutron yields/cm² as a function of the final plasma temperature for the ¹³C + ⁴He and ⁷Li + d reactions at 10 PW. The estimates have been obtained assuming to use a carbon foil of 10 mm thickness and 10²⁰ He/cm³ as gas jet density for the generation of ¹³C + ⁴He plasma and a 1 mm thick lithium foil and 10²⁰ d/cm³ for the ⁷Li + d plasma.

III.10 NUCLEAR REACTIONS IN PLASMAS

In the extrapolation of the cross section σ (E) of a charged-particle-induced nuclear reaction to astrophysical energies E one uses the equation [Rol88] [Rai02] [Lip10] [Atz04]

$$\sigma(E) = \frac{S(E)}{E} \exp(-2\pi\eta),$$

where S(E) is the astrophysical factor, and η is the Sommerfeld parameter,

$$\eta = \frac{Z_1 Z_2 e^2}{4\pi\varepsilon_0 \hbar} \sqrt{\frac{m_r}{2E}}.$$

Here, Z_1 and Z_2 are the charge numbers of the interacting nuclei and m_r is their reduced mass, $m_r = m_1 m_2 / (m_1 + m_2)$, where m_1 and m_2 are the masses of the nuclei.

The cross section provided in previous equation assumes that the Coulomb potential of the interacting nuclei is that resulting from bare nuclei. However, nuclear reactions could be drastically changed inside plasmas, owing to the electron screening. In weakly coupled plasmas, i.e., the Coulomb interaction energy between the nucleus and the nearest few electrons and nuclei is small compared with the thermal energy $k_B T$, the nuclear reaction rate is enhanced by a factor [Sal54] [Gru98] [Atz04]

$$g_{scr} = \exp\frac{Z_1 Z_2 e^2}{T\lambda_D}$$

where n is the baryon density and λ_D is the Debye length,

$$\frac{1}{\lambda_D^2} = 4\pi n e^2 \zeta^2 / T,$$

with

$$\zeta = \left[\sum_i X_i \frac{Z_i^2}{A_i} + \left(\frac{f'}{f}\right)\sum_i X_i \frac{Z_i}{A_i}\right]^{1/2}.$$

Here, X_i, Z_i, and A_i are the mass fraction, the nuclear charge, and the atomic weight of ions of type i, respectively. f is the Fermi-Dirac function,

$$f(\xi) = \int\limits_0^\infty dx\, x^{1/2}\left[\exp(x-\xi)+1\right]^{-1},$$

and f' is the first derivative $f(\xi)$.

Therefore the nuclear reaction rate in plasmas can be written as

$$\left\langle \sigma v \right\rangle_{screening} = g_{screening} \left\langle \sigma v \right\rangle$$

where $\left\langle \sigma v \right\rangle$ is the averaged reactivity neglecting screening.

III.11 THE CASE OF $^{13}C(^{4}He,n)^{16}O$

In this section, we show the results for the case of $^{13}C(^{4}He,n)^{16}O$[Wu16]. In fig. III-15, we show the enhancement factor $g_{screening}$,that it has been defined in the discussion about electron screening, as a function of the temperature T. Then we show in fig. III-16 the data of the astrophysical factor $S(E_{cm})$ and the cross section $\sigma(E_{cm})$. We show, for an example case, in fig. III-17 the number of accelerated ^{13}C ions per unit energy from TNSA in one laser pulse, and in fig. III-18 the number of neutron events per laser pulse per unit energy of the incident ^{13}C ions in the c.m.s. frame. Then we list in Table III-1 total number of neutron events per laser pulse for selected thicknesses of the TNSA target.
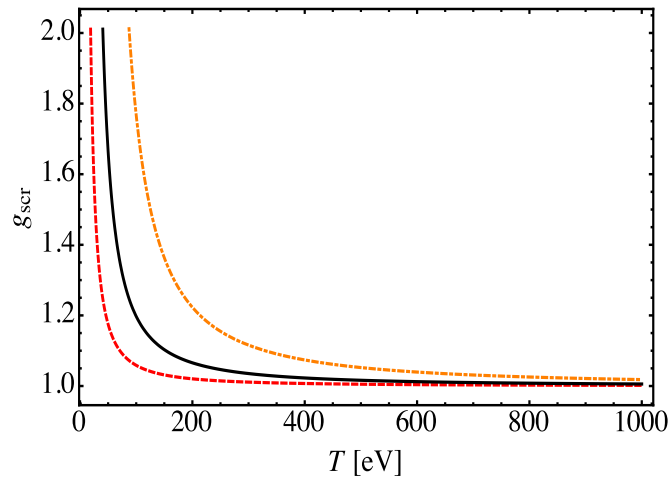
fig.III- 15 The enhancement factor $g_{screening}$ as a function of the temperature T for the reaction $^{13}C(^{4}He,n)^{16}O$ in ^{4}He plasmas. Dot-dashed orange curve: for the case where the ^{4}He density n_{He} is 10^{21} cm^{-3}. Solid black curve: for the case where the ^{4}He density n_{He} is 10^{21} cm^{-3}. Dashed Red curve: for the case where the ^{4}He density n_{He} is 10^{20} cm^{-3}.
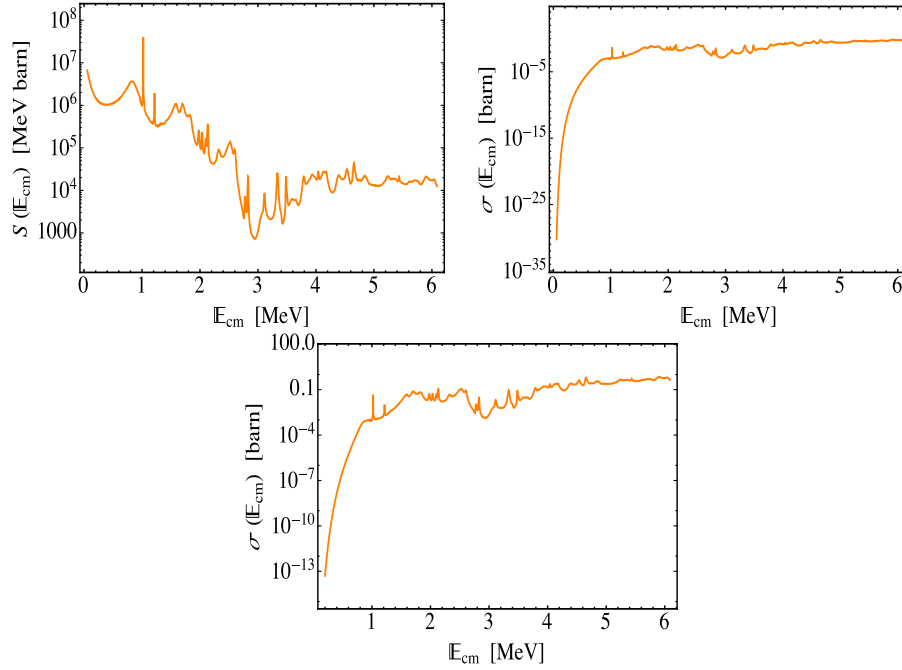
fig.III- 16 The astrophysical factor $S(E_{cm})$ and the cross section $s(E_{cm})$ for the reaction $^{13}C(^4He,n)$ ^{16}O. We adopt the fit of the $S(E_{cm})$ in the [Xu-13] for low energy part ($E_{cm}<0.97$ MeV), and the data form [Har05] for high energy part ($E_{cm}>0.97$ MeV).

Table 1: The total number of neutron events per laser pulse for selected thicknesses of the TNSA target. In the TNSA part, the intensity of the incident laser is 10^{20} W/cm^2, the energy of the laser pulse is 250 J, and the pulse duration is 25 fs. The ^{4}He plasma density n_{He} is 10^{21} cm^{-3} , the temperature of the ^{4}He plasma is 100 eV, and the thickness of the ^{4}He plasma is 10 mm. For comparison, we also show the results for the ^{13}C ions interact with the ^{4}He target with density 10^{21} cm^{-3} and thickness 10 mm.

Table III- 1 Thickness of the TNSA Target

thickness of the TNSA target (μm)	10	1	0.1
^{4}He plasma	6049	8533	8575
^{4}He target	5056	7132	7164
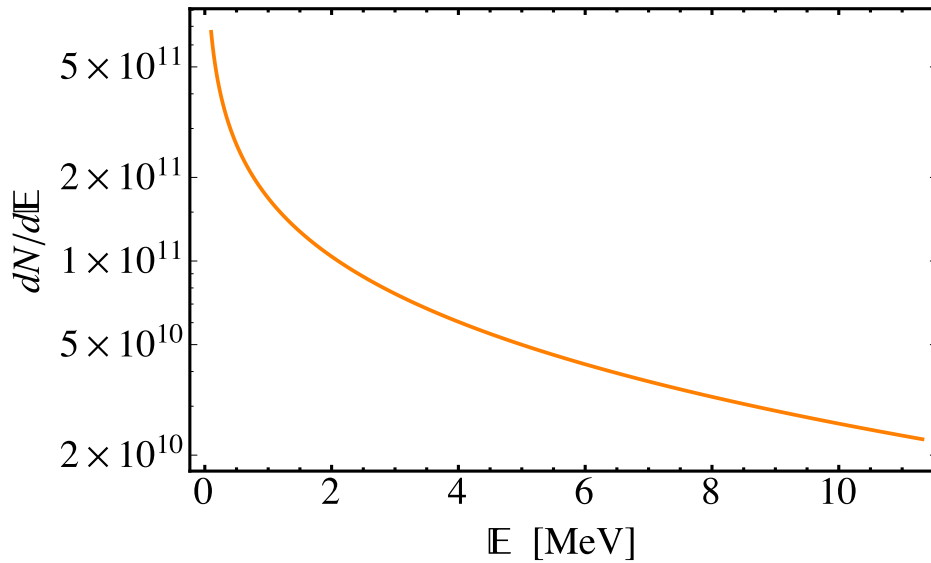
fig.III- 17 The number of accelerated ^{13}C ions per unit energy from TNSA. The thickness of the ^{13}C target is 1 mm. The intensity of the incident laser is 10^{20} W/cm^2, the energy of the pulse is 250 J, and the pulse duration is 25 fs.
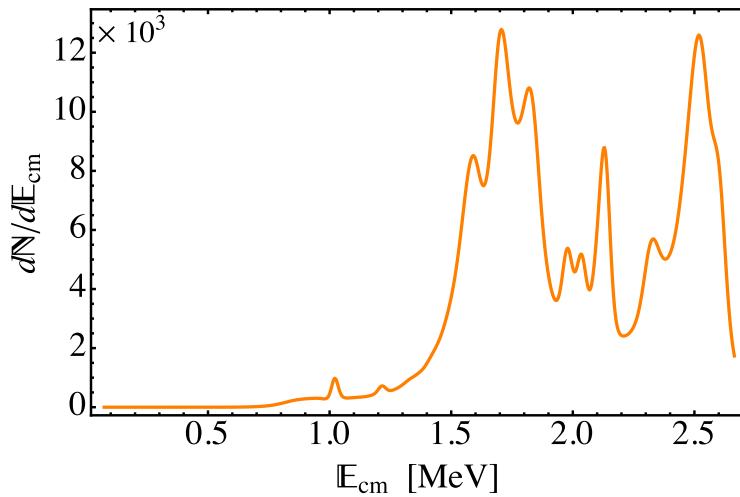
fig.III- 18 The number of neutron events per laser pulse per unit energy of the incident ^{13}C ions in the c.m.s. frame. In the TNSA part, the thickness of ^{13}C target is 1 mm, the intensity of the incident laser is 10^{20} W/cm^2, the energy of the laser pulse is 250 J, and the pulse duration is 25 fs. The ^4He plasma density n_{He} is 10^{21} cm^{-3}, the temperature of the ^4He plasma is 100 eV, and the thickness of the ^4He plasma is 10 mm.

III.12 References

[Akl07]K.U. Akli et al., Phys. Plasmas 14, 023102 (2007)

[Alb06] B.J. Albright et al., Phys. Rev. Lett. 97, 115002 (2006)

[Alf39]H. Alfven, Phys. Rev. 55, 425 (1939)

[Ang10]R.Angeluccietal.,PhysicaE42,1469(2010).

[Atz04]S. Atzeni and J. Meyer-ter-Vehn, The Physics of Inertial Fusion (Clarendon Press, Oxford, 2004)

[Aug89]S. Augst et al., Phys. Rev. Lett. 63, 2212 (1989)

[Bah69]N.A. Bahcall and W.A. Fowler, Astrophys. J. 157, 645 (1969). ?

[Bat02]D. Batani et al., Phys. Rev. E 65, 066409 (2002)

[Bel06]A.R. Bell et al., Plasma Phys. Contr. F. 48, 37 (2006)

[Bor04] M. Borghesi et al., Phys. Rev. Lett. 92, 055003 (2004).

[Bor06]M. Borghesi et al., Fusion Sci. Technol. 49(3), 412 (2006)

[Boy93]Boyd et al., Phys. Rev. C 47, 236 (1993).

[Bra15]C. BRADY et al Users Manual for the EPOCH PIC codes (2015)

[Buf10]S. Buffechoux et al., Phys. Rev. Lett. 105, 015005 (2010).

[Buf10]S. Buffechoux et al., Phys. Rev. Lett. 105, 015005 (2010).

[Car10] D.C. Carrol et al., New J. Phys. 12, 045020 (2010).

[Car10] D.C. Carrol et al., New J. Phys. 12, 045020 (2010).

[Cla00]Clark, E.L., et al.: Phys. Rev. Lett. 84, 670 (2000)?

[Coc10]A. Coc et al., Astrophysical Journal 744 158 (2010).

[Cow04] T.E. Cowan et al., Phys. Rev. Lett. 92, 204801 (2004)

[Cro75]Crow, J.E., Auer, P.L., Allen, J.E.: J. Plasma Phys. 14, 65 (1975)?

[Dav02]J.R. Davies, Phys. Rev. E 65, 026407 (2002)

[Dav04]J.R. Davis, Phys. Rev. E 69, 065401 (R) (2004)

[Dav09] J. R. Davies, Plasma Phys. Control. Fusion 51, 014006 (2009)

[Dro80] M.Drosgetal.,Nucl.Instr.Meth.176,477(1980).

[Dze10] T. Dzelzainis et al., Laser Part. Beams 28, 451 (2010).

[Dze10] T. Dzelzainis et al., Laser Part. Beams 28, 451 (2010).

[Efi09]V. Efimov, Nature Phys. 5, 533–534 (2009).

[Eli02]S. Eliezer The Interaction of High Power Lasers with Plasma (IOP Publishing, Bristol/ Philadelphia, 2002)

[Fuc03]J. Fuchs et al., Phys. Rev. Lett. 91, 255002 (2003)

[Fuc06] J. Fuchs et al., Nature Phys. 2, 48 (2006).

[Fuc06]J. Fuchs et al., Nature Phys. 2, 48 (2006)

[Fuc06]J. Fuchs, et al., Nature Phys. 2, 48 (2006)

[Fuc07] J. Fuchs et al., Phys. Plasmas 14, 053105 (2007)

[Gib05]P. Gibbon, "Short Pulse Laser Interactions with Matter", Imperial College press (2005).

[Gru98]A. V. Gruzinov and J. N. Bahcall, The Astrophysical Journal 504, 996 (1998)

[Han07] F. Hannachi et al., Plasma Phys. Control. Fusion B 49, 79 (2007).

[Har05]S. Harissopulos, H. W. Becker, J. W. Hammer, A. Lagoyannis, C. Rolfs, and F. Strieder, Phys. Rev. C 72, 062801(R) (2005)

[Heg02]M. Hegelich et al., Phys. Rev. lett 89, 085002 (2002)

[Hoy46]F. Hoyle, Monthly Notices of the Royal Astronomical Society 106, 343 (1946)

[Hoy46]F. Hoyle, Monthly Notices of the Royal Astronomical Society 106, 343(1946)

[Hum08]S. Humphries, Charged Particle Beams (Wiley, New York, 2008)

[Kir12]O.S. Kirsebom et al. Phys. Rev. Lett. 108 202501 (2012).

[Lab13] C. Labaune et al., Nature Comm. DOI: 10.1038/ncomms3506 (2013).

[Lab13]C Labaune et al., Nature Comm. DOI: 10.1038/ncomms3506 (2013)

[Lan07]K.L. Lancaster et al., Phys. Rev. Lett. 98, 125002 (2007)

[Lan54]L.D. Landau, E.M. Lifshitz, Mekhanika sploshnykh sred (Mechanics of Continuous Media)(Gostekhizdat, Moskva, 1954)

[Lev14]M. C. Levy, et al., Nature Communication 5, 4149 (2014)

[Lim06] B.N. Limata, Eur. Phys. J. A 27, s01, 193 (2006).

[Lip10]M. Lipoglavšek, et al., Eur. Phys. J. A 44, 71 (2010);

[Lip10]M. Lipoglavsek et al., Eur. Phys. J. A 44, 71 (2010)

[Mac02]A.J. MacKinnon et al., Phys. Rev. Lett. 88, 215006 (2002)

[Mac13] A. Macchi et al., Rev of Mod. Phys. 85 751 (2013).

[Mac13] A. Macchi et al., Rev. Mod. Phys. 85, 751 (2013).

[Mac13]A.Macchi ,A Superintense Laser-Plasma Interaction Theory Primer, Springer, 10.1007/978-94-007-6125-4,(2013)

[Mak00] Maksimchuk, A., Gu, S., Flippo, K., Umstadter, D., Bychenkov, V.Y. Phys. Rev. Lett. 84, 4108,(2000)

[Mal07]L.Malferrari et al.,Mat.Lett.61,2896(2007).

[Mal09] L. Malferrari et al., Journal of Nanotechnology, Article ID 149691 (2009)

[Mal96] G. Malka and J. L. Miquel, Phys. Rev. Lett. 77, 75 (1996)

[Mas10] D. Mascali et al., Rad. Eff. and Def. in Sol. 165, 730 (2010).

[Mas10]D. Mascali et al., Advances in Plasma Astrophysics, Proc. IAU Symposium 274,44, (2010)

[Mas10]D. Mascali et al., Rad. Eff. and Def. in Sol. 165, Issue 6-10, 730 (2006)

[Mey94]B. Meyer, Annu. Rev. Astron. Astrophys. 32 153 (1994).

[Mor03] P. Mora, Phys. Rev. Lett. 90, 185002 (2003)

[Mor03]P. Mora, Phys. Rev. Lett. 90, 185002 (2003)

[Mor05] P. Mora, Phys. Plasmas 12, 112102 (2005)

[Mor05bis] P. Mora, Phys. Rev. E 72, 056401 (2005)

[Mor56]H. Morinaga, Phys. Rev. 101, 254 (1956).

[Nacre]http://pntpm.ulb.ac.be/Nacre/nacre.htm

[Nis05] H. Nishimura et al., PLasma Phys. Contr. F. 47, 823 (2005)

[Nur09]F. Nu?rnberg et al., Rev. Sci. Instrum. 80(3), 033301 (2009)

[Pas04] Passoni, M., Lontano, M.: Laser Part. Beams 22, 163 (2004)?

[Pas04]M. Passoni, M. Lontano, Laser Part. Beams 22, 163 (2004)

[Pas08]M. Passoni, M. Lontano, Phys. Rev. Lett. 101, 115001 (2008).

[Pas08]M. Passoni, M. Lontano, Phys. Rev. Lett. 101, 115001 (2008).

[Pas10]Passoni, M., Bertagna, L., Zani, A.: New J. Phys. 12, 045012 (2010)

[Pat03]P.K. Patel et al., Phys. Rev. Lett. 91, 125004 (2003)

[Pel10]A. Pelka et al., Phys. Rev. Lett. 105, 265701 (2010)

[Pin08]Y. Ping et al., Phys. Rev. Lett. 100, 085004 (2008)

[Pis00]F. Pisani et al., Phys. Rev. E 62, R5927 (2000)

[Puk01] A. Pukhov, Phys. Rev. Lett. 86, 3562 (2001)

[Rad11]Ad. R. Raduta et al., Phys. Lett. B 705, 65 (2011).

[Rai02]F. Raiola, et al., Eur. Phys. J. A 13, 377 (2002);

[Rol88]C. Rolfs and W.S. Rodney, Cauldrons in the Cosmos (University of Chicago Press, 1988)

[Rot01]M. Roth et al., Phys. Rev. Lett. 86, 436 (2001)

[Sal54]E.E. Salpeter, Aust. J. Phys. 7(3), 373 (1954).

[San02]J.J. Santos et al., Phys. Rev. Lett. 89, 025001 (2002)

[Sch06]J. Schreiber et al., Phys. Rev. Lett. 97, 045005 (2006)

[Sch08]M. Schollmeier et al., Phys. Plasmas 15, 053101 (2008)

[Sch12] K. Schmid et al., Rev. Sci. Instr. 83, 053304 (2012).

[Sen07]Y. Sentoku et al., Phys. Plasma 14, 122701 (2007)

[Sna00] Snavely, R.A., et al.: Phys. Rev. Lett. 85, 2945 (2000)

[Spi11]C. Spitaleri et al., Phys. Atom. Nucl. 74, 1725 (2011)

[Tow05] R. P. Town, et al., Nucl. Instrum. Methods Phys. Res. A 544, 61 (2005)

[Tsa09] C. Tsallis, "Introduction to Nonextensive Statistical Mechanics",Springer (2009).

[Wil01]Wilks, S.C., et al.: Phys. Plasmas 8, 542 (2001)

[Wil92] S. C. Wilks, et al., Phys. Rev. Lett. 69, 1383 (1992)

[Wu16] Y. Wu, et al., arXiv:1612.06884 [physics.plasm-ph](2016)

[Xu-13]Y. Xu, K. Takahashi, S. Goriely, et al., Nuclear Physics A 918 61 (2013)

[Zon04] Rui-Long Zong et al., J. Phys. Chem. B 108, 16713 (2004).

CHAPTER IV

PRELIMINARY TESTS OF IONS ACCELERATION

IV.1 Introduction

In the previous chapters we have analyzed the physic case that will be tested at laser facility ELI-NP in Bucharest. In preparation of these nuclear physics activities in plasma laser, two different areas are studied: ions acceleration and detectors prototypes realization. It is well known that high power laser pulses can accelerate electrons, protons and heavy-ions to high energies, theoretically, enough to produce almost all known types of nuclear reaction. At ELI-NP, the reactions induced by accelerated high density ion bunches with secondary targets (solid, gaseous or a laser generated plasma), will be extensively studied to analyse specific phenomena that cannot be easily realized at accelerator based nuclear facilities. At intensities approaching 10^{23} W/cm^2, and beyond, that will be achievable at ELI-NP, the dominance of RPA (Radiation Pressure Acceleration) mechanism for ion acceleration over TNSA (Target Normal Sheath Acceleration) is expected [Rob08]. Especially in the "light sail" regime of RPA, quasi-neutral quasi-monoenergetic bunches with solid state density are predicted to be produced, that is about 10^{14} higher ion densities compared to existing ion beam accelerators. In the following paragraphs will be described different measurement campaigns conducted in Pisa at Intense Laser Irradiation Laboratory (ILIL).

IV.2 Intense Laser Irradiation Laboratory (ILIL)

The research activity of the Intense Laser Irradiation Laboratory (ILIL), in Pisa in the area of CNR-INO, is focused on fundamental studies of high-intensity laser interactions with matter and their applications. At ILIL, flexible high-power laser systems and multi-purpose interaction chambers are combined with the capability of performing high temporal resolution spectroscopy from the IR to the X-ray region. Fundamental studies include plasma formation and heating by laser beams, laser-induced instabilities and other non-linear processes, atomic physics of highly ionised plasmas, ultra-short X-ray emission and acceleration of charged particles. The ILIL-PW upgrade includes a power amplifier and a fully shielded target area. The power amplifier, when completed, will deliver 250 TW power pulses at a repetition rate up to 5Hz. The currently available 10 TW/10Hz system output will continue to be delivered to the existing interaction target chambers for laser-gas and laser-solid interactions respectively. In this context, we carried out a systematic experimental investigation to identify the role of target properties in TNSA, with special attention to target thickness and dielectric properties. It has been used a full range of ion, optical and X-ray diagnostics to investigate laser-plasma interaction and ion acceleration. We focused on the results obtained using a Thomson Parabola Spectrometer (TPS). By means off TPS, often used in such experiments, ions with different charge-to-mass ratios are separated into distinct parabolas. This allows extracting information for each ion species when several ions are generated simultaneously in a given solid angle.

IV.3 The experimental setup @ILIL

On 2015, the experiment was carried out at the Intense Laser Irradiation Laboratory using the 10 TW Ti:Sa laser system which delivers up to 450 mJ on target and features an M^2 to 1.5 [Giz16]. As shown schematically in fig. IV-1,
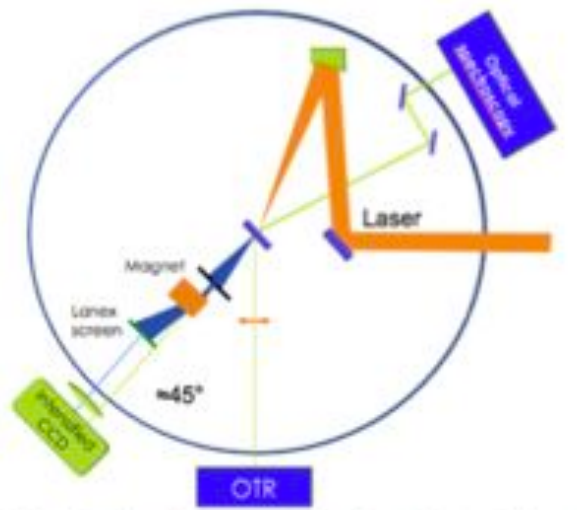
fig.IV- 1 Sketch experimental setup ILIL in Pisa.

Fig. IV-1 Schematic view of the experimental setup showing the main diagnostics including the optical spectroscopy of the specular reflection, the rear side optical imaging and the magnetic electron spectrometer of the forward escaping electrons.

fig.IV- 2 Image of Vacuum chamber

the laser was focused, at an angle of incidence of 15°, using an f/4.5 Off-Axis Parabolic mirror (OAP), in a spot size of 6.2 μm FWHM, giving a nominal intensity on target of about $2 \ 10^{19}$ W/cm^2.
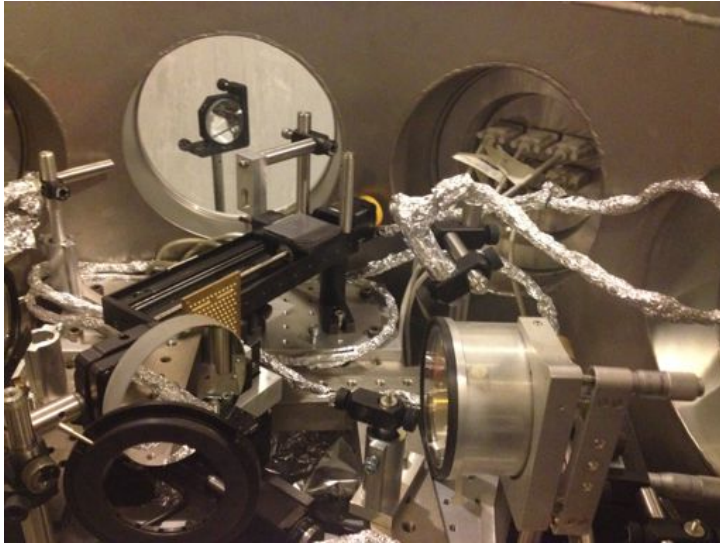
fig.IV- 3 Vacuum Chamber Inside View

The nanosecond temporal contrast of the pulse set by the Amplified Spontaneous Emission (ASE) was better than 10^{10}, thus enabling a pre-plasma free interaction with the solid target (see image) down to the picosecond temporal regime.
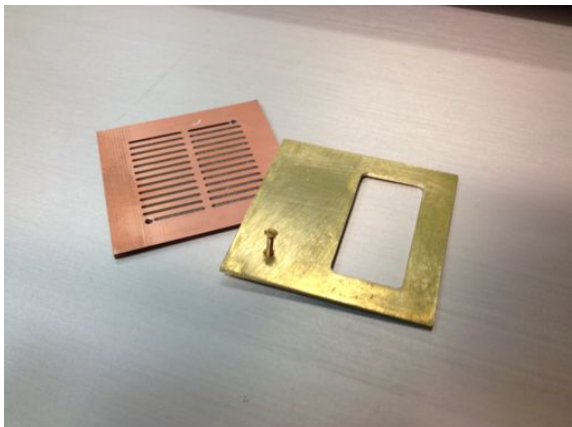
fig.IV- 4 Target View. It has been necessary to use a multi windows target because the high intensity of laser multifragments the single window target. Then we carry out other different targets optimizing the number of possible spots.

In view of this, in the reminder of this paper we will refer to "pre-plasma" as the short scale-length plasma generated by the picosecond pedestal of the laser pulse, typically arising from imperfections of the pulse compression. In fact, as shown by the cross-correlation curve of in fig. IV-5, the laser contrast remains better than 10^{10} up to 10 ps before the peak of the pulse and decreases to 10^6 at 1 ps before

the peak of the pulse. Taking into account this temporal profile, we expect plasma formation to start not earlier than 10 ps before the peak of the pulse. In this case, the plasma formed in front of the solid target is expected to have a very steep density gradient [Baf14]
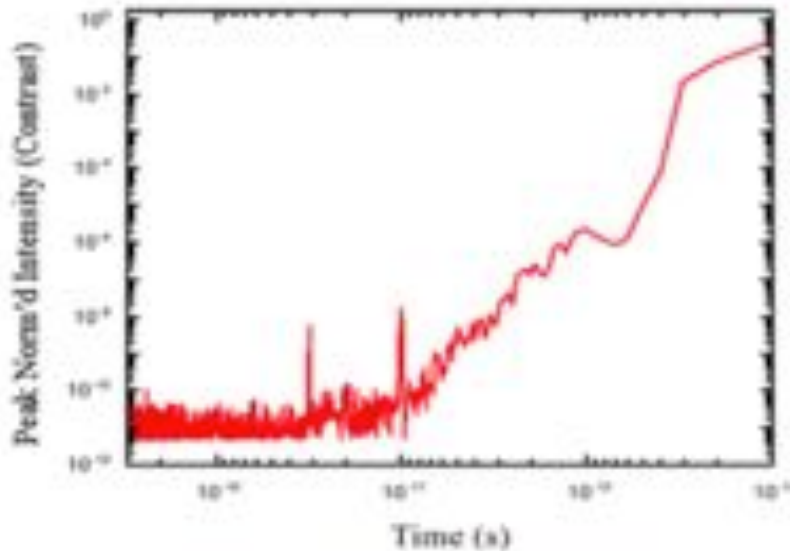
fig.IV- 5 Log-log plot of the measured laser contrast of the ILIL system. The sub-nanosecond ASE contrasti s better 10^9 up to 10 ps before the peak of the pulse and reaches 10^6 at 1 ps

The beam is focused on the target at an angle of incidence of 15° using an off-axis parabolic mirror; the corresponding maximum intensity on target was up to 2 x 10^{19} W/cm². The target was mounted on a three-axis translational stage system at the center of a 640 mm diameter interaction chamber. Targets consisting of different materials were used. Here we focus on deuterated plastic (CD_2) foil targets of 10 μm thickness. TPS has been employed to characterize ion beams produced in TNSA regime. The working principle of TPS is widely described in literature [Har08,Jun11,Cob11].

IV.4 Thomson Parabola Spectrometer (TPS)

fig.IV- 6 Image TPS mounted at ILIL (april 2015)

A typical Thomson Spectrometer has been developed in the framework of the INFN "LILIA" (Laser Induced Light Ion Acceleration). The aim of LILIA project is to study the mechanism of charged particles acceleration with high power laser. The spectrometer developed at INFN-LNS has two pinholes upstream as collimator, the deflection is provided by a magnetic field, produced by two resistive coils, and an electric field, produced by two electrodes placed in the magnetic gap. The detector is a micro-channel plate coupled to a phosphor screen which allows an online monitoring of beam particles.

IV.4.1 Motion of charged particles in electric and magnetic fields

The working principle of a Thomson-type spectrometer is based on the motion of a charged particle in an electric and magnetic fields. In the following it is proposed a brief and general relativistic treatment of the problem and than it is scaled to the non-relativistic case of interest for the energy involved in the practical use of the spectrometer. As starting point we recall the Lagrangian for the electromagnetic field [Rus00][Jack75], that is:

$$L = -mc^2 \sqrt{1 - \frac{u^2}{c^2}} - q\,\varphi + q\,\boldsymbol{u} \cdot \boldsymbol{A}$$

The first term on the right hand side is the Lagrangian of the free particle, where m is its proper mass and $\boldsymbol{u}$ its velocity, and the other two terms represent the Lagrangian of interaction with the potentials φ and A. The particle energy in an electromagnetic field is given by its Hamiltonian

$$H = \boldsymbol{u}\,\frac{\partial L}{\partial \boldsymbol{u}} - L$$

where the derivative of L with respect of the velocity is the particle canonical momentum:

$$\boldsymbol{P} = \frac{\partial L}{\partial \boldsymbol{u}} = \boldsymbol{p} + q\,\boldsymbol{A}$$

with $\boldsymbol{p} = \dfrac{m\,\boldsymbol{u}}{\sqrt{(1 - u^2/c^2)}}$ its relativistic momentum. Thus the Hamiltonian can be written as:

$$H = \frac{mc^2}{\sqrt{1 - u^2/c^2}} + q\,\boldsymbol{u} \cdot \boldsymbol{A} + mc^2 \sqrt{1 - \frac{u^2}{c^2}} + q\,\varphi - q\,\boldsymbol{u} \cdot \boldsymbol{A} = \frac{mc^2}{\sqrt{(1 - u^2/c^2)}} + q\,\varphi = \varepsilon + q\,\varphi$$

where:

$$\varepsilon = \frac{mc^2}{\sqrt{(1 - u^2/c^2)}}$$

is the energy of the free particle which can be also expressed, using the relativistic energy momentum relation, as $\varepsilon^2 = (pc)^2 + (mc^2)^2$.

IV.4.2 Motion of a charged particle in electrostatic field

Consider a charged particle, q>0 in an uniform electrostatic field, namely a particle moving in a parallel plate capacitor large enough to neglect edge effects. We suppose that the particle enters the capacitor at the time t=0 with initial velocity u0 along the positive direction of abscissas and the entry point matches with the axes origin. The motion equation of the particle in the electrostatic filed E=(0, E, 0) of the capacitor is:

$$\frac{d\,\boldsymbol{p}}{dt} = q\,\boldsymbol{E}$$

.

Projecting the motion equation along the three spatial directions we get three scalar equations that can be solved using the initial conditions to get a system of equations which ensures that the motion is on the x-y plane (planar motion) and the momentum along the x direction is constant. From a classical point of view at a constant momentum corresponds a constant velocity while in the relativistic case it does not hold true [Jac75]. The x component of the particle velocity is:

$$u_x(t) = \frac{c^2}{\varepsilon} p_x(t) = \frac{p_{ox}c^2}{\sqrt{\varepsilon_0^2 + (qEct)^2}}$$

After integration the initial condition x(0)=0 the kinematic equation of the particle is:

$$x(t) = \frac{p_{ox}c}{qE} settsenh\left(\frac{qEct}{\varepsilon_0}\right)$$

which has a hyperbolic dependence on time. In the non-relativistic case we find a linear dependence on time and the corresponding equation is:

$$x(t) = u_{x0}\,t$$

.

We can proceed in an analogous way to solve the y component of the particle motion, to get the equation:

$$y(t) = \frac{\varepsilon_0}{qE}\left[\sqrt{1+\left(\frac{qEct}{\varepsilon_0}\right)^2} - 1\right]$$

It can combined the equation to get and equation that can be easily scaled to the classical case:

$$y(t) = \frac{\varepsilon_0}{qE}\left[\cosh\left(\frac{qEx}{p_{0x}c}\right) - 1\right] .$$

In the non relativistic case, u<<c and p<<mc², we can use MacLaurin expansion to get the classical trajectory of the particle:

$$y(t) = \frac{qE}{2\mathrm{m}}t^2 = \frac{1}{2}qE\frac{x^2}{mu_{x0}^2} .$$

IV.4.3 Motion of a charged particle in magnetostatic field

It is considered now an external magnetic field B=B$\hat{z}$ produced by an infinite length solenoid and a probe charge with a nonzero initial velocity. The motion equation for the particle is:

$$\frac{d\,\boldsymbol{p}}{dt} = q\,\boldsymbol{u}\wedge\boldsymbol{B} .$$

The magnetic field does no work, in fact according to the work-energy theorem, we have:

$$\frac{d\,\varepsilon}{dt} = \frac{dL}{dt} = \frac{dK}{dt} = \boldsymbol{F}\cdot\boldsymbol{u} = q(\boldsymbol{u}\wedge\boldsymbol{B})\cdot\boldsymbol{u} = 0$$

which means that the energy ε is a constant. As a consequence the modulus of momentum p is a constant and then u² is a constant as well, hence ε does not depends on time. In this situation, the differential equation to be solved to find the particle trajectory is:

$$\frac{d\,\boldsymbol{u}}{dt} = \frac{c^2}{\varepsilon}\frac{d\,\boldsymbol{p}}{dt} = \frac{c^2}{\varepsilon}q\,\boldsymbol{u}\wedge\boldsymbol{B} .$$

Projecting the previous equation along the three spatial directions we get three scalar equations:

$$
\begin{cases}
\dfrac{du_z}{dt}=0 \\[2mm]
\dfrac{du_y}{dt}=-\dfrac{qc^2}{\varepsilon}u_x B \\[2mm]
\dfrac{du_x}{dt}=-\dfrac{qc^2}{\varepsilon}u_y B
\end{cases}
$$

The integration of the first equation gives an important result, in fact:

$$u_z(t)=u_z(0)\quad \forall t$$

and we have said that u^2 is a constant, hence:

$$u^2(0)=u^2(t)\quad \Rightarrow \quad u_x^2(0)+u_y^2(0)+\cancel{u_z^2(0)}=u_x^2(t)+u_y^2(t)+\cancel{u_z^2(t)}$$

which means that the transverse component of the velocity is constant as well as the sum of the square of $u_x(t)$ and $u_y(t)$, namely:

$$u_x^2(t)+u_y^2(t)=u_T^2=const\quad \forall t$$

The last two equations are coupled via the velocity and can be solved to get the parametric equation of the particle trajectory:

$$
\begin{cases}
x(t)=\dfrac{u_T}{\omega}\sin(\omega t+\phi) \\[2mm]
y(t)=\dfrac{u_T}{\omega}\cos(\omega t+\phi)
\end{cases}
$$

This result is analogous at the classical one, the main difference is in the cyclotron frequency ω. In fact remembering that $u^2=u_T$ we can write, in the relativistic case:

$$\omega=\frac{qB}{\varepsilon/c^2}=\frac{qB}{m}\sqrt{1-\frac{u_T^2}{c^2}}=\omega(u_T)$$

and the frequency depends on the transverse velocity. In the classical limits, i. e. when

pc<<mc² it's possible to have:

$$\omega = \frac{qB}{m}$$

IV.5 TPS @ILIL

In our experiments the position Thomson Parabola was at 0° in forward direction shown in fig.IV-7
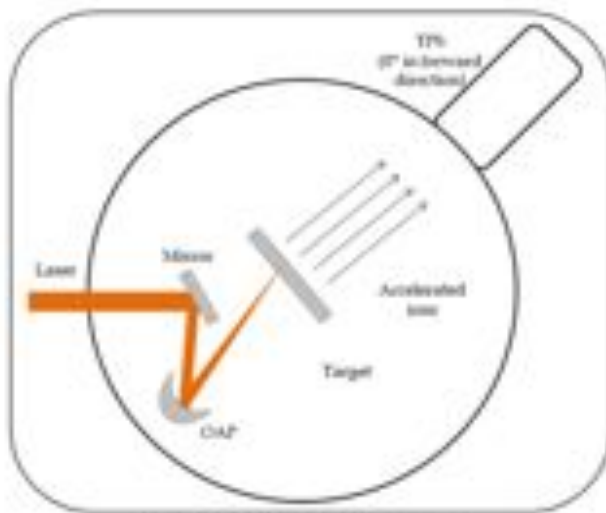
fig. IV- 7 Sketch of T.P. and experimental setup.

 The (TP) spectrometer, invented in 1912 by J. J. Thomson, the discoverer of the electron, is successfully used as charged particles analyser for studying ion beams ejected from laser-generated plasmas. The deflection sector of the Thomson spectrometer consists of parallel electric and magnetic fields and both perpendicular to the direction of the incident beam. The main feature of this kind of spectrometer is to provide information on energy, momentum, charge-to-mass ratio, ect., of the deflected ions simultaneously. Assuming that both field are

uniform over a length L and zero outside, using the theory exposed above and a small angle approximation by setting $tg\theta \sim \theta$, it can be shown that the trajectories of non-relativistic ions moving perpendicularly to the electric field is parabolic and the deflection angle at the exit of the electrodes is:

$$\theta_e = \frac{ZeEL}{A \mu v^2} = \frac{ZeEL}{2 E_{kin}}$$

where θ_e is the electric deflection angle in radians, Z is the charge state of the ion, e is the electronic charge, EL is the product of the electric field and its length, A is the ion mass number, μ is the unit nucleon mass base, v and E_{kin} are the velocity and kinetic energy of the ion. Similarly the trajectories of ions moving perpendicularly to the magnetic field is circular and the deflection angle at the exit of the magnets is:

$$\theta_m = \frac{ZeBL}{A \mu v} = \frac{ZeBL}{\sqrt{2A \mu E_{kin}}}$$

where θ_m is the magnetic deflection angle in radians and BL is the product of the electric field and its length [Rhe84]. Since the fields are parallel the corresponding deflections are orthogonal each other. The electric and magnetic deflections are proportional to the corresponding deflection angles by:

$$\theta_i = x_i / D$$

where $i=e,m$ stays for electric or magnetic angle and D is the drift length between the electromagnetic device and the detector plane. Thus assuming that the magnetic field deflects on x axis and the electric field deflects on y axis, from the above equations one gets:

$$y = \frac{qELD}{2 E_{kin}} \qquad x = \frac{qBLD}{\sqrt{2} mv}$$

where $q=Ze$ is the ion charge and $m=A\mu$ is its mass in kilograms [Har08].Solving the second equation for v and replacing it in the first one we get the parabolic equation:

$$y = \frac{mE}{qLDB^2} x^2$$

which means that particles with the same charge-to-mass ratio and different energies are deflected on a parabolic trace on the detector plane. The previous equation shows that a TP provides a separation of all ion species and charge state according to their q/m. Every single parabola on the detector belongs to a different ion charge-to-mass state ratio. The ions velocity is found by taking the ratio as:

$$v = \frac{EL}{BL} \frac{\theta_m}{\theta_e}$$

which is independent on charge or mass. This means that any straight line crossing the origin of the deflection coordinates is a constant velocity line. The charge-to-mass ratio of ions is found as:

$$\frac{Ze}{A\mu} = \frac{EL}{(BL)^2} \frac{\theta_m^2}{\theta_e}$$

Thus ions of different energies with the same charge-to-mass ratio form a parabolic trace on the deflection plane.
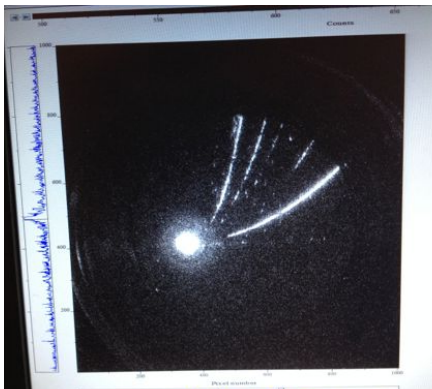
fig.IV- 8 TPS screen image captured during experimental campaign.

IV.6 Microchannel Plates Detector

Microchannel plates (MCPs) are compact electron multipliers of high gain. A typical MCP consists of a huge number of closely packed channels in a glass matrix with diameter of about *10 μm*. Each channel acts as an independent photomultiplier and parallel electrical contact to each channel is provided by depositing of a metallic coating on the front and rear surface of the MCP, being then the input and output electrodes. When a particle, whatever its nature, hits the channel wall a fraction of its energy is transferred to the electrons in the channel surface. Thus the electrons energy can be enough to be pushed form the channel surface and a current due to secondary emission is formed. A bias tension, applied to the surface of the plate creates an electric field accelerating the electrons in the channels. Because of the electric field the electron trajectories are parabolic and they hits the channel wall increasing the secondary electrons emission. An avalanche of electrons is then produced reaching the channel ending where a scintillating screen takes place. The high-voltage applied across the MCP surface produce also a current flowing through the plate surface. The electrons forming this current, called strip current, refill the electron depleted regions of the channel wall for the secondary emission. If the depleted regions would not be filled it would be prohibited the process of secondary emission since there would not be any electron available to be knocked out.

IV.7 TPS Algorithm

The data is sorted and sequentially divided into different directories in order to be analyzed in the following processes of analysis, with the use of a processing algorithm of digital images developed with MATLAB.

The algorithm is based on a digital image processing system which has the purpose, through a series of stages, to divide and analyze the images for the

automatic recognition of the ionic lines, and then the ions, separating them in function of their mass and of their state of charge, in order to analyze the results and make direct comparisons between the basic theories and the actual results achieved during the experimental stages. Spectrograms analysing procedure consists of different steps. First step is to crop the image in the parabolas vertex and overlap the theoretical parabolas to the spectrogram. Then the energy spectra of different on species and charge states are reconstructed by cutting out the events associated to the parabolas and by using one of the equations [Alt16] related to the magnetic or electric deflections.
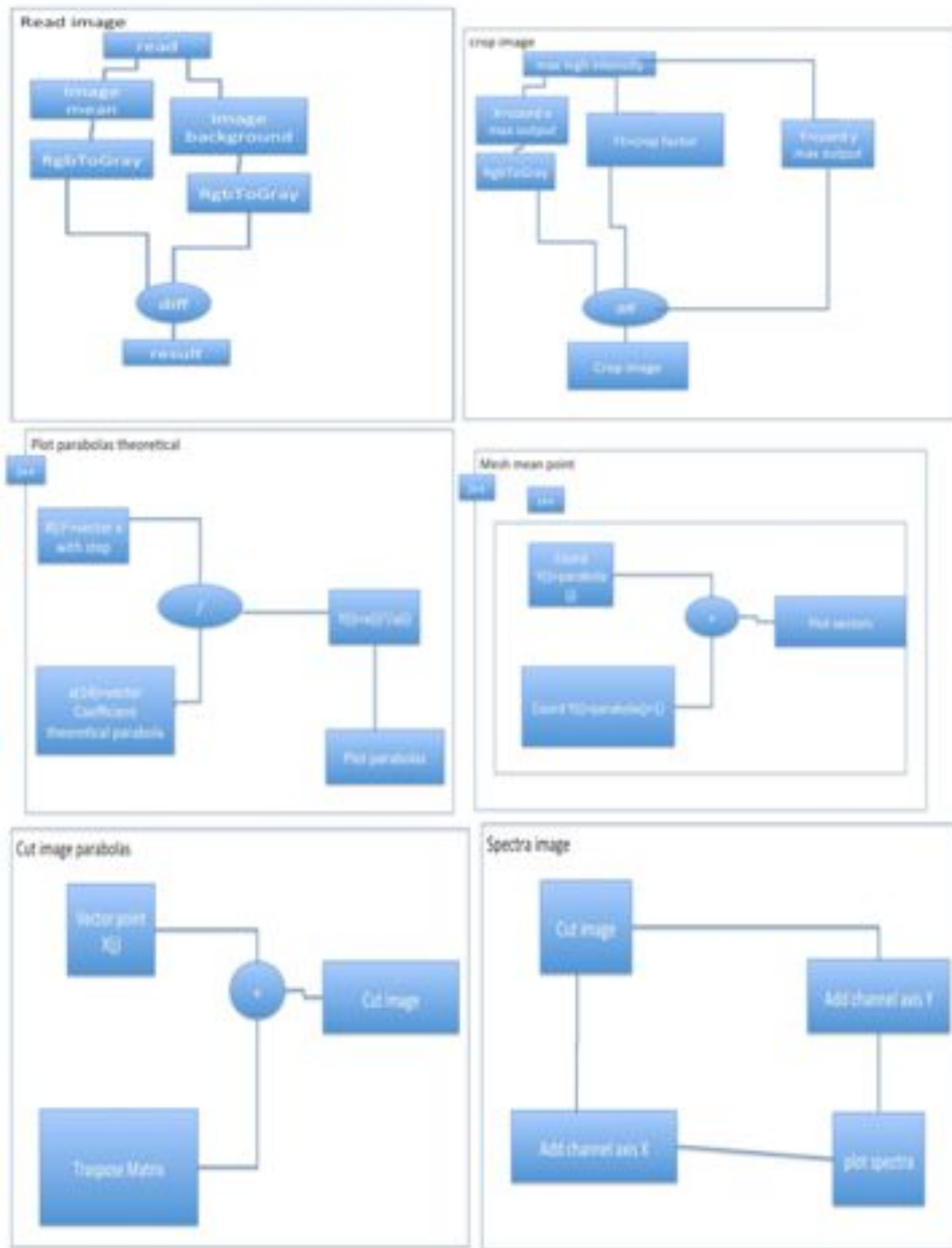
fig.IV- 9 Sketch of algorithm for analysis.

The spectrogram images of EMCCD contain a bright halo, which constitutes the origin of the parabolic ion traces, due to x-radiation and neutral particles propagating straight through the electromagnetic field, and parabolic traces associated to proton and behaviour ions outgoing from the bright region, as shown in fig. IV- 10
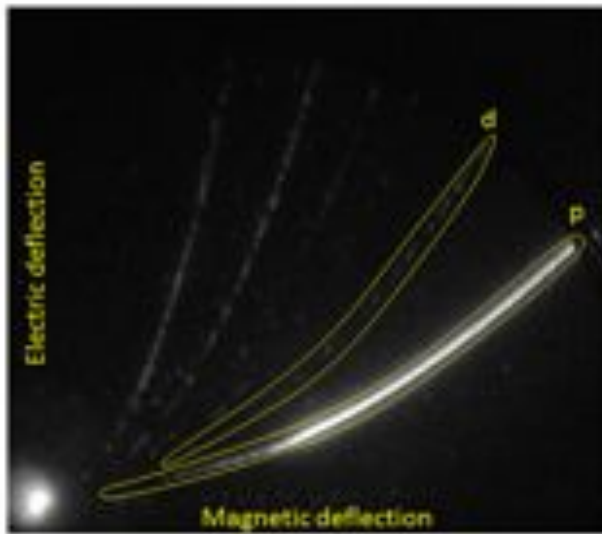
fig.IV- 10 TPS spectrogram from CD$_2$ target: protons, deuterons and carbon with different charge states are detected. The yellow curves represent the cuts used in order to reconstruct the spectra for protons and deuterons.

The data analysis provides an estimate of ion energy distribution and temperature. By means of TPS calibration it is possible to determine the kinetic energy of different ions (protons, deuterons, etc.) distributed along the parabola lines and therefore reconstruct the whole spectrum [Sch14]. The fig. IV-11 shows as an example such reconstruction for proton emitted during the irradiation of a CD$_2$ target: the trend of the MCP brightness is shown as a function of the ion's kinetic energy obtained by means of magnetic deflection. The brightness of the traces is correlated with the number of particles.
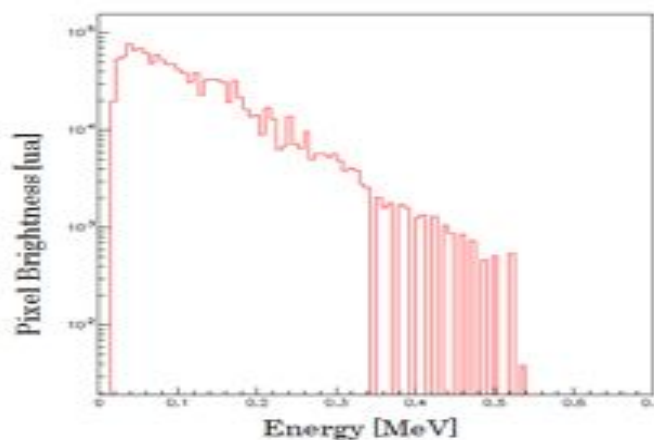
fig.IV- 11 Proton spectrum obtained by means of magnetic field.
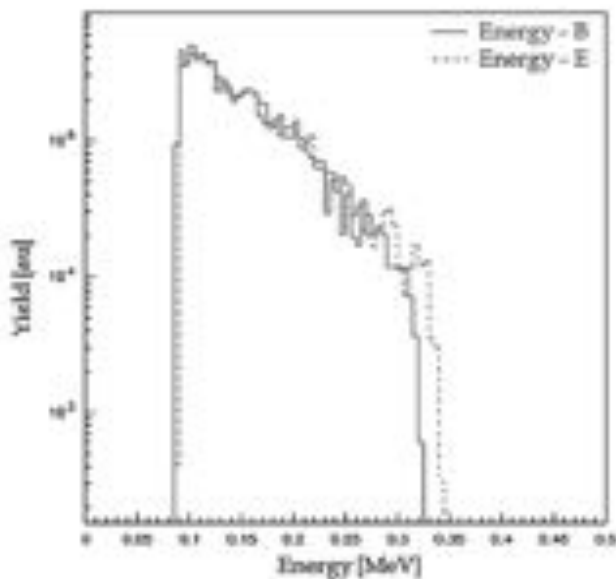
fig. IV-12. A simple proton spectra by mean of magnetic (solid line) and electric (dotted line) deflections. The trend of the MCP brightness is shown as a function of the ion's kinetic energy. The spectra are overlapped.

Assuming a Maxwell-Boltzmann distribution for the ions energy, the theoretical curve is given by the following equation [Hut87]:

$$J(E) = C(E)\exp(-\frac{E}{kT}).$$

By fitting the spectra one can calculate the ion temperature. Then, the coefficient C of the fit gives information related to the total number of ions.

IV.8 Data Analysis and Results

The objective of these preliminary experiments was to study and optimize the experimental set up to ELI-NP, which concerns the use of TNSA mechanism, discussed in chapter III. During the different measurements they have been used the targets in the following Table IV-1.

Table IV- 1 Targets characteristic used in Pisa measurements campaign.

	Chemical Elements	Thin (µm)
METAL	Ti	5
	Cu	8
	Al	2-3-6-10-12
PLASTIC	CH_2	3-6-10-12-23
	CD_2	10
PLASTIC+METAL	CH_2+Al	10
	CH_2+Au	12
	CH_2+Cu	10
	CD_2+Al	10

IV.9 Metal targets

We have studied the different metal layer targets during acceleration mechanism TNSA. The fig. IV-13 shows the trend of the maximum values of cut-off energies for protons (MeV) versus the target thickness of the aluminum values (2, 3, 6, 10 and 12 μm);
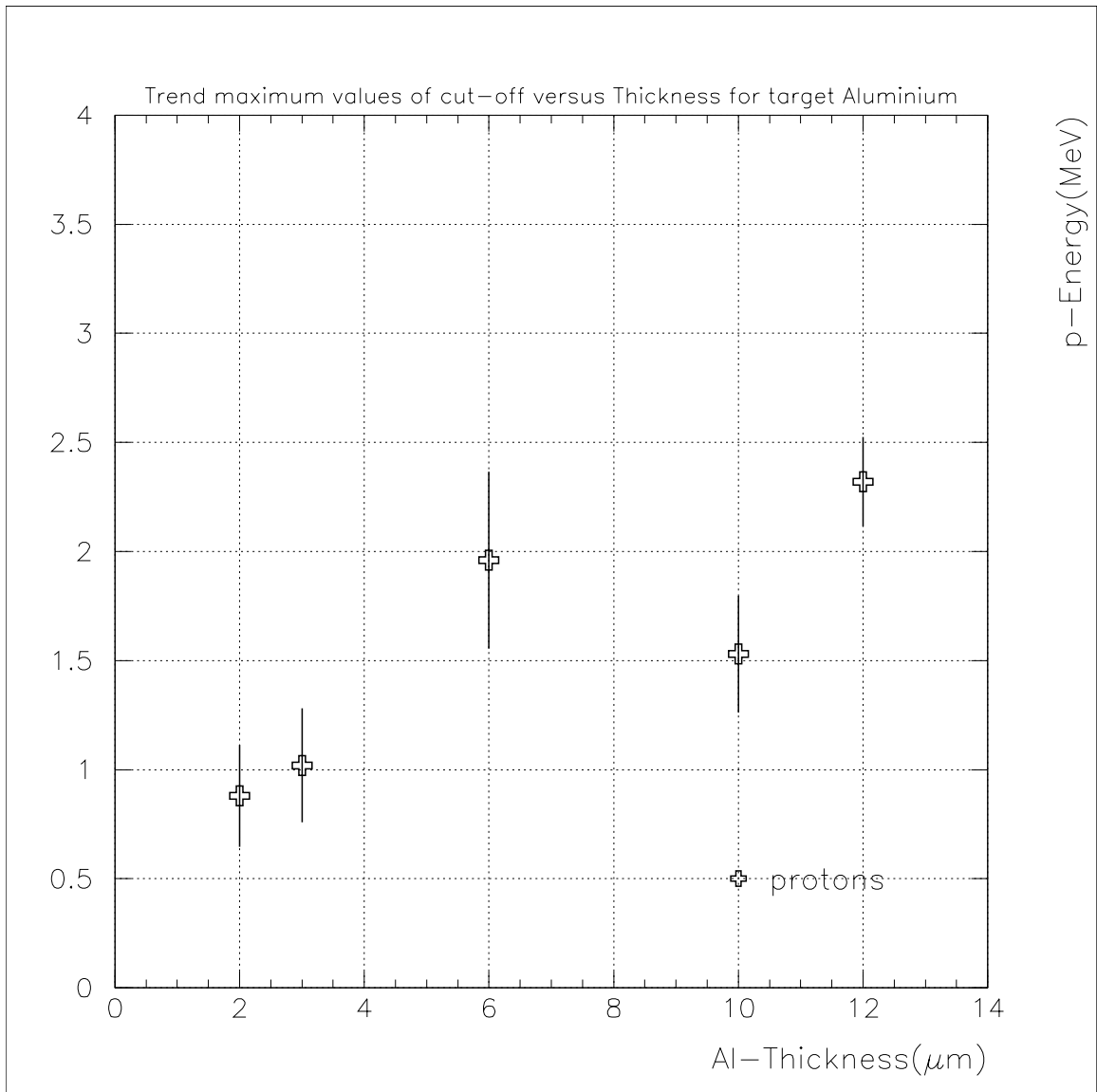
fig. IV-13 Trend off maximum values of Energy cut_off versus Aluminum thickness for protons.

The energy distribution trends for the target of 2-3 and 6 μm are the same; in fig. IV-14 for Al 2um thickness the distribution of protons cut off energy is shown.

Trend values of cut−off versus Zfocus for target=2μm Aluminium
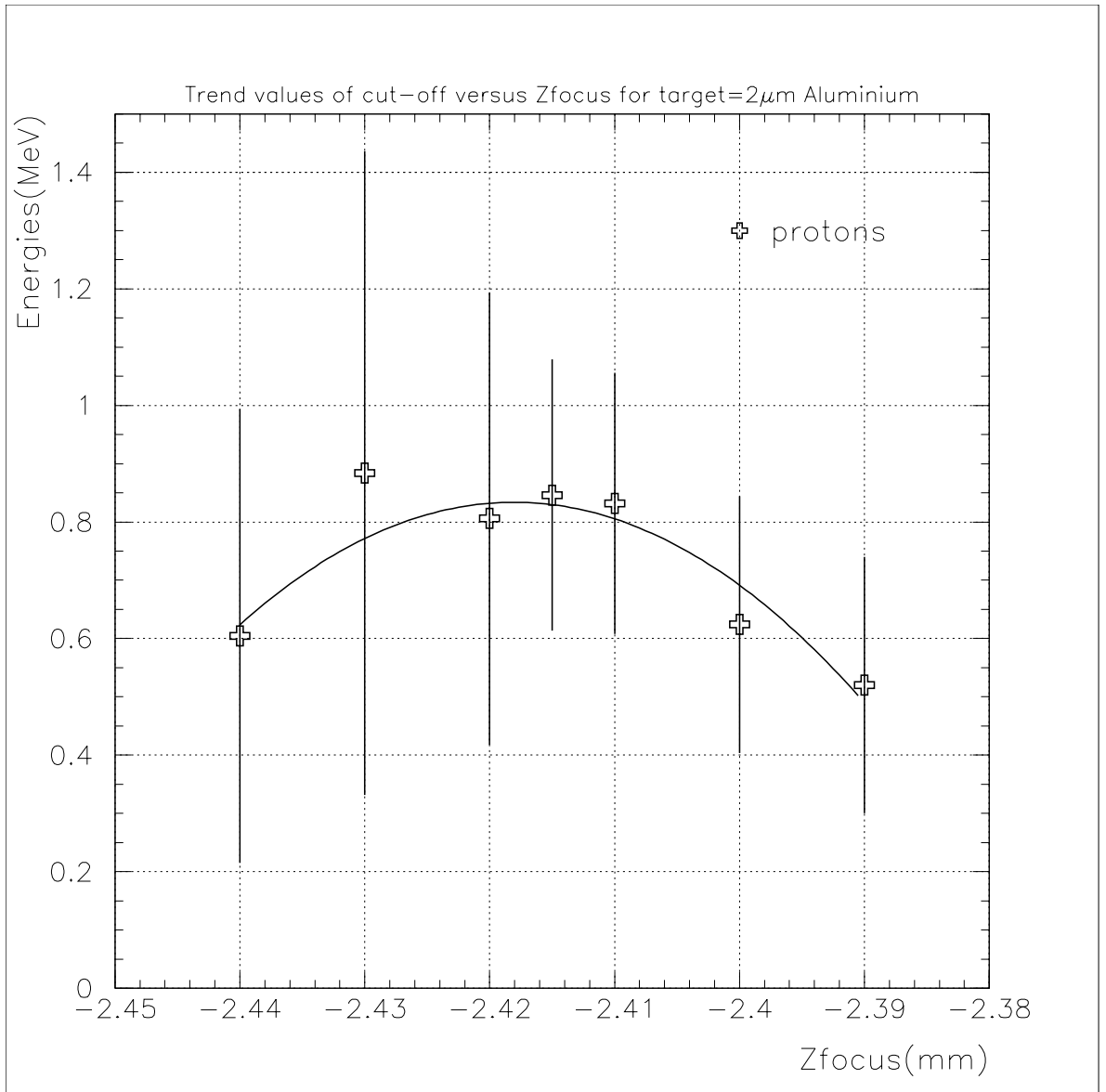
fig. IV-14 Distribution cut_off energy protons versus z-focus for aluminum 2 μm thickness

While for thicker target instead (as of 12 μm) is lost the characteristic pattern found previously in favour of a plateau. In the case of metal targets it was commonly assumed that protons originate from impurity layers on the target

surfaces and that they are accelerated by an electrostatic field generated by hot electrons. It is possible to justify this behaviour as follows: in the thick target accelerated ions have to travel through the material more losing much of their energy before being expelled. For each duration of the pre-pulse (ASE) exists an optimal thickness to which are achieved the higher energies, while the cut-off energies depend on the intensity of the laser.

IV.10 Atomic mass dependence

The fig. IV-15 shows the maximum cut-off energy for protons between different metal targets (Al, Ti and Cu), with similar thicknesses.
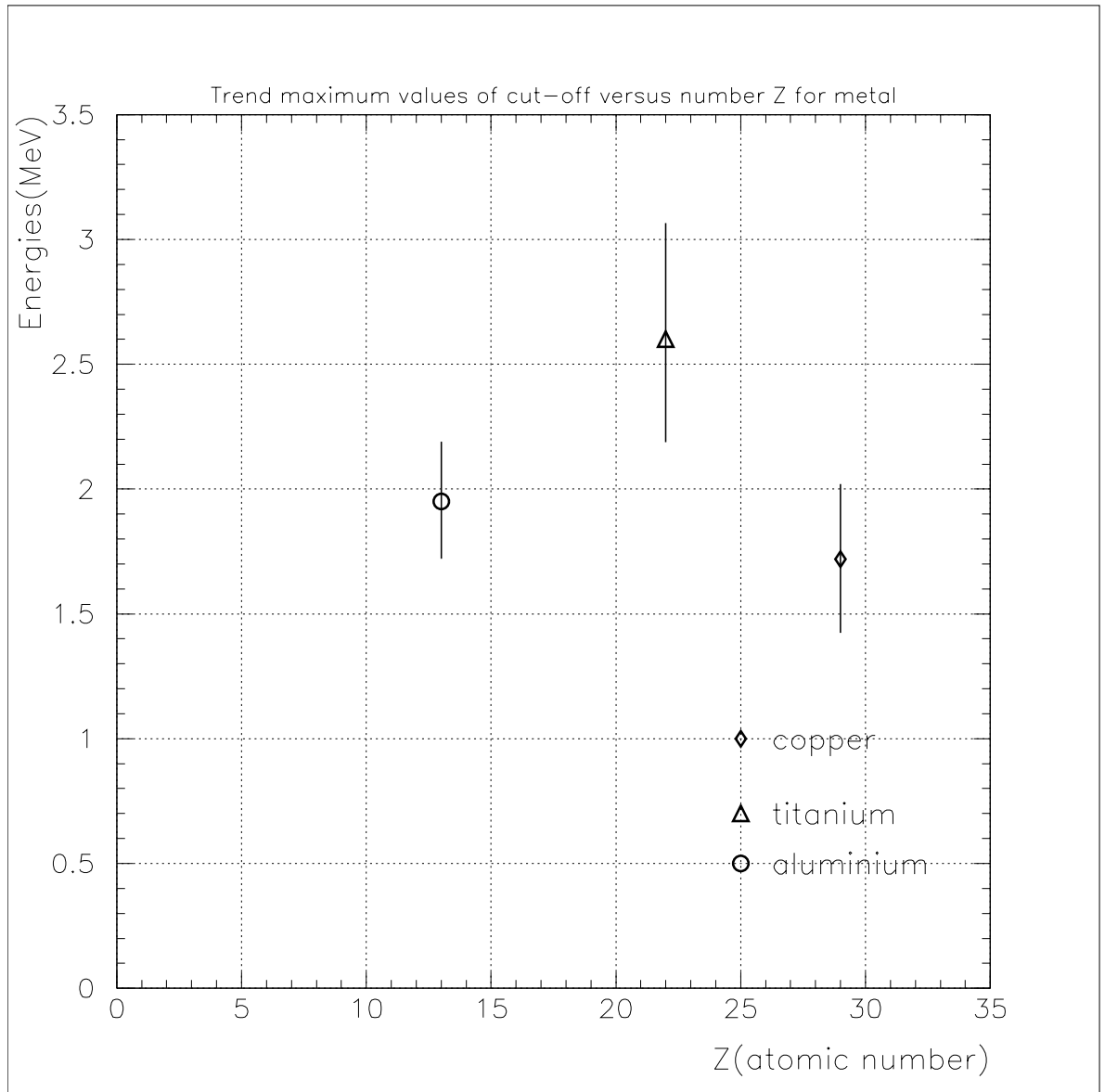
fig.IV-15 Comparison between different metal target maximum cut off versus atomic number. Titanium target has a thickness of 5μm and reaches a maximum energy of cut_off 2.6 MeV; Aluminium target has a thickness of 6μm and reaches a maximum energy of cut_off 1.9 MeV ; Copper target has a thickness of 8 μm and reaches a maximum energy of cut_off 1.7 MeV.

It is not clear dependence between atomic number and the production of fast electrons.

IV.11 Plastic targets

IV.11.1 Surface versus bulk dependence

The fig. IV-16 shows simple proton and deuteron spectra by mean of electric deflections; the spectra are overlapped.
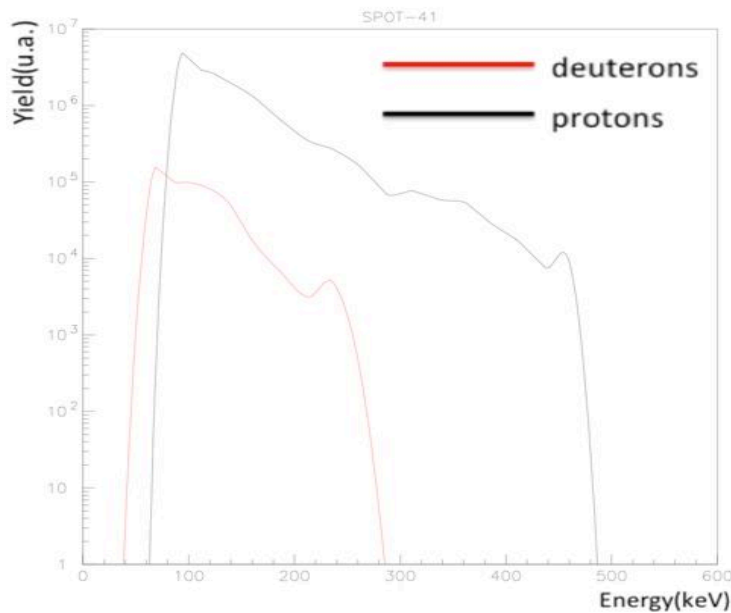
fig.IV-16 Comparison between deuterons and protons energy distributions.

The fig. IV-17 shows the comparison between the maximum energy obtained for the target of Al and CH_2; it can be observed that we obtain the highest energy protons in the metal target.

The trend of the maximum values of protons cut-off energies (MeV) in relation to the target thickness CH_2 (mylar) values (3, 6, 10, 12, 23μm) is shown in fig. IV-17.

In figures IV-13 and IV-17 is possible to observe that the maximum cut-off energy for protons is at 12 μm. In cases of CH_2 target the maximum energy increases up to an optimum thickness and then falls down with increasing target thickness.
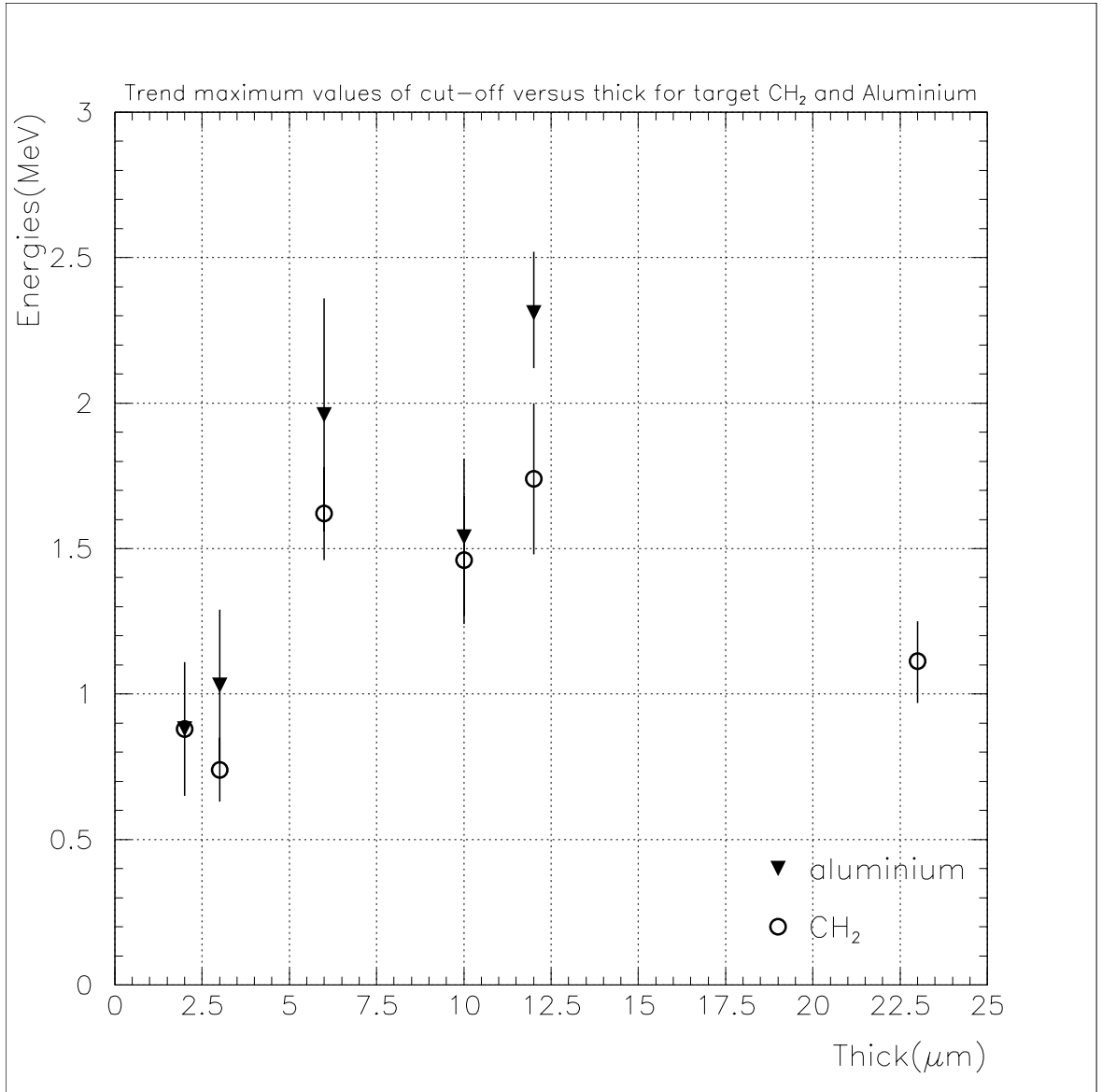
fig.IV-17 Comparison between aluminium and CH_2 target , maximum values of cut_off versus thickness

The accelerated ions, in target CH_2 and CD_2, whereas the accelerated carbon ions and deuterons from the production target are generated. The fig. IV-18 shows the maximum of the cut-off energy (for deuterons and protons) with CD_2 target (thickness 10 μm) in relation to the z-focus.
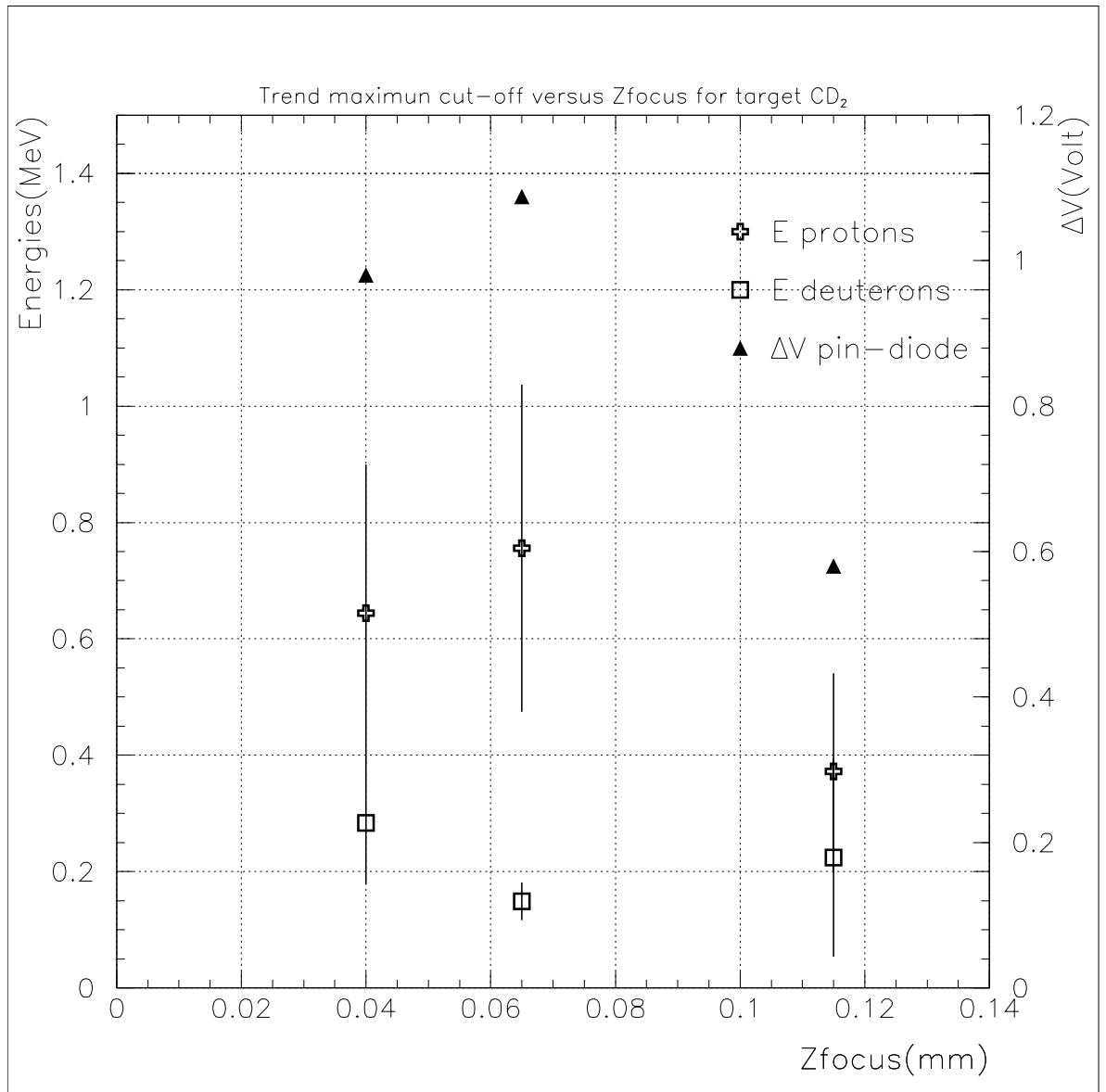
fig.IV-18 Trend maximum values of cut_off versus z-focus for target CD_2. The axis on the left indicates values of energy of the protons and deuterons; the axis on the right shows the pin-diode values.

.

In fig. IV-18 a pin-diode, which gives information X-rays emitted from the plasma, and it is used for monitoring the focal position. It can be observed that the optimum focus condition corresponds to the maximum cut-off energy for protons, while minimum for deuterons; protons and deuterons exhibit an opposite trend of maximum cut-off energies. The energy decreases moving away from best z-focus

for protons while increases for deuterons. In conclusion, the contribution of surface seems to prevail in the optimal z-focus, away from that location instead the two contributions (surface and bulk target) tend to equalize. [Tud16] The following figures IV-19 shows the yield versus Zfocus for target CD_2; to obtain these results, the spectra of protons and deuterons were integrated.
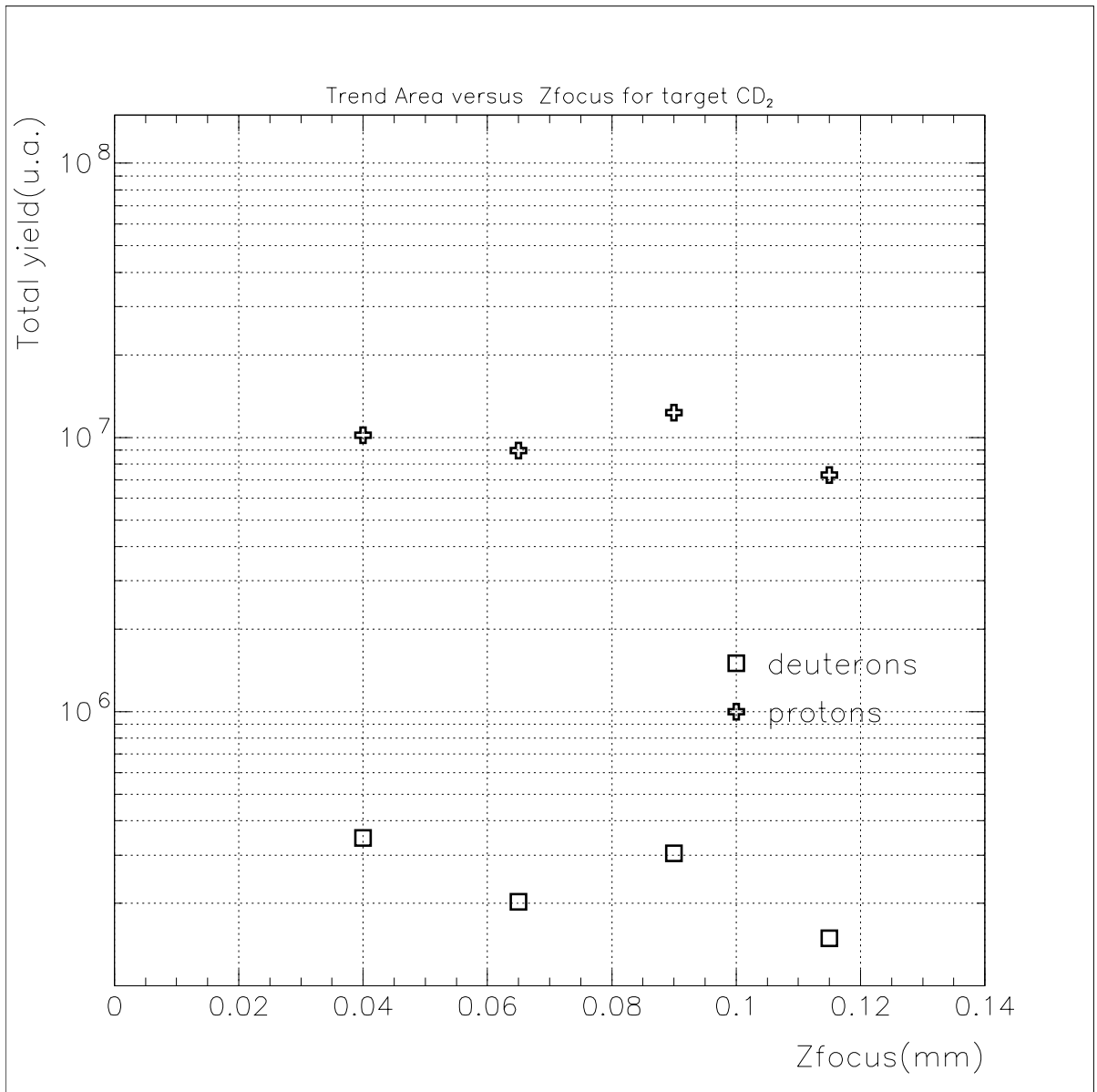
fig.IV-19 We call Area the integration of deuterons(or protons) energy distributions (see fig.IV-16). In this fig. we show the Area versus Z-focus for target CD_2. Protons(cross) and deuterons (square).

In fig. IV-19 the number of protons is much higher than the number of heavier deuterons, although the target was made of bulk CD_2. The protons result from the hydrocarbon contamination on the rear target surface. The above observation confirms that surface ion contribution is dominant with respect to volume contribution, as shown schematically in fig. IV-20 [Alt16]. It is possible that the protons are accelerated first and shield the heavier ions from electric field, coming later.
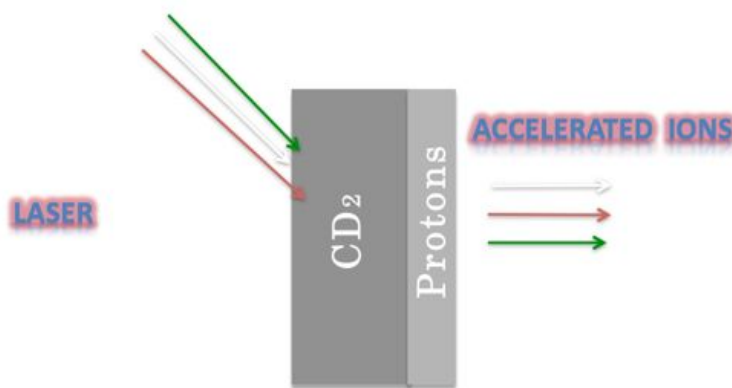
fig.IV- 20 Schematic representation of surface and volume emission

All these experimental evidence are explained by Radiation Pressure Acceleration (RPA) [Mac13]. For RPA, a sufficiently thin foil target is expected to be accelerated as a whole. The intense radiation pressure of the laser pulse pushes the surface of over-dense plasma inwards, steepening the density profile. For a realistic laser beam of finite width, the radiation pressure action drives a parabolic like deformation of the plasma surface allowing the laser pulse penetrating deeply into the target; this process is commonly named "hole boring" (HB), even when referring to a planar geometry, and it is associated with ion acceleration at the front side of the target. Experimental evidence of HB acceleration in solid targets is less clear at present [Ba04]. These results were interpreted using a model of "ponderomotive skin-layer acceleration" at the critical surface, a concept that sounds rather similar to HB-RPA. This process leads to the production of a narrow bunch of fast ions that penetrates into the plasma bulk. Hole Boring RPA applies to a "thick" target, i.e. much thicker than the skin layer in which ion acceleration by

the space-charge field occurs. The laser pulse penetrates deeper as far as adjacent surface layers are pushed into the target by a repeated cycle of ion bunch acceleration. The situation changes when a target is thin enough that all the ions are accelerated before the end of the laser pulse, i.e. a complete hole boring occurs. In such a case, the laser pulse is able to further accelerate ions to higher energies since the ions are not screened by background plasma anymore. The thin target regime of RPA has been named "Light Sail" (LS) as the term is appropriate to refer to a thin object of finite inertia, having large surface and low mass, so that it can receive a significant boost from radiation pressure[For84]. According [Esi04], in order for RPA to become the dominant acceleration mechanism the ions have to acquire relativistic energies already within one laser cycle, so that they can promptly follow electrons which are displaced in the longitudinal direction by the ponderomotive force. Later theoretical studies of such so-called Radiation Pressure Dominant (RPD) regime include Rayleigh-Taylor-like instability of the foil [Peg07] and the effects of radiation friction, which play a significant role at ultra-relativistic intensities [Tam10]. Of particular interest is the possibility of a self-regulated regime where the transverse expansion of the foil decreases the density along the axis allowing for an increase of the ion energy at the expense of the to number of accelerated ions [Bul10a],[Bul10b].

IV.12 Plastic + Metal Targets

In Table IV-2 it is possible to observe the increasing trend for cut-off energies of protons for CH_2 uncoated and CH_2 coated of Aluminium, with the same thickness target 10μm; same result, for CD_2 uncoated and CD_2 coated of Aluminium, with equal thickness target.

The effect of Al layer on the protons energies can be justified by the more efficient generation of hot electrons in Al than in plastic due to the higher electron density

in the interaction region, which can also compensate the increase of target thickness due to the 10um Al layer.

Table IV-2 Comparison between different targets with the same thickness (10mm). The values reported show that protons energies increase if CH_2 and CD_2 targets are coated with aluminum.

	CH_2	CH_2+Aluminium
Energy (MeV)	1.46 ± 0.11	1.49 ± 0.08
	CD_2	CD_2+Aluminium
Energy (MeV)	0.75 ± 0.28	1.73 ± 0.08

The Table IV-3 shows in two different columns, the deuterons cut-off energy for CD_2 and CD_2+Aluminium; it can possible to observe different trend of cut-off energies : it decreases for deuterons that come out from CD_2+Al target.

Table IV- 3 Deuterons cut-off energies trend versus CD_2 targets uncoated and coated with Al thickness (10μm)

	CD_2	CD_2+Aluminium
Energy_deuterons (MeV)	0.28 ± 0.06	0.43 ± 0.12
Total yield protons (u.a.)	$9.67 \ 10^6$	$1.82 \ 10^7$
Total yield deuterons (u.a.)	$2.51 \ 10^5$	$6.20 \ 10^5$

In the fig.IV- 21 the maximum cut-off energy versus different thicknesses is compared for the targets mylar+metal and CD_2(mylar). Various metals were used: copper, aluminum and gold; the trend of the target mylar + metal follows the trend of the mylar target.
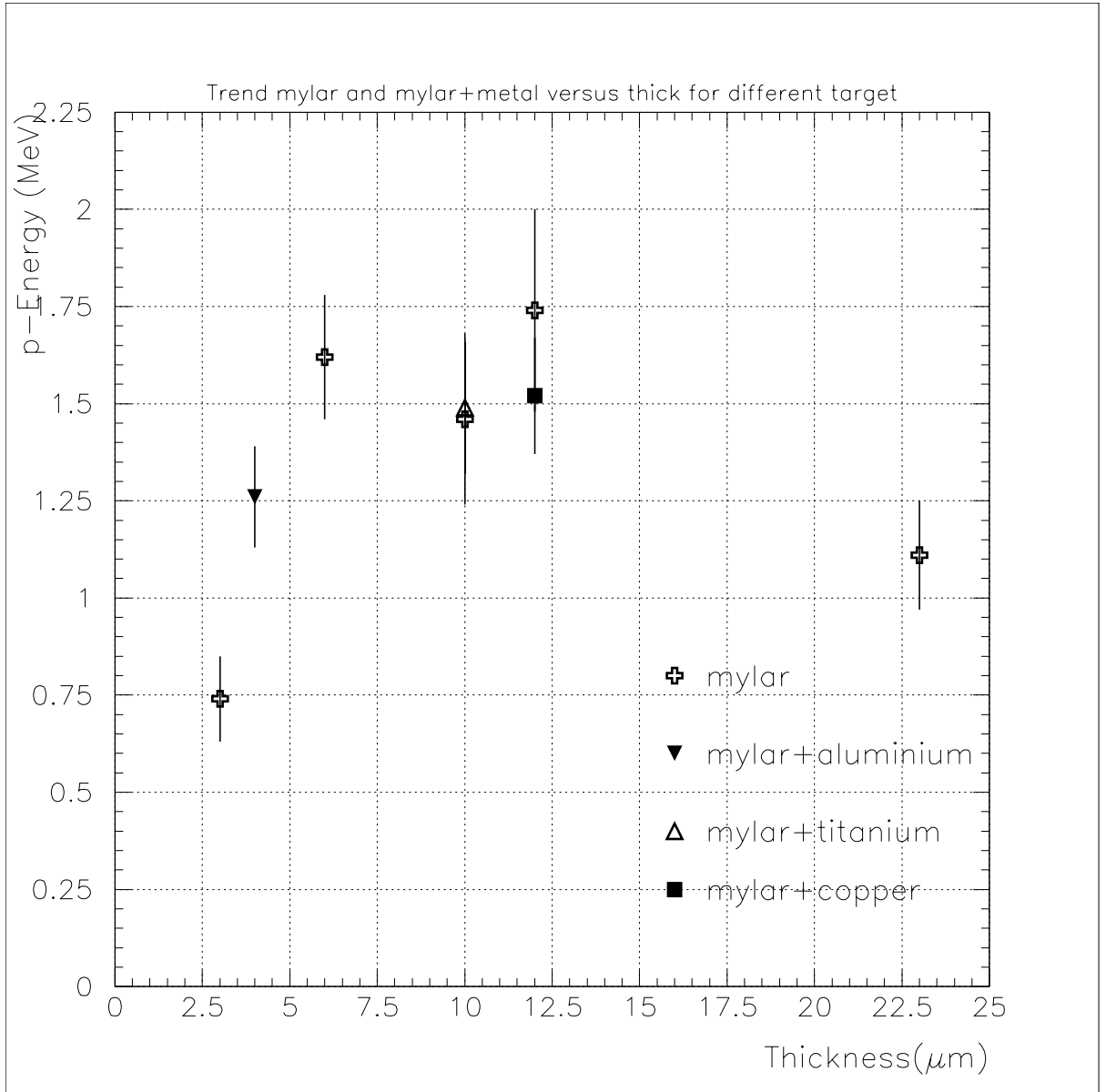
fig.IV-21 Comparison between CD₂ ,and CD₂ + metal targets at maximum values of cut-off energy versus thickness, There are different metal with various thickness: aluminium, titanium and copper.

.

IV.13 Carbon Ions Analysis

In the following analysis, we focalise our attention on the carbon ions comparing the data with 4 different targets: CH_2, CD_2, $CH_2 + Al$ and $CD_2 + Al$.

Figure IV-22 shows an example of such the detected ions coming from CD_2 target.

(a)

(b)
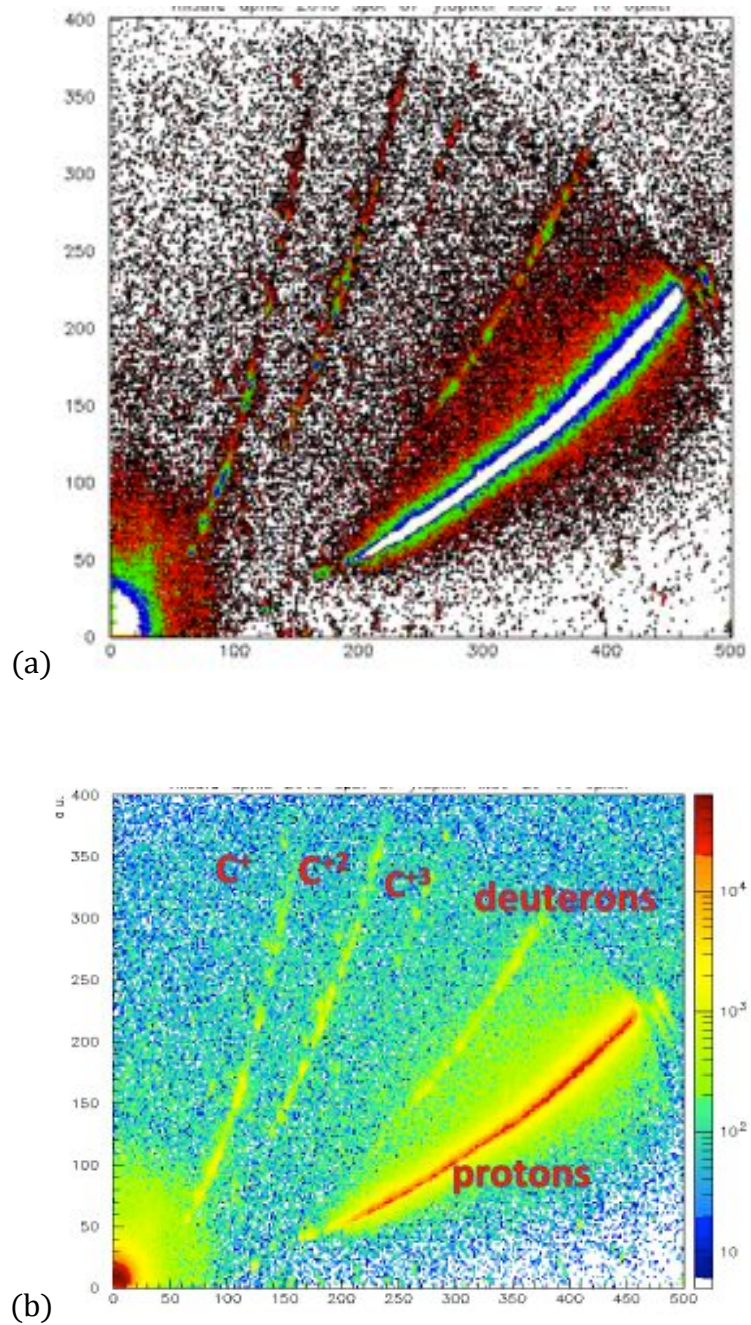
fig.IV-22   2D-histograms from TPS before analysis (a) and after (b) with line parabolic of five different charges: carbons ions (+1,+2,+3), deuterons and protons.

The analysis was conducted for all the identified species, by using a graphical cuts procedure. The selected events has been projected on the electric and magnetic field axis, as shown in fig. IV-9 and described in paragraph IV-7.
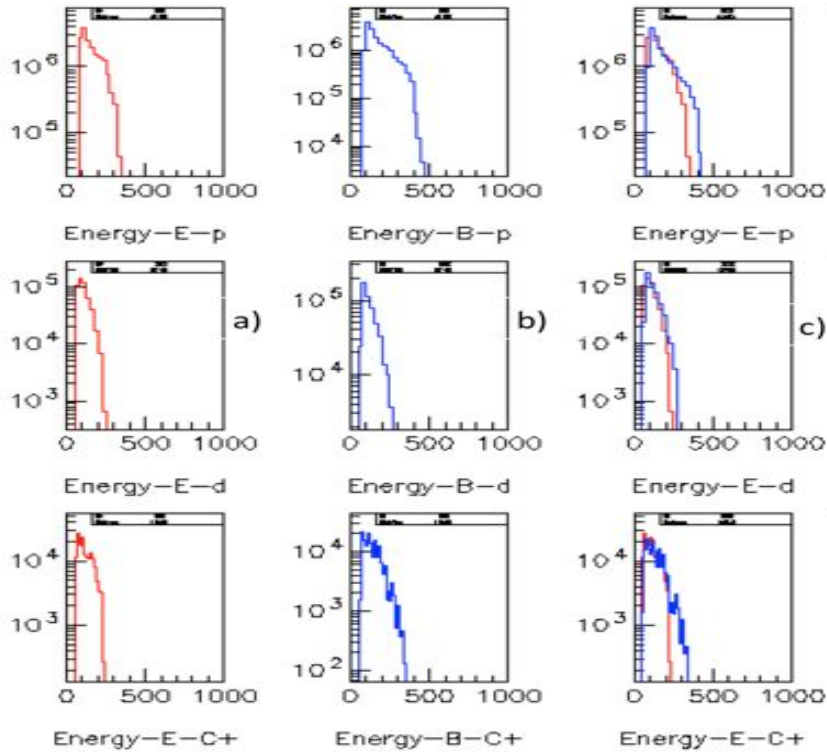
fig.IV- 23 These pictures show the yields for : protons(first line top-down), deuterons(second line top-down), carbon charge states(third line top-down). a) Energy (keV) projection on the electric field; b) Energy (keV) projection on the magnetic field; c) overlapping of previous Energy projections to identify differences between the two yields.

After the calibration phase of the two axis and a fast superposition of the obtained spectra to verify misalignment, we got the energy spectra of the different species. In fig. IV-24 we show an example of the obtained carbon energy spectra, by projecting on the electric field axis.
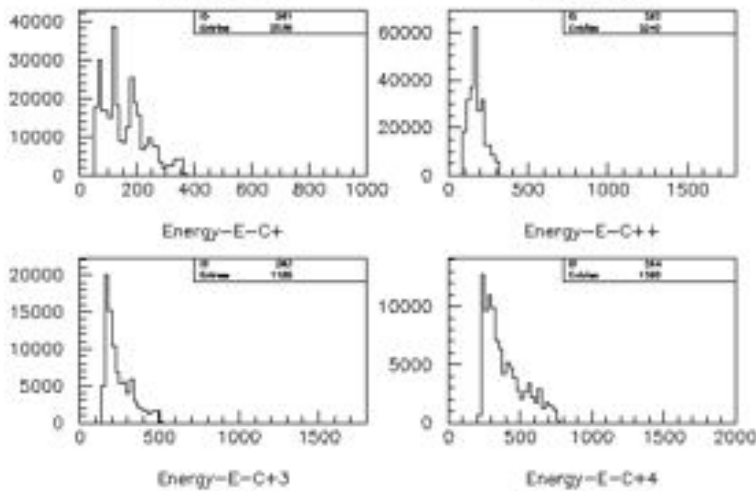
fig.IV- 24 Projection on the electric field axis for different carbon charge state.

In fig. IV-25 we show overlap spectra to display the Coulomb shift effect. Such spectra are related to the CD_2 target. As can be notice, each spectrum presents an energy threshold, which is shifted versus the higher energies in relation to the different charge state.
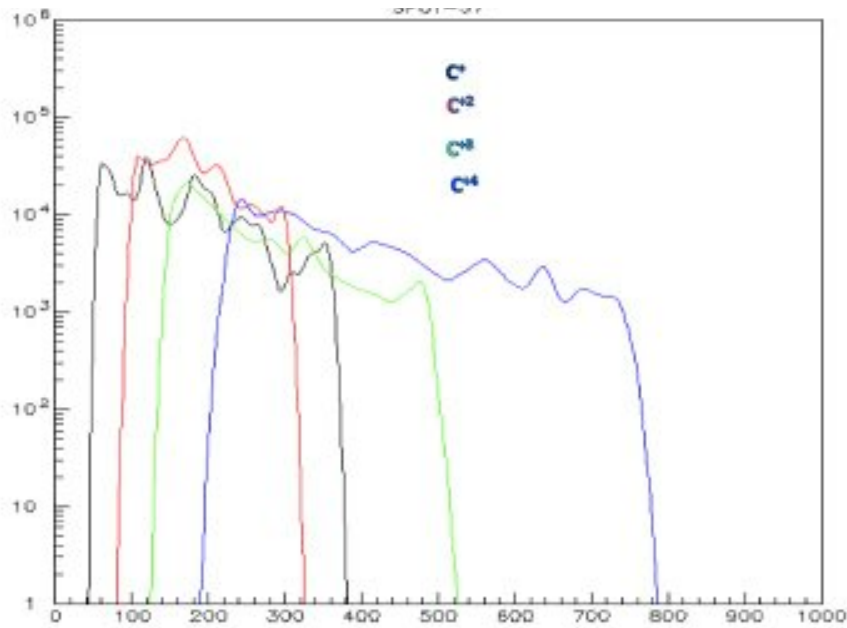
fig.IV- 25 This picture shows overlap Carbon (C^+,C^{+2},C^{+3} and C^{+4}) spectra showing the Coulomb shift. The x axis shows Energy of electric field (keV), the y axis shows yields (u.a.).

Such shift scale seams in agreement with following relation $E_{Th} = q\ V_c$ where q is the charge state and V_c is a Coulomb potential the acceleration Coulomb potential which has been estimated in the order of 40-45 keV.

In the next figure, it was calculated potential, at different z-focus, like slope between energy versus the charge states. For example the following were analyzed for the target CD_2 with z-focus=0.04mm.
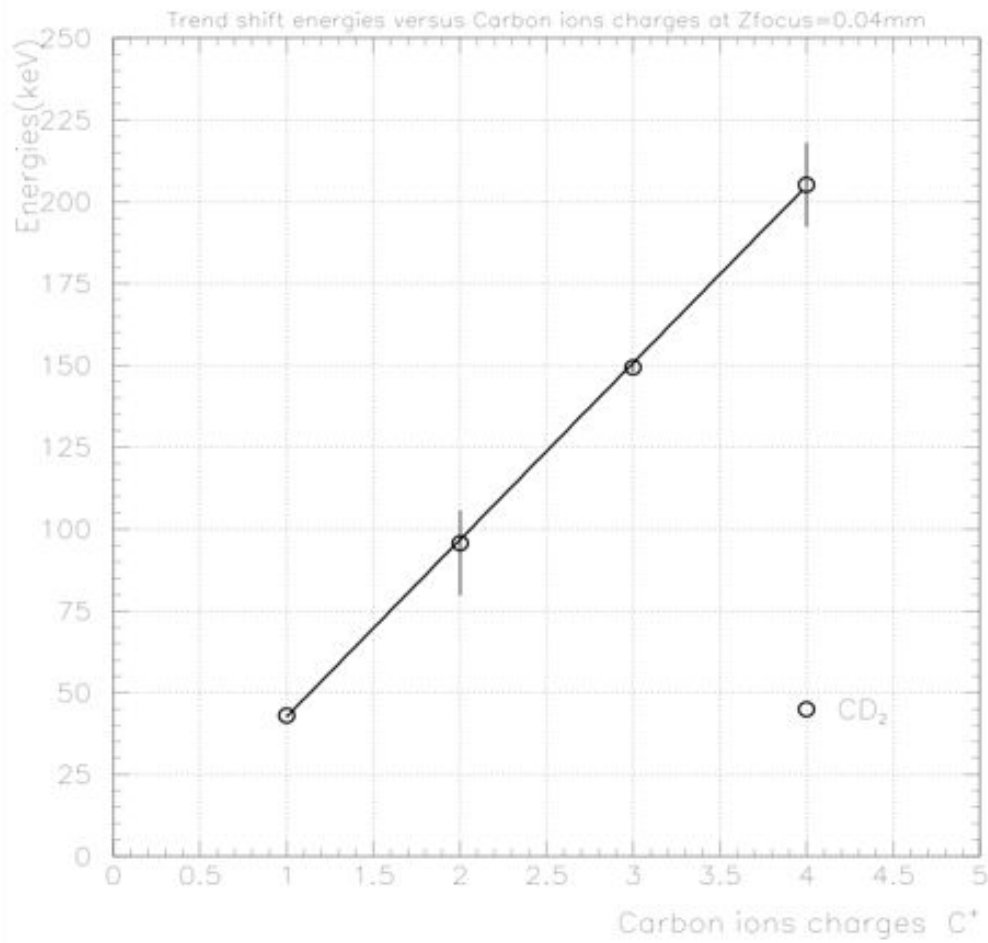
fig.IV- 26 *Energy distribution versus different carbon's ions at z-focus=0.04; the best straight interpolated is y=54,307 X -13,2.*

The next graph shows the potential versus z-focus for target CD_2; the comparison was made with the pin-diode.
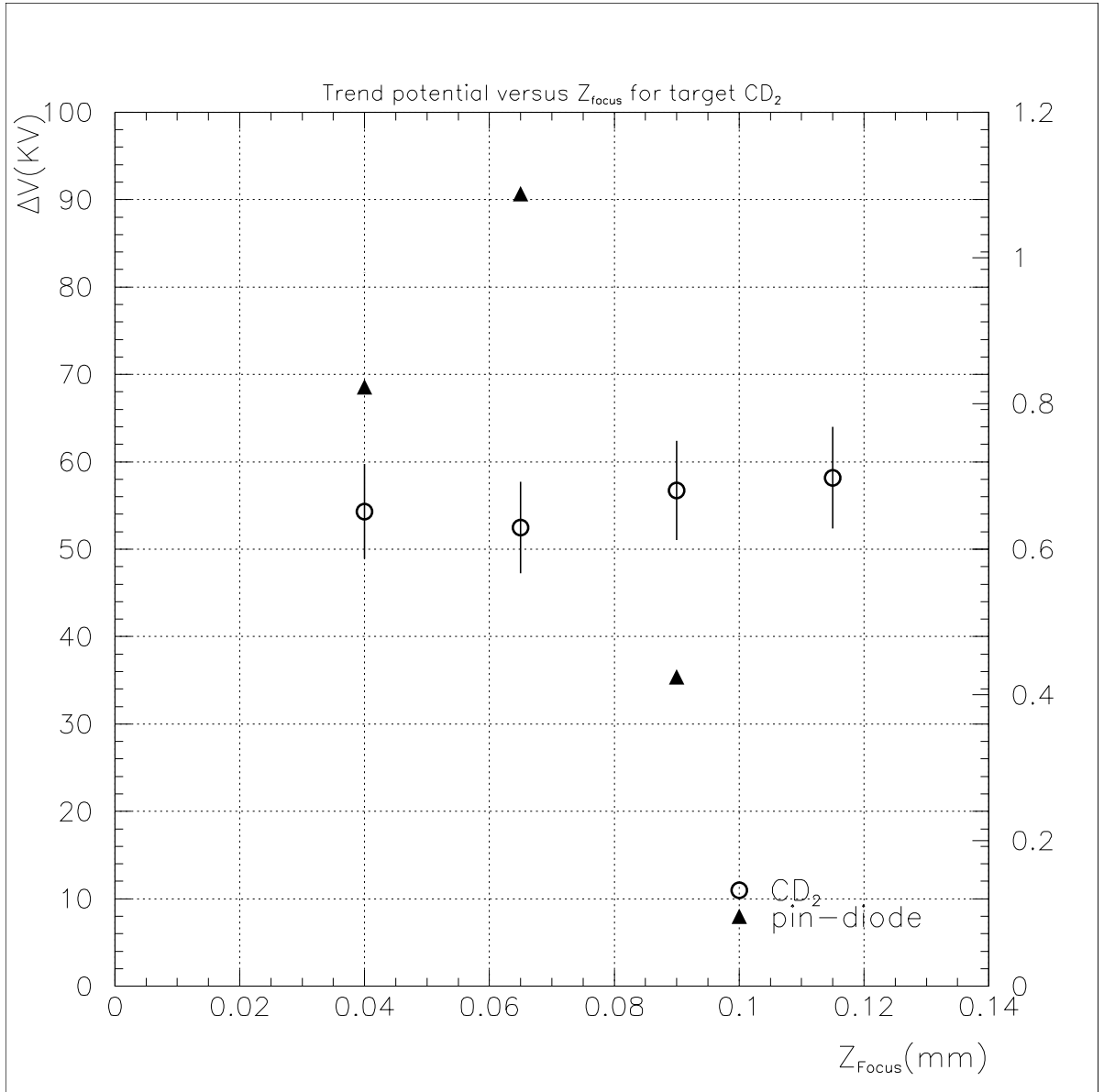
fig.IV- 27 Trend shift Potential versus z-focus with target CD₂. Different scales for axis Y have been plotted : left scale (KV) for Potential and right scale (Volt) for Pin Diode.

The different carbons spectra were successively integrated in order to got information on total yield, assuming an independence of the light detected on the phosphor screen from the charge state detected.

The result of such procedure is reported in fig. IV-28 as a function of the z-focus parameter. The total yield is in agreement with the pin diode trend, which indicates the position of the best focus. We also observed how the much higher intensity is at the opposite of trend shift energies versus z-focus.
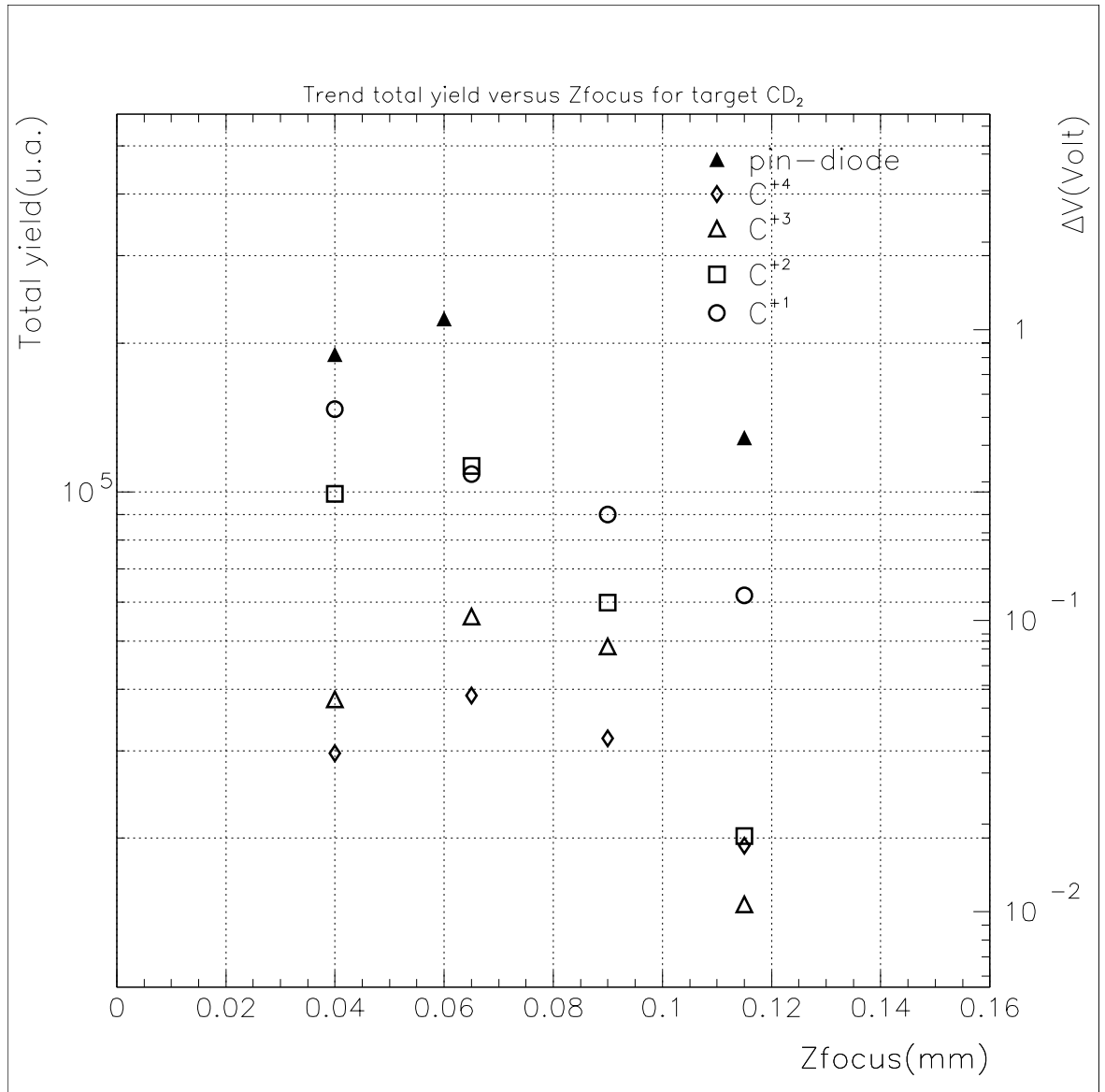
fig.IV- 28 Trend Area versus z-focus target CD₂, for different carbon states, according to pin-diode. Different scales for axis Y have been plotted : left scale (a.u.) for Energy Integration Area and right scale (Volt) for Pin Diode.

The same procedure, for CD_2 target, has been done for the CH_2 target at energy analysis. Also in the fig.IV-29 it is shown the trend of Coulomb potential versus z-focus for CH_2 target.
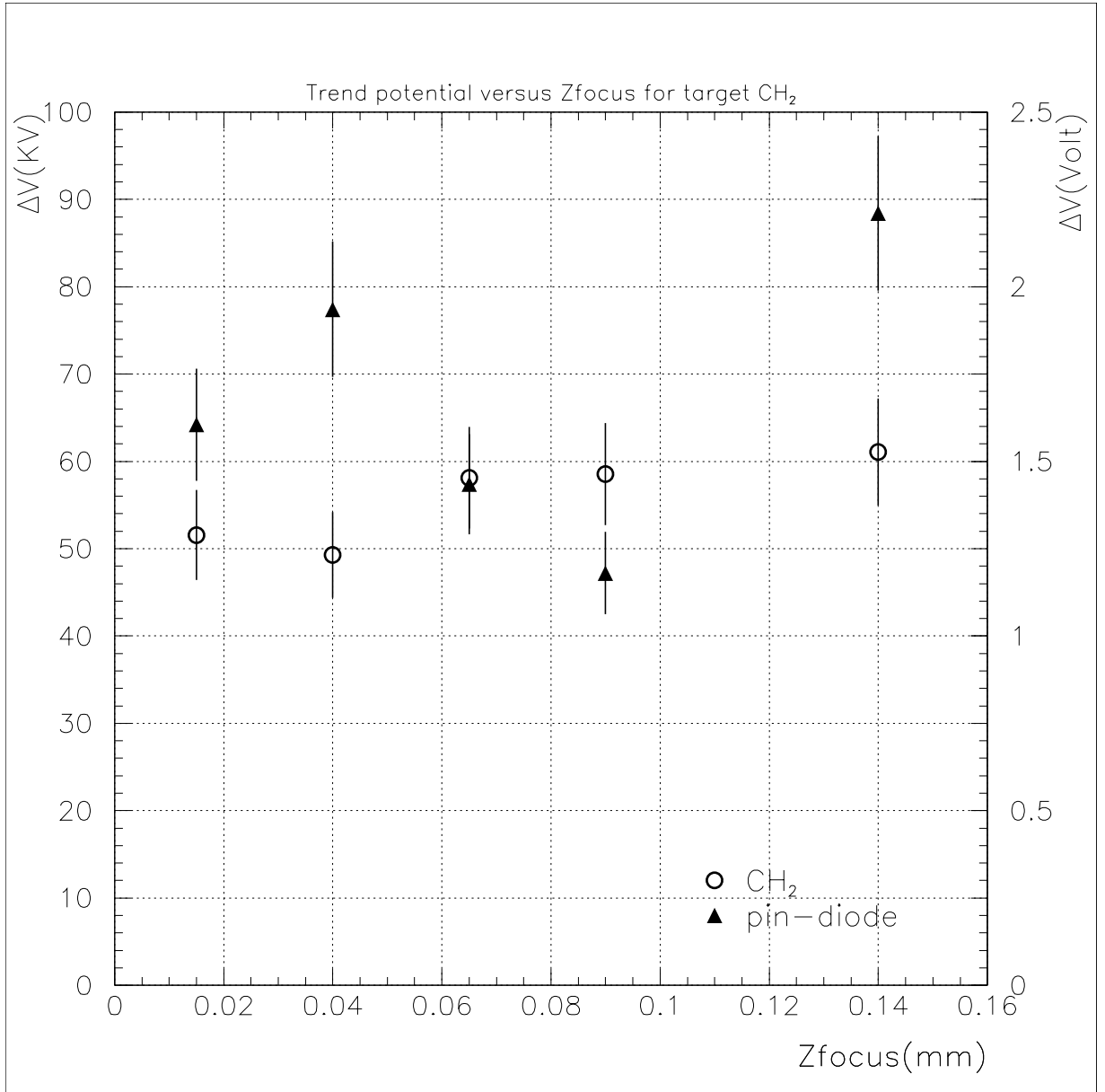
fig.IV- 29 A comparison between Potential and Pin-diode distribution. Different scales for axis Y have been plotted : left scale (KV) for Potential and right scale (Volt) for Pin Diode.

Similarly the yield of CH_2 target follows the pin diode trend. Also in this case the area trend is at the opposite of trend shift energies versus z-focus.

The same procedure, for CD_2 and CH_2 targets, has been done for the $CH_2 + Al$ target at energy analysis. The next figure indicates the potential versus z-focus for the target $CH_2 + Al$; the sketch summarizes the data analysis done previously, for the other target.
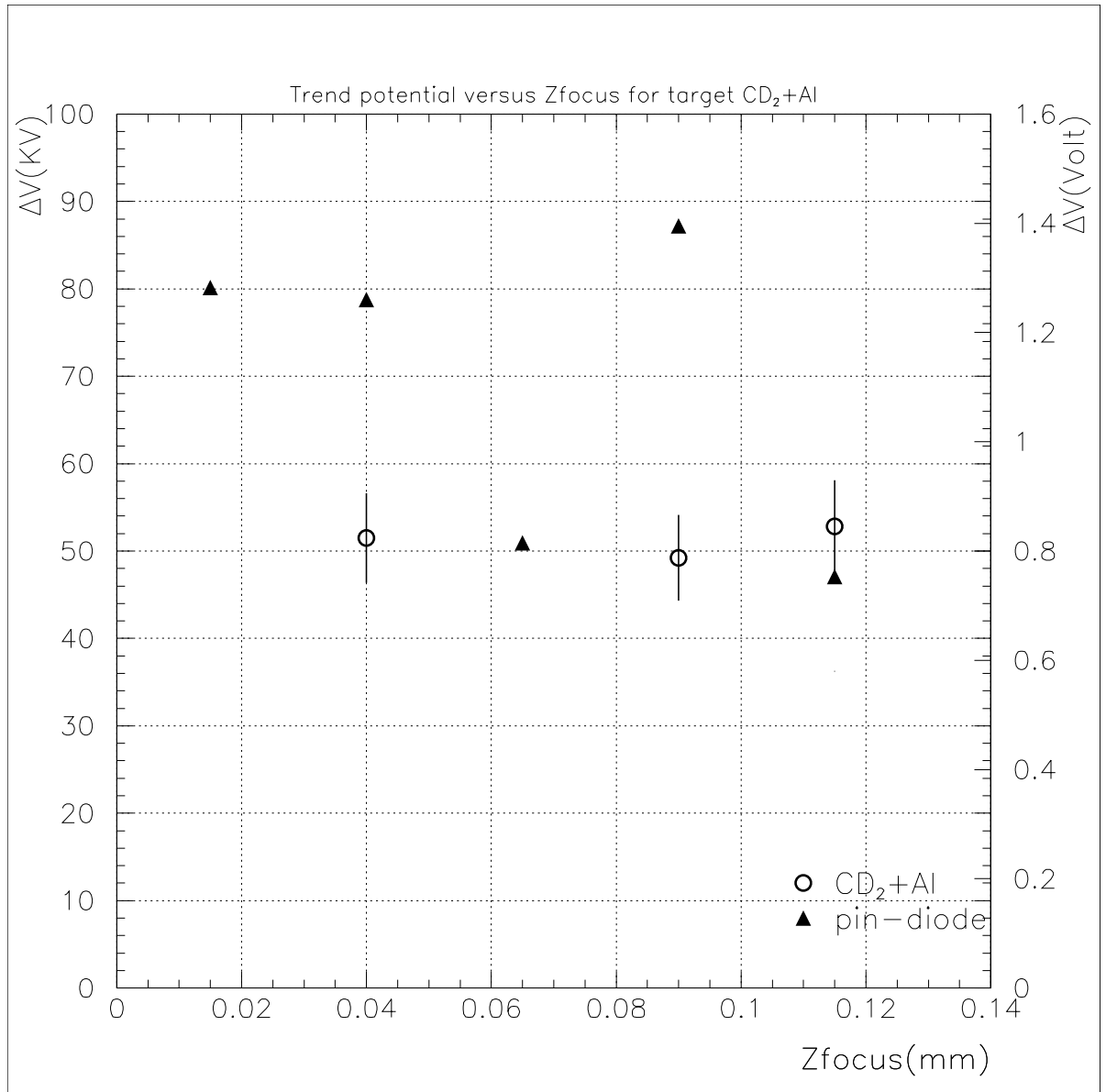
fig.IV- 30 Trend of Potential versus z-focus with target CD₂ + Al. Different scales for axis Y have been plotted : left scale (KV) for Potential and right scale (Volt) for Pin Diode.

The fig. IV-31 shows, the trend of the area values of carbon ions energy (u.a.) in relation to z-focus.
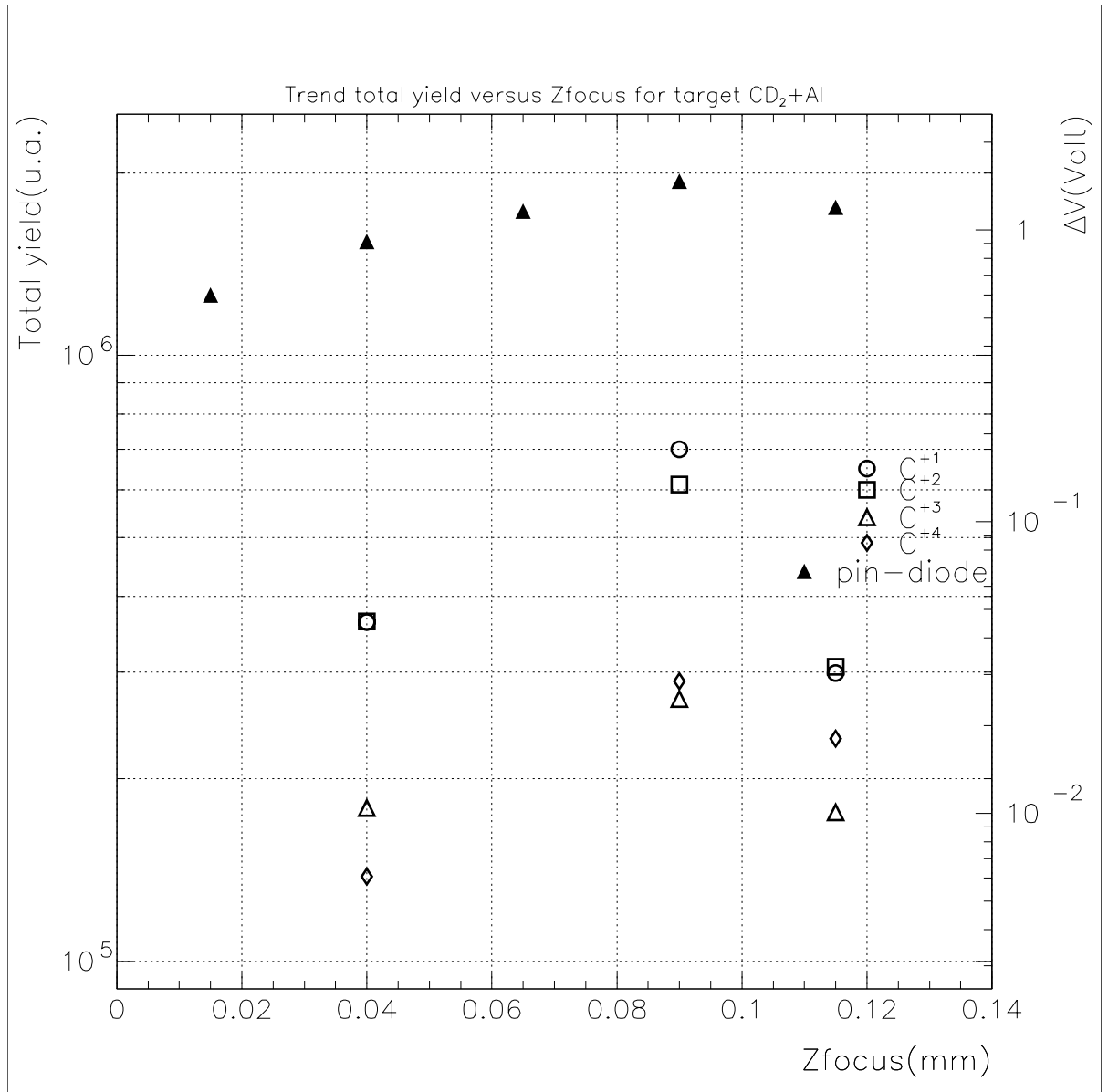
fig.IV- 31 Trend Area versus Z-focus target CD_2 + Al for different carbon states, according to pin-diode. Different scales for axis Y have been plotted : left scale (a.u.) for Energy Integration Area and right scale (Volt) for Pin Diode.

The next figure indicates the potential versus z-focus for the target CH_2 + Al; the sketch summarizes the data analysis done previously, for the other target.
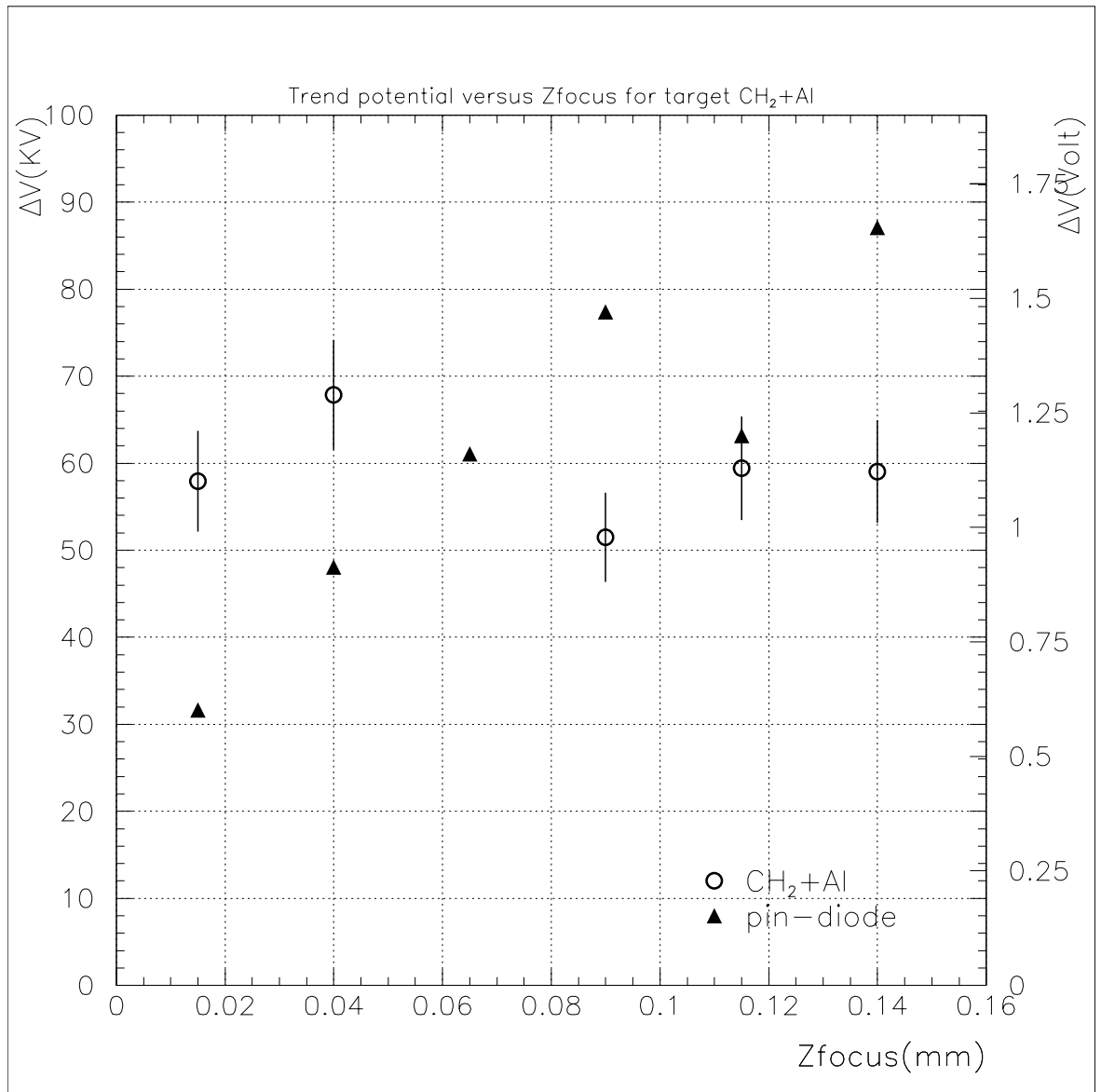
fig.IV- 32 Trend shift energies versus Z-focus with target CH_2+ Al for different Carbon states.

The Table IV-4 shows four different columns; the potential increases that come out from CH_2 and CH_2+Aluminium targets.

Table IV- 4 Maximum value of potential, total yield C^+ and total yield C^{+2} versus different targets.

	CD_2	CH_2	CD_2+Al	CH_2+Al
Potential (KV)	58.17 ± 0.46	61.07 ± 0.45	52.84 ± 0.47	62.84 ± 0.44
Total yield C^+ (a.u.)	$1.55 \ 10^5$	$3.12 \ 10^5$	$6.99 \ 10^5$	$1.09 \ 10^5$
Total yield C^{+2} (a.u.)	$1.13 \ 10^5$	$2.59 \ 10^5$	$6.12 \ 10^5$	$1.17 \ 10^5$

IV.14 References

[Rob08] A.P.L. Robinson et al., New J. Phys. 10 (2008) 013021

[Tud16] Tudisco at al.; Investigation on target normal sheath acceleration through measurements of ions energy distribution Review of Scientific Instruments 87, 02A909; http://dx.doi.org/10.1063/1.4934691 (2016)

[Alt16]Altana et al., Investigation of ion acceleration mechanism through laser-matter interaction in femtosecond domain, Nuclear Instruments and Methods in Physics Research A 829 (2016) 159–162, http://dx.doi.org/10.1016/j.nima.2016.02.016 (2016)

[Bad04]Badziak, J., S. Glowacz, S. Jablonski, P. Parys, J. Wol owski, and H. Hora (2004), Appl. Phys. Lett. 85, 3041.

[For84]Forward, R. L. (1984), J. Spacecraft 21, 187.

[Esi04]Esirkepov, T., M. Borghesi, S. V. Bulanov, G. Mourou, and T. Tajima (2004), Phys. Rev. Lett. 92, 175003.

[Peg07] Pegoraro, F., and S. V. Bulanov (2007), Phys. Rev. Lett. 99, 065002.

[Tam10] Tamburini, M., F. Pegoraro, A. D. Piazza, C. H. Keitel, and A. Macchi (2010), New J. Phys. 12, 123005.

[Bul10a]Bulanov, S. V., E. Y. Echkina, T. Z. Esirkepov, I. N. Inovenkov, M. Kando, F. Pegoraro, and G. Korn (2010a), Phys. Plasmas 17, 063102.

[Bul10b]Bulanov, S. V., E. Y. Echkina, T. Z. Esirkepov, I. N. Inovenkov, M. Kando, F. Pegoraro, and G. Korn (2010b), Phys. Rev. Lett. 104, 135003.

[Mac13] Macchi et al: Rev. Mod. Phys. 85, 751 ,doi:https://doi.org/10.1103/RevModPhys.85.751(2013)

[Baf14]F. Baffigi, G. Cristoforetti, L. Fulgentini, A. Giulietti, P. Koester, L. Labate, L.A. Gizzi, Physics of Plasmas 21 (7) (2014) 072108, http://dx.doi.org/10.1063/ 1.4886977.

[Har08]K. Harres et al., Rev. Sci. Instrum., vol. 79, 093306, 2008.

[Jun11]D. Jung et al., Rev. Sci. Instrum., vol. 82 , 013306, 2011.

[Cob11]J.A. Cobble et al., Rev. Sci. Instrum., vol. 82, 113504, 2011.

[Giz16] L.A. Gizzi, et al. "Role of laser contrast and foil thickness in target normal sheath acceleration"Nuclear Instruments and Methods in Physics Research A829, 144–148 (2016)

[Rhe84]M. J. Rhee, Compact Thomson spectrometer, Rev. Sci. Instruments 55 (8), August 1984.

[Har08]K. Harres et al., Development and calibration of a Thomson parabola with microchannel plate for the detection of a laser-accelerated MeV ions, Rev. Sci. Instruments **79,** 093306 (2008).

[Sch14]F. Schillaci et al. JINST, vol. 9, T10003, 2014.

[Hut87]I. H. Hutchinson, Principles of Plasma Diagnostics, Cambridge University Press, Cambridge, (1987).

[Alt16]C.Altana et al.,Review of Scientific Instruments 87,(2016)

[Jac75] J.D. Jackson, Classical Electrodynamics, John Wiley & Sons, Inc., 1975.

[Rus00] G. Russo, Classical Electrodynamics, lectures notes.

CHAPTER V

ELI-NP DETECTORS

V.1 Experimental methodology @ELI-NP

As we mentioned in Chapter III to perform the proposed experiments, providing relevant data concerning the afore mentioned reactions and others, we aim to take advantage from the excellent and unique performance of the ELI-NP facility and realise an experimental set-up where two laser beams generate two colliding plasmas. The reaction products (neutrons and charged particles) will be detected through a new generation of plastic scintillators wall and through a new silicon carbides wall. The sketch of this configuration is drawn in fig.V-1.
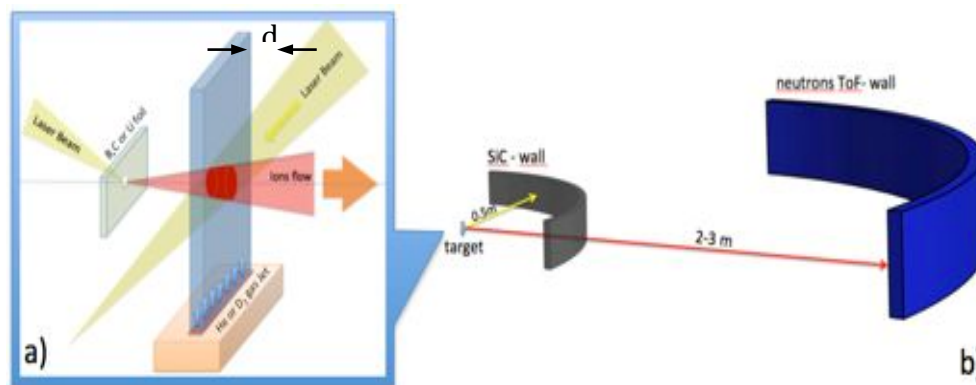
fig. V- 1 Layout of the experimental set up. a) Target configuration, the main laser pulse impinging on B, C or Li thin foil generates a primary plasma which impacts on a second plasma slab produced through the interaction of a secondary laser pulse on a He or D_2 gas jet target. b) Layout of the detectors configuration; the set-up combine high granularity SiC charged particles detectors (in vacuum) and a new generation of neutrons time-of-flight detectors (in air).

A first laser pulse imping on a ^{13}C, ^{7}Li or ^{11}B solid thin target (few micro-meters) producing, through the well-known TNSA (Target Normal Sheath Acceleration) acceleration scheme, boron, carbon or lithium plasma. The rapidly streaming plasma impacts on a secondary plasma, prepared through the interaction of a second laser pulse on a gas jet target (made by ^{4}He, D_2 or ^{3}He). The produced ions (intensity 10^{18}-10^{20} W/cm^2) expand along a cone, whose axis is normal to the target surface, with a low emittance. The experimental observations are well described and predicted by theoretical models ([Pas08] and ref.). The total number of accelerated ions obviously depends on the target composition [Mac13], but we can estimate that it roughly corresponds to the removed mass from target.

The unique opportunities provided by ELI-NP (high rep. rate and peta-watts laser) to operate in the TNSA domain (few 10^{18} W/cm^2) in order to ensure, by using large focal spots, the production of a *very large flux* of ions.

As already mentioned before, after the production, B, C or Li ions forward-streaming towards the gas-jet made by ^{4}He, D_2 or ^{3}He. There, a second laser pulse synchronized with the first one, can be used to obtain a helium or deuterium (depending on the reaction under analysis) plasma with a low centre of mass velocity, but with densities ranging in the 10^{18} - 10^{20} ions/cm^3 domain [Sch12]. High plasma densities are expected.

The proposed activity requires also the construction of a highly segmented detection system for neutrons and charged particles. The segmentation is required for the reconstruction of the reaction's kinematic. In the next two paragraphs characteristics and kinds detectors for Scintillators and Silicon Carbide detectors will be illustrated.

V.2 Neutrons Detectors

The "ideal" neutron detection module for reaction's kinematic studies must have:

- high efficiency,
- good discrimination of gammas from neutrons,

- good timing performance for ToF neutron energies reconstruction.

In addition, it must be able to work in *hard environmental conditions*, like the ones established in the laser-matter interaction area. Good part of these aspects may be met by configuration based on plastic scintillators.

Very recently, the possibility of manufacturing plastic scintillators with efficient neutron/gamma pulse shape discrimination (PSD) was demonstrated at the LLNL laboratory [Zai12] by using a system of a PolyVinylToluene (PVT) polymer matrix loaded with a scintillating dye, 2,5-diPhenylOxazole (PPO) and at INFN-PD by using PolySiloxane [Dal12]. First characterization results show that PSD in plastic scintillators can be of similar magnitude or even higher than in standard commercial liquid scintillators. The result is a consequence of the large amount of scintillation dying material used in the polymer, a possibility never tested in the past.

Another recent result obtained by our collaboration is the implementation of new photo-detectors based on silicon technology (Silicon PhotoMultipliers SiPM) [Pri08]. These are now commercial devices, characterized by a high photo-detection efficiency, high gain, single photon sensibility, excellent timing performance, low operative voltage and insensitivity to large electric and magnetic fields. These make such devices particularly suitable for applications in severe environmental conditions, such as those ones foreseen around the laser-matter interaction area at the future ELI-NP facility.

A third important aspect is the signal processing, for which a relevant expertise has been developed within our collaboration [Cav13]. We propose to implement a totally digital acquisition of the multi-hit signals foreseen in the proposed physics case. This is based on the use of commercial digitizers, developed in collaboration with the CAEN (Italy) company, and ad-hoc read-out software.

These basic technologies will be the pillars of our proposed detection system (see fig.V-2). It consists on an array of about 400 modules, each including one 25 cm^2 area scintillator, 5 cm thick, one SiPM and a digital read-out channel. This allows for a modular structure with easily adapted configurations around the interaction

area. As an example, at 2 m distance the total efficiency is estimated as large as about 18 % for 2 MeV neutrons and 6% for 13 MeV neutrons [Dro80]. In such conditions, the array can detect up to about 10^5 neutrons per shot, which represents a challenging demand for measurement at ELI-NP. Efficient digital shape analyses can handle a multi-component folded signal, still preserving the timing of each neutron detection and the n-γ discrimination. We are confident to get in the worst case a neutron energy resolution of the order of 3% at the higher energies.

The best solution for the wall should be a 50x50x50 mm³ PPO-Plastic scintillator plus a SiPM read-out and a totally digital acquisition of the multi-hit signals. A sketch of the overall set-up is shown in figure V-2.
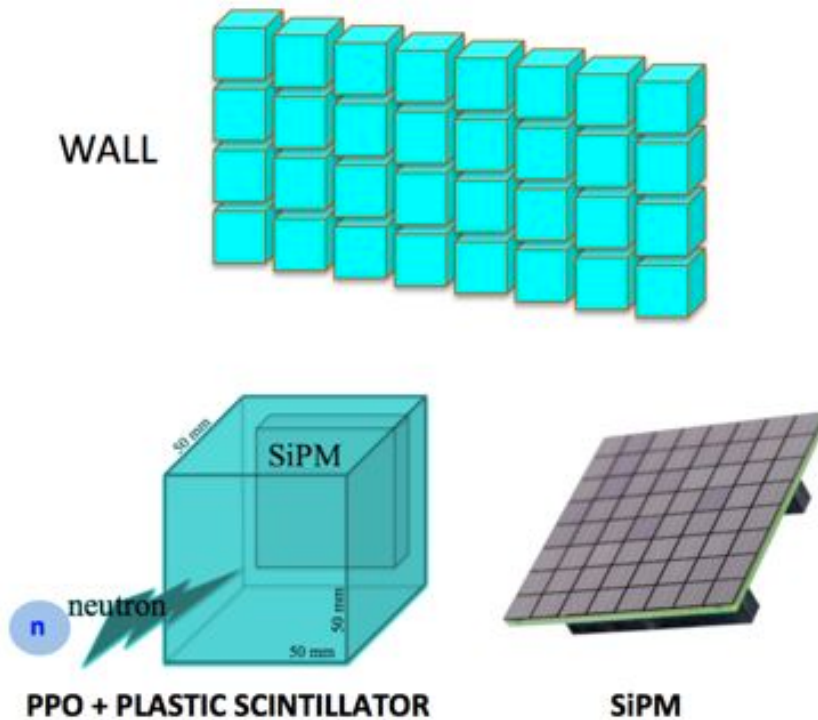
fig. V- 2 Neutron detection system. Single module configuration based on 50x50x50 mm³ PPO Plastic scintillator and SiPM read out.

V.2.1 Introduction to Scintillators

The wide spread use of scintillators in experimental physics began in the mid nineteen hundreds and continues to be used today due to the many advantages they have over other types of equipment. There are several different types including organic and inorganic scintillators that can be plastic, liquid or gaseous. The type of scintillator used in an experiment is chosen based on qualities such as high density, fast operation speed, or cost. Scintillators are materials that produce light when exposed to radiation. According to Knoll [Kno00], the ideal scintillator should have the following characteristics:

- High efficiency for converting energy from radiation into scintillation light that can be detected by the photocathode of a photomultiplier.
- Behave linearly to the quantity of energy that creates light.
- Not absorb the scintillation light that it produces.
- The induced luminescence should have a short decay time to facilitate timing applications.
- Be of sufficient purity and absent of non-scintillating material, and producible in the size desired;
- Have a refraction index that matches the Photomultiplier Tube.

The ability to meet the above criteria is a measure of the quality of the material for use as a scintillator. They can be broken into two groups, stemming from differences in their chemical makeup. First, inorganic scintillators are frequently alkali halides, the most widely used is sodium iodide (NaI). Inorganic scintillators tend to have linear response and superior light output when compared to organic scintillators. On the other hand they typically have slow response times. Organic scintillators make up the second group, they tend to have a lower light yield but faster response [Kno00]. The first organic scintillator on record was crystal naphthalene, developed by Kallman and Broser in 1947. Many organic scintillators followed including pure crystal, liquid and plastic, with a variety of dopants to tailor the scintillator's response.

Some of the popular compositions are listed in Table V-1 and some of the common scintillator solvents and ingredients used in organic scintillators are given in Table 2. The fast response and no hight cost of production have made the organic scintillators such as PPO [2,5-diphenyloxazole] $C_{15}H_{11}NO$ a our logical choice where no large detectors are necessary. The response times as low as » 200 ns. As the size of a scintillator increases, so does the probability that incident radiation will interact and be measured.

Table V- 1 Some common plastic scintillator compositions [Tsir65]

Bulk	1st *fluor*	2nd *fluor*
Polystyrene	2% TP	0.1% POPOP
Polyvinyl xylene	2% TP	0.1% POPOP
Polyvinyl toluene	2% TP	0.1% POPOP
Polystyrene	1.5% TP	-
Polystyrene	1.5% DF	-
Polystyrene	1.5% BPO	-
Polystyrene	1.5% PPO	-
Polystyrene	1.5% BαNE	-
Polystyrene	1.5% BPO	-
Polystyrene	1.5% TP	-
Polystyrene	2.0% TP	0.1% POPOP
Polystyrene	2.0% TP	0.1% BBO
Polystyrene	2.0% TP	0.1% 3P-Δ^2
Polystyrene	2.0% TP	0.4% BBE

Table V- 2 A partial list of popular scintillator ingredients adapted from Brook's [Tor02]

	Compound	Formula	Application[a]
1	Benzene	C_6H_6	S
2	Toluene	$C_6H_5(CH_3)$	S
3	p-Xylene	$C_6H_4(CH_3)_2$	S
4	1,2,4 Trimethylbenzene (psuedo-comene)	$C_6H_3(CH_3)_3$	S
5	Hexamethylbenzene	$C_6(CH_3)_6$	S
6	Styrene monomer	$C_6H_5(C_2H_3)$	S
7	Vinyltoluene monomer	$C_6H_4(CH_3)C_2H3$	S
8	Napthalene	$C_{10}H_8$	S',C
9	Anthracene	$C_{14}H_{10}$	C
10	Biphenyl	$C_{12}H_{10}$	S'
11	TP[p-Terphenyl]	$C_{18}H_{14}$	C,PS
12	p-Quarterpenyl	$C_{24}H_{18}$	C
13	trans-Stilbene	$C_{14}H_{12}$	C
14	Diphenylacetylene	$C_{14}H_{10}$	C
15	1,1',4,4'-tetraphenylbutadiene	$C_{28}H_{22}$	SS
16	Diphenylstilbene	$C_{26}H_{20}$	SS
17	PPO [2,5-diphenyloxazole]	$C_{15}H_{11}NO$	PS
18	α-NPO[2-(1-Naptyl),5-phenyloxazole]	$C_{19}H_{13}NO$	PS
19	PBD [2-Phenyl,5-(4-biphenylyl)-1,3,4-oxadiazole]	$C_{20}H_{14}N_2O$	PS
20	BBO[2,5-Di(4-biphenyl)-oxazole]	$C_{27}H_{19}NO$	SS
21	POPOP[1,4-Bis(2-(5-phenloxazolyl))-benzene]	$C_{24}H_{16}N_2O_2$	SS
22	TOPOT[1,4-Di-(2-(5-p-tolyloxazolyl))-benzene	$C_{26}H_{20}N_2O_2$	SS
23	BiMePOPOP [1,4-Di(2-(4-methyl-5-phenyloxazolyl))-benzene]	$C_{26}H_{20}N_2O_2$	SS
24	DF [2-(diethoxylphenyl)-5-phenyl-1,3,4-oxadiazole]		PS
25	BPO[2-phenyl-5-(4-biphenyl)-1,3-oxazole]		PS,SS
26	3P-Δ^2[1,3,5-triphenyl-Δ^2-pyrazoline]		SS
27	BBE[1,2-di-(4-biphenylol)-ethylene]		SS
28	BαNE[1-(4-biphenylyl)-2-(α-naphthyl-ethlene]		PS

[a] S-primary solvent; S'-secondary solvent; PS-Primary solute; SS-secondary solute; C-crystal scintillator

V.2.2 Liquid Scintillators and Solute Materials

Noting similarities between liquid and plastic scintillators Birks [Bir64] identifies several primary fluors as p-terphenyl(TP), 2,5-diphenyloxazole (PPO), and 2Phenyl,5-(4-biphenylyl)-1,3,4-oxadiazole(PBD). With effective secondary fluors being 1,4-Bis(2-(5-phenloxazolyl))-benzene(POPOP) as wavelength shifters. Notable differences are: that unlike the liquid cousins, plastic scintillators are

somewhat dependant on the method used to prepare them. The quantum efficiency is appreciably higher in plastic scintillators than in liquids and higher solute concentrations are needed to get optimum efficiency. A comparison between the pulse heights produced by various sources in plastic and liquid is presented in Table V-3. The wavelength of fluorescent emission from the organic solute is typically in the UV. The efficiently-designed scintillator solution consists of one or more additional species, Y, into the solution to produce excited electronic states that are of lower energy than the excited states of the solvent.

Table V- 3 Relative Scintillation Efficiency of Polystrene solutions [Bri64]

γ-ray	E (MeV)	Plastic scintillator		Liquid scintillator	
		Pulse height of peak (arbitrary units)	Half - resolution $\eta_{1/2}$ %	Pulse height of peak (arbitrary units)	Half - resolution $\eta_{1/2}$ %
^{137}Cs	0.66	9.7	26	12.0	33
^{60}Co	1.17	21.3	26 (combined peak)	26.6	24 (combined peak)
	1.33				
^{40}K	1.46	26.1	14.5	32.4	16
^{22}Na	1.28			29.2	18.5
	0.51			8.4	43

V.2.3 The Scintillation Process.

Consider a fast electron incident on an efficient scintillator that dissipates the whole of its energy, E, inside the scintillator. A fraction of that energy, S, is converted to N fluorescence photons with an average energy, E_p. The value S is the absolute scintillation efficiency. The emission spectrum of a single component scintillator is equivalent to its fluorescence spectrum. In a binary system the energy from the excited solvent is transferred to the solute making the scintillation spectrum equal to the fluorescence spectrum of the solute. The designer of a multiple-component scintillator frequently adds multiple solutes so that energy is

transferred to a molecule with the desired emission spectrum; usually well below the absorption spectrum of the bulk scintillator molecule.

The fluorescent time of a single component scintillator, apart from self-absorption, is approximately equal to that of the fluorescent decay arising from excitation via an ultraviolet source. For binary and ternary systems the emission timing is approximately that of the photo-fluorescence decay of the emitting solute [Bri64]. The rise time, however, may be lengthened, due to the finite time of energy transition from the solvent to the emitting species. The fast scintillation decay time is then on the order of 2 to 30 nsec [Bri64]. For many scintillators about » 10% of the decay, is slow scintillation, and does not decay exponentially, having a duration that lasts » 10sec [Tor02].

The number of scintillation photons produced is strongly dependant on the particle type and its energy. Heavy particles will damage the molecules of a scintillator as they interact with the scintillator. Multiple damaged molecules often combine locally to reduce the number of excited electrons pi-states in a process called quenching.

V.2.4 Relationship between pulse height and energy and type of incident energy

To measure the energy of the incident particle with a scintillator, the relationship between the pulse height and the energy deposited in the scintillator must be known. Because the pulse height is proportional to the output of the photomultiplier, which output is in turn proportional to the light produced by the scintillator, it is necessary to know the light-conversion efficiency of the scintillator as a function of type and energy of incident radiation. Techniques for accurate discrimination between neutrons and photons interacting with liquid scintillators have been established for a long time. These are based on the property of most of the scintillator materials, that exhibit a light pulse-shape characteristic of the ionizing radiation [Bro79]. Generally, the light output of a scintillator contains fast

and slow components with decay times ranging from few to some hundreds of nanoseconds. This provides a way for particle discrimination between gamma-rays and neutrons, for instance. Gamma-ray induced fast electrons generate a larger fraction of their scintillation light within the prompt component as compared to recoil protons from neutrons scattering.

V.2.5 Liquid Scintillators

This scintillator exhibits excellent pulse shape discrimination (PSD) properties, particularly for fast neutron counting and spectrometry in the presence of gamma radiation. It is identical to the widely reported NE-213 and, therefore, exhibits all of the properties of that scintillator.

EJ-301 can be supplied ready for immediate use encapsulated at the factory in sealed aluminum or glass cells of a variety of types made to the customer's required dimensions. It is also supplied in bottles or drums sealed under inert gas. However, after being transferred to a cell or tank it should be deoxygenated again by sparging with pure nitrogen or argon for a duration proportional to the cell size immediately before sealing in order to achieve excellent PSD performance.

Pulse Shape Discrimination

PSD figure of merit, M, is defined as the separation between the neutron and gamma peaks divided by the sum of the FWHM of the neutron and gamma peaks at 1 MeV electron energy. Measurements of 3.5 (see fig.V-3)[Win7] have been reported.
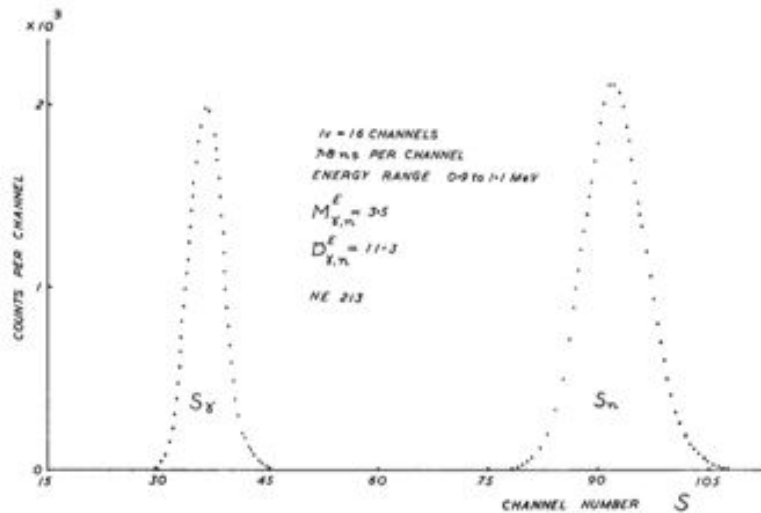
fig. V- 3 Neutron-gamma discrimination in NE213 at 1MeV electron energy

PSD figure of merit, D, defined as the separation between the neutron and gamma peaks divided by the variance in the PSD signals at 1 MeV electron energy is 11.3 (see fig.V-3). For values of M and D at other energies and for electron rejection ratios, see Figs. 3a, 3b & 4 of [Win7] and Fig. 6 of [Ada7].

Neutron and Gamma Spectrometry

The absolute differential efficiency and neutron spectra for a nominally 5 cm dia. x 5 cm cell for energies between 0.2 and 22 MeV are presented in [Ver68]. Gamma spectra analysis at energies above 3 MeV taken with three different sized scintillators is presented in [Bue93]. Methods of analyzing neutron and gamma spectra are compared in [Koo93].

V.2.6 PPO Detector

A possibility of manufacturing plastic scintillators with efficient neutron/gamma pulse shape discrimination (PSD) is demonstrated using a system of a polyvinyltoluene (PVT) polymer matrix loaded with a scintillating dye, 2,5-diphenyloxazole (PPO). According to a commonly accepted mechanism [Bir64,Bro79], both gamma and neutron induced pulses contain a short decay (prompt) and a long decay (delayed) fluorescence components. The prompt

component results from the direct radiative de-excitation of excited singlet states(S1), while the slow component is determined by the kinetics of the triplet(T1) exciton diffusion process preceding the triplet–triplet interaction and annihilation: T1+T1->S0+S1, which leads to the excitation of additional singlet states decaying with the same spectral distribution (see fig V-4).

The mechanism of triplet–triplet annihilation was first discovered and demonstrated [Bro59,Phi53,Wri56,Owe58,Bol61] in a number of unitary systems of organic single crystals(anthracene, trans-stilbene, p-terphenyl, and p-quaterphenyl), among which stilbene became known for its superior discrimination properties. A similar discrimination properties were found inorganic liquid scintillators, which typically are binary or ternary systems composed of highly efficient fluorescent dyes(e.g. p-terphenyl, PPO, PBD, or POPOP)dissolved in aromatic solvents(e.g.toluene or xylene) [Bir64]. Liquid scintillator mixtures were made using anhydrous p-xylene(>99%), 2,5-diphenyloxazole(PPO,99%).
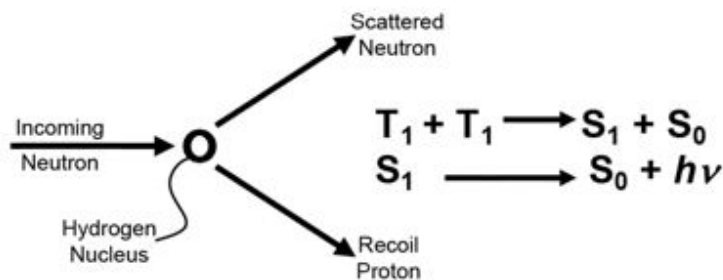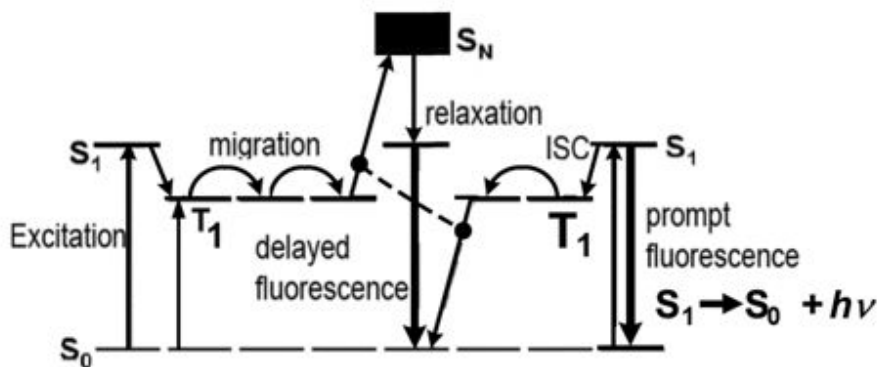
fig. V- 4 One particularly useful type of radiation detection, pulse shape discrimination (PSD), which is exhibited by some organic scintillators, involves subtle physical phenomena which give rise to the delayed luminescence characteristic of neutrons, providing a means of distinguishing neutrons from the preponderance of prompt luminescence arising from background gamma interactions. The mechanism by which this occurs begins with the excitation process which produces excited singlet (S1) and excited triplet (T1) states nonradiatively relaxes to the configuration, as shown .The basic physical processes leading to the delayed fluorescence characteristic of neutron excitation of organics with phenyl groups is shown.Since the triplet is known to be mobile in some compounds, the energy migrates until the collision of two triplets collide and experience an Auger upconversion process, shown as Equation 1:T1+T1→S0+S1 .In Equation 1, T1 is a triplet, S0 is the ground state, and S1 is a first excited state. Finally, the delayed singlet emission occurs with a decay rate characteristic of the migration rate and concentration of the triplet population, which is represented as Equation 2: S1→S0+hv .In Equation 2, hv is fluorescence, while S0 is the ground state and S1 is a first excited state. The enhanced level of delayed emission for neutrons arises from the short range of the energetic protons produced from neutron collisions (thereby yielding a high concentration of triplets), compared to the longer range of the electrons from the gamma interactions. The resulting higher concentration of triplets from neutrons, compared to gamma interactions, leads to the functionality of PSD. The observation of PSD is believed to be in part related to the benzene ring structure, allowing for the migration of triplet energy.

V.2.7 SiPM Detector

The first avalanche photodiodes (APD) were developed more than 40 years ago. For a long time APDs remained red and near-infrared sensitive detectors with an active area below 1mm². During the last ten years a large progress has been made in the development of large area (tens of square millimetres) APDs sensitive to scintillation light in the blue and near-ultraviolet wavelength region. These APDs started to find their fields of application in experimental nuclear and particle physics.

The use of silicon photodiodes for reading scintillators has recently attracted a strong interest to the introduction of Silicon Photomultiplier, photodiode arrays that allow not only the detection of the photons, but also a *good linearity* of response. The results are :

Advantages:

- – Fast response time
- – Construction and operation simple ➙ cheap and reliable
- – Lower VBias

SiPM are photon counting devices consist of a matrix of SPAD (Single Photon Avalanche Photodiode) connected in parallel on a common substrate used and operates in limited Geiger mode [Buz11].

Table V- 4 APD characteristic Parameters

APD	
Parameters	**Values**
Area	(1x1) mm²......(5x5) mm²
N. APD for mm²	≈100..............≈1000
Area for pixel	10%...................50%
Efficiency for single photon	20%...................30%
Voltage	30V.................100V
Gain	10^4..................10^7
Time for APD	≈ 1μs
Noise	10^5...........10^6 count/mm² s

The SPAD is a APD photodiode with a reverse voltage higher than the breakdown voltage, this operation is called Geiger mode. The operation principle of an APD is based on the conversion of the energy of photons into free charge carriers in the semiconductor bulk and their further multiplication via the process of impact ionization. Under the reverse bias an electric field exists in a certain volume of the device close to the junction, and this volume becomes depleted of free charge carriers. The charge carriers created in the depleted region drift in the electric field towards the corresponding electrodes. The feature distinguishing an APD from a Photodiode (PD) is a build-in region with very high ($>10^5$ V/cm) electric field. The charge carriers traversing this region acquire enough energy to produce electron-hole pairs by impact ionization. The newly created charge carriers may create new ones, and so on. Thus there is an avalanche of electrons and holes moving through the detector. These current pulses are then detected in an external circuit. The high energy supplied by polarization means that the gain is higher in the order of about 10^6 against the 10^2 of the APD in a linear shape.

So each carrier generated by photons or thermally gives rise to a Geiger-type discharge. This Geiger discharge is stopped when the voltage goes down below

breakdown value due to external resistor R on each pixel. Because all SiPM pixels work together on common load, the output signal is a sum of the signals from all pixels fired. So such a number of pixels, where each element operates digitally as a binary device, work as an analogue detector, which can measure light intensity.

V.2.8 Pulse Shape Discrimination (PSD)

It is well-known that the emission from organic scintillation detectors comprises both fast and slow components. For the vast majority of applications it is the prompt emission that is most useful. However, pulse shape discrimination is a special case in that it is the slow component of emission which is of greatest importance. For scintillators exhibiting the PSD phenomena the delayed fluorescence can be directly related to the type of incident radiation[Kno00], i.e. it can be used to distinguish between pulses caused by neutrons and gamma rays in a way that other scintillators cannot. Thus a PSD system can help end the reliance on a dwindling supply of 3He for national nuclear security.

PSD is most strongly observed within the category of organic liquid scintillators such as EJ-309 [Poz09],[Cla09],[Fla07]. The chemical properties of these materials make them undesirable for mass deployment, especially in situations where they would require regular maintenance by personnel.

Conversely, plastic scintillators are known for their stability and ruggedness, making them a far more suitable prospect for a long-term deployment with possible public exposure. With the development of EJ-299-33 [Zai12], a plastic scintillator exhibiting PSD properties, there appears to be a solution to the absence of neutron detection capability.

All scintillators require a coupled sensor to detect the emission of light, a role generally filled by the photomultiplier tube (PMT). Unfortunately, PMTs usually require a high voltage power supply, presenting an electrical hazard to their deployment, as well as the nature of their operation being such that they remain

unsuitable for use with magnetic fields [Cri95]. The silicon photomultiplier (SiPM) is an alternative which solves these issues[Haw07], and with recent technological improvements the high dark current of previous generations has been greatly reduced [Tag16].

V.2.9 Pulse Shape Characterization

The response of the scintillator will vary depending on the type of radiation that enters the detector and the energy of such radiation. The integrated amplitude of the peak produced by the scintillating process depends linearly on the energy deposited by the radiation. However, the shape of the peak depends on the type of radiation. For example, gamma rays produce more fluorescent energy than neutrons resulting in larger detector output amplitudes for gamma rays than neutrons [Jam12]. The reason is that gamma rays deposit energy in the detector through Compton scattering interactions with electrons in the detector while neutrons deposit energy primarily through elastic scattering with the nuclei of hydrogen atoms in the detector. [Jam12] Gamma rays, therefore, deposit energy in the detector through electrons while neutrons deposit energy through protons. Due to the difference between protons and electrons, the protons will deposit energy more densely than electrons causing a difference in the output signal. It is this difference that allows us to characterize the pulse shapes of both neutrons and gammas. [Chi00]

The pulse shape characterization of scintillators is done using an Am-Be standard source. Pulses of neutrons and gammas will differ in their tail area as shown below where tail area is the integral of the pulse starting at the maximum or some other predefined point.
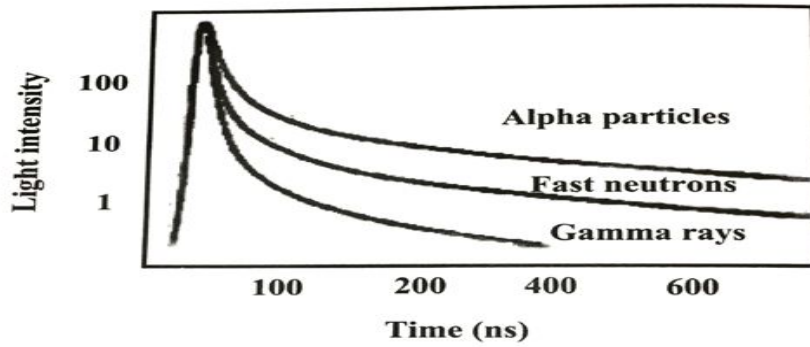
fig. V- 5 The response of EJ-301 to different particles and electromagnetic radiation.

This signal shapes give us a technique for accurate discrimination between neutrons and photons interacting with plastic scintillators. Generally, the light output of a scintillator contains fast and slow components with decay times ranging from few to some hundreds of nanoseconds. This provides a way for particle discrimination between gamma-rays and neutrons; in fig.V-6 the fast–slow components are illustrated.

Am-Be sources emit both neutrons and gammas by following reaction :

$$\frac{4}{2}\alpha + \frac{9}{4}\text{Be} \rightarrow \frac{12}{6}\text{C} + \frac{1}{0}\text{n} + \gamma$$
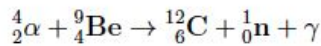
which makes them excellent for pulse shape characterization because we can compare the pulse shapes of the emitted signals to that of the purely gamma ray sources we used in the energy calibration experiments.
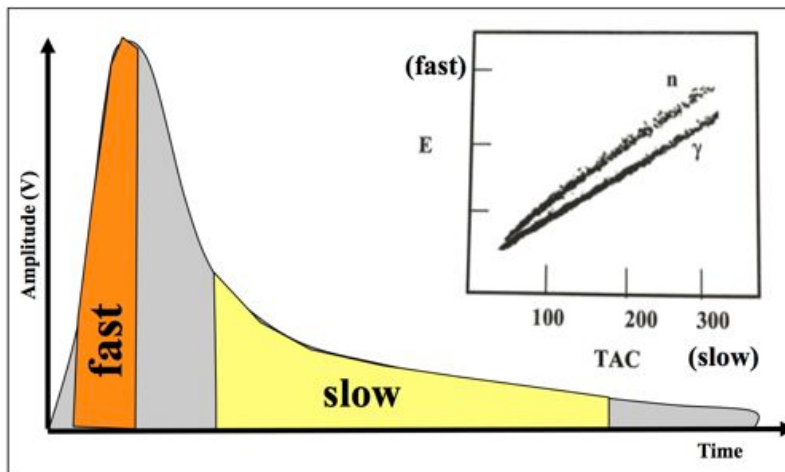
fig. V- 6 Sketch of single response, with the two selection : fast and slow. The "fast" component was calculated integrating the signal between the times at which the pulse-form crosses 10% and 100% of the full pulse height relative to baseline, while the "slow" component was calculated integrating the signal between the times at which the pulse-form becames 3 and 5 times the rise time of full pulse.

Also we can observe that the response of photons produced versus charge particles energy is able to separate different particles. See fig. V-7
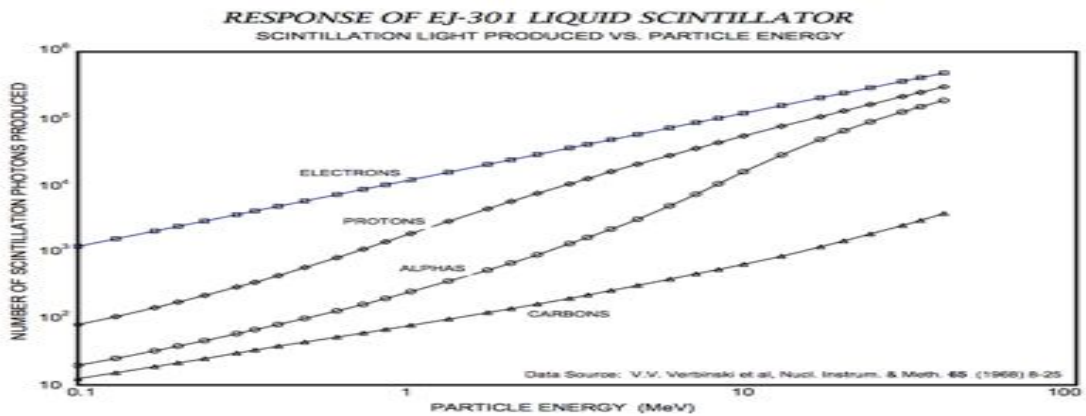
fig. V- 7 Number of scintillation photons produced versus particle (e,p,alpha,Carbon) energy [Ver68].

V.3 Tested Scintillators

The following tests were made with experimental setup described in the following paragraph. Two different kind of detectors have been used : EJ301 and EJ-299. A source of Am-Be with neutrons and gammas-ray radiations has been used. A dedicated Data System Set-Up with 16-channels BaF-Pro module, using a sophisticated analog fast stretcher circuit, has been used to determine the fast and slow components of the scintillator light signal. The comparison between the two scintillators is discussed at the end of this paragraph.

V.3.1 Data System SET-UP

Test PVT-based scintillators. The boundaries of the system, include the detector (scintillator), the timing circuit, the light collection system, and the data acquisition system. The voltage pulse signal, created by a photon interaction with the PMT, travelled inside the BaF Pro box. It splits the original signal in two components: Fast and Slow; the output of discriminator is sent to Gate Generator that give start to acquisition ADC Silena Module.

Finally, a computer recorded the Fast and Slow events that made it through the light collection system.Gamma-ray induced fast electrons generate a larger fraction of their scintillation light within the prompt component as compared to recoil protons from neutrons scattering.

Various techniques have been developed over the years and several electronic circuits have been described in literature to perform the pulse-shape discrimination. One of the main requests of such systems is to operate properly over a wide range of pulse amplitudes, with the ability to successfully accept small pulses, thus achieving high neutron detection efficiencies at low energies.
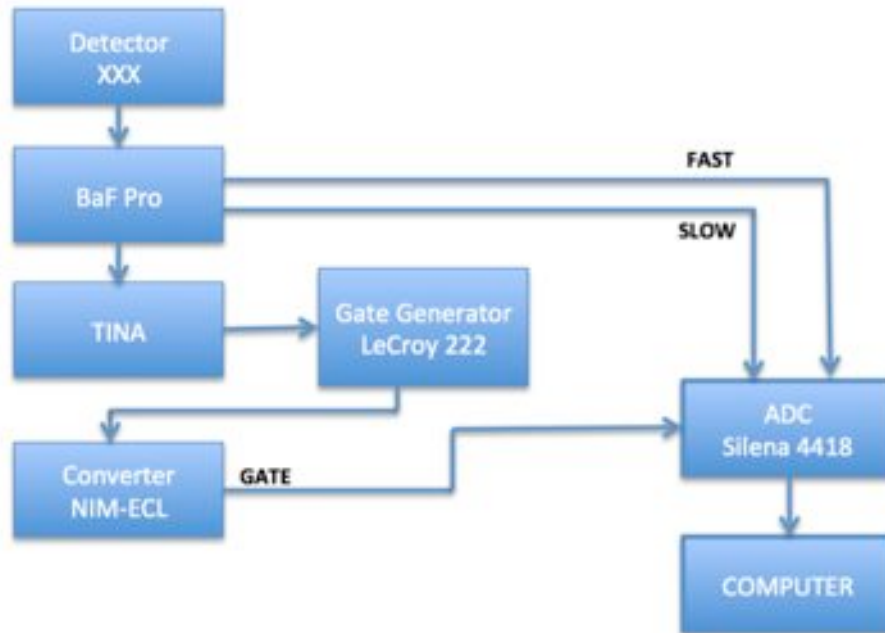
fig. V- 8 Block diagram of the electronic used for the pulse-shape discrimination.

A typical technique for processing signals from a scintillator detector where the light emission mainly exhibits a fast and slow component is the double charge integration method [Ada78]. It is based on the use of two QDCs (Chargeto-Digital-Converter) or a double QDC [Dre03] with two different integration windows, generated by separate GDG (Gateand-Delay-Generator) modules. An alternative way to the pulse-shape analysis consists of an analog treatment of the scintillator signal based on a fast stretcher which captures the highest peak of the fast component of the signal, while remaining in sensitive to the slow component. A Gaussian signal is generated at the exit of the stretcher through an appropriate shaping. A second bipolar Gaussian, which contains the information about the total energy of the event, is also generated by integrating the input signal. These signals can be easily delayed and digitized via a peak-sensing Analog to Digital Converter (ADC).Such technique has been studied [Boi06] and the circuit originally realized [Boi08] for processing signals of Barium Fluoride(BaF2) scintillator detectors.

BaF-Pro Electronics

The 16-channel BaFpro module makes use of a sophisticated analog fast stretcher circuit to determine the fast component of the light output scintillator (indicated as "fast") and an integration section that provides the total energy of the signal (indicated as "slow") A simplified schematic block diagram of these two stages of the circuit is show in fig.V-9
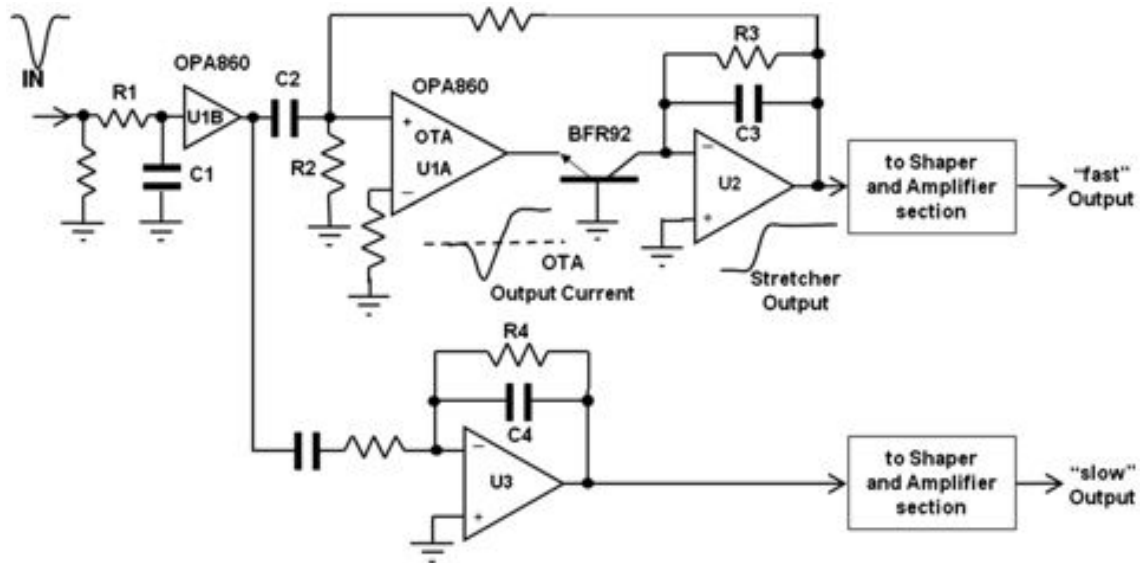
fig. V- 9 Here is the electrical wiring diagram template used. In this diagram is displaied the physical connections and physical layout of circuit BaF-Pro Electronics

The photomultiplier (PMT) anode signal of the fast scintillator detector is first integrated with a time constant (R1C1) of 4 ns to reduce possible effects of light reflections within the detector or impedance mismatching. The signal is then buffered by the integrated circuit OPA860 (U1Bin fig. V-9) to properly drive the following circuit sections. In the fast stretcher circuit, the input signal is first differentiated with a time constant (C2R2) of 2 ns and then linearly converted into a current pulse by means of a fast Transconductance Operational Amplifier OPA860 (U1A). This pulse remains negative until the PMT signal reaches its peak value and after that changes sign. The small value of the differentiation time constant guarantees a fast polarity change. A high-frequency NPN transistor (BFR92) inhibits the conduction of the positive part of the current to the following integrator, which remains charged to the peak value of the input signal. Thus the integration (with a time constant R3C3 of 1 μs) of only the negative part of this

current gives the information of the maximum value of the PMT signal. A shaper amplifier with a time constant of 0.5 μs is finally used to transform the integrator output into a wide Gaussian pulse. The part of the circuit that provides the total energy of the signal consists of an integrator with a constant of 0.5 μs (R4C4) followed by a bipolar shaper of CR-RC² type as described in Ref.[Boi08]. A DC restoring circuit allows to recover the original baseline. The amplitudes of both "fast" and "slow" Gaussian signals are controlled by adjustable fine and coarse gains [Boi06, Boi08].

Characteristics:

• 16 Channels Acquisition System for Scintillation Detectors developed in Milano

• NIM standard module

• Provides:

– Energy(<1%)

– Time(through CFD,<100ps)

– PSD (through fast vs slow technique)

RS485 dedicated software control Coarse & Fine Gain, CFD thresholds
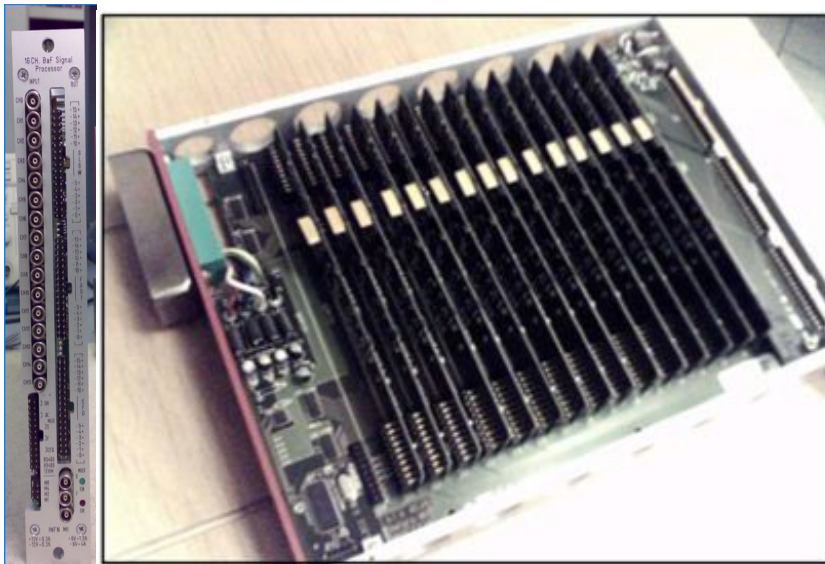
fig. V- 10 BaF-Pro Electronics

V.3.2 EJ301 Liquid Scintillator

The first test on detectors was performed on liquid scintillator EJ301 + PMT Photo Multiplier Tube Hamamatsu R 1250 (fig.V-11)

fig. V- 11 Photography is shown in the scintillator EJ301 coupled with phototube; the radioactive source of Am-Be placed on the red box is visible

The liquid scintillator has been assembled and oriented in front of Am-Be source, collimator thickness of 2 cm and a diameter of 5 mm, to minimize the discrepancy path of the particles in the sparkling part, less than 5%.

The typical signal of EJ301 + PMT Photo Multiplier Tube Hamamatsu R 1250 is shown in fig. V-12
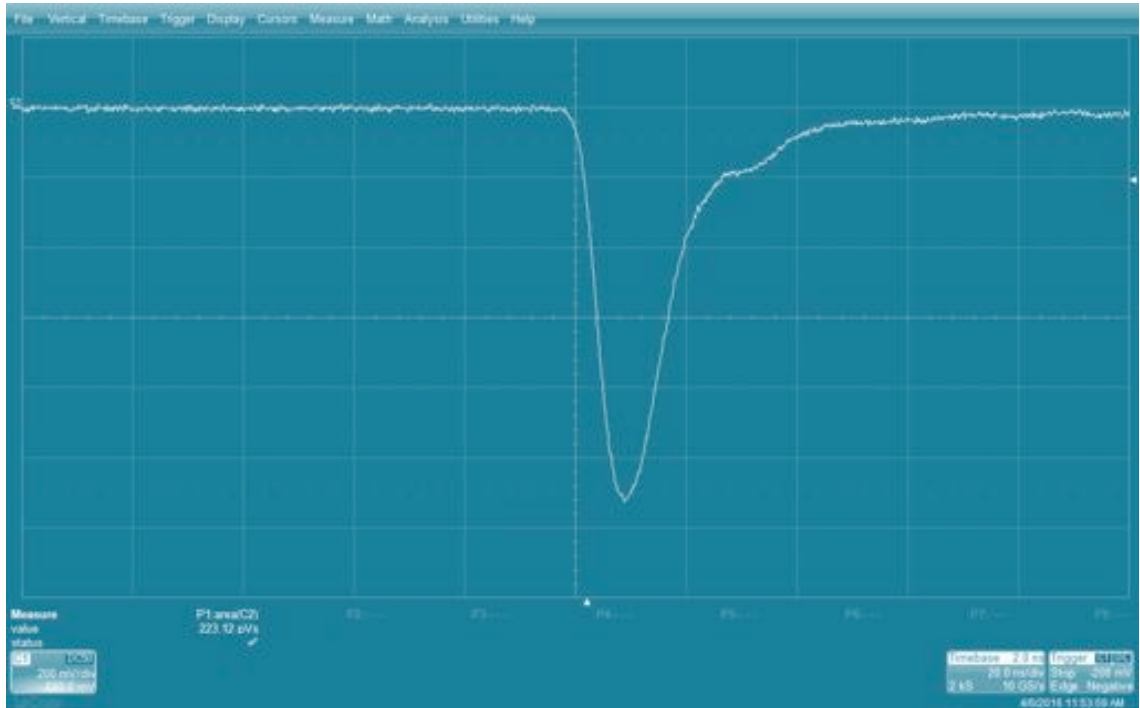
fig. V- 12 Signal EJ301 + PMT Photo Multiplier Tube Hamamatsu R 1250   from oscilloscope LeCroy.

In the fig.V-13 gamma rays and neutrons are separate. Neutrons are bounded in a red rectangle.
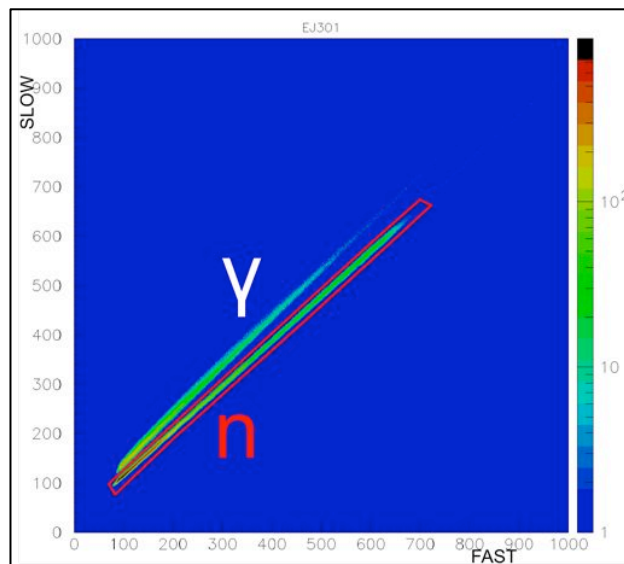
fig. V- 13 Pulse-shape discrimination (PSD) performance for EJ301 ; the pulses are from a Am-Be standard source. Red box only selects detected neutrons.

The upper of fig.V-14 shows: on the left side the projection on the slow component for the neutrons and on the right side the projection on the slow component for the gamma rays. The bottom of fig V-14 shows the comparison between the two different waveforms.

fig. V- 14 Mono-dimensional spectra of neutrons and gamma-rays in arbitrary-units for EJ301 scintillator.

V.3.3 EJ299 Plastic Scintillator(POP)

EJ-299-33A pulse-shape discriminating (PSD) plastic scintillator enables the separation of gamma and fast neutron signals on the basis of their timing characteristics using conventional PSD electronics systems. Cylinders up 127 mm diameter x 127 mm long can be supplied.
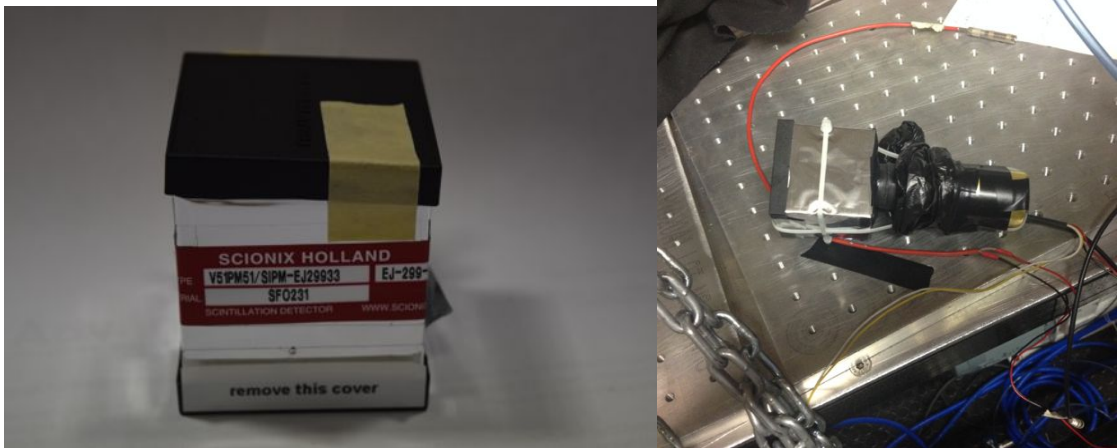
fig. V- 15 EJ299 assembled with Phototube R1924 Hamamatsu

The plastic scintillator has been assembled and oriented in front of Am-Be source, collimator thickness of 2 cm and a diameter of 3 mm, to minimize the discrepancy path of the particles in the sparkling part, less than 5%.

The typical signal of EJ299 + PMT Photo Multiplier Tube Hamamatsu R 1924 is shown in fig. V-16
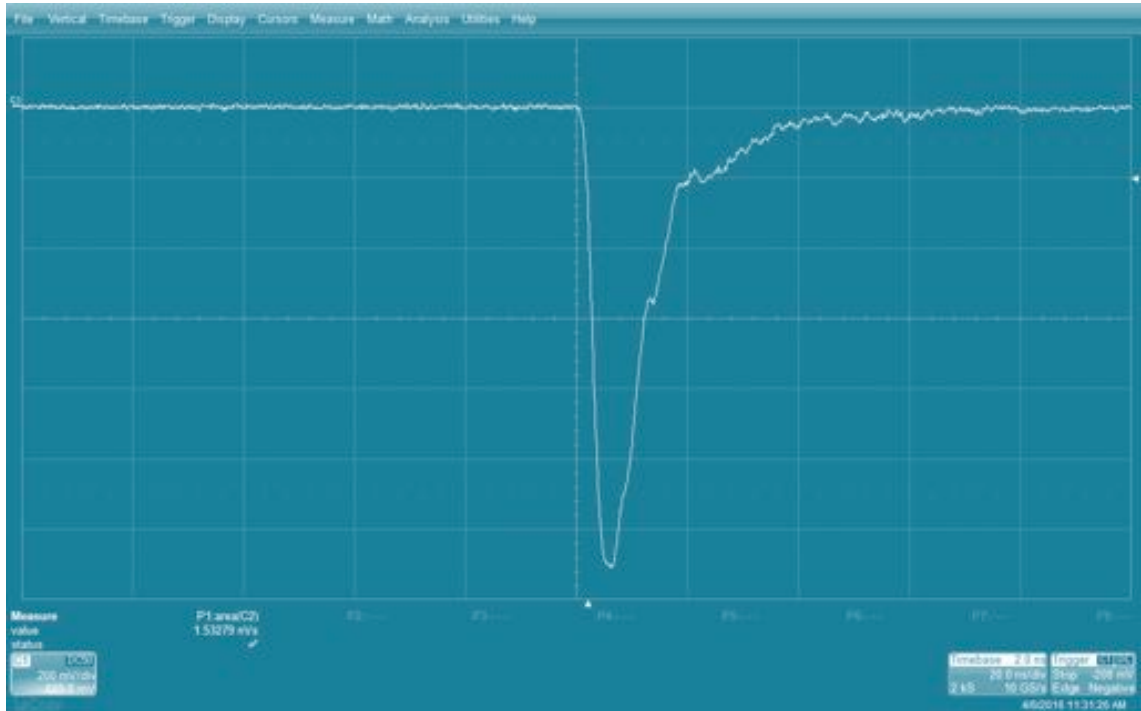
fig. V- 16 Signal EJ299 + PMT Photo Multiplier Tube Hamamatsu R 1924 from oscilloscope LeCroy.

 In the fig.V-17 gamma rays and neutrons are separate. Neutrons are bounded in a red rectangle.
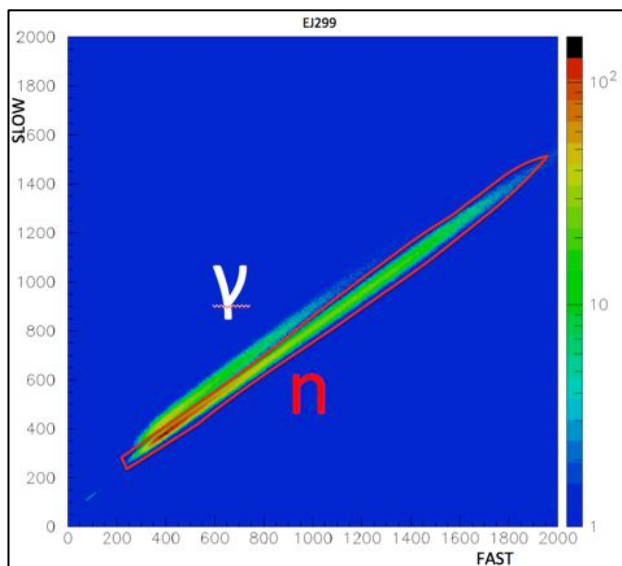
fig. V- 17 Pulse-shape discrimination (PSD) performance for EJ299 ; the pulses are from a Am-Be standard source. Red box selects detected neutrons.

The upper of fig.V-18 shows: on the left side the projection on the slow component for the neutrons and on the right side the projection on the slow component for the gamma rays. The bottom of fig V-18 shows the comparison between the two different waveforms.
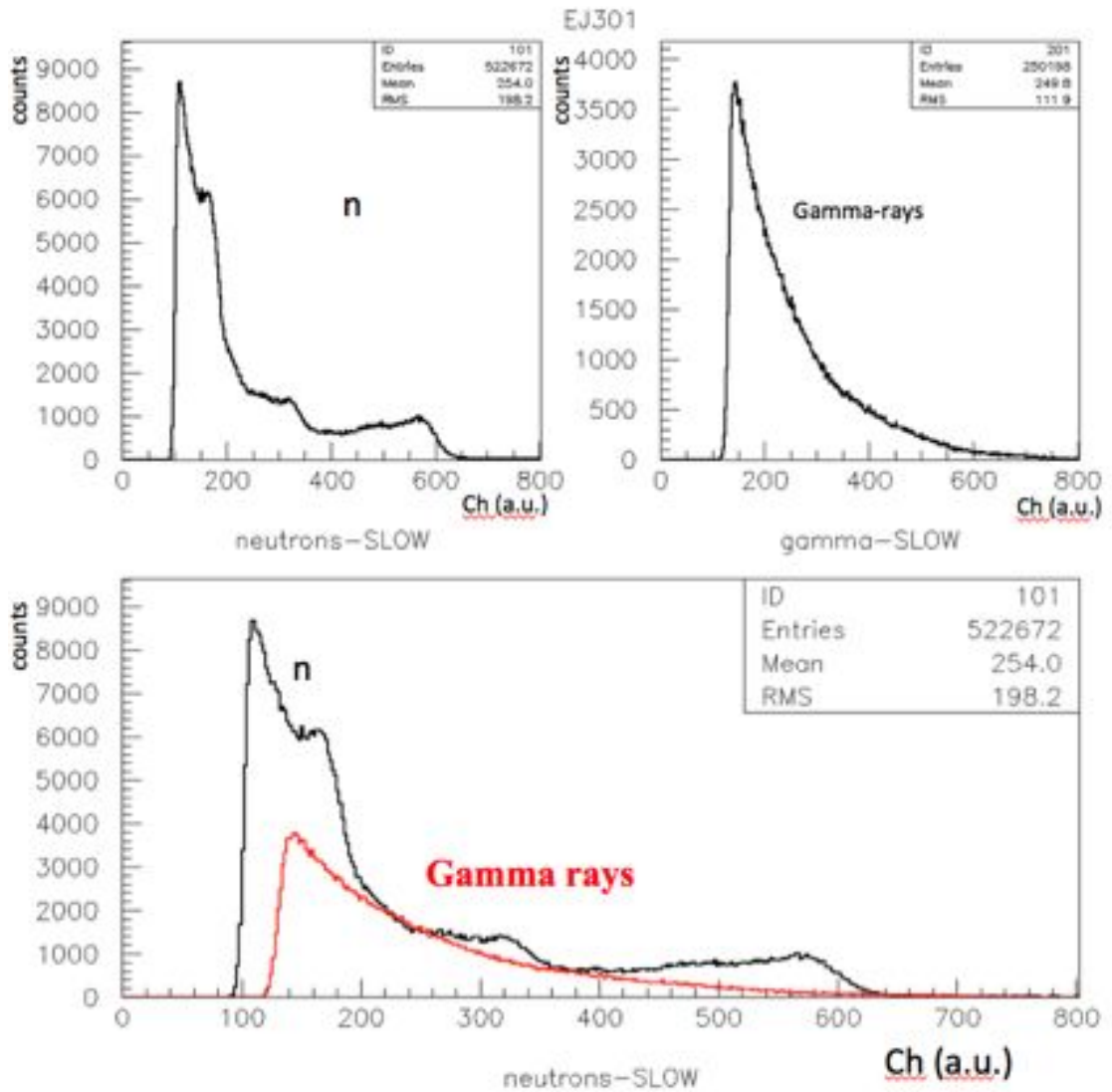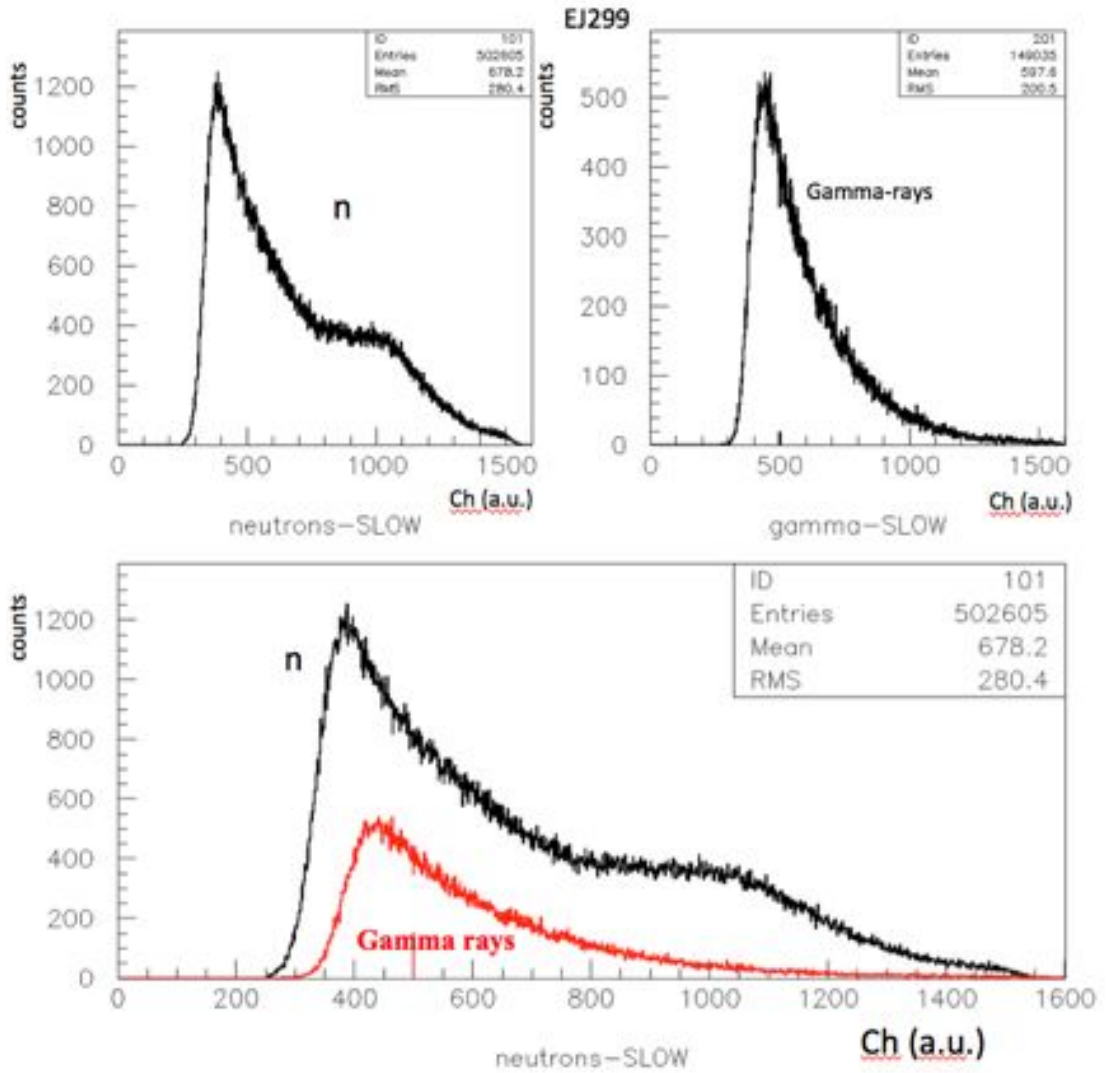

fig. V- 18 Mono-dimensional spectra of neutrons and gamma-rays in arbitrary-units for POP scintillator.

V.3.4 Comparison between EJ-301 and POP

Quantitative evaluation of PSD was made using figures of merit:

FOM=S/$\delta_{neutrons}$ +δ_{gammas}

where S is the separation between gamma and neutron peaks, and $\delta_{neutrons}$, δ_{gammas}

are full width at half maximum (FWHM) of the corresponding peaks (see the picture).

The separation S was calculated as a difference between the mean delayed light, for neutrons and gammas taken as a normal distribution in PSD over a specified energy range.
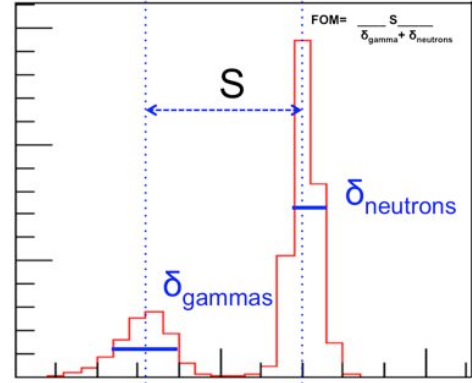
Considering that a reasonable definition for optimum separated Gaussian distributions of similar population sizes is S must be great than 3 ($\sigma_{neutrons}$ +σ_{gammas}), where σ is the standard deviation for each corresponding peak and noting that $FWHM \approx 2.36\sigma$,

$$FOM_{best} = \frac{S}{\delta_{gammas} + \delta_{neutrons}} > \frac{3(\sigma_{gammas} + \sigma_{neutrons})}{2.36(\sigma_{gammas} + \sigma_{neutrons})} = 1.27$$

was used as a reference parameter to define efficient PSD in the tested samples.

It is also possible give a definition for good separated Gaussian distributions of similar population sizes is S must be great than 1.18 ($\sigma_{neutrons}$ +σ_{gammas}),

$FOM_{good} > \dfrac{1.18(\sigma_{gammas} + \sigma_{neutrons})}{2.36(\sigma_{gammas} + \sigma_{neutrons})} = 0.5$. In our case, for good separated Gaussian

distributions of different population sizes (P4/P1=neutrons/gammas≈10) has been used $FOM^{*}_{good} > 0.58$

In analysis data we have used the following fit parameters correspondence :

P2=S_{gammas}, P3=σ_{gammas} , P5=$S_{neutrons}$, P6=$\sigma_{neutrons}$, with S= $S_{neutrons}$ - S_{gammas}
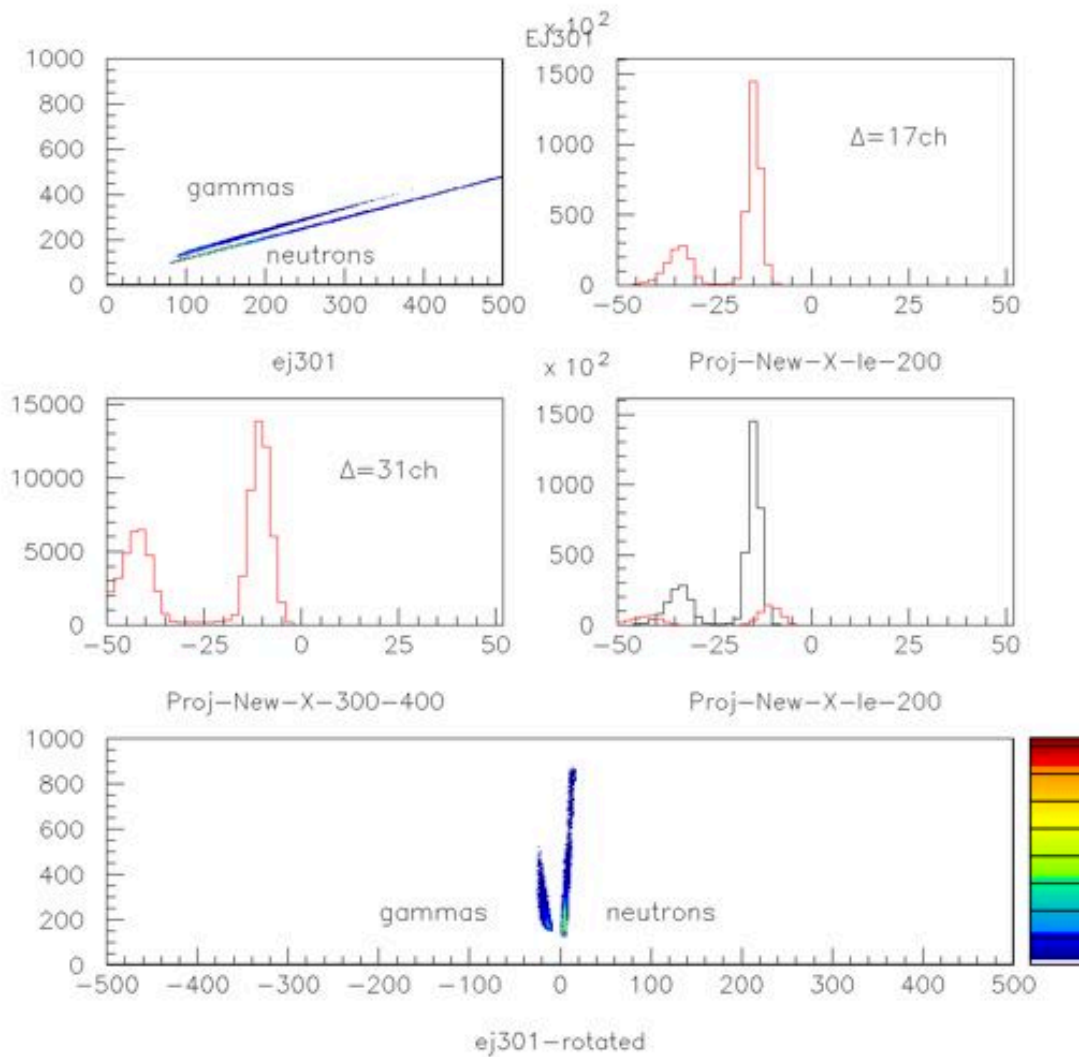
fig. V- 19 The figure shows spectra about EJ-301 scintillator. The Top-left panel shows the Fast Component as a function of Slow Component. The top right, medium left and right panels are the projection of rotated Fast-Slow matrix (shown in the lower panel) versus the new x' axis (FAST-r). In these 3 mono-dimensional spectra the neutrons and gamma-rays (a.u.) are shown for two different ranges of channels : 0<x'<200ch (top right panel) or 300<x'<400ch (medium left panel) . Finally in the medium right panel are showed the overlap between the two previous mono-dimensional spectra. The symbol Δ indicates the difference between the neutrons and gamma-rays peaks.

fig. V- 20 The figure shows spectrum about EJ-301 scintillator. In these mono-dimensional spectra the neutrons and gamma-rays (a.u.) are shown for channels range between 0<x'<200 . The fit curves (black) are calculated with the parameters from P1 until P6. The fit parameters values are shown in the top right window. The FOM is calculated and showed together with the widths ($\delta_{neutron}$ and δ_{gamma}) of the neutrons and gamma-rays peaks.
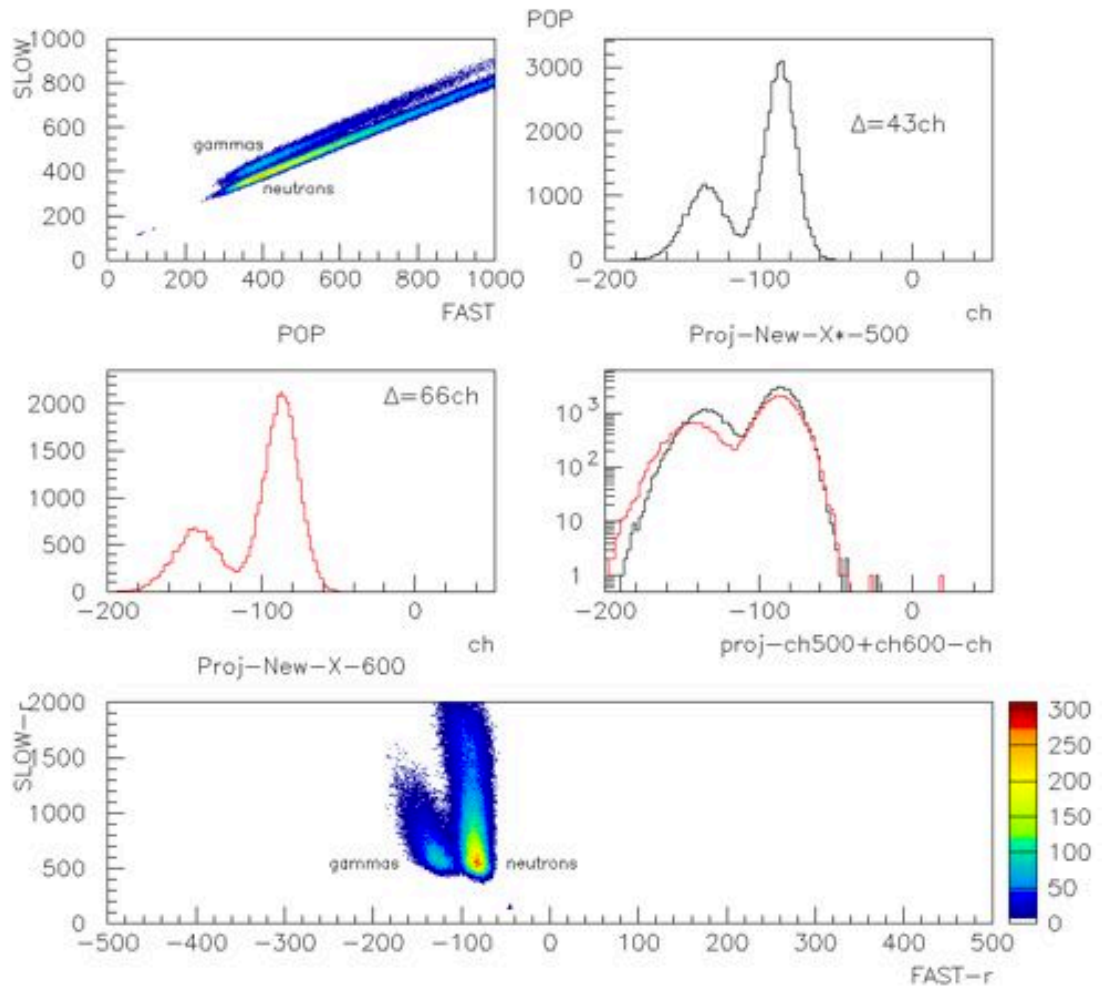
fig. V- 21 The figure shows spectra about POP scintillator. The Top-left panel shows the Fast Component as a function of Slow Component. The top right, medium left and right panels are the projection of rotated Fast-Slow matrix (shown in the lower panel) versus the new x' axis. In these 3 mono-dimensional spectra the neutrons and gamma-rays (a.u.) are shown for two different ranges of channels : 500<x'<600ch (top right panel) or 500<x'<600ch (medium left panel) . Finally in the medium right panel are showed the overlap between the two previous mono-dimensional spectra. The symbol Δ indicates the difference between the neutrons and gamma-rays peaks.
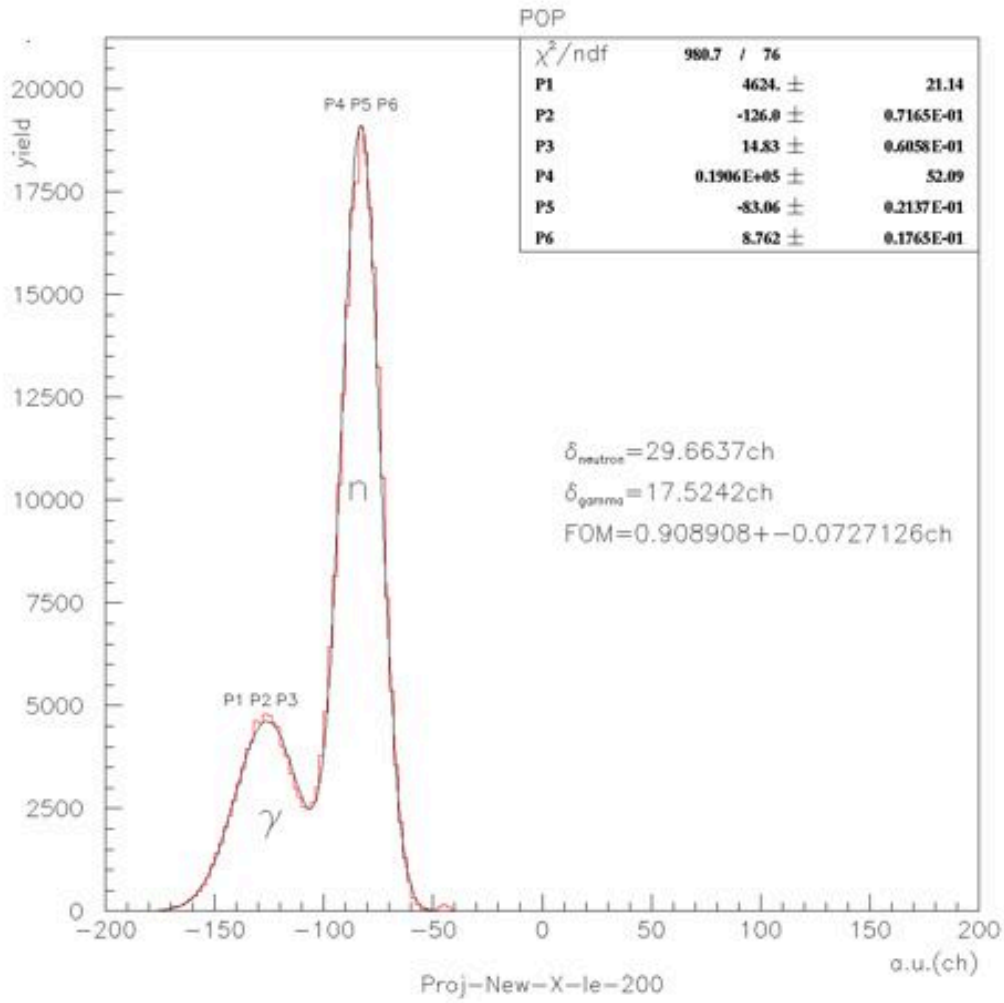
fig. V- 22 The figure shows spectrum about POP scintillator. In these mono-dimensional spectra the neutrons and gamma-rays (a.u.) are shown for channels range between 500<x'<800 . The fit curves (black) are calculated with the parameters from P1 until P6. The fit parameters values are shown in the top right window. The FOM* is calculated and showed together with the widths ($\delta_{neutron}$ and δ_{gamma}) of the neutrons and gamma-rays peaks.
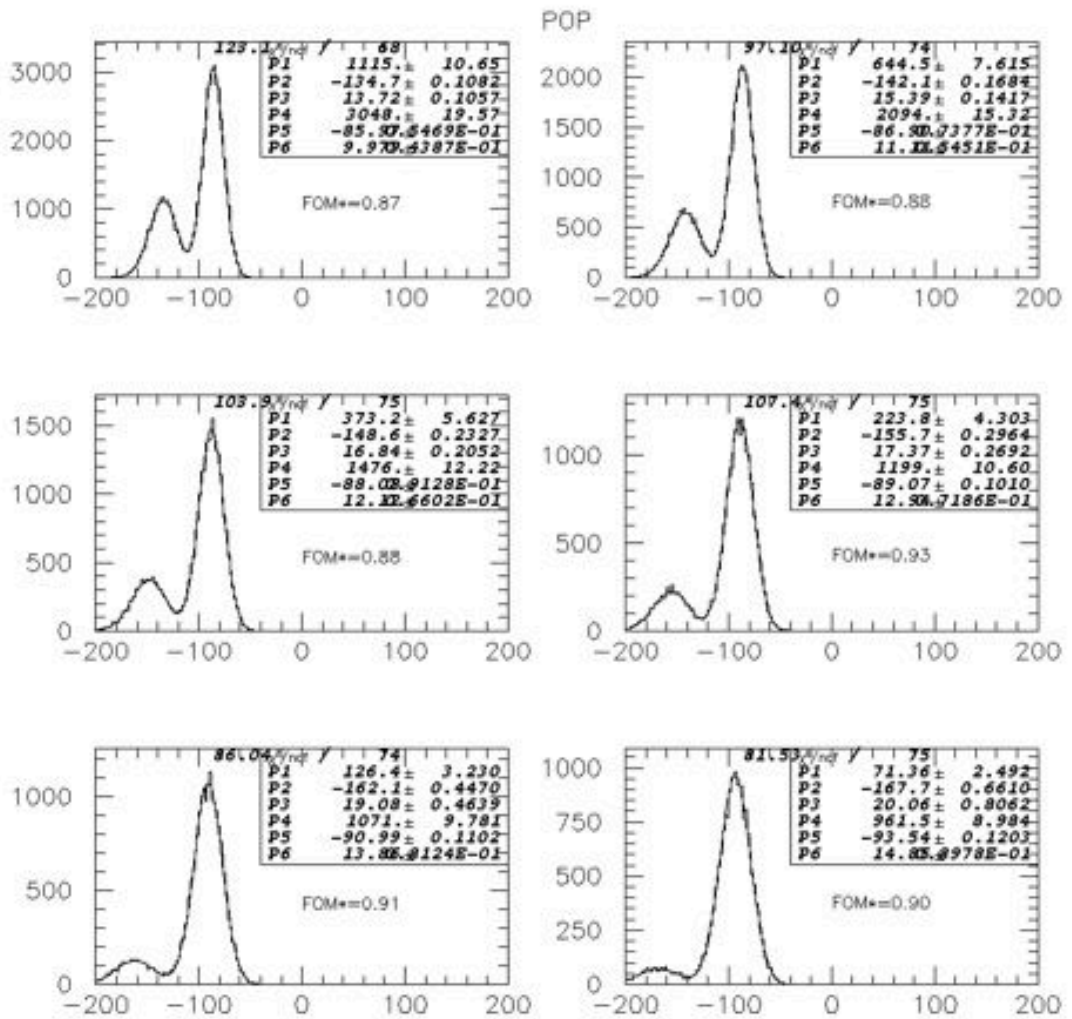
fig. V- 23 The figure shows spectra about POP scintillator. In these six mono-dimensional spectra the neutrons and gamma-rays (a.u.) are shown sequentially the channels range: 500<x'<550, 550<x'<600, 600<x'<700, 700<x'<800, 800<x'<900 and 900<x'<1000 . The fit curves are calculated with the parameters from P1 until P6. The fit parameters values are shown in the top right window. The FOM* are calculated and they are greater than FOM*$_{good}$.
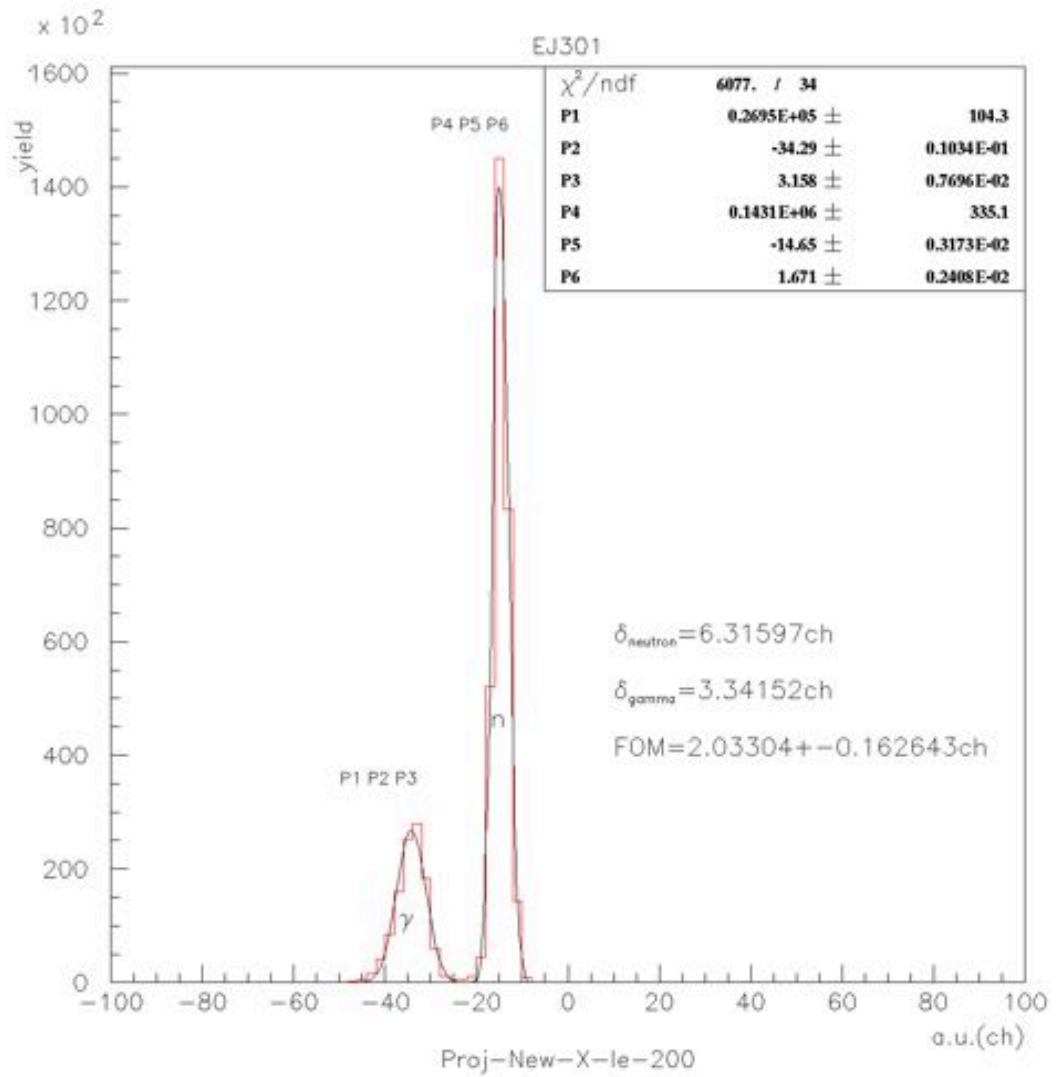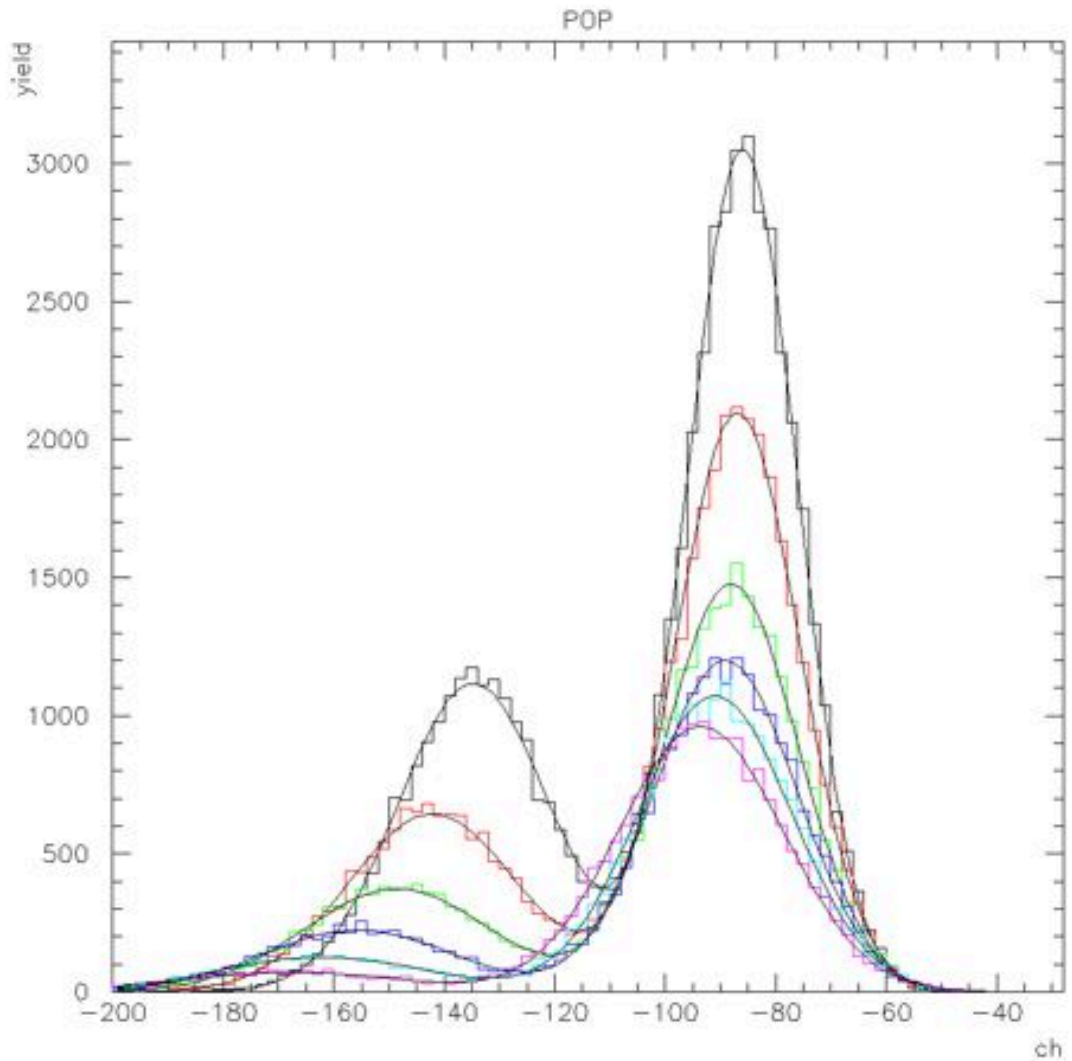
fig. V- 24 The figure shows spectra about POP scintillator. In these six spectra the neutrons and gamma-rays (a.u.) are shown with different colours the channels range: 500<x'<550 (black), 550<x'<600 (red), 600<x'<700 (green), 700<x'<800 (blue), 800<x'<900 (light blue) and 900<x'<1000 (magenta). The fit curves show a greater monotone shift of gammas peak than that of neutrons peak.

V.4 The particles detectors

The activities proposed at ELI-NP require the construction of SiC-wall detectors for charged particles detection in plasma environment. SiC-Wall has been chosen mainly because it is insensible to visible light, since this property is fundamental to perform the experiments. The SiC detectors, which are part of the wall, should be of about 100-200 μm of thickness. They will be placed at 0.5 – 1.5m from the target for ToF identification. They will be equipped with a proximity front-end and digital read-out electronics. This last item could be an important point to perform ions identification by the pulse-shape analysis and to minimize the effects of Electro-Magnetic noise (typical of peta-watts Laser facilities) on data transmission and storage.

V.4.1 SiC Material

Silicon carbide is a semiconductor with a wide, indirect band gap. Due to its composition SiC it is the only stable compound in the binary phase diagram of the two groups IV elements, silicon and carbon. It is thermally stable up to about 2000 °C, even in oxidizing and aggressive environments. Among all the wide band gap semiconductors, silicon carbide is presently the most intensively studied one and the one with the highest potential to reach market maturity in a wide field of device applications. Silicon carbide was discovered in 1824 by the Swedish scientist Jons Jakob Berzelius [Ber24], in the same year when he also discovered elemental silicon [Eng82]. Rapidly recognized for its extreme hardness of about 9.5 on the ten point Mohs scale, silicon carbide has since then been commercialized as abrasive under the trademark Carborundum, a contraction of the words carbon and corundum (another name for alumina used as abrasive). Silicon carbide is also used for fireproof, high-temperature ceramics and resistive heating elements utilized in silicon device manufacturing. In the early years of solid state physics at the beginning of the 20th century, the British physicist Round discovered that

certain pieces of silicon carbide emitted light when an electric current was passed through these samples. It was also discovered that silicon carbide had rectifying properties. In spite of the comparatively high turn-on voltage, silicon carbide crystal detectors were used in the early days of radio telecommunication under its brand name Carborundum. With the emerging semiconductor technology focusing on germanium and silicon in the 1930s, silicon carbide was abandoned as semiconductor material. In the search for semiconductor materials suitable for blue light emitting diodes, silicon carbide came into focus again in the late 1970s, but it was soon replaced by direct band gap semiconductors of the III-nitride group, i.e. compounds of one or more group III metal (Al, In, and Ga) and the group V element nitrogen. However, the advances in technology and the need for high-power electronic devices resulted in the ongoing research activity on this particular material, which led to the availability of high quality silicon carbide material and to the commercialization of silicon carbide devices in the beginning of the 21st century. Silicon carbide crystallizes in the form of silicon-carbon bilayers with a bond length of d = 1.9 Å, which also is the arithmetic average between the C-C bond in diamond and the Si-Si bond in crystalline silicon. In the silicon carbide crystal lattice these bilayers are closely packed. Silicon carbide has the quite unique property of showing a large variation in crystal lattices, which are all built up by these stacked bilayers.

V.4.2 Silicon Carbide properties

Silicon carbide (SiC) is a semiconductor material with highly suitable properties for high-power, high-frequency, and high-temperature applications. It is a wide bandgap semiconductor with high breakdown electric field strength, high saturated drift velocity of electrons, and a high thermal conductivity. For these physical and electrical properties in many fields SiC overcomes silicon (Si), that is the dominating material of electronic industry. SiC is characterized by a wide bandgap that varies between 2.39 eV to 3.33 eV, depending on the structural configuration of the crystal (polytypic nature). This property makes possible to use

SiC for very high temperature operation. Thermal ionization of electrons from the valence band to the conduction band, which is the primary limitation of Si-based devices during high temperature operation, is not a problem for SiC based devices because of this wide bandgap. For power-device applications, perhaps the most notable and most frequently quoted property is the breakdown electric field strength, Emax. This property determines how high the largest field may be before material breakdown occurs. This type of breakdown is obviously referred to as catastrophic breakdown. The absolute value of E_{max} for SiC is frequently quoted as the relative strength of the E_{max} against that of Si. E_{max} of SiC is 10 times that of Si, thus a Si device constructed for a blocking voltage of 1 kV has a critical field strength of about 0.2 MV/cm, against the 2.49 MV/cm of the corresponding SiC device. The second most important parameter for power and high-frequency device applications is the material's thermal conductivity. An increase in temperature generally leads to a change in the physical properties of the device, which normally affects the device in a negative way. Most important is the carrier mobility, which decreases with increasing temperature. Heat generated through various resistive losses during operation must thus be conducted away from the device and into the package. The thermal conductivity of SiC is comparable and sometimes higher than cooper and silver at room temperature. SiC is considered a valid material for the production of radiation hard ionizing particle detectors for use in high-temperature and high radiation conditions under which conventional semiconductor detectors cannot adequately perform. SiC is considered a valid material for the production of radiation hard ionizing particle detectors for use in high-temperature and high radiation conditions under which conventional semiconductor detectors cannot adequately perform. The wide bandgap energy and low intrinsic carrier concentration (10^{-7} cm^{-3} in SiC against 10^{10} cm^{-3} for Si at room temperature) allow SiC to maintain semiconductor behaviour at much higher temperature than silicon, which in turn permits SiC semiconductor detector functionality at much higher temperatures than silicon detectors [Kon97]. A wide bandgap is useful in a detector, as it reduces significantly the rate of thermally generated charge carriers raising the noise level. Semiconductor detectors work

well even at high temperatures, when the dark current is low enough so that its associated noise is acceptable for the particular application. Furthermore, as the temperature increases, the dark current increases and consequently also the parallel white noise component with the consequent worsening of the energy resolution capability [Bal96]. SiC detectors can be used in high radiation condition for its high threshold displacement energy (Ed = 30 - 40 eV), being the minimum energy to displaced an atom from its lattice site. This value is comparable with the threshold displacement energy of diamond (Ed = 40 eV), one of the most precious material for detectors; thus SiC as diamond are more resistant to radiation with respect to Si (Ed = 13 eV). A low defect concentration on a material is a fundamental properties for a particle detector because defects can act as trapping centres for the charge carriers leading to incomplete charge collection and to a worse energy resolution.

V.4.3 Crystal structure and defects

Silicon carbide is a binary compound, tetrahedrally bonded, made by the same quantity of Si and C atoms, which are both group IV element materials [Nea03, Yu95]. The approximate distances between Si-C and Si-Si or C-C atoms are 1.89 Å and 3.08 Å, respectively. The basic structural unit in SiC is shown in fig. V-23
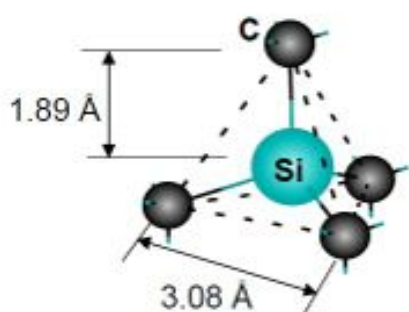

fig. V- 25 Tetragonal bonding of a central silicon atom with the four nearest carbon neighbours

The SiC compound exists in more than 200 different polytypes [Mat97], but the 3C, 4H and 6H structures are the most common. Each SiC bilayer can be situated in one of three possible positions with respect to the lattice, called arbitrarily A, B and C.

All crystals are characterized by the presence of defects, defined as a lack of crystal perfection in a certain region of the material. Defects may be classified into four categories according to their geometry and size inside the crystal structure.We can distinguish: zero-dimensional or "point defects" and "point-like defects"; one-dimensional or "line defects"; two-dimensional or "planar defects" and three-dimensional or "volume defects". A point defect is a deviation in the lattice periodicity at a single atomic site. It is due to a non equilibrium condition, such as during crystal growth or during thermal or mechanical material processing.They can be classified as intrinsic (or native) defect if it involves an atom of crystal and extrinsic defect if it is related to a foreign atom. The extrinsic defect usually comes from the dopant atom in a semiconductor material and is typically defined as an impurity. The extrinsic defect determines the electrical properties of a semiconductor crystal and is classified as a donor or acceptor impurity. In a SiC crystal, for example, nitrogen has a donor function and aluminium an acceptor function. The intrinsic defects consist in an erroneous arrangement of atoms inside the crystal lattice. There are many kinds of point defects. The lack of an atom in own lattice site is known as a vacancy. In SiC obviously we can distinguish between carbon vacancy V_C and silicon vacancy V_{Si}, depending on the configuration.

Unlike most other semiconductor materials of technological interest, silicon carbide does not show a liquid phase. The only way to synthesize, purify and grow silicon carbide raw material for device processing is by means of gaseous phases. Still research is carried out on the field of liquid phase epitaxy where silicon carbide layers are deposited from a supersaturated solution of carbon in silicon or silicon and carbon in a different solvent at high temperatures, but these techniques are merely used in experimental work. Silicon carbide can be synthesized by reducing sand ($SiO2$) in the presence of excess carbon in electrical arc furnaces. In this process, developed by Acheson in 1891, silicon carbide is formed as a sintered mass of small crystallites. Under certain growth conditions, larger single crystalline platelets of silicon carbide can be found in cavities and at the outer surface of the synthesized material. The focus during the recent years has been to increase the diameter of the wafers while at the same time reducing the density of

extended material defects such as micro-pipes and dislocations. For large area detectors, killer defects such as micro-pipes limit the potential yield from a wafer, rendering the process unaffordable due to the large waste. Secondly, defects such as basal plane dislocations act as recombination centres, which are detrimental when trying to optimise the detectors performance.

Due to the aforementioned imperfections still present in state-of-the-art silicon carbide wafers, these cannot be directly used for the active regions in electronic components. The achievable doping concentrations and inhomogeneities are generally too high, as well as the concentration of extended crystal defects. Therefore the commercially available silicon carbide wafers are mainly used as a substrate to support the epitaxially grown active layers. Epitaxy allows for a much more precise control of layer thickness, doping and homogeneity than achievable in bulk material growth. The gaseous source materials are available with a higher purity than solid silicon carbide source materials. The dopants are also provided by means of gaseous precursors, and a free control over the ratio between those different source gases determines the amount of incorporated doping impurities. The incorporation of dopants is not only controlled by the concentration of the dopant species, but also by means of a site competition affected by the Si/C ratio of the source gases.

V.4.4 Particles Detection

Radiation damage can affect various properties of a detector. Phenomena connected with the alteration of these properties are the increase of the leakage current, the decrease of charge collection efficiency (CCE) and the removal of free carriers from the conductive regions of the device. Radiation hardness is the inertness of these device parameters to high doses of particle irradiation [Leb02]. SiC, due to its wide gap and strength of its chemical bonds, has been seriously considered as a valid alternative to silicon for the production of radiation hard ionizing particle detectors. The usual design of a detector includes a p+/n, n+/p or a p+/ i /n+ diode structure or metal-semiconductor barriers, operating under reverse bias. A space charge region is formed, and the p+ and n+ regions act as

electrodes. Ionizing particles produce ionization in a semiconductor when they are slowed down or absorbed. Thus, electron-hole pairs are formed, which are then separated by the electric field and collected at the electrodes, yielding a current pulse in the detection circuit. The current generated is well correlated with the impinging particle energy. A detector should have a low concentration of impurities and defects, because these cause a diminution in the current pulse amplitude due to recombination of electron-hole pairs and scattering of charge carriers. Moreover, a low concentration of dopant impurities extends the thickness of the space charge region, i.e. the detection active region. The wide band-gap is useful, as it reduces significantly the rate of thermally generated charge carriers raising the noise level. On the other hand, it also represents a disadvantage: a particle with certain energy, ideally transforming all its energy for the generation of electron-hole pairs, generates 3 times more charge carriers in Si than in SiC. Detectors based on SiC, therefore, have lower pulse amplitudes. However, for low signals, the reduction of the noise level is more important than the reduction of the signal level, so that the overall signal-to-noise ratio (SNR) is improved for SiC-based detectors. Furthermore, SiC-based detectors still have a high SNR at temperatures which are unattainable for Si-based devices, needing external cooling to keep the intrinsic carrier level sufficiently low [Leb04].

SEMICONDUCTOR JUNCTIONS - Apart from being one of the simplest semiconductor device to study, the junction between two different materials is also the basic building block of all other semiconductor devices. Several possible material combinations can form electrically active junctions, and these can roughly be grouped into two classes:

- Metal-Semiconductor; whenever a metal contact is attached to a semiconductor this type of junction is formed. The physical parameters of the metal and the semiconductor determine the characteristics of this junction. Most important types are ohmic contacts and Schottky junctions.

- Homo-junctions; two pieces of the same semiconductor material but with different doping type and/or concentration are in metallurgical contact to each other. The most important type is the p/n junction. Here the basic principles of the

device electrical behaviour will be presented, starting from the ideal rectifier to the real device.

The ideal rectifier would allow current transport without loss in one direction while it would impose an infinite resistance on the current in the reverse direction. In real devices performance is limited by the physics of carrier transport over a potential barrier at the junction.

LEAKAGE CURRENT - The leakage current of a p-n junction consists of diffusion current from the quasi-neutral areas and generation current from the depletion area [Sze69]

$$J_R = J_{diff} + J_g \qquad 1)$$

where

$$J_{diff} \approx T^{\left(3 + \gamma/2\right)} \exp(-E_g / KT) \qquad 2)$$

depends essentially on the temperature T and on the energy gap E_g. Increasing the E_g from 1.1 eV (Si) to 3.2 eV (4H-SiC) we have a reduction of the diffusion term of the leakage current of about 17 orders of magnitude at room temperature. Furthermore, it can be observed that this diffusion current density does not depend on the reverse bias.

$$J_g \approx N_t (V_{bi} + V)^{1/2} \qquad 3)$$

where N_t is the density of the traps, V_{bi} the internal potential and V the external bias. This term is exactly the same in the case of the Schottky diodes. Instead, the term of the leakage current JR is extremely different in the case of the Sckottky diode with respect to the p/n junction. In fact, the leakage current density in this case is equal to:

$$J_R \approx A^{**}T^2 \exp\left[-q\left(\Phi_B + \Delta\Phi_B\right)/KT\right] \qquad 4)$$

where Φ_B is the Schottky barrier height and generally is qΦ_B<E_g/2. Furthermore, we have that the second term in the exponential factor $\Delta\Phi_B$ (Schottky Barrier Lowering), depends on the bias with the following expression:

$$\Delta \Phi_B \approx \left(qE_m / 4\pi\varepsilon \right)^{1/2} \quad \text{where } E_m = \left[\frac{2qN_D}{\varepsilon} \left(\frac{V + V_{bi} - KT}{q} \right) \right] \qquad 5).$$

E_m is the maximum electric field, N_D the doping concentration in the epitaxial layer, q the electronic charge, V_{bi} the internal potential and K the Boltzman constant. Then if we compare the reverse current density of a p/n junction J_{diff} (eq. 2) and the same parameter of a Schottky diode J_R (eq. 4) we can observe that the leakage current density of the p/n diode is lower with respect to the Schottky diode because in the exponential factor the p/n junction has a factor 2 (at least) in the barrier height and in the first case no dependence on the reverse bias is observed. For this reason the p/n junction can be of great interest in the realization of particle detectors where is essential to have the lowest leakage current at high voltage (necessary to deplete all the epitaxial layer) in such a way to improve the signal/noise ratio. The Schottky diodes are instead extremely easer in the realization process and can have a lower cost. For this reason they can be also interesting for some detectors applications.

V.4.5 Radiation Damage

The three main effects (bulk and surface defects) introduced by radiation are:

• displacement of atoms from their positions in the lattice (bulk).

• transient and long-term ionization in insulator layers (surface), but this is not our case.

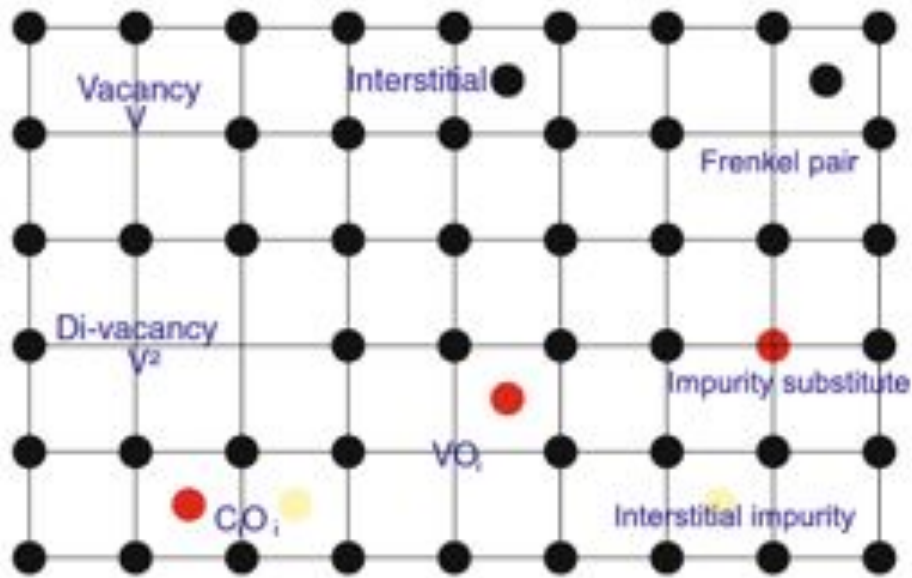• formation of interface defects (surface).

fig. V- 26 The figure shows an exemplary selection of atomic displacements in the lattice after collision with traversing particles. These vacancies, interstitials and complex clusters are creating new levels in the energy scheme of the semiconductor and therefore change the elementary properties.as abbreviation, vacancies are labelled V, interstitials I, di-vacancies V2. Impurities are labeled with their atomic sign, their index defines their position as substitute or interstitial, e.g. C_s or C_i.
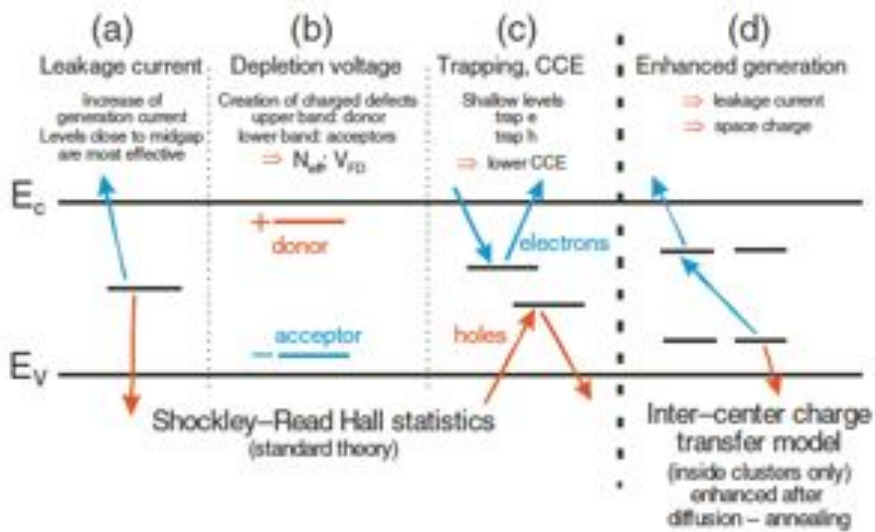

fig. V- 27 The different defect level locations and their effects.

Fig. V-27 shows all relevant defect levels due to radiation located in the forbidden energy gap.

a) Mid-gap levels are mainly responsible for leakage current generation, according to the Shockley-Read-hall statistics and decreasing the charge carrier lifetime of the material.

b) Donors in the upper half of the band gap and acceptors in the lower half can contribute to the effective space charge.

c) Deep levels, with trapping times larger than the detector electronics peaking time, are detrimental. Charge is "lost" the signal decreases and the charge collection efficiency is degraded. Defects can trap electrons or holes.

d) The theory of inter-centre charge transfer model says that combinations of the different defects in so called defect clusters additionally enhance the effects.

To understand electrical characteristics the voltage or current of an irradiated sensor the damage of the lattice created by traversing particles have to be taken into account. Traversing particles are not only ionizing the lattice but they also interact with the atomic bodies via the electromagnetic and strong forces. Atoms are displaced and create interstitials I, vacancies V and more complex constructs, e.g. di-vacancies. V_2 or even triple-vacancies V_3, also di-interstitials I_2 are common. All these defects deform the lattice. Some examples are depicted in fig.. In addition diffusing Si atoms or vacancies often form combinations with impurity atoms, like oxygen, phosphorus or carbon, again with different properties. All these lattice displacements populate new levels with no beneficial or malevolent results for detector operation in the band gap, changing the initial semiconductor properties. The resulting macroscopic property changes are:

i) increase of leakage current;

ii) change of depletion voltage level (N_{eff}) due to creation of mainly additional acceptor levels;

iii) decrease of charge collection efficiency due to defect creation, acting as traps for the generated carriers.

Defect analysis and even defect engineering was investigated in the R&D collaborations Rose, RD48, RD50 at CERN.

The defect distribution and clustering in fig. V-28 clearly show the difference between charged and neutral particles and their different energy levels. Especially the additional Coulomb force of a charged particle enhances small energy transfer and therefore local short distance defects, known as Frenkel pairs. Neutral particles, like neutrons, acting via the strong force result mainly in long-range cluster defects. With enough energy the initial primary knock on atom acts further on several additional lattice atoms. Clearly the long-ranging Coulomb force favours a small energy transfer and therefore point defects, while the strong force produces mostly clusters.

V.5 Simulations on the ion irradiation effects in SiC

The first activity carried out for the development of the detectors has been the realization of a series of simulation to investigate the effects of ion irradiation on the SiC material. Radiation damage can affect various properties of a detector.
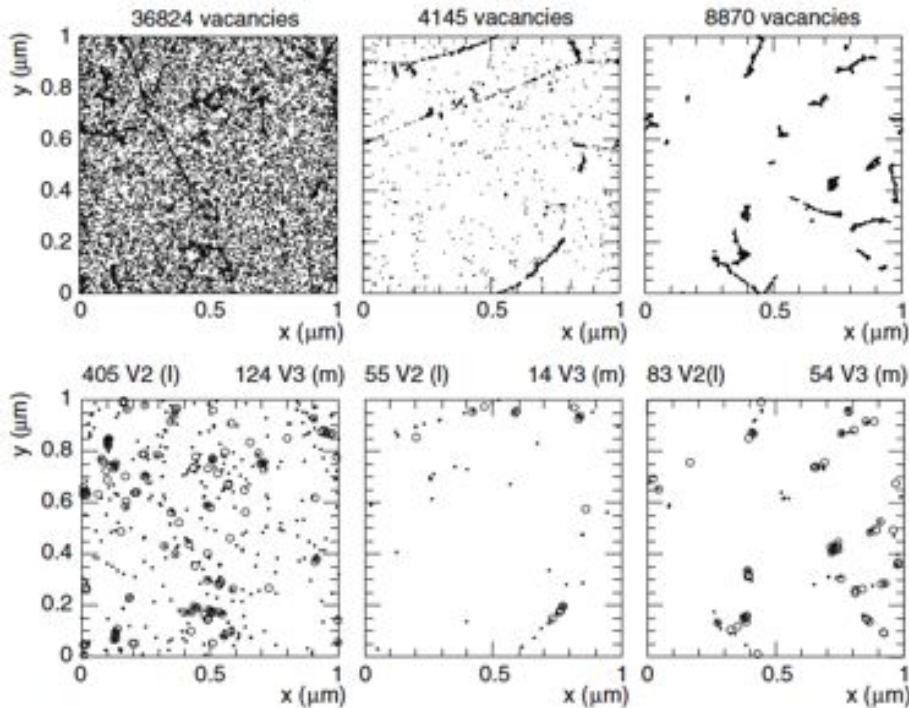

fig. V- 28 Simulation of defects formation with radiation and diffusion. The upper three simulations show the microscopic picture of defect distribution. About 10 MeV protons (left) produce a quite homogeneous vacancy distribution, while more energetic protons with 24 GeV (middle) form more

clustered and discrete defects. Neutrons with 1 MeV (right), interacting only due to strong interaction, do produce more isolated clustered defects. The plots are projections over 1µm of depth (z) and correspond to a fluence of $10^{14} n_{1MeV}/cm^2$. The lower three figures are displaying final constellations after a certain annealing time and therefore diffusion effects occurred. Many initial defects decay, e.g. Frenkel pairs, where interstitials recombine with vacancies. Others form more local clusters, like formations of di- and triple vacancies, with again different levels and therefore different properties.

Phenomena connected with the alteration of these properties are the increase of the leakage current, the decrease of charge collection efficiency (CCE) and the removal of free carriers from the conductive regions of the device. Radiation hardness is the inertness of these device parameters to high doses of particle irradiation. SiC, due to its wide gap and strength of its chemical bonds, has been seriously considered as a valid alternative to Si for the production of radiation hard ionizing particle detectors. The leakage current of a p-n junction consists of diffusion current from the quasi-neutral areas and generation current from depletion area [Sze69]. The second term depends essentially on the temperature T and on the energy gap Eg . Increasing the Eg from 1.1 eV (Si) to 3.2 eV (4H-SiC) determines a reduction of the diffusion term of the leakage current of about 17 orders of magnitude at room temperature($\sim$ 300K). Following these indications we started the research work using simulation with the aim to study the point of view of defects dislocation generated by an^{18}O at 25 MeV/A. Simulations of irradiation were made for SiC with ion beams O^{18} 60 MeV.A and 2 MeV. For this work we used the SRIM [Zie69] software; it is a collection of packages which calculate many features of the transport of ions in matter. During the collisions, the ion and atom have a screened Coulomb collision, including exchange and correlation interactions between the overlapping electron shells.

The fig. V-29 shows the distributions of the induced defects (plots are projections on 1 micron of depth and correspond to a dose of 10^{14} particles (MeV.A / cm^2)
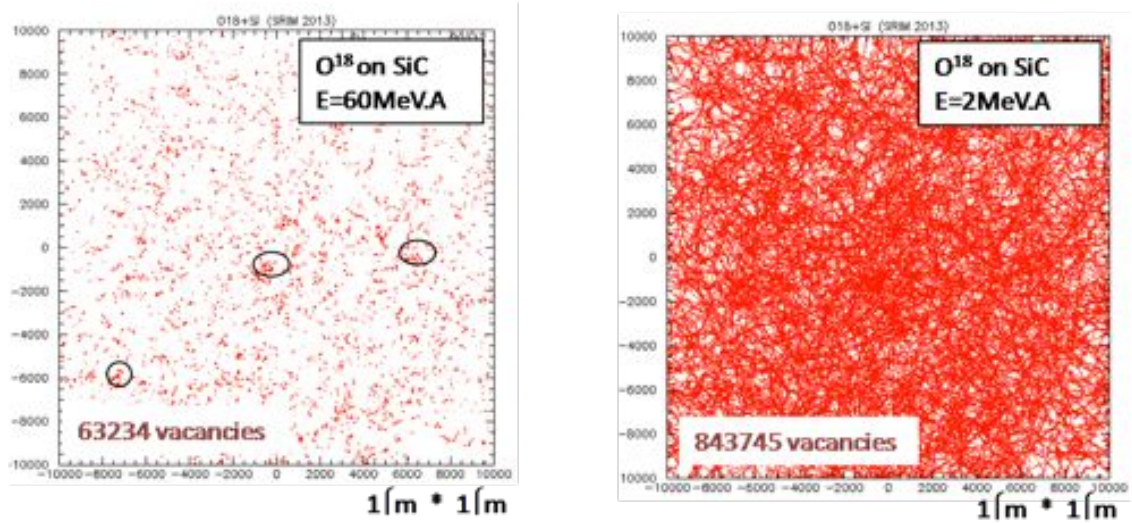
fig. V- 29 Distributions of induced defects in SiC, according to SRIM simulations, from O^{18} ions from 60MeV.A (left) and from 2 MeV.A (right).

The less energy beam (O^{18} 2 MeV.A) causes a very homogeneous distribution of holidays, the high-energy beam (O^{18} 60 MeV.A) instead determines the formation of clusters and more complex defects. The following fig. V-30 shows the number of simulated vacancies as function of protons (at 25 MeV and 1 GeV) and ^{18}O (25 MeV/A) ions fluency. One can notice that the number defects create in the same stage from protons beam at 25 MeV/A is about two orders of magnitude smaller then the corresponding number coming from heavy oxygen ions of 25 MeV/A. In fig. V-31, we show the results of such calculation; we can be notice as several order of magnitude of leakage current increased are expected at high doses irradiation/fluency. Such increase could be acceptable for SiC detectors; they have a leakage current five order of magnitude less than Silicon detectors. (Where the maximum of acceptable fluency is about 10^9 heavy ions/cm^3).
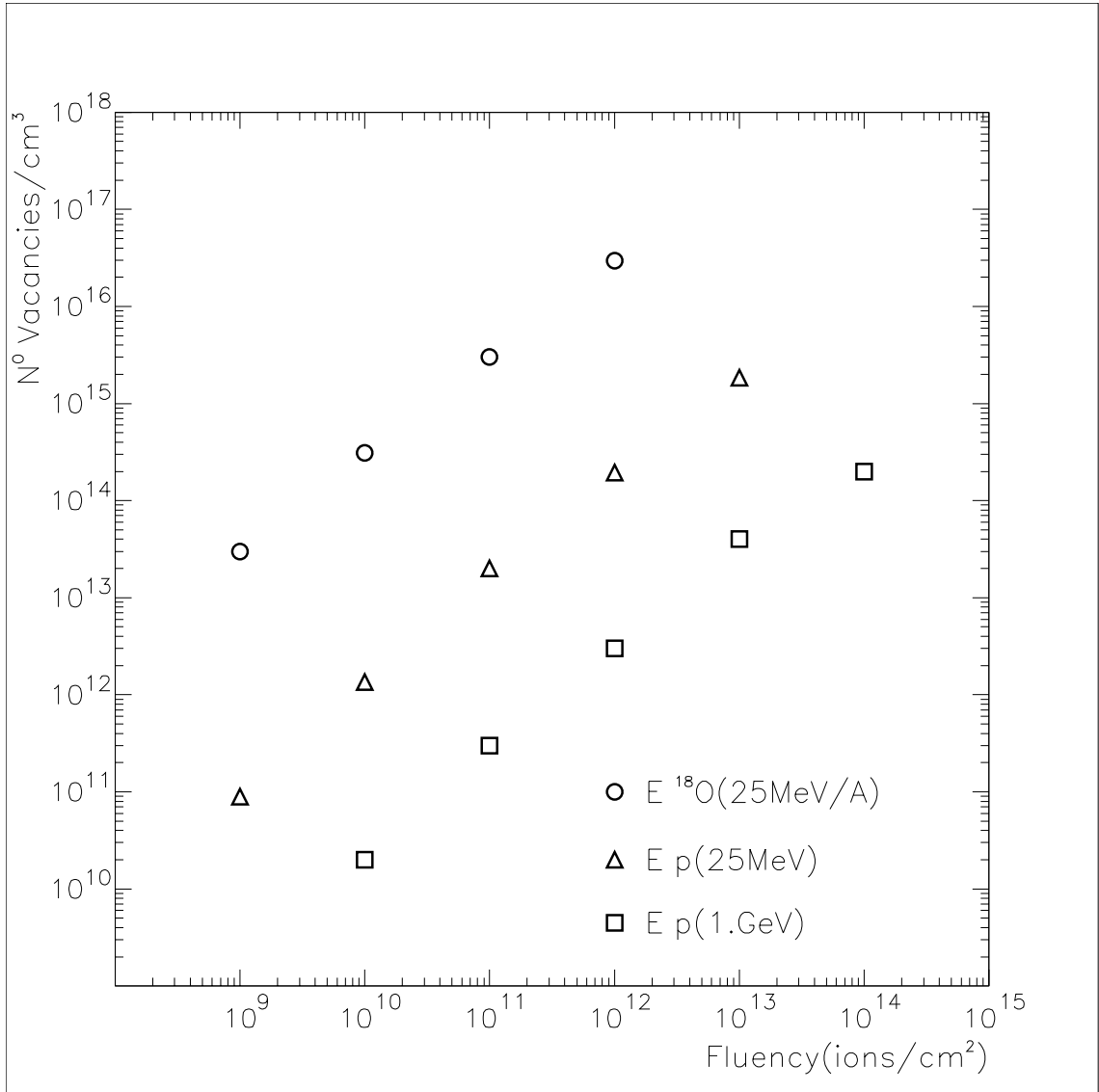
fig. V- 30 The figure shows the comparison of Number of silicon vacancies%Fluency in SiC stage; the solid symbols indicate the stage of the detector (with a thickness of 100μm. The following energies has been simulated: oxygen ions at 25 MeV/A (circle), protons ions at 25 MeV/A(triangle) and protons ions at 1 GeV/A(square).
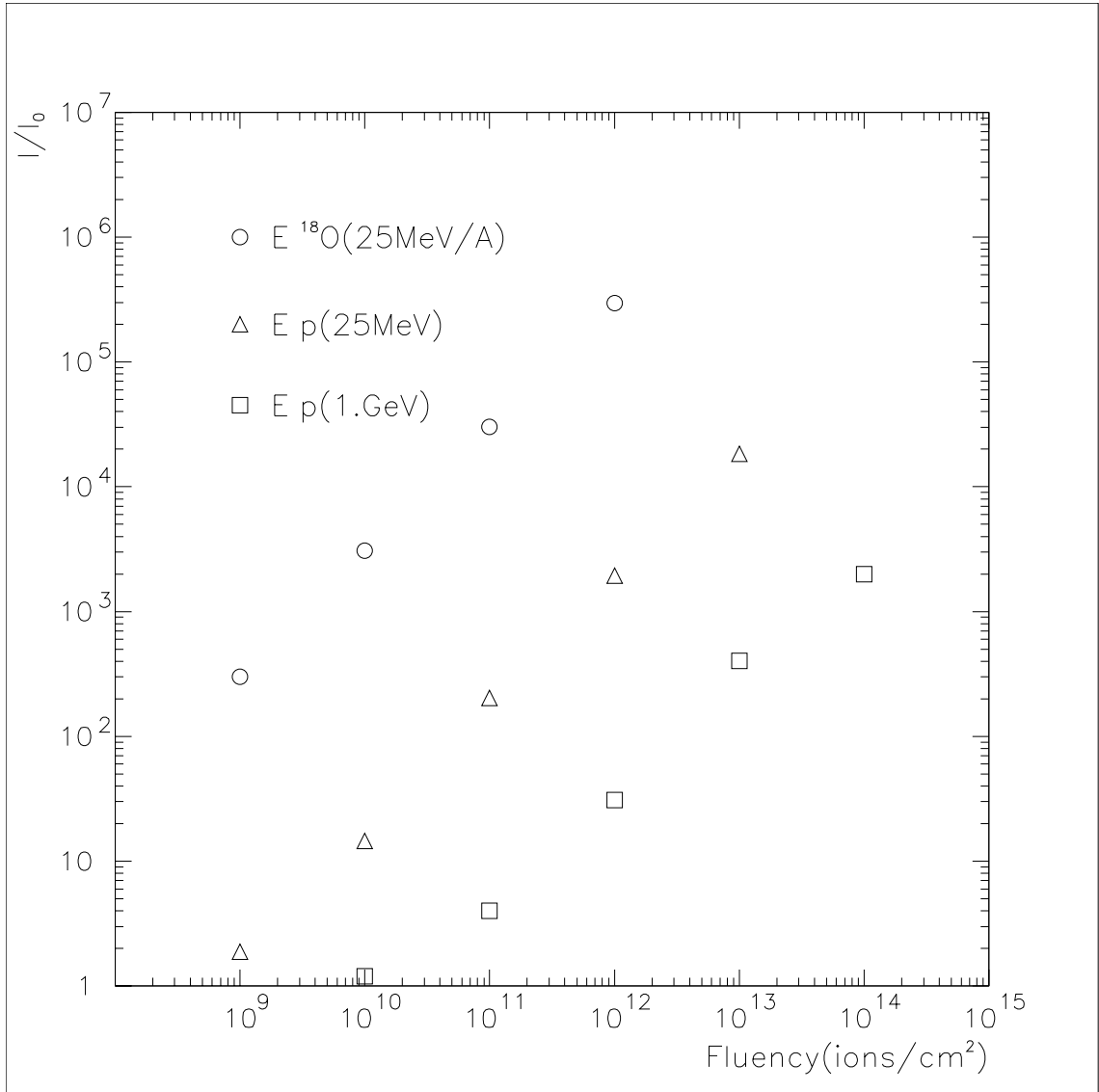
fig. V- 31 The figure shows the comparison of Increment of current leakage%Fluency. The solid symbols indicate the stage of the detector (with a thickness of 100μm). The following energies has been simulated: oxygen ions at 25 MeV/A (circle), protons ions at 25 MeV/A(triangle) and protons ions at 1 GeV/A(square).

Several works concerning radiation hardness of SiC material are available in literature. Some of them have been previously mentioned, in particular in relation to the radiation hardness of MIP (the results of R&D collaborations Rose, RD48, RD50 at CERN). The radiation damage of MIP particles is quite different respect to that of intermediate energies heavy ions, where huge number of defects is created in this last case. This situation is clearly visible in the results of TRIM simulation reported in fig. V-32.
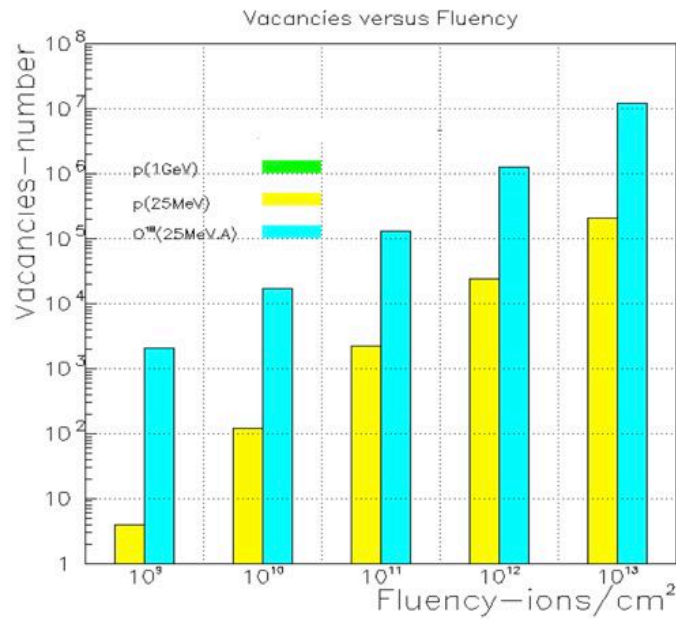
fig. V- 32 Number of simulated vacancies as function of protons (25MeV and 1GeV) and $^{18}O(25MeV/A)$ ions fluence This is related to the 100um stage detector.

V.6 Experimental setup

Tests were carried out for the preparation of the experimental set-up which have provided for the following activities:

testing with old generation devices

preparing of radiation lines

tests for comparison devices

V.6.1 Test and set-up

The old generation detectors, products from CNR-IMM in Catania, were the Schottky diodes (metal-semiconductor junctions) in 4H-SiC realized on epitaxial films of thickness equal to 37 microns and the n-type doping equal to $N_D = 4.8$ $x10^{14}$ cm^{-3}, the metal used for the Schottky contact is the Ni_2Si.
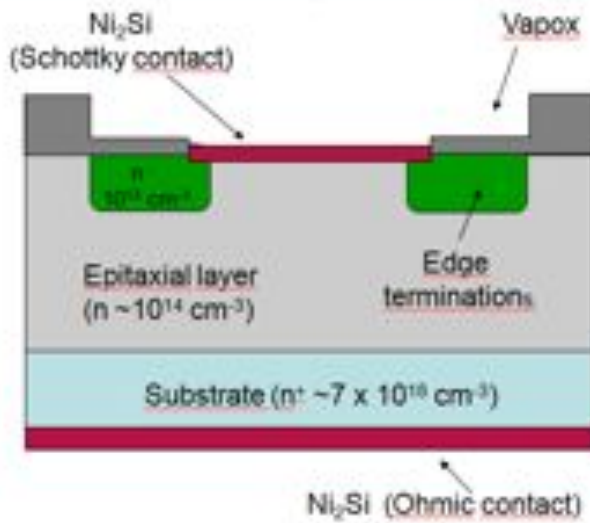
In fig. V-33 the sketch shows the device in cross-section.

fig. V- 33 Sketch of device in cross-section.

The devices used for tests contain two diodes square with area A = 1 mm² and one with A = 2.25 mm², as shown in fig. V-34. Then each module contains three analysable detectors.

fig. V- 34 SiC detectors with different area A = 1 mm² and 2.25 mm²

Measurements, under reverse bias regime, were carried out to test SiC diodes at negative voltages; they represent the biasing system used for the detectors.

The SiC diodes, with area A = 2.25 mm², worked, under reverse bias regime, up to 600Volt (see fig. V-35); instead the SiC diodes, with area A = 1mm², worked up to 1000Volt getting at a reverse current of I_R = 4.5 x 10^{-7} A.
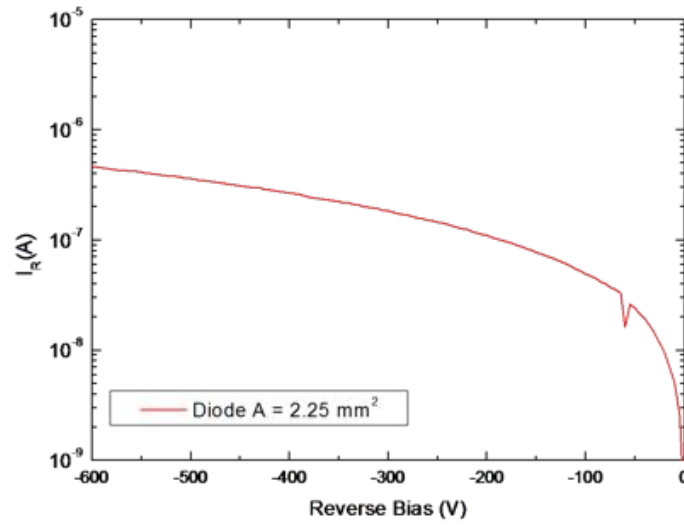
fig. V- 35 Reverse current for SiC diode with area A = 2.25 mm²

The measures, in reverse bias system, evaluated the operability of the range for devices.

The detectors are mounted on the custom PCB golden, shown in the next figure.
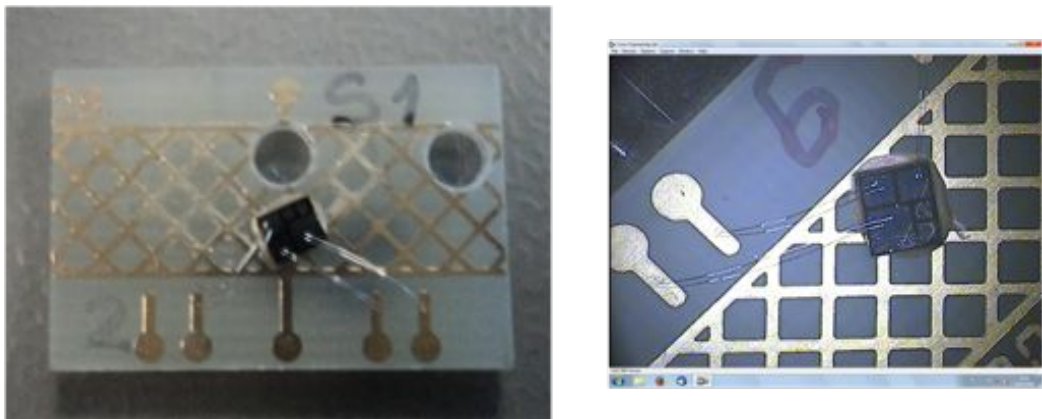

fig. V- 36 Bonding on SiC detectors for test

For a resolution were carried out testing by exposure to an alpha source with three peaks (^{239}Pu - ^{241}Am – ^{244}Cm). The next figure represents block diagram for experimental setup.
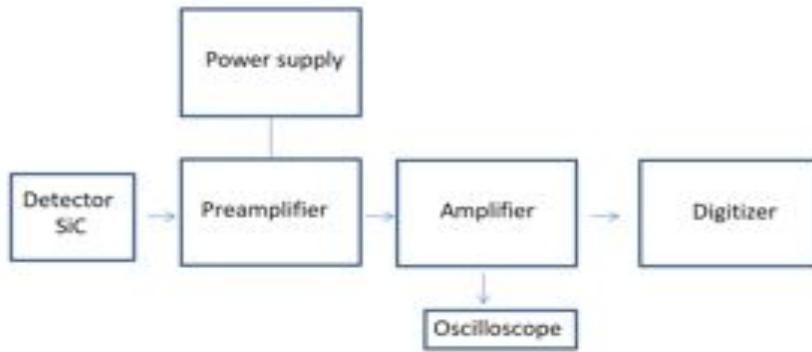
fig. V- 37 Block diagram for experimental setup

A first prototype, with preamplifier read-out, has been developed at LNS as shown in the fig.V-38.
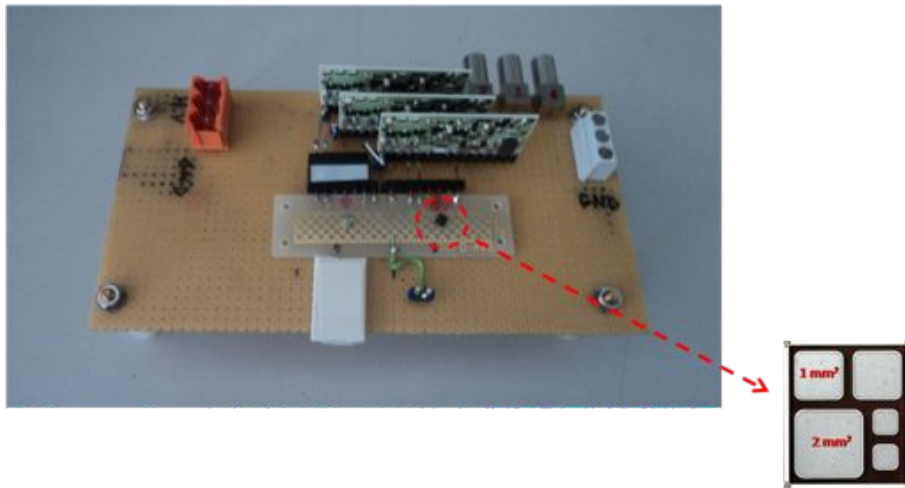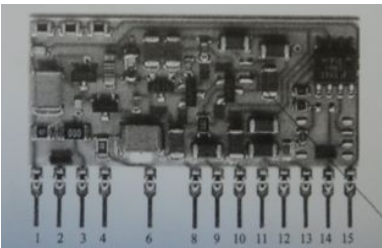
fig. V- 38 Circuit realized for prototype testing detectors

The next figure shows the features of the integrated preamplifier.

Energy sensitivity	90mV MeV
Output Voltage	8V max. (4V on 50ohm Term.)
Decay Time	600uS
Noise	1.5 KeV (0 pF) 12 eV/pF Slope
HV to Input resistance	100 Mohm
Max HV input	200V
Test capacitance	1pF
Power consumption	250mW

fig. V- 39 Features integrated preamplifiers used for testing

The fig. V-40 shows the circuit with the detector and the source placed above.
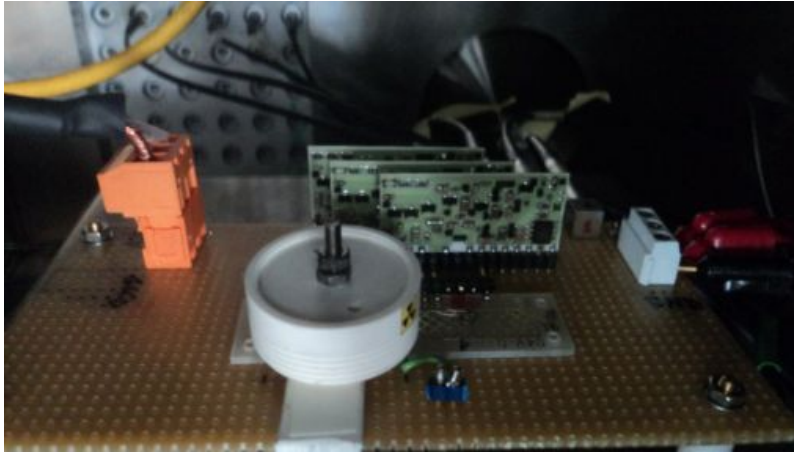
fig. V- 40 Experimental set-up with the source placed inside of the vacuum chamber.

In the preliminary phase of the testing it was necessary to optimize the geometry, since the area of prototype detectors is very small; we have operated with detectors with an area of 1 mm^2 and 2.25 mm^2. Another problem has been to minimize the distance between the detector and the source, placing it above such as not to cause breakage of the bonding.

In the next figures the experimental setup is shown for tests: in the left side the vacuum chamber with detector and the alpha source inside and in the right side the electronics chain.

a)   (b)

fig. V- 41 Experimental set-up a) vacuum chamber b) electronics chain

Next figures show the spectrum obtained after exposure to the alpha source using the digitizer 16 channel CAEN family 742.

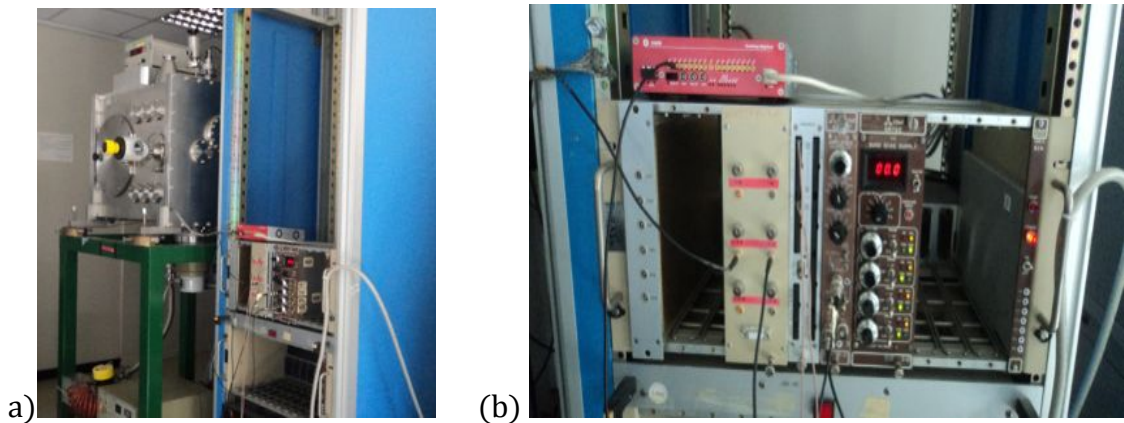The analysis carried out the energy resolution of the detectors. The following figures show spectra obtained after exposure to the alpha source using the digitizer 16 channel CAEN family 742 using different shaping times (0.5 μs, 1 μs, 2 μs and 3 μs).

fig. V- 42 SiC spectrum detector from exposure to the alpha source with three peaks acquired with shaping time 0,5 μs.

The Table V-5 shows the resolution obtained for different peaks.

Table V- 5 Energy resolution obtained on a SiC detector test exposure to the alpha source with three peaks acquired with shaping time 0,5 μs

Peak	Centroid [keV]	FWHM [keV]	Resolution [%]
^{239}Pu	5135,38	43,6	0,85
^{241}Am	5476,52	40,63	0,74
^{244}Cm	5799,58	44,33	0,76

fig. V- 43 SiC spectrum detector from exposure to the alpha source with three peaks acquired with shaping time 1 μs.

The Table V-6 shows the resolution obtained for different peaks.

Table V- 6 Energy resolution obtained on a SiC detector test exposure to the alpha source with three peaks acquired with shaping time 1 μs

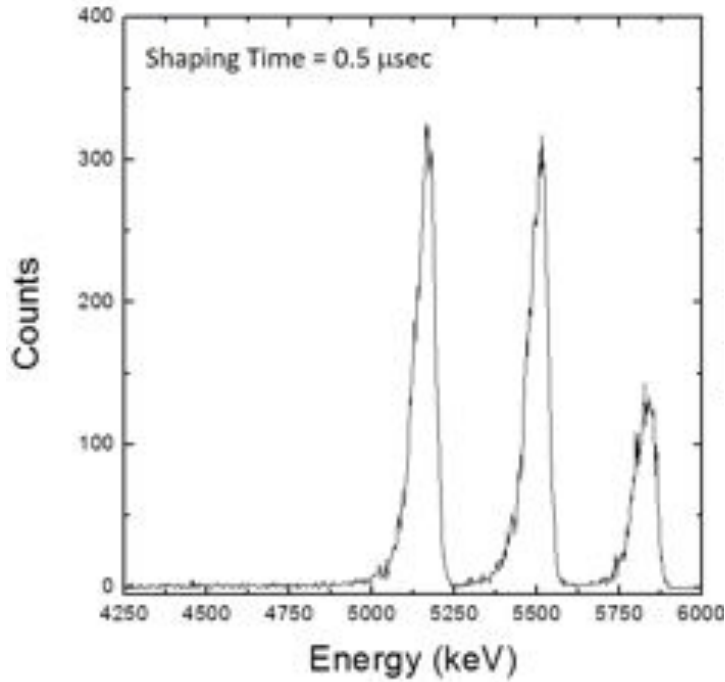| Peak	Centroid [keV]	FWHM [keV]	Resolution [%]
^{239} Pu	5137,39	37,57	0,73
^{241} Am	5478,97	31,95	0,58
^{244} Cm	5805,39	30,37	0,52

fig. V- 44 SiC spectrum detector from exposure to the alpha source with three peaks acquired with shaping time 2 μs

The Table V-7 shows the resolution obtained for different peaks.

Table V- 7 Energy resolution obtained on a SiC detector test exposure to the alpha source with three peaks acquired with shaping time 2 μs

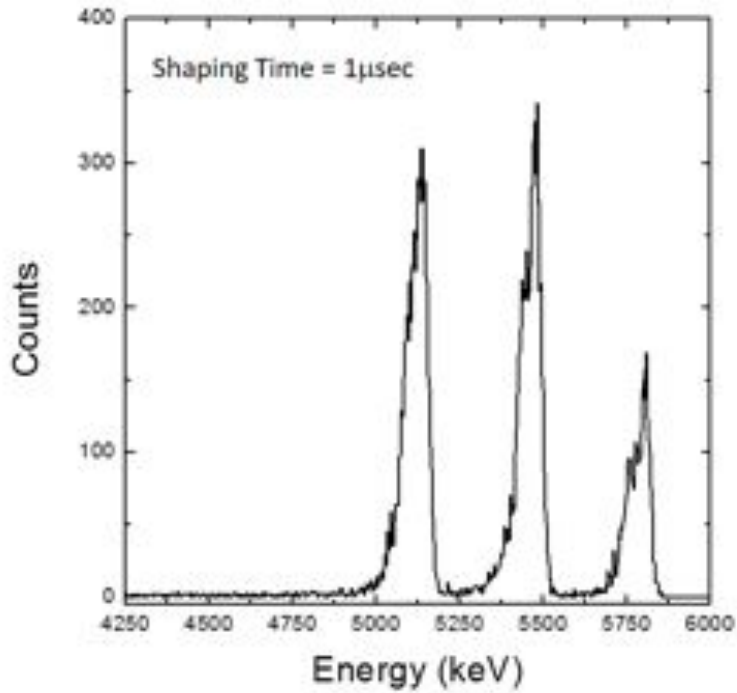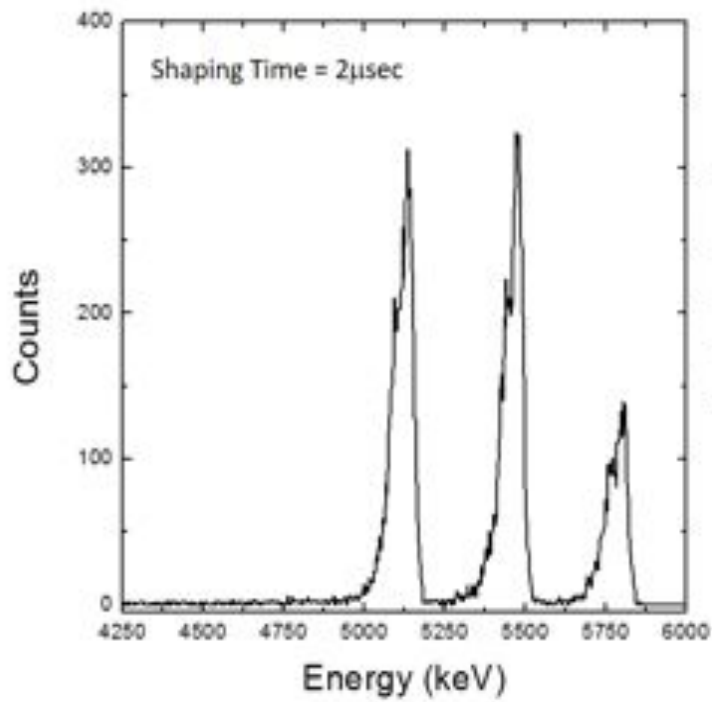| Peak	Centroid [keV]	FWHM [keV]	Resolution [%]
^{239} Pu	5137,92	33,43	0,65
^{241} Am	5477,83	29,42	0,54
^{244} Cm	5803,51	30,52	0,52
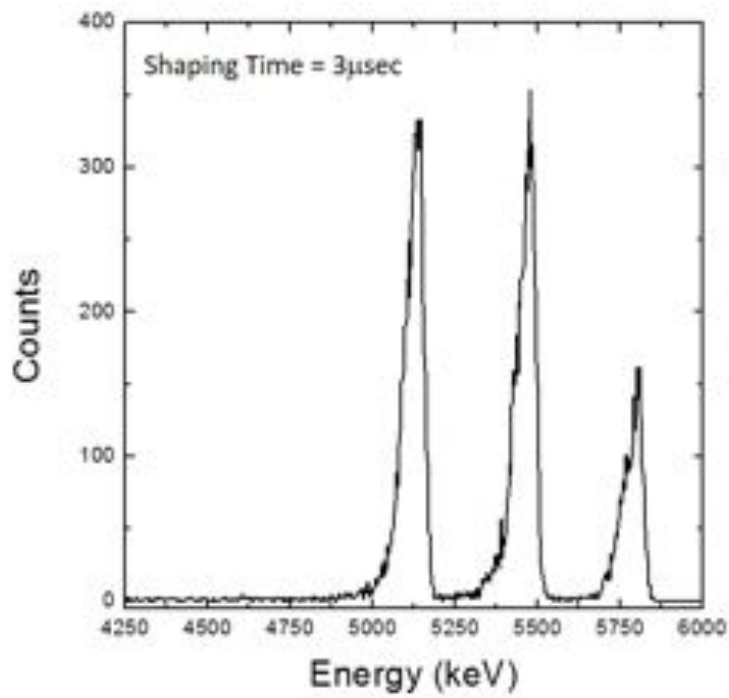
fig. V- 45 SiC spectrum detector from exposure to the alpha source with three peaks acquired with shaping time 3 µs

The Table V-8 shows the resolution obtained for different peaks.

Table V- 8 Energy resolution obtained on a SiC detector test exposure to the alpha source with three peaks acquired with shaping time 3 µs

Peak	Centroid [keV]	FWHM [keV]	Resolution [%]
^{239} Pu	5138,47	35,83	0,70
^{241} Am	5478,80	30,71	0,56
^{244} Cm	5804,53	29,32	0,50

V.7 References

[Ada78] J.M. Adams and G.White, Nucl. Instr. Meth. 156 (1978) 459-476

[Bal96] Baliga, B. J., Power Semiconductor Devices, Boston, MA: PWS Publishing Company, (1996), p. 74

[Bec76] Becchetti, F. D., Thorn, C. E., and Levine, M. S., Nucl. Instrum. Meth. 138:93 (1976).

[Ber24]J. J. Berzelius: Annalen der Physik 1, p. 169 (1824).

[Bir64] Birks, J. B., The Theory and Practice of Scintillation Counting, McMillan Co., New York, 1964.

[Boi06] C. Boiano, et al., IEEE Transactions on Nuclear Science NS53 (2) (2006) 444.

[Boi08] C.Boiano,et al., IEEE-Nuclear Science Symposium Conference RecordN30–46 (2008).

[Bol61] L.M. Bollinger, G.E. Thomas, Rev. Sci. Instrum. 32 (1961) 1044.

[Bra68]Brand, W., Dobrin, R., Jack, H., Aubert, R. L., and Roth, S., Con. J. Phys. 46:537 (1968).

[Bro59]F.D. Brooks, Nucl. Instr. and Meth. 4 (1959) 151.

[Bro74]Brooks, F. D., and Jones, D. T. L., Nucl. Instrum. Meth. 121:69 (1974)

[Bro79]F.D. Brooks, Nuclear Instruments and Methods 162 , 477,(1979)

[Bue93]L.Buermann et al, Nucl. Instr. & Meth.in Phys. Res. A332 ,483-492,(1993)

[Buz11]P. Buzhan et al. An advanced study of Silicon Photomultiplier. ICFA Instrum.Bull. 23 (2001) 28-41

[Cav13]M. Cavallaro et al. NIM A 700 65 (2013)

[Cho52]Chou, C. N., Phys. Rev. 87:376, 904 (1952)

[Cla09] Clarke S D, Flaska M, Pozzi S A and Peerani P, (2009) Nucl. Instr. Meth. A 604 618-623

[Cra70]Craun, R. L., and Smith, D.L., Nucl. Instrum. Meth.,80,239,(1970)

[Cri95] Christensen N L, Hammer B E, Heil B G and Fetterly K 1995 Phys. Med. Biol. 40 691-697

[Dal12]G.F. Dalla Betta, C. Da Via, et al, JINST 7(2012) c10006

[Dre03]P. Drexler, et al., IEEE Transactions on Nuclear Science NS50 (4) (2003) 969.

[Dro80]M. Drosg et al. NIM 176 477 (1980).

[Eng82]S. Engels and A. Nowak: Auf der Spur der Elemente (VEB DeutscherVerlag fur Grundstoffindustrie, Leipzig, 1982), 3rd edn.

[Fla07]Flaska M and Pozzi S A 2007 Nucl. Instr. Meth. A 577 654-663

[Fly64]Flynn, K. F., et al., Nucl. Instrum. Meth., 27, 13, 1964

[Geant] http://geant4.cern.ch/index.shtml

[Haw07]Hawkes R, Lucas A, Stevick J, Llosa G, Marcatili S, Piemonte C, Guerra A D and Carpenter T A 2007 IEEE NSS MIC Conf. Rec. vol M18-118 pp 3400-3403

[Ing77]Ingersoll, D. T., and Wehring, B. W., Nucl. Instrum. Meth. 147:551 (1977).

[Kno00]Knoll, G.F. Radiation detection and Measurement.. John Wilsey & Sons, 2000.

[Kol04]Kolar, Z. I., and den Hollander, W., J. Appl. Radiat. Isotop. 61:261 (2004).

[Kon97]A. O. Konstantinov, Q. Wahab, N. Nordell and U. Lindefelt, Appl. Phys. Lett., Vol. 71, No. 1, (1997), pp. 90–92

[Koo93]R. Koohi-Fayegh et al, Nucl. Instr. & Meth. In Phys. Res. A329 (1993) 269-276

[LaV06] F. La Via, G. Galvagno, G. Foti, M. Mauceri, S. Leone, G. Pistone, G. Abbondanza, A. Veneroni, M. Masi, G.L. Valente, D. Crippa, Chemical Vapour Deposition, 12, 509 (2006).

[LaV08] F. La Via, G. Izzo, M. Mauceri, G. Pistone, G. Condorelli, L. Perdicaro, G. Abbondanza, L. Calcagno, G. Foti, D. Crippa, Journal of Crystal Growth, 311, 107 (2008).

[LaV14] F . La Via, M. Camarda, A. La Magna, Applied Physics Review, 1, 31301 (2014).

[Leb02]A.A. Lebedev, V.V. Kozlovski, N.B. Strokan, D.V. Davydov, A.M. Ivanov, A.M. Strel'chuk and R. Yakimowa, Fiz. Tekh. Poluprovodnikov 36, 1354 (2002).

[Leb04]A.A. Lebedev, A.M. Ivanov, N.B. Strokan, Fiz. Tekh. Poluprovodnikov 38, 129 (2004).

[Lel55]J. A. Lely: Berichte der Deutschen Keramischen Gesellschaft 32, p. 229 (1955).

[Mac13]A. Macchi et al., Rev of Mod. Phys. 85 751 (2013).

[Mat97] H. Matsunami and T. Kimoto; Materials Science and Engineering, Vol. R20 (1997) pp. 125-166

[Nea03]D.A. Neamen; Semiconductor Physics and Devices, Basic Principles, 3rd ed., Mc Graw Hill, 2003

[Owe58] R.B. Owen, I.R.E. Trans. Nucl, Sci. NS-5 (1958) 198.

[Pas08]M. Passoni, M. Lontano, Phys. Rev. Lett. 101, 115001 (2008)

[Phi53] B.H. Phillips, K.R. Swank, Measurements of scintillation lifetimes, Rev. Sci. Instrrum. 24 (1953) 611.

[Poz09] Pozzi S A, Clarke S D, Flaska M and Peerani P, (2009) Nucl. Instr. Meth. A 608 310-315

[Pri08]S. Privitera et al. Sensors 2008, 8(8), 4636-4655

[San13]K. Sandeep et al. NIM A 728 97?101(2013).

[Sch12]K. Schmid et al. Rev. of Sci. Instr. 83 053304 (2012).

[Sze69]S.M. Sze, "Physics of Semiconductor Devices" (Ed. Wiley), (1969).

[Tag16]Taggart M.P. et al, Journal of Physics: Conference Series 763 (2016) 012007

[Tor02]Torrisi, Lorenzo. "Radiation damage in polyvinyltoluene (PVT)", Radiation Physics and Chemistry, 63 (2002).

[Tsir65]Tsirlin, Yu. A., et al. "Light yield of plastic scintillators in relation to the energy of external electrons", Zhurnal Prikladnoi Spektroskopii, 3 (1965).

[Ver68]V.V. Verbinski et al, Nucl. Instr. & Meth. 65 (1968) 8-25

[Vol66]Voltz, R., Lopes da Silva, J., Laustriat, G., and Coche, J. Chem. Phys. 45:3306 (1966).

[Vol68]Voltz, R., du Pont, H., and Laustriat, G., J. Physique. 29:297 (1968).

[Win7]R.A. Winyard and G..W. McBeth, Nucl. Instr. & Meth. 98 (1972) 525-533

[Wri53]Wright, G. T., Phys. Rev. 91:1282 (1953).

[Wri56] G.T. Wright, Proc. Phys. Soc B69 (1956) 358.

[Yu95] P.Y. Yu, and M. Cardona; Fundamentals of Semiconductors. Physics and Material Properties, Springer, Berlin, 1995

[Zai12] Zaitseva N, Rupert B L, Pawelczak I, Glenn A, Martinez H P, Carman L, Faust M, Cherepy N and Payne S (2012) Nucl. Instr. Meth. A 668 88-93

[Zie69]J.F.Ziegler et al.   The   stopping   and   range   of   ions   in   matter(Ed. Wiley).(1969).

CONCLUSIONS

In this thesis has been reported and discussed all the activities which has been developed during the period of the PhD treeing.

The work aim to prepare the program studies on nuclear physics and astrophysics, which will be conducted at the new ELI-NP Laser facility, which actually is under construction in Bucharest, Romania.

One of the key points of the realised work has been the simulations activity, which has been addressed to qualify all the aspects of the conceptual design study.

For the arguments treated, such activity has required also a multidisciplinary approach and knowledge in the fields of nuclear physics, astrophysics, laser and plasma physics join with also some competences on solid state physics related to the radiation detection.

The obtained results have been used to write the technical design report, which has been submitted at ELI-NP panel and successively approved by an international advisory committee.

In this respect the simulation activity has been related to the interaction of laser beam with the primary target in order to produce the main plasma stream, and successive interaction of this with the plasma target realised by the interaction of a secondary laser pulse with a gas jet target.

Has been simulated also all the nuclear events expected from the two plasmas interaction, taking in to account of the consolidate knowledge of nuclear phenomena like cross sections, reaction mechanisms, interaction models, etc.

Simulation has been conduced also in respect to particles detection, to evaluate the required performance and the main skills of the ideal detectors.

The second part of the PhD work has concerned to the experimental test, which have been performed in in several laboratories and in order to study and increase the level of knowledge on the different parts of the project.

In particular has been performed studies on the laser matter interaction at the ILIL laboratory of Pisa Italy and at the LENS laboratory in Catania, where (by using different experimental set-ups) has been investigated some key points concern the production of the plasma stream.

Test has been performed on several target configurations in terms of: composition, structure and size.

All the work has been devoted to optimize the conditions of target in order to have the best performance on the production yields and on energies distribution of the inner plasma ions.

A parallel activity has been performed in order to study the two main detectors, which will constitute the full detections system, which will be installed at the ELI-NP facility.

The selected detectors have been: the new generation of plastic scintillators for the neutrons detection and the new Silicon Carbide detectors. They are chosen for the excellent performances and work capabilities in hard environment such as the one generated by Laser-Matter interaction.

In conclusion the presented Ph.D has been developed in a frame of complexity coming out from the multidisciplinary of the arguments involved. This aspect has improved my personal skills, which will be used for the future of the project.

APPENDIX A

It 'was modified the acquisition system software for the digitizer CAEN 742

The 742 is a family of 12-bit, 5 GS/s Switched Capacitor Digitizers based on the DRS4 chip (Paul Scherrer Institute design). Considering the sampling frequency and the bit number, it is well suited for very fast signals generated by scintillators coupled to PMTs, Silicon Photomultipliers, APD, Diamond detectors and others. The analog input signals are continuously sampled into the DRS4 chip in a circular memory buffer (1024 cells) at the default frequency of 5 GS/s (200 ps of sampling period); frequencies of 2.5 or 1 GS/s can also be selected. As a trigger signal arrives, all the analog memory buffers are frozen and then digitized with a resolution of 12 bits into a digital memory buffer with independent read and write access. During the analog to digital conversion process, the x742 cannot handle further triggers, thus generating a Dead Time.

The problem was to use these data without stop the acquisition. To solve this problem we have used the IPC process, and we have used the shared memory to share a given region of memory. It was used the Shared memory and not other IPC concept, as semaphore or queue, because the Shared Memory is faster and the APIs use the mutex in order to use a memory without the OS can change it with background process.

The only trick in using shared memory is synchronizing access to a given region, the client shouldn't try to access the datat until the server is done. The memory used is redundant because we used the technique CoW(Copy on Write). The Cow implements a "duplicate" or "copy" operation on modifiable resources. If a resource is duplicated but not modified, it is not necessary to create a new resource; the resource can be shared between the copy and the original. Modifications must still create a copy, hence the technique: the copy operation is deferred to the first write. By sharing resources in this way, it is possible to significantly reduce the resource consumption of unmodified copies, while adding a small overhead to resource-modifying operations. The Computing reads the data in shared memory, using the copy ready and calculates the max values.

The idea is to implement a concept of server and client, as server the CAEN sw and client the new sw.

To implement the new sw, it was decided to use the C++ language, to guarantee the a sw plug and play, in the other word, to fulffil all C++ requirements, encapsulation, trasportability and more performance.

Here following the UML diagrams of our concept, in add it is possible to have more details of sw surfing the doxygen documentation
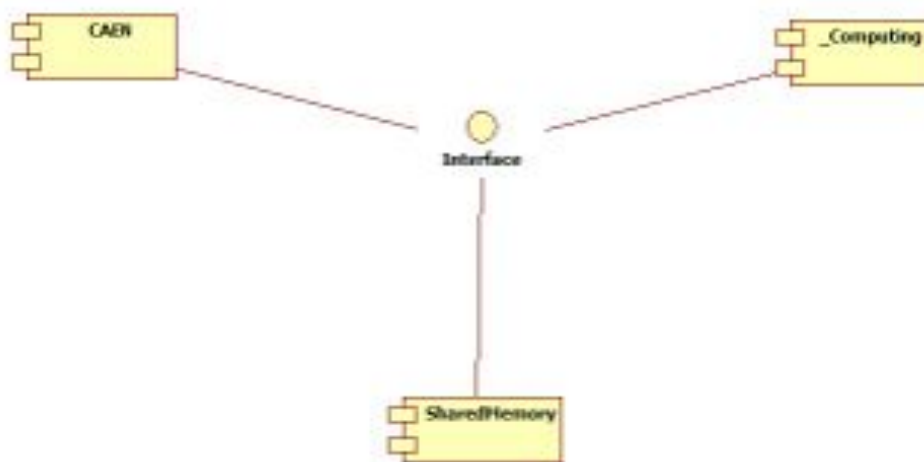
Here the core diagram of concept. We have a CAEN component that creates the data and in the translation unit Wavedump open a Shared Memory and copy the data fulffilling the structure t_sm with the data.

The Computing process open the Shared Memory, at the same memory location and reads the data ready. Once stored the data, it is called the method that computes the max value.

The Interface is the structure used t_sm
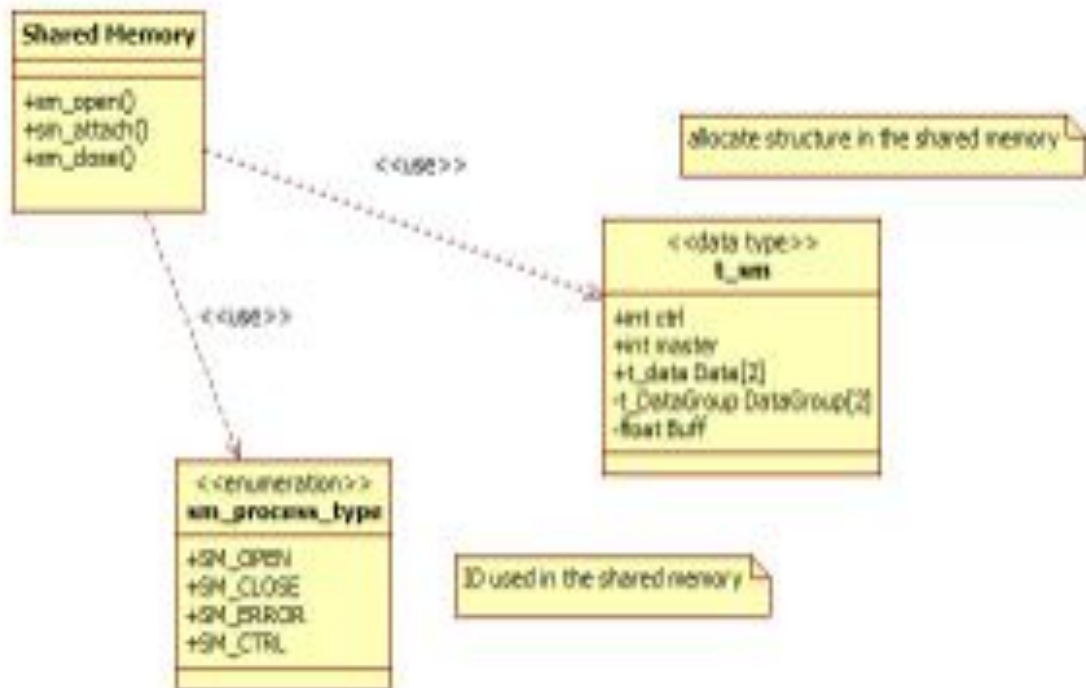
In this class diagram is the our Shared Memory. The idea is to pass some between two processes run simultaneously. We have two processes one serverf and other client. The server processi s the CAEN sw meanwhile the client is the Compunting.

In the Shared Memory it was implemented a data structure(t_sm) using the concept of CoW.

To initialize the shared memory, to open it and to attach the pointer to the struct t_sm, have been used the IPC(interprocess communication) functions.
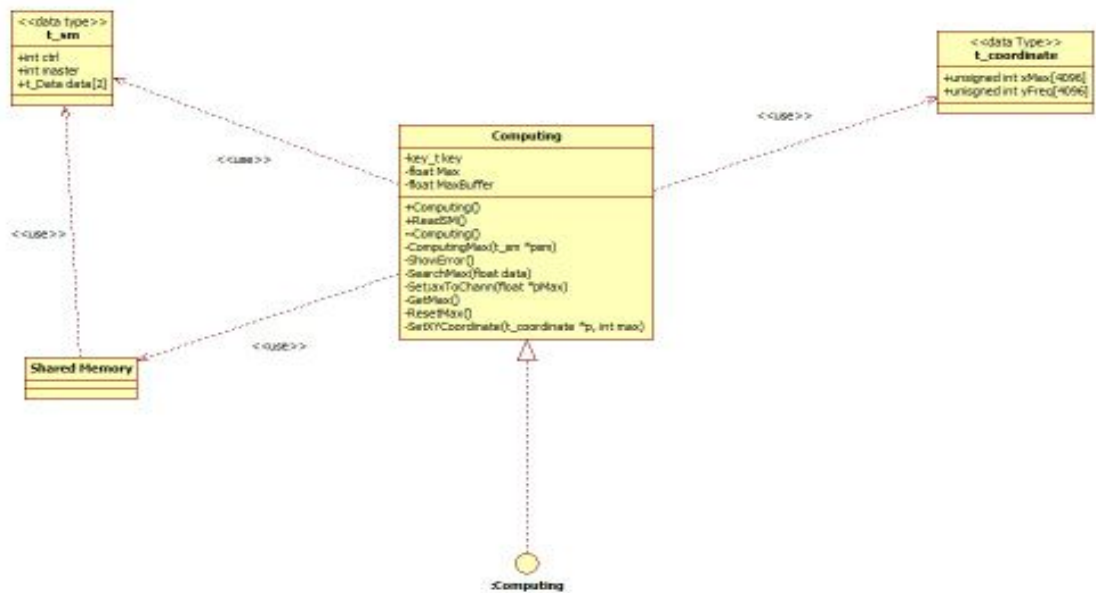
Here the computing class diagram. The process Computing is implemented in C++ language. The main class is Computing has the public function ReadSM and other private functions used to compute the max and the file to send to gnuplot.

Gnuplot is a graphic utility of Linux and it`s cross plattform. The tool, as Linux concept, uses the command line to plot some data.

The file create for gnuplot is the tollowing:
- first column is the XValue [0..4096],
- other column are the frequency of each value for channel.

At the end we have a matrix of frequency driven from channels

The Computing process run unsynchronized from the server process(CAEN), and can be terminate manually. The computing is the client process.

13/12/2016

Last Print